A STUDY ON THE FLOW CHARACTERISTICS OF AN INDUSTRIAL RADIANT TUBE BURNER

A Thesis submitted to Aston University for the degree of

DOCTOR OF PHILOSOPHY

In the Department of Chemical Engineering & Applied Chemistry

By

NICK TSIOUMANIS

School of Engineering and Applied Science

2008

ABSTRACT

The thesis presents an experimentally validated modelling study of the flow of combustion air in an industrial radiant tube burner (RTB). The RTB is used typically in industrial heat treating furnaces. The work has been initiated because of the need for improvements in burner lifetime and performance which are related to the fluid mechanics of the combusting flow, and a fundamental understanding of this is therefore necessary. To achieve this, a detailed three-dimensional Computational Fluid Dynamics (CFD) model has been used, validated with experimental air flow, temperature and flue gas measurements.

Initially, the work programme is presented and the theory behind RTB design and operation in addition to the theory behind swirling flows and methane combustion. NOx reduction techniques are discussed and numerical modelling of combusting flows is detailed in this section. The importance of turbulence, radiation and combustion modelling is highlighted, as well as the numerical schemes that incorporate discretization, finite volume theory and convergence.

The study first focuses on the combustion air flow and its delivery to the combustion zone. An isothermal computational model was developed to allow the examination of the flow characteristics as it enters the burner and progresses through the various sections prior to the discharge face in the combustion area. Important features identified include the air recuperator swirler coil, the step ring, the primary/secondary air splitting flame tube and the fuel nozzle. It was revealed that the effectiveness of the air recuperator swirler is significantly compromised by the need for a generous assembly tolerance. Also, there is a substantial circumferential flow maldistribution introduced by the swirler, but that this is effectively removed by the positioning of a ring constriction in the downstream passage. Computations using the k-ε turbulence model show good agreement with experimentally measured velocity profiles in the combustion zone and proved the use of the modelling strategy prior to the combustion study. Reasonable mesh independence was obtained with 200,000 nodes. Agreement was poorer with the RNG k-ε and Reynolds Stress models.

The study continues to address the combustion process itself and the heat transfer process internal to the RTB. A series of combustion and radiation model configurations were developed and the optimum combination of the Eddy Dissipation (ED) combustion model

and the Discrete Transfer (DT) radiation model was used successfully to validate a burner experimental test. The previously cold flow validated k-ε turbulence model was used and reasonable mesh independence was obtained with 300,000 nodes. The combination showed good agreement with temperature measurements in the inner and outer walls of the burner, as well as with flue gas composition measured at the exhaust. The inner tube wall temperature predictions validated the experimental measurements in the largest portion of the thermocouple locations, highlighting a small flame bias to one side, although the model slightly over predicts the temperatures towards the downstream end of the inner tube. NOx emissions were initially over predicted, however, the use of a combustion flame temperature limiting subroutine allowed convergence to the experimental value of 451 ppmv. With the validated model, the effectiveness of certain RTB features identified previously is analysed, and an analysis of the energy transfers throughout the burner is presented, to identify the dominant mechanisms in each region.

The optimum turbulence-combustion-radiation model selection was then the baseline for further model development. One of these models, an eccentrically positioned flame tube model highlights the failure mode of the RTB during long term operation. Other models were developed to address NOx reduction and improvement of the flame profile in the burner combustion zone. These included a modified fuel nozzle design, with 12 circular section fuel ports, which demonstrates a longer and more symmetric flame, although with limited success in NOx reduction. In addition, a zero bypass swirler coil model was developed that highlights the effect of the stronger swirling combustion flow. A reduced diameter and a 20 mm forward displaced flame tube model shows limited success in NOx reduction; although the latter demonstrated improvements in the discharge face heat distribution and improvements in the flame symmetry. Finally, Flue Gas Recirculation (FGR) modelling attempts indicate the difficulty of the application of this NOx reduction technique in the Wellman RTB.

Recommendations for further work are made that include design mitigations for the fuel nozzle and further burner modelling is suggested to improve computational validation. The introduction of fuel staging is proposed, as well as a modification in the inner tube to enhance the effect of FGR.

DECLARATION

No portion of the work referred to in this thesis has been submitted in support of an application for another degree or qualification of this or any other university or institute of learning.

COPYRIGHT

ACKNOWLEDGEMENTS

I would like to thank above all my academic supervisor Dr John Brammer for his invaluable supervision and assistance during the course of this research project. Also, my industrial supervisor for his industrial support and guidance. Furthermore, the Ansys CFX support team for their assistance, in addition to the CFD and computing support at Aston by the Department of Chemical Engineering and Applied Science's IT staff.

I would like to express my deep gratitude to all the staff at Wellman Furnaces Ltd and at the Department of Chemical Engineering and Applied Science in Aston University, Birmingham, for their theoretical and technical support, manufacture of components and industrial testing required undertaking this project.

Finally I would like to thank my family for their support during my research.

DEDICATIONS

I dedicate this work to one of the greatest car designers of all times who lived and created in Birmingham, UK, but came from Greece....

"One thing that I learnt the hard way – well not the hard way, the easy way – when you're designing a new car for production, never, never copy the opposition..."

"...mathematics is the enemy of every truly creative man..."

"...a camel is a horse designed by committee..."

Sir Alexander Issigonis (1906-1988)

PREFACE

The author was born in Greece in 1973 where he finished his primary and secondary education. From 1991 he studied in the UK where he was awarded a Bachelor of Engineering Honours Degree in Aerospace Engineering in July 1995. In 1997 he completed a Diploma in International Business and in 1998 he accomplished a study by research in low speed Aerodynamics and was awarded the Degree of Masters of Philosophy, all the above at the University of Manchester.

Later, he was employed for almost 4 years by the largest space company in Europe, Astrium UK, where he worked initially as a Spacecraft Structural Design Engineer and later Test Engineer in Spacecraft Propulsion.

He accomplished his military service in his home country as a Maintenance Engineer in UH-1H helicopters, based at the Stefanivikio base in Volos, central Greece.

In 2002, returning in the UK he contracted for a short period as Engineering Lead in firms at Harlow, Essex and Manchester, North West of the country.

Since September 2006 he has worked as an Aerospace Systems Engineer in the Aircraft Design Office at Marshall Aerospace Ltd, which is based in Cambridge and currently works for the C-130K Hercules aircraft support engineering and design team. Design and modifications cover aircraft projects for the RAF and different NATO forces. This company is the Design Authority of the aircraft type in Europe and the one of the largest in the Aircraft Maintenance industry sector worldwide.

He plays the drums, listens to different types of music, has been a member of different sports clubs and enjoys swimming and cycling.

CONTENTS

List of Figures

CHAPTER 5

List of Tables

Nomenclature

A, B	reactants and products limiter constants (-)
$\tilde{C}$	reaction progress variable (-)
C_μ, C_1, C_2, σ_k, σ_ε	k-ε turbulence model contain adjustable constants (-)
G_X	axial flux of axial momentum (N)
G_Θ	axial flux of swirl momentum (Nm)
k	kinetic energy of turbulence (m^2/s^2)
l	length scale (m)
l	radiation equation, total radiation intensity (-)
M_i	molecular weight (g/mol)
n	refractive index (-)
p	pressure (N/m^2)
Re	Reynolds number (-)
R_{ij}	Reynolds stress term (-)
R_i	reaction rate (-)
r_f	stoichiometric coefficient (-)
r, R	radius or positioning vector (m)
s	path length (m)
S_L	laminar burning velocity (m/s)
S_T	turbulent burning velocity (m/s)
S_F	explosion flame velocity (m/s)
S	swirl number (-)
t, dt	time (s)
T	temperature (degrees)
$\overline{u_1'^2}, \overline{u_2'^2}, \overline{u_3'^2}, \overline{u_1'u_2'}, \overline{u_1'u_3'}, \overline{u_2'u_3'}$	Reynolds stresses (-)
u', $\bar{u}$	RMS and mean value of fluctuating velocity component (m/s)
$v_{fuel}, v_{oxidant}, v_{product}$	volumes of species (-)
v_u	horizontal velocity or velocity component ($m\ s^{-1}$)

v_θ	tangential velocity (m s^{-1})
v_r	radial velocity (m s^{-1})
x, y, z	horizontal, vertical and depth spatial co-ordinate (m)
Y_f, Y_o, Y_p	mass fractions of fuel, oxidant and product (-)
$\tilde{Y}_\alpha$	TFC model, reaction progress variable (-)
y+	dimensionless grid constant (-)
Greek characters	
a	absorption coefficient (m^{-1})
β	turbulence factor (-)
Γ	diffusion coefficient (-)
δ	Kronecker term (-)
ε	dissipation energy of turbulence (m^2/s^3)
ς	direction vector (-)
ς'	scattering direction vector (-)
θ	velocity scale (m/s)
λ_u	molecular heat transfer coefficient (-)
λ	kinematic viscosity (m^2/s)
μ_t	turbulent viscosity (kg/ms^{-1})
μ	dynamic viscosity (kg/ms^{-1})
π	geometrical pi (-)
ρ	density (kg/m^3)
σ_s	scattering coefficient (m^{-1})
σ	Stefan-Boltzmann constant (5.672 x 10^{-8} W/m^2K^4)
τ_{ij}	stress tensor (N/m^2)
Φ	equivalence ratio (-)
Φ	scalar or vector property (-)
Φ	radiation equation, phase function (-)
ω	vorticity (s^{-1})
Ω'	radiation equation, solid angle (-)

1. INTRODUCTION

1.1 Project Description

The work presented in this thesis, comprises a study of the flow, combustion and heat transfer phenomena in a 20 kW (typically) Radiant Tube Gas Burner (RTB), using Computational Fluid Dynamics[1] modelling (CFD) validated by theory and full-scale experimentation. The work is a collaboration between Aston University and a local furnace and burner manufacturer, Wellman Furnaces Ltd and is funded by an EPSRC CASE award. Wellman Furnaces is based in Birmingham in the West Midlands of the UK and supplies a range of industrial process heat-treating atmosphere furnaces that are heated using either electric heating or gas fired RTBs[2]. These furnaces are utilised in varies industries including metal production, automotive, manufacturing and aerospace and have to meet demanding process requirements. The Wellman design of RTB has suffered with premature failure in certain parts of the combustion zone. The work has been initiated because of the need to address these mechanical failures in the burner which are related to the fluid mechanics of the combusting flow[3] and also to improve performance and to reduce emissions by investigating more radical design options.

In order to achieve these objectives a fundamental understanding of the fluid mechanics, thermodynamics and combustion behaviour is required. To this end a comprehensive modelling study of the complex three dimensional geometry of the complete burner is undertaken. Such a study has not been previously reported in the literature as presented in Chapter 3 of this Thesis.

1.1.1 General Design of Radiant Tube Burners

Besides energy cost issues, heating systems such as RTBs play an important role in the performance of a heat treating furnace, especially regarding temperature uniformity within the furnace and heat treated end product quality. The RTBs are powered down (turn down) automatically via the furnace gas control module, when the desired furnace temperature is reached, and then restarted when required.

The RTB design has a direct effect on:

- Net heat input and productivity, energy efficiency and operating costs
- Maintenance, burner tube life, furnace downtime and operating costs
- Flue gas emissions and pollution
- Ease of operation, investment costs.

The two main groups of radiant-tube concepts are non-recuperative and recuperative[4]. All non-recuperative radiant tubes have a burner at one end of the tube and the flue gas outlet at the other end of the tube, usually at the opposite wall in the furnace. In this way, the atmosphere internal to the furnace remains clean from burner exhaust gases and usually inert gases are used to control the surface treatment or annealing process of the heat treated parts. This category includes so-called diluted flame (or Flameless Oxidation - FLOX) burners[5]. In this type combustion requires a very high velocity flame, hence the need for complex and expensive burner set-up and the provision of high pressures for inlet air and fuel. However the majority of FLOX burners do not have a radiant tube and fire directly into the furnace.

In the recuperative RTB, flue gases exit through an exhaust that is located on the same side as the burner, thus removing the need for two holes in the furnace walls. This type of burner is also referred to as a single-ended RTB. Recuperative RTBs circulate the combustion gases within the radiant tube. The combustion products flow down an inner tube (the combustion chamber), impact the end of the radiant tube, turn through 180^{o} and reverse through the long annulus between the inner and outer (radiant) tubes. During this process, mainly due to the heat exchange between the flue gas and the two tubes, heat is distributed evenly over the radiant tube surface, reducing hot spots on both tubes, in comparison with the non-recuperative RTB.

The hot flue gas annulus extends the full length of the combustion air passage, thereby providing recuperative heat exchange with the combustion air. Devices to optimize the heat transfer between the two flows are frequently used in this region, such as flow vanes or helical coils. This heat transfer increases the overall thermal efficiency of the RTB.

For the manufacture of the RTB, high temperature corrosion resistance and good thermal property materials are used, such as stainless steel alloys and different Inconel alloys. In many applications ceramic materials and composites such as Silicon Carbide (SiC) are used, due to their advantageous thermal properties and strength in high temperature environments. These ceramic composites are increasingly used for the manufacture of outer (radiant) and inner burner tubes, although they represent higher cost in comparison with the metal tubes.

1.1.2 The Wellman 20 kW Radiant Tube Burner

Figure 1 presents a section of the Wellman RTB (WRTB). It represents a typical industrial recuperative, single-ended design and important burner components are pointed out.

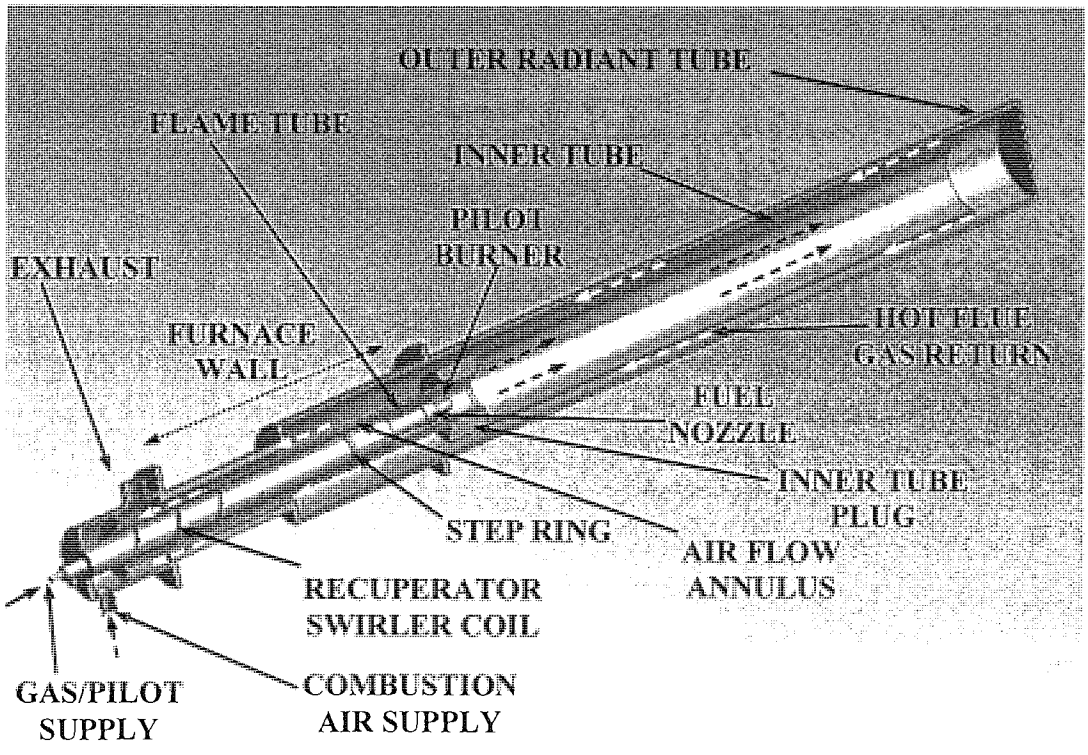

Figure 1: Typical section of the WRTB

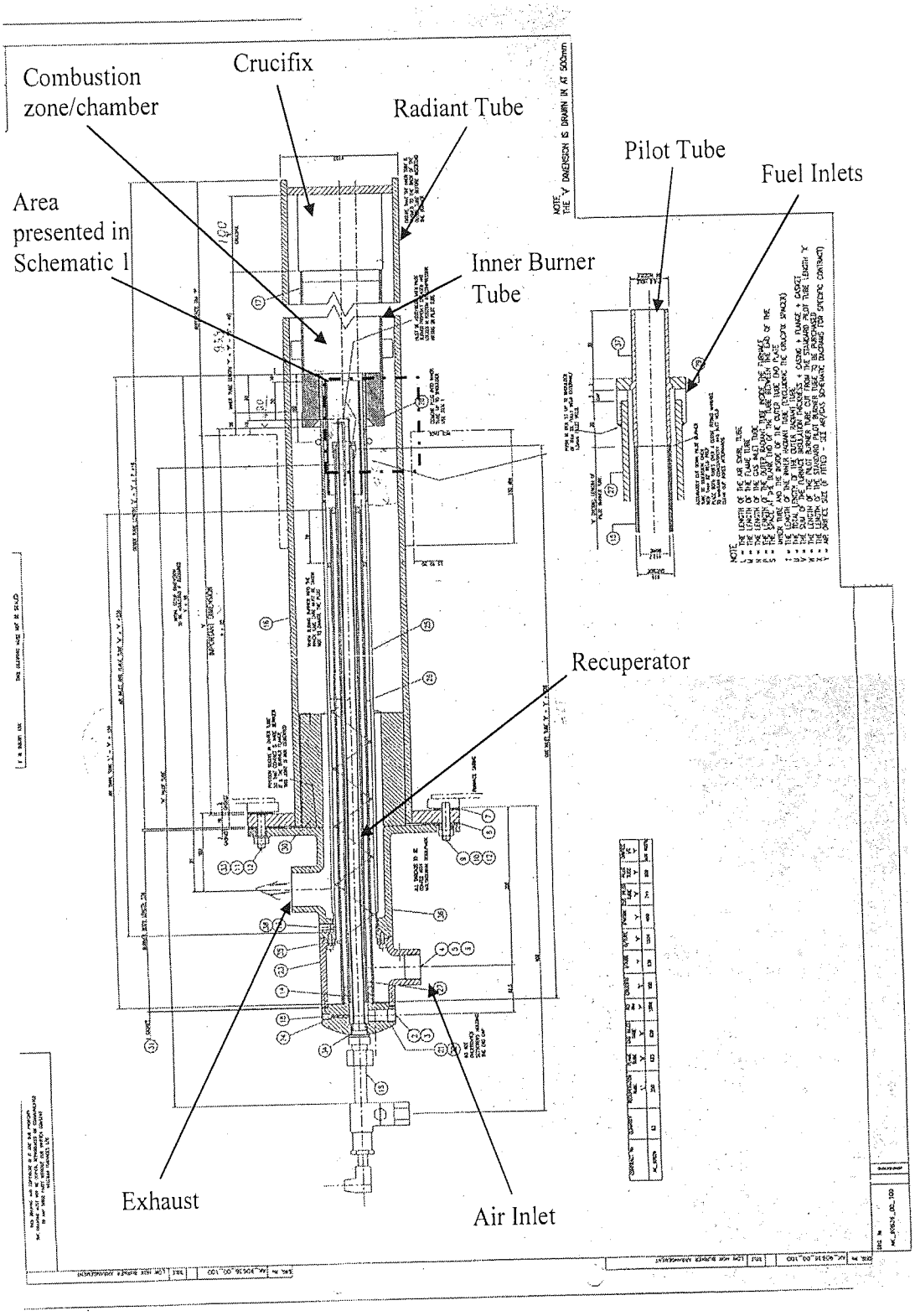

Figure 2: WRTB schematic (Sheet 1)

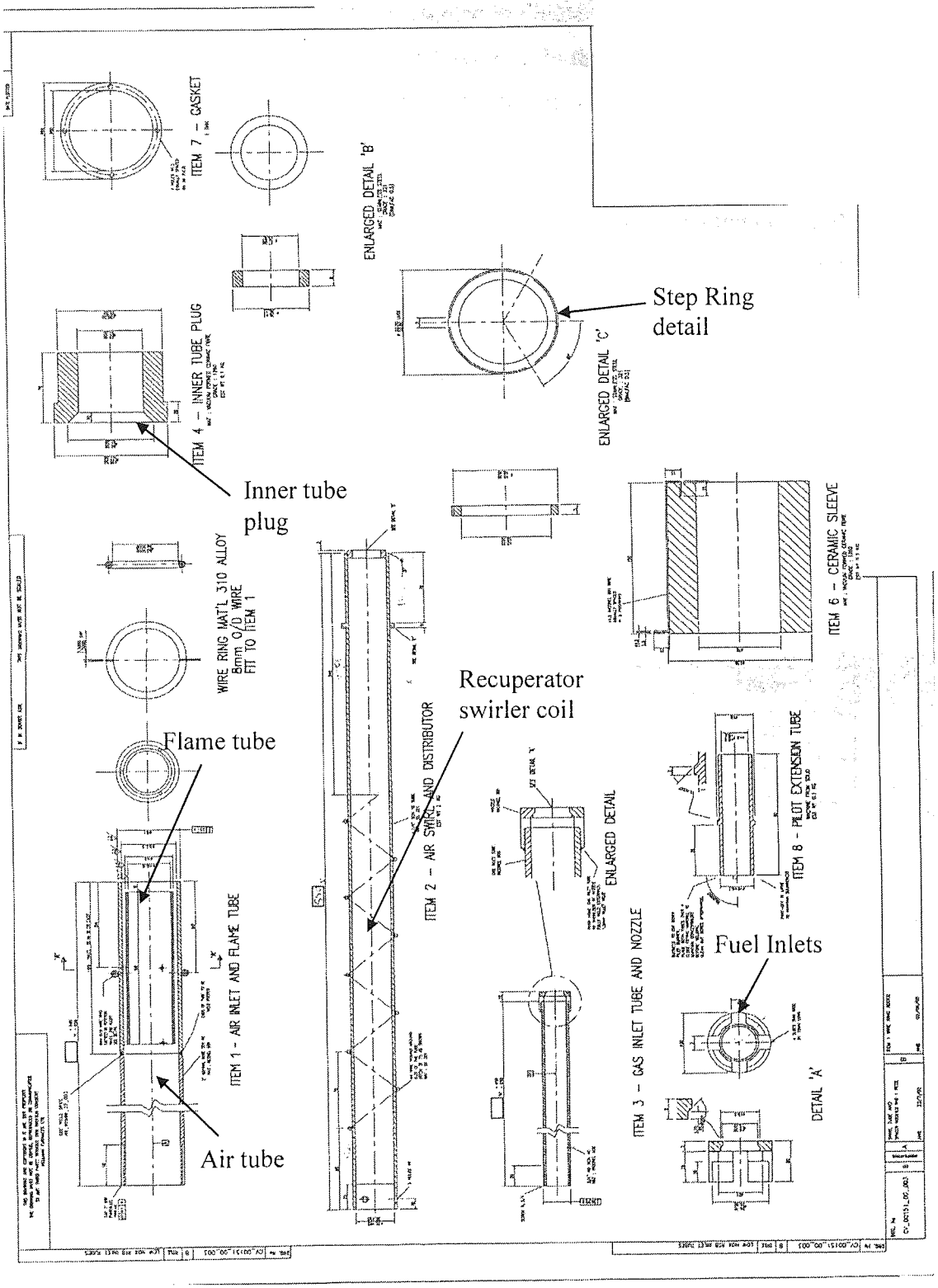

Figure 3: WRTB detail parts schematic (Sheet 2)

A schematic drawing of the WRTB is presented in Figure 2 and its main detail parts, which are of interest to this research exercise, in Figure 3. In the figures, WRTB and component serial numbers and manufacturing standards are omitted for confidentiality reasons. Table 1 and Figure 4 indicate the key WRTB face locations.

All the burner metal tubes are made of Inconel 600, an alloy commonly used in high temperature or corrosive environments, while the ceramic plug is made out of fibre Grade 1260.

End of recuperator swirler coil air	Face 1
Total air distribution swirl limiter ring	Face 2
Total air supply	Face 3
Inlet to flame tube and primary/ secondary air division	Face 4
Main burner gas supply	Face 5
Pilot tip and Main flame development	Face 6
End of flame tube	Face 7
Flame discharge	Face 8

Table 1: WRTB key design faces

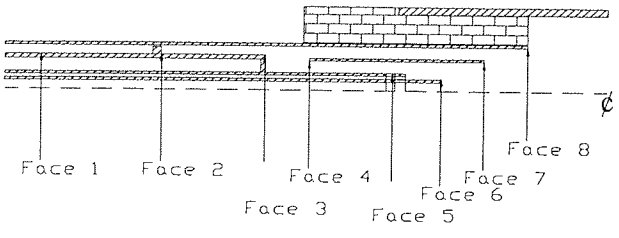

Figure 4: WRTB key design faces schematic

The WRTB is operated with a pilot burner located at the inlet and centre of the combustion chamber. The pilot tube burner is a Krom Shroder, model ZMI 16 x 800 LG[6]. An ignition electrode is located at the end of the pilot tube, to ignite a premixed pilot stream of fuel and air. This is also used to measure the ionization level of the main flame through a digital display, thus informing the user of a main burner flame out.

The outer radiant tube is approximately 1500 mm in length, 153 mm outer diameter and 10 mm wall thickness. The burner inner tube is approximately 939 mm in length, with an outer diameter of 105 mm and 3 mm wall thickness. In order to locate the inner tube concentric with the outer tube small fins and a metal crucifix are welded on the sides and at the end of the inner tube respectively.

The part of the burner that delivers the combustion air (the "main" air) to the combustion zone is a long annulus defined by the air tube and the burner inner wall. It also incorporates a recuperator coil section where the gases accelerate and heat exchange between the flue gas and combustion air is enhanced. The air tube is approximately 730 mm long, 52.5 mm inner diameter and at the end is centrally attached to the inner tube through a ceramic fibre plug. The latter is a vacuum formed, compressed ceramic fibre cylindrical plug and its main purpose is to support the central position of the burner air tube assembly in the inner tube and to form a part of the combustion chamber wall.

The recuperator section's main feature is a 4 mm diameter metal wire coiled around the burner inner wall, referred to as the swirler coil. It incorporates a small gap from the air tube wall of approximately 1 mm. The swirler coil is located approximately 80 mm from the air tube front end, has an overall length of 234 mm and a coil pitch of 75 mm. These dimensions define the coil pitch angle and thus the theoretical swirl angle of the combustion air flow in the absence of any bypass, as it exits the recuperator section.

Further downstream, another feature can be found welded on the burner inner wall, a metal ring of rectangular section and 5 mm width. This design feature, referred to as the step ring, is positioned approximately 240 mm from the exit of the swirler coil section. The height of the step ring forms a physical barrier to the combustion air flow. The gap between the step

ring and the air tube internal wall is 1.5 mm. The intended function of the ring is to remove some swirl, thus control accordingly the flame lentgh[6,7] and additionally to reduce circumferential maldistribution of the hot air flow, a characteristic that has been witnessed in previous variants of the WRTB.

Downstream of the step ring, the burner inner wall reduces in diameter and the air is split into primary (inner) and secondary (outer) streams by a cylindrical tube, the flame tube. This is important for the control of the production of oxides of nitrogen (NOx) [4,7] (see Section 1.2). The flame tube is 150 mm long, 46 mm outer diameter, 2.6 mm wall thickness and is positioned 10 mm upstream of the end of the discharge face. At this point the "main" fuel is admitted radially to the primary stream through four equally spaced rectangular ports in the burner inner wall, each measuring 5 mm x 7 mm area. This method enhances the mixing process through cross-flow induced turbulence.

The mixture thereafter enters the combustion chamber and is ignited by the centrally-located pilot flame of premixed air and fuel. The swirling flow expands, creating a complex flow profile with recirculating vortices that determine the location of the flame front.[4] The combustion products then exit the combustion chamber, reverse, and flow back along the outer annulus and ultimately to the flue. More information with regards to some WRTB design features is presented in Chapter 2.

The most common type of fuel used in the WRTB is natural gas, and this is assumed here. The pilot burner is operated with a premixed mixture of air and gas. The main burner is operated with a mixture of preheated air and gas fuel that enters the combustion chamber through the 4 fuel inlets.

The main burner (i.e. main fuel and air flows) is operated at 12% excess air (i.e. percentage above stoichiometric). The pilot burner is operated at 1 kW thermal input with 5% excess air; the gas flow rate is 1.655 l/min and the air flow rate is 16.54 l/min. The overall burner operates with 3% O_2 in the exhaust. Air and gas flow rates to the main burner are given in Table 2 for a range of power levels.

Pressure at air inlet [mbar]	Air flow rate [L/min]	Pressure at gas inlet [mbar]	Gas flow rate [L/min]	Power [kW] Nett CV
20.80	300	2.66	25.0	15.30
22.60	320	2.78	26.8	16.41
25.70	340	3.00	28.5	17.45
28.50	360	3.33	31.0	18.98
31.20	380	3.53	32.5	19.90
34.30	388	3.80	34.5	20.81

Table 2: WRTB Operating Air/Fuel gas flow rates

1.1.3 In-service Failure

The main premature failure experienced in service is between Faces 6 and 8 and results in a disturbance in the secondary airflow, thus changing the characteristics of the combustion flow. In more detail, after certain hours of operation the burner flame tube fails to sustain its shape and expands outwards at its downstream end, reducing the secondary airflow area between the air inlet tube and the outer flame tube wall. Figures 5, 6, 7 and 8 represent a typical in-service failure of the burner. They are taken from different WRTBs that were installed in a heat treating furnace, operating as part of a car assembly line in the USA.

Figures 5 and 6 indicate that the burner air tube failure is primarily due to thermal fatigue and corrosion from excessive temperatures around the discharge face area. In addition the high temperature region appears to be biased to one side, resulting in the non-symmetrical deformation that is clearly visible. The discoloured flared edge of the air tube demonstrates that the mechanical properties and strength of the material are diminishing rapidly, an indication of the high temperatures in this region.

These high temperatures are also likely to be responsible for the distortion of the edge of the flame tube (Figure 5), which follows the trend of the air tube. The distressed grey areas inside the flame tube are an indication of flame impact with the tube walls.

The result of this distortion of the air and flame tubes is the disturbance of the flame structure prior to entering the main combustion zone after the discharge face, and local variations in the flame stoichiometry. This has implications for the lifetime of the WRTB as the inner tube fails eventually, with the consequent failure of the radiant tube to follow. It also has implications for emissions, notably CO and NOx.

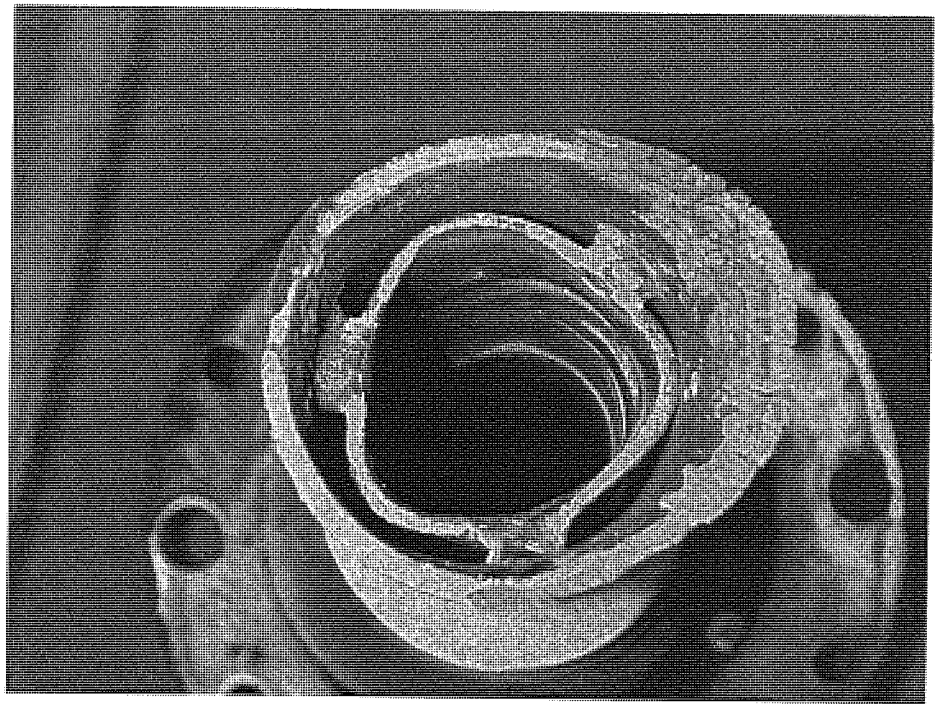

Figure 5: Air tube/Flame tube failure

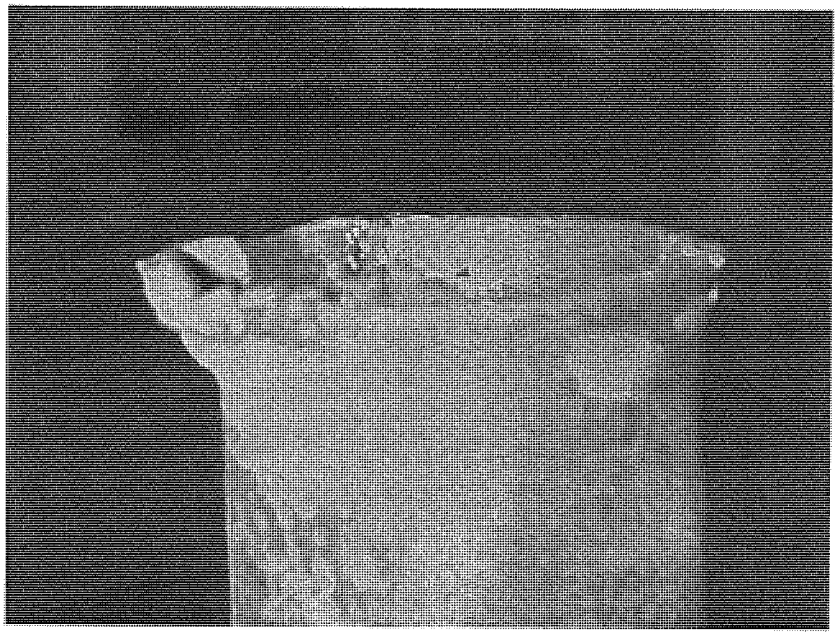

Figure 6: Air tube failure (side view)

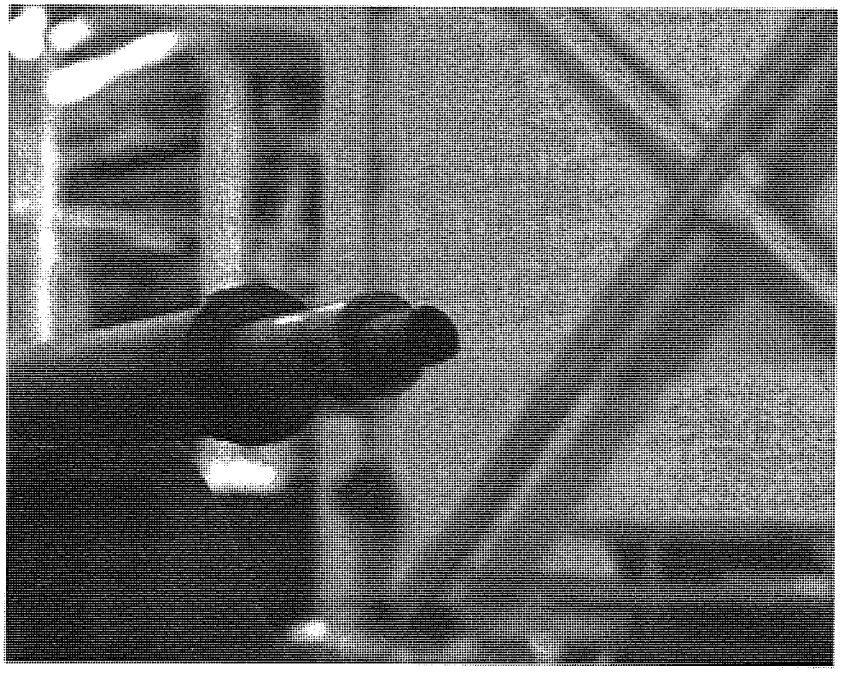

Figure 7: Fuel nozzle/Pilot tube overheat

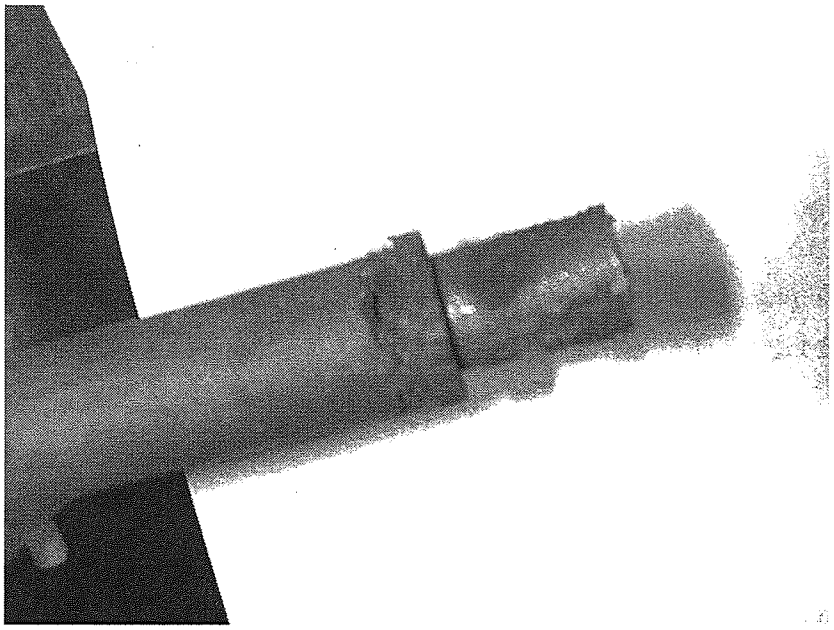

Figure 8: Pilot tube overheat

Figure 7 shows heat damage and deposits on the pilot tube nozzle end. The pilot tube circular section is distorted due to thermal fatigue and the end of the ignition electrode has melted, indicating possible flame attachment. The fuel nozzle shows also discoloration as a result of the high temperatures.

Figure 8 shows another failure mode of the pilot burner tube outlet, with the Inconel pilot tube end overheated, to the point of melting, possibly due to flame impingement at the nozzle. Carbon deposits and material flaking are clearly visible. This implies ignition taking place possibly on the actual wall itself, which is contrary to intended operation.

1.2 Industrial Burners and NOx emissions

Natural gas is a widely used fuel in industrial process furnaces due to its availability and clean combustion, and can deliver much lower energy costs compared with electrical heating systems, provided that an efficient design is used. For natural gas, NOx emissions[8] are of concern as high operating temperatures in RTBs (up to 3000 K), confined flow conditions and high air preheat temperatures contribute strongly to the formation of NOx.

In combustion systems, NOx generally includes nitric oxides NO and nitrogen dioxide NO_2, although it may include nitrous oxide N_2O. Nitric oxide directly affects the nervous system, has an irritant effect in small doses and a toxic effect in high concentrations. It is also a harmful gas for the environment, as it contributes to the formation of photochemical smog and acid rain.

One of the most difficult challenges in industrial heating is the reduction of NOx emissions from high-temperature furnaces[9]. Strict environmental regulations demand lower NOx levels from industrial sources, forcing companies to look for ways to improve combustion efficiency[10], while simultaneously reducing emissions. Many high-temperature processes (> 1000 K) require maintaining these temperatures for prolonged periods, conditions that favour increased NOx formation[11]. Future air quality standards will require even further reductions of NOx levels in industrial furnaces.

The three primary NOx formation mechanisms[7] are thermal NOx (formed by the high temperature reaction of nitrogen with oxygen), prompt NOx (formed by reactions between nitrogen, oxygen and hydrocarbon radicals) and fuel NOx (formed by the direct oxidation of fuel-bound nitrogen compounds). Fuel NOx formation is non existent with natural gas due to the absence of any fuel bound nitrogen compounds. The radical chain reaction process of the thermal mechanism overwhelms the contribution of prompt NOx formation in a majority of high-temperature, natural gas-fired processes. Primary factors affecting thermal NOx yields are time, temperature and oxygen availability.

Common methods of in-flame burner NOx control are flue-gas recirculation (FGR), steam or water injection and staged combustion. Only the latter is currently employed in the WRTB design. Further analysis in this topic is presented in Chapter 2, as well as a more thorough presentation of NOx emissions and reduction techniques in RTBs.

1.3 CFD Software and Combusting Flows

Computational Fluid Dynamics is a sophisticated computational modelling method that enables the user to study the dynamics of flows. The equations governing the flow of fluids are based on the following three fundamental physical principles:

1. Conservation of mass.
2. Conservation of momentum, Newton's second law of motion.
3. Conservation of energy.

Each one of those can be used to perform a balance (of mass, momentum or energy) across a control volume in a fluid.

The variables in these equations vary depending on the properties of the flow in question and additional equations are solved for flows as in this study that involves heat transfer and chemical species transport[12]. In addition, transport equations are also solved if the flow is turbulent. These equations are then replaced by equivalent numerical descriptions that are solved by a finite difference method, to give solutions for the flow at discrete locations within the flow field.[2] Results include flow velocity, temperature, turbulent characteristics and species concentrations at any point within the flow domain. CFD not only predicts fluid behaviour (including turbulence), but also the transfer of heat, mass, phase change (such as freezing or boiling) and chemical reaction, such as combustion[1,4].

1.3.1 The Benefits of CFD Analysis

General-purpose CFD software codes allow for a complete three-dimensional simulation of combustion devices. CFD can be used to investigate aspects of flows, such as individual burner combustion aerodynamics and complex flows in complete combustion systems[3] and has been applied to the prediction of the performance of combustion processes since the 1960s[13]. Modelling industrial burners using CFD can reduce the time to develop innovative product modifications and designs and can result in reductions in NOx emissions from conventional designs[14,15].

Lohner[16] describes the reasons behind the introduction of CFD:

Insight: There are many devices and systems that are difficult to prototype. Often, CFD analysis shows parts of the system or phenomena happening within the system that would not otherwise be visible through any other means. CFD gives means of visualising and enhanced understanding of designs.

Foresight: Because CFD is a tool for predicting what will happen under a given set of circumstances, it can answer many 'what if?' questions very quickly. It requires variables and it produces outcomes. In a short time, it can predict how the design will perform, and test many variations until arriving at an optimal result. All of this is done before physical prototyping and testing. The foresight we gain from CFD helps us to design better and faster, thus reducing significantly the development time and costs.

Efficiency: Better and faster design or analysis leads to shorter design cycles. Time and resources are saved. Products get to market faster. Equipment improvements are built and installed with minimal downtime. CFD is a tool for compressing the design and development cycle.

Cost: Cost of experimentation, that is the only alternative to simulation, is high.

Practicality: Impossibility of experiments is, in some instances, a feared fact. For example, atmospheric nuclear explosions and biomedical situations would endanger the eco system or patient life.

Computer speed and memory: In 1965, Intel cofounder Gordon Moore made a memorable observation that data density doubled approximately every 18 months; this gave rise to what is known as Moore's law. At the same time, algorithm development continues to improve the accuracy and performance of models.

1.3.2 Research software code

When using CFD to look at fluid dynamic problems, it is important to give consideration to the following steps:

Definition of the modelling goals – The specific results that are required from the CFD model, how they are utilised and the degree of accuracy that is required from the model.

Choice of the computational model – The definition of the boundary conditions, the choice between two or a three dimensional model and the type of grid topology that is best suited to the model.

Choice of physical model – The nature of the flow is important such as inviscid, laminar, or turbulent and steady or unsteady; as well as the presence of heat transfer.

Determination of the solution procedure – The timescale that the problem will take to converge on the computer and convergence acceleration with a different solution procedure.

Consideration of these steps reduces computer-processing time and contributes to the success of the modelling, prior to selecting a CFD code.

The stages of a CFD simulation are:

Geometry/Mesh: This interactive process is the first pre-processing stage. Its aim is to produce a mesh for input to the physics pre-processor. Before a mesh can be produced a closed geometric solid is required. The "solid" is the flow domain of interest and the "mesh" divides it into computational nodes.

Physics Definition: This interactive process is the second pre-processing stage and is used to create the input for the solver. The mesh files are loaded into the physics pre-processor, and the properties of the fluid and boundary conditions are defined. Turbulence, combustion and radiation models are defined at this stage as well as solver control parameters.

The Solver: The solver is the main engine of the program that uses FORTRAN programming language and subroutines to numerically simulate the boundary and flow conditions. The solution process requires no user interaction and is therefore usually carried out as batch process. The file of results is then past to the post-processor.

The Post-processor: The post-processor is the component used to analyse, visualise and present the results interactively. Post-processing includes obtaining point values, complex animated sequences, and graph creation.

The CFD code used for this research is a commercial code, CFX 10, provided by ANSYS Software Solutions. It is capable of modelling[3]:

- Steady-state flows.
- Transient flows.
- Laminar flows.
- Turbulent flows.
- Subsonic, Transonic, and Supersonic flows.
- Heat transfer and Thermal radiation.
- Buoyancy and Non-Newtonian flows.
- Transport of non-reacting scalar components.
- Multiphase flows.

- Combustion.
- Flows in multiple phase of reference.
- Particle tracking.

The code consists of the following components:

- ANSYS Design Modeller computer aided design package for the creation of geometry,
- CFD4-CFX mesh calculator for meshing the geometry models,
- CFX Pre physics processor for defining the boundary conditions for the simulation,
- CFX Solver Manager which is the main calculating program and runs in FORTRAN,
- CFX Post processor for analysis and processing of the results of the simulation.

A thorough analysis of the different computational models, such as turbulence, combustion and radiation models used in this research, can be found in the Theory section of this Thesis in Chapter 2.

For the present work, CFX was installed on a Pentium 4 Dell computer and simulations were performed using 2.5 GB of RAM memory.

1.4 References

1. CFX 10 User Manual, ANSYS UK Software Solutions, Abingdon, Oxford, 2006.
2. Chomiak J, Combustion A study in Theory, Fact and Application, Abacus Press 1990.
3. Baukal C.E., The John Zink Combustion Handbook, CRC Press, Boca Raton, FL, 2001
4. Gupta A K, Lilley D G and Syred N, Swirl Flows, Abacus Press, 1984.
5. Weber R.,Verlaan A.L.,Orsino S. and Lallemant N., Journal of the Institute of Energy, 72, pp. 77-83 (1999), On emerging furnace design methodology that provides substantial energy savings and drastic reductions in CO2, CO and NOx emissions.
6. Krom Shroder, model ZMI 16, product manual 7.1.2.2, Edition 11.04 D/GB/F.
7. Andrews G, Proceedings of course "Combustion in boilers and furnaces", March 2004 University of Leeds, UK.
8. Zarnescu V. & Pisupati S.V, Energy and Fuels 2002, 16:3:622-633, An integrative approach for combustor design using CFD methods.
9. De Joannon M.,Langella G.,Beretta F., Cavaliere A. and Noviello C., Combustion Science and Technology, 153, pp. 33-50 (2000), Mild combustion: Process Features and technological constrains.
10. Plessing T., Peters N. and Wünning J.G., 27th Symposium (International) on Combustion, The Combustion Institute, Laser-optical investigation of highly preheated combustion with strong exhaust gas recirculation, 1998.
11. Orsino S. and Weber R., Combustion Science and Technology, 170, pp. 1-34 (2001), Numerical simulation of combustion of natural gas with high-temperature air.
12. Ferziger, J.H.; Peric, M.: Computational Methods for Fluid Dynamics, Springer Verlag, 1999.
13. Warnatz J., Maas U. and Dibble R.W., Combustion-Physical and Chemical Fundamentals, Modelling and Simulation, Experiments, Pollutant formation, Springer 3rd Edition 2001.
14. Hasegawa T. and Tanaka R., JSME International journal, 41 n°4, pp. 1079-1084 (1998), High Temperature air combustion - Revolution in combustion technology - (Part I: New findings on High Temperature air combustion).

15. Nishimura M., Suzuki T., Nakanishi R. and Kitamura R., Energy Conversion Management, 38 n°10-13, pp. 1353-1363 (1997), Low-NOx combustion under high preheated air temperature condition in an industrial furnace.
16. Lohner R., Applied CFD Techniques, (2001), An introduction based on finite element methods, John Willey & Sons Ltd, West Sussex, UK.

2. THEORY

This chapter describes the theoretical basis of this research, focusing on swirling flows, turbulence and combustion in computational fluid dynamics.

2.1 Swirling Flows in Radiant Tube Burners

The definition of a swirling flow is one undergoing axial and rotational motion simultaneously. Laboratory flow visualisation tests of confined swirling flows such as those found in the combustion zone of an RTB show the fluid particles follow a spiralling motion with two major components, axial and tangential. Figure 1 shows a qualitative representation of tangential velocity against non-dimensional radius in such a flow.

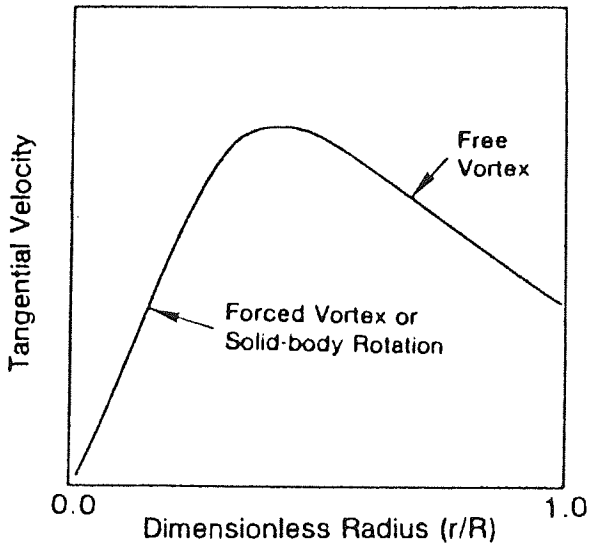

Figure 1: Tangential velocity over radius in swirling flows

At low radii, the flow behaves as a forced vortex (i.e. solid body rotation) with tangential velocity proportional to radius, whereas at larger radii the flow behaves as a free vortex with tangential velocity inversely proportional to radius. This combination is known as a Rankine vortex.

In a swirling flow the degree of swirl is usually expressed by the non-dimensional swirl number, S. The swirl number is related to the flow swirl angle, which in turn, is a function of the forward and rotational velocity components of the flow, and it is expressed as:

$$S = \frac{G_\Theta}{G_X R} \tag{2.1}$$

where G_X, the axial flux of axial momentum, is given by:

$$G_X = 2\pi \int_r^R \rho v_u^2 r dr \tag{2.2}$$

and G_Θ, the constant axial flux of swirl momentum at steady pressure conditions, by:

$$G_\Theta = 2\pi \int_r^R v_u v_\theta \rho r^2 dr \tag{2.3}$$

A major characteristic of a swirling flow expanding into a confined or non-confined space and therefore following a sudden step increase in the flow passage area is the formation of recirculation zones. The nozzle geometry and confining walls influence the shape and extent of the recirculation zones.

A typical flow pattern[1] of a co-axial swirling free (uncontained) jet is shown in the Figure 2, plotted as lines of constant stream functions for various swirl numbers. Figure 2 shows a central recirculation zone formed just downstream of the jet wall boundaries. Associated with the formation of the central recirculation zone is the occurrence of a characteristic flow structure identified as the Precessing Vortex Core (PVC).

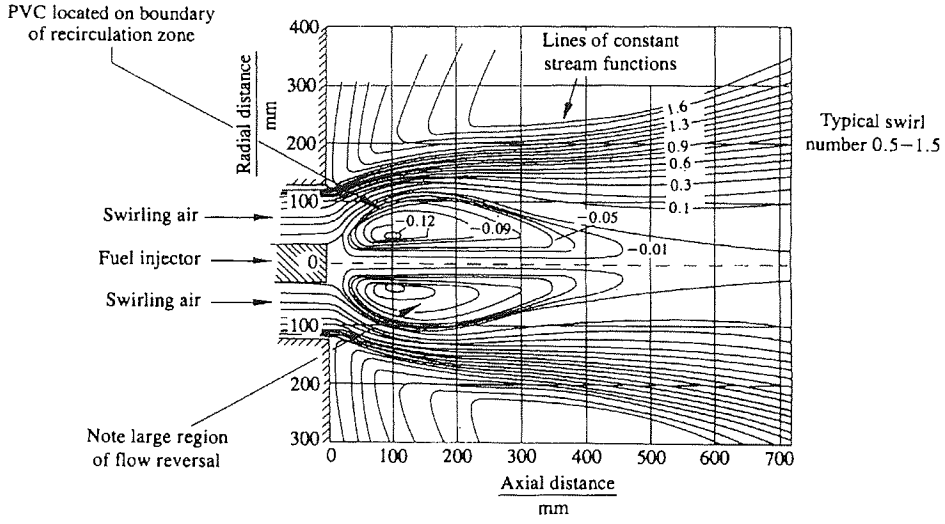

Figure 2: Typical flow pattern of a swirling free jet

This occurs when the central vortex core becomes unstable and starts to fluctuate about the central axis with a regular periodic frequency. The PVC locates itself on or around the boundary of the recirculation zone and at the peak of the tangential velocity profile. The PVC flow structure however, is rarely seen in confined co-axial swirling jets such as those observed in an RTB; nevertheless, its existence can be present at low frequency magnitudes.

In combusting flow, the forward acceleration of the flow due to the increase in temperature and consequent reduction in density will reduce the swirl number, as swirl momentum is unaffected. The combustion swirl number is related to the isothermal value by:

$$S_{combustion} = S_{isothermal} \times \frac{T_{isothermal}}{T_{combusting}} \qquad (2.4)$$

The following Table 1 shows the range of swirl numbers for a number of engineering devices:

Device	Swirl Number
Swirl Burner	1-2
Cyclone Dust Separator	3-5
Cyclone Combustor	4
Vortex Amplifier	2-6

Table 1: Swirl numbers for different engineering devices

2.2 Turbulence in Combusting Flows

The study of turbulence is an interdisciplinary activity, which has a very large range of applications. Although most flows occurring in nature and engineering applications are turbulent it is difficult to give a precise definition of turbulence. Turbulent flows are irregular, contain vorticity, and are three-dimensional and unsteady. Some general characteristics[2] of turbulent flows are listed below:

- *Irregularity*: All turbulent flows are irregular, or random. This makes a deterministic approach impossible; instead there is the need to rely on statistical methods.
- *Diffusivity*: The diffusivity of turbulence, which causes rapid mixing and increased rates of momentum, heat and mass transfer, is another important feature of all turbulent flows.
- *Large Re numbers*: Turbulent flows always occur at high Reynolds (Re) numbers. Turbulence often originates as an instability of laminar flows as the Re number increases. The Re number is a dimensionless quantity defined as the ratio of inertial forces to viscous forces $(\rho uL/\mu)$. At high Re numbers (turbulent flows), inertia forces dominate the viscous forces and tend to produce random flow eddies and vortices.
- *Dissipations*: Turbulent flows are always dissipative. Viscous shear stresses perform deformation work, which increases the internal energy of the fluid at the expense of the kinetic energy of the turbulence. Turbulence needs a continuous supply of energy to make up for these viscous forces.

- *Continuum*: Turbulence is a continuum phenomenon, governed by the equations of fluid mechanics. Even the smallest scales occurring in a turbulent flow are ordinarily far larger than any molecular scale.
- *Turbulent flows*: Turbulence is not a feature of fluids but of fluid flows. Most of the dynamics of turbulence is the same in all fluids, whether they are liquid or gases, if the Re number of the flow is large enough; the major characteristics of turbulent flows are not controlled by the molecular properties of the fluid in which the turbulence occurs. The characteristics of turbulence depend on its environment.

The turbulence-chemistry interaction is a well-studied field. The flow reaction rates, as known from previous studies in chemical kinetics, are strongly affected when the constituents of the reaction are not well mixed. Conversely, the chemical transformation of the constituents and their associated energy levels influences the localised motion of the fluid, thus affecting the local turbulence levels. The level of turbulence-chemistry interaction depends on the time scales involved, both the turbulent time scale and the chemical-reaction-rate time scale.

When the chemical reaction time scale is large in comparison with the turbulent time scale, then the reactants will mix relatively quickly while the reaction proceeds relatively slowly, and the reaction rate can be approximated by the determined kinetic reaction rate using mean values. When the chemical reaction time scale is small, the controlling mechanism is the mixing of the reactants and the reaction can be assumed to reach equilibrium instantaneously. Various CFD combustion models attempt to derive turbulence-controlled reaction rates - see Section 2.7.

In addition, turbulence increases the burning velocity by several orders of magnitude. The burning velocity can be regarded as the speed at which a flame travels through a stationary flammable mixture, and is a function of the kinetics of the combustion reaction, such as mixture composition, temperature, pressure and turbulence.

When a turbulent mixture is ignited, combustion is faster than when the same mixture is burning in a laminar mode. The turbulence factor β expresses the ratio of turbulent to laminar burning velocity.

$$\beta = \frac{S_T}{S_L} \tag{2.5}$$

The correlation of β to turbulent flow properties and the combustion properties of the mixture can be given with reasonable agreement with most experimental turbulent combustion data[3] as the following expression.

$$\beta = 1 + 2\frac{u'}{S_L} \tag{2.6}$$

where u' is the root mean square (RMS) of the fluctuating velocity component.

Turbulent flows have been investigated for more than a century, but a fundamental solution to the challenges of modelling turbulence is still lacking. One problem is the solution of the non-linear equations, which describe three-dimensional flows without simplification (e.g. linearization) and approaches involve the use of mathematical statistics and probability theory. As a consequence, in order to complete the mathematical description of flows used in CFD codes, the introduction of turbulence models is necessary. Those models that have been used in this research are described in Section 2.6.

2.3 Methane Combustion

Methane (CH_4) is by far the largest constituent of natural gas, representing 85-95% by volume, the remaining combustible constituents being mainly ethane and small amounts of propane. In the modelling work described in this study, natural gas is represented as methane to make the modelling more tractable (see Chapter 6). Methane combustion is one of the most widely researched topics in the field of engineering combustion.

CH_4 in laminar combustion has a burning velocity S_L = 0.4 m/s and an explosion flame velocity S_F = 3 m/s. In turbulent combustion, magnitudes are substantially greater with the burning velocity being S_T = 12-40 m/s and the explosion flame velocity being S_F = 100-300 m/s.

The stoichiometric (chemically correct) combustion of CH_4 in air satisfies the following equation:

$$CH_4 + 2O_2 + 7.52N_2 \rightarrow CO_2 + 2H_2O + 7.52N_2 \qquad (2.7)$$

In many applications however, excess air is used in order to reduce combustion temperature and to ensure complete combustion of the fuel. If 18% excess air is used, the reaction in equation (2.7) changes to:

$$CH_4 + (1.18)2O_2 + (1.18\times 7.52)N_2 \rightarrow CO_2 + 2H_2O + 0.36O_2 + (1.18\times 7.52)N_2$$

and about 3 % by volume of O_2 remains in the products. Higher excess air percentages tend to reduce overall thermal efficiency by reducing temperature, and a 3% oxygen flue gas concentration is commonly adopted as a design condition.

In a real combustion environment however, the number of chemical reactions that take place presents a complex grid of combinations between reacting species and their backwards reactions. Modelled reaction schemes have evolved from 75 elementary steps (and their 75 backward reactions) with 25 species[4] to 325 elementary steps and 52 species[5].

2.4 NO formation and reduction mechanisms

Nitric oxide (NO) formation is an important parameter in combustion because of its contribution to air pollution, specifically acid rain and photochemical smog. Three primary NO formation mechanisms[6,7] exist in combustion. The first and most important in the case

of natural gas combustion is the thermal or Zeldovich mechanism. In this case, NO is formed by the high temperature reaction of N_2 with O_2. In the second, the prompt or Fenimore mechanism, NO is formed by reactions between N_2, O_2 and HC radicals. The last formation mechanism is fuel NO, formed by the direct oxidation of fuel-bound N_2 compounds.

Fuel NO formation is non-existent with natural gas due to the absence of any fuel-bound N_2 compounds. Also the radical chain reaction process of the thermal mechanism overwhelms the contribution of prompt NO formation in a majority of high-temperature, natural gas-fired processes including RTBs[6,7]. Hence for the present work, the thermal route is the only significant mechanism.

Primary factors affecting thermal NO yields are time, temperature and oxygen availability. Air preheating can thus increase the level of thermal NO due to increased flame temperatures. There are over 70 reactions in the Zeldovich mechanism.

In simple terms, the first step is the rupture of the N_2 by an O atom according to equation (2.8):

$$N_2 + O \Leftrightarrow NO + N \qquad (2.8)$$

which is followed by the reaction of these radicals with available O_2 to generate NO by:

$$N + O_2 \Leftrightarrow NO + O \qquad (2.9)$$

The rate constants for two reactions (2.8) and (2.9) in cm^3/mole s are:

$$K_1 = 7.6\times10^{13} \exp\left(-\frac{75.4}{RT}\right)$$

$$K_2 = 6.4\times10^{10} \exp\left(-\frac{6.25}{RT}\right)$$

In near stoichiometric and fuel-rich flames a contribution to NO formation can also be supplemented from the reaction with OH radicals (extended Zeldovich mechanism):

$$N + OH \Leftrightarrow NO + H \tag{2.10}$$

The rate constant here is $K_3 = 1.6 \times 10^{13}$ cm³/mole s.

The overall formation rate of NO can be shown by the following equations:

$$\frac{d[NO]}{dt} = k(T)[N_2]\sqrt{[O_2]} \tag{2.11}$$

$$[NO] = (K_1 e^{(-K_2/T)}[N_2]\sqrt{[O_2]})t \tag{2.12}$$

where [] denotes mole fraction and *k (T)* is the temperature-dependent rate reaction coefficient. Equation (2.11) shows that the formation of thermal NO increases with the reaction rate coefficient and therefore temperature, oxygen concentration and reaction time. Indeed thermal NO production increases exponentially with temperature, and is particularly pronounced at temperatures above 1800K.

The basic methods for reduction of NO production in burners can be summarised as follows:

- Staged fuel combustion (or lean/lean)
- Staged air combustion (or rich/lean)
- Flue or exhaust gas recirculation (FGR or EGR)

Staged combustion is one of the most common methods used in gas burner applications to reduce thermal NO, without adding costly hardware and controls. By suitably proportioning air and fuel inside the burner and/or furnace, it is possible to form a fuel-rich zone with little NO generation, followed by a lean burnout zone where additional NO production also is

low. Most importantly, both zones have a reduced reaction temperature. The fuel rich zone can lead to an increase of CO production, but this can be oxidised to CO_2 in the lean zone.

In the case of an RTB the staging of air is considered easier than that of fuel. The WRTB follows this approach. The air is split into primary and secondary streams and the fuel is mixed into the primary air for the rich combustion zone. The aim is that NO formation will take place entirely in the rich zone, which could have a local equivalence ratio as high as 2. This will generate very low NO, and increased CO, which is burned out in the lean zone where the secondary air enters.

The equivalence ratio, Φ, is commonly used to indicate quantitatively whether a fuel-oxidizer mixture is rich, lean, or stoichiometric. It is defined as the ratio of the stoichiometric air/fuel mass ratio to the used air/fuel mass ratio. Therefore, for $\Phi<1$ the mixture is fuel lean, for $\Phi>1$ the mixture is fuel rich and when $\Phi=1$, then the mixture is stoichiometric.

An alternative or supplementary NO reduction technique that is particularly effective in burners with high flame temperature is Flue Gas Recirculation. FGR reduces the peak temperature in the combustion zone by simple dilution with lower temperature gases. FGR can be combined with staging to reduce NO further, but the effectiveness diminishes as the baseline flame temperature reduces. High levels of FGR reduce the O_2 concentration in the flame region and this can affect flame stability. If air is preheated using flue gas recuperation, as in the case of the WRTB, then the stability limits are extended and the tolerance for FGR will be higher. For an air preheat of approximately 400 °C, the limiting FGR percentage of overall flue gas flow rate is about 40%. In practice FGR ratios greater than 25% are rarely used because of flame stability problems, and approximately 60% NOx reduction can be achieved at 25% FGR[7].

Lowering further the flame temperature with the use of FGR can result in an inherent increase in CO emissions. To counteract this increase in CO more combustion O_2 can be used but this, adversely, can increase NOx. Consequently, there is a CO emissions level

limitation on the application of FGR. In addition, other work[8] has shown efficient FGR application only into the primary air (fuel rich zone), in comparison to the whole of the combustion chamber, which resulted in lowering NO emissions without a detrimental effect on the flame stability.

2.5 Numerical Modelling of Flows

The analysis of the behaviour of fluids is based upon the fundamental laws of applied mechanics[9,10] that relate to the conservation of mass-energy and the force-momentum equations. These equations and models are presented in this section.

2.5.1 The Mass Conservation Equation

The Conservation of Mass or Continuity law applied to a fluid passing through a fixed volume can be written as follows:

$$\frac{\partial \rho}{\partial t} + \frac{\partial (\rho u)}{\partial x} + \frac{\partial (\rho v)}{\partial y} + \frac{\partial (\rho w)}{\partial z} = 0 \qquad (2.13)$$

Or in a more compact vector notation:

$$\frac{\partial \rho}{\partial t} + div(\rho u) = 0 \qquad (2.14)$$

Equation (2.14) is the general form of the mass conservation equation and is valid for compressible fluids. The first term on the left-hand side is the rate of change in time of the density (mass per unit volume). The second term is concerned with the net flow of mass out of an elemental body of fluid and is called the convective term.

2.5.2 The Momentum Conservation Equation

Newton's second law states that the rate of change of momentum of a fluid particle equals the sum of the forces acting on the particle. Applying this to a fluid passing through a fixed volume, yields the following equation:

$$\frac{\partial(\rho u)}{\partial t} + div(\rho uu) = -gradp + div(\tau) + \rho g + F \qquad (2.15)$$

Inertia Pressure Viscosity Body forces

In the i[th] direction:

$$\frac{\partial(\rho u_i)}{\partial t} + \frac{\partial(\rho u_i u_j)}{\partial x_i} = -\frac{\partial p}{\partial x_i} + \frac{\partial \tau_{ij}}{\partial x_j} + F_i \qquad (2.16)$$

Note that the gravitational term ρg has been accounted for in the body forces F_i. The stress tensor τ_{ij} is given by:

$$\tau_{ij} = \left[\mu\left(\frac{\partial u_i}{\partial x_i} + \frac{\partial u_j}{\partial x_j}\right)\right] - \frac{2}{3}\mu div(u)\delta_{ij} \qquad (2.17)$$

where δ (the Kronecker term) is a function of two variables, usually integers, which is 1 if they are equal and 0 otherwise. In other words, δ_{ij}=1 if i=j, and δ_{ij}=0 if $i \neq j$.

The 3D form of Newton's law of viscosity for compressible flows involves two constants of proportionality: dynamic viscosity μ, to relate stresses to linear deformations and kinematic viscosity λ, to relate stresses to the volumetric deformation.

Substitution of (2.17) into (2.16) yields the Navier Stokes Equations.

In the *x direction*: (2.18)

$$\rho\frac{Du}{Dt}=-\frac{\partial p}{\partial x}+\frac{\partial}{\partial x}\left[2\mu\frac{\partial u}{\partial x}+\lambda divu\right]+\frac{\partial}{\partial y}\left[\mu\left(\frac{\partial u}{\partial y}+\frac{\partial v}{\partial x}\right)\right]+\frac{\partial}{\partial z}\left[\mu\left(\frac{\partial u}{\partial z}+\frac{\partial w}{\partial x}\right)\right]+F_X$$

In the *y direction*: (2.19)

$$\rho\frac{Dv}{Dt}=-\frac{\partial p}{\partial y}+\frac{\partial}{\partial y}\left[2\mu\frac{\partial v}{\partial y}+\lambda divu\right]+\frac{\partial}{\partial x}\left[\mu\left(\frac{\partial u}{\partial y}+\frac{\partial v}{\partial x}\right)\right]+\frac{\partial}{\partial z}\left[\mu\left(\frac{\partial v}{\partial z}+\frac{\partial w}{\partial y}\right)\right]+F_Y$$

In the *z direction*: (2.20)

$$\rho\frac{Dw}{Dt}=-\frac{\partial p}{\partial z}+\frac{\partial}{\partial z}\left[2\mu\frac{\partial w}{\partial z}+\lambda divu\right]+\frac{\partial}{\partial y}\left[\mu\left(\frac{\partial v}{\partial z}+\frac{\partial w}{\partial y}\right)\right]+\frac{\partial}{\partial x}\left[\mu\left(\frac{\partial u}{\partial z}+\frac{\partial w}{\partial x}\right)\right]+F_Z$$

2.5.3 Transport Equation for Scalar Properties

The equations governing various physical phenomena can be put into a generic form, thus allowing a systematic approach for a computer simulation. A general dependant variable Φ (scalar or vector) can be introduced to represent the form of these equations, including scalar quantities such as temperature and species concentration. It is given in the following form:

$$\frac{\partial(\rho\phi)}{\partial t}+div(\rho\phi u)=div(\Gamma grd\phi)+S_\phi \qquad (2.21)$$

In words, it translates as the rate of increase of Φ fluid element + net rate of flow of Φ out of fluid element = rate of increase of Φ due to diffusion + the rate of increase of Φ due to sources.

The transport equation for a property Φ is given in equation (2.21) and highlights the various transport processes: the rate of change term and the convection term on the left hand side and the diffusive term (Γ is the diffusion coefficient) and the source term respectively on the right hand side. It is the integration of this equation over a three-dimensional control volume which is the method used by CFX to create discrete values of scalars.

2.6 Turbulence Modelling

Turbulent flows such as those seen in burners are characterised by velocity fields of fluctuating nature. These fluctuations mix transported quantities such as momentum, energy and species concentration and cause those quantities to fluctuate as well. However, these fluctuations can be of small scale and high frequency and are too computationally expensive to simulate directly. Instead the exact instantaneous governing equations can be averaged in a number of ways in order to remove the small scales resulting in a set of equations that are less resource consuming to solve. Nevertheless, these new equations contain a set of unknown variables and turbulence models are needed to determine these new variables in terms of the known quantities.

2.6.1 Averaging Techniques for Turbulent Flows

To resolve a turbulent flow field by direct numerical simulation (DNS) requires that all relevant length scales be resolved from the smallest eddies to scales in the order of the dimensions of the computational domain. This means that the whole range of spatial and temporal scales of the turbulence must be resolved. The smallest dissipative scales (known as Kolmogorov micro scales) are related to the kinematic viscosity ν and to the rate of kinetic energy dissipation ε.

This requires massive computational resources and is really a technique which can only be applied to very simple flows at low Reynolds numbers; even then however, the computational cost of DNS is very high. For the Reynolds numbers encountered in most industrial applications, the computational resources required by a DNS would prohibit the application. However, direct numerical simulation is a useful tool in fundamental research into turbulence.

There are two main schools of turbulence modelling. The first follows the classical definition of turbulence as a time average at a fixed point in space while the second approach is concerned with all fluctuations occurring at scales smaller than those resolved

by the discrete sized control volume used in numerical calculation. This is usually expressed in terms of a space average at a fixed point in time.

As the complete time dependent solution of the exact Navier-Stokes Equations is presently unavailable, these two methods can be adopted to transform the Navier-Stokes Equations to a form where the small scale turbulent fluctuations do not have to be directly simulated.

The Reynolds-averaged Navier-Stokes Equations (RANS) represent transport equations for the mean flow quantities with all the scales of turbulence being modelled. The equations are derived by decomposing the dependant variables in the conservation equation into time mean (obtained over an appropriate time interval) and fluctuating components and then time averaging the entire equation. A pictorial description of this can be seen in Figure 3.

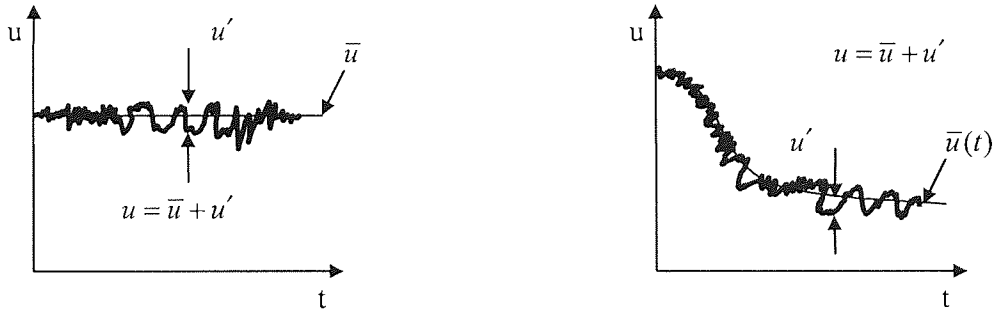

(a) STEADY FLOW (b) UNSTEADY FLOW

Figure 3: Relationship between u, $\overline{u}$ and u' for steady and unsteady flow

The alternative space averaged approach includes techniques such as the Large-Eddy Simulation (LES) is also another option. The large scale structure of turbulent flow is computed directly in a manner that uses a set of filtered equations. Filtering is simply a manipulation of the Navier-Stokes equations to remove only eddies that are smaller than the size of the filter, which is usually taken as the discrete control volume. As with Reynolds averaging, the filtering process creates additional unknown terms that must be modelled in order to obtain closure.

LES requires less computational effort than DNS but more effort than those methods that solve the RANS. The computational demands also increase significantly in the vicinity of walls, and simulating such flows usually exceeds the limits of modern computers. For this reason, zonal approaches are often adopted, with RANS or other empirically-based models replacing LES in the wall region.

The main advantage of LES over computationally cheaper RANS approaches is the increased level of detail it can deliver. While RANS methods provide "averaged" results, LES is able to predict instantaneous flow characteristics and resolve turbulent flow structures. The advantage of this approach is that by modelling less turbulence (and solving more), the errors induced by the turbulence model will be reduced.

2.6.2 Reynolds Averaged Navier-Stokes Equations

The RANS methods use mean quantities only instead of the exact ones and this approach greatly reduces the computational effort. The exact or instantaneous variables are decomposed into the mean and fluctuating components, for example the velocity component would be:

$$u_i = \overline{u}_i + u_i' \tag{2.22}$$

Where $\overline{u}_i$ and u_i' are the mean and instantaneous velocity components. This format is the same for pressure and other scalar quantities, e.g.

$$\Phi_i = \overline{\Phi}_i + \Phi_i' \tag{2.23}$$

where Φ_i denotes a scalar such as pressure, energy or species concentration. Substituting variables of this form into the instantaneous continuity and momentum equations and taking a time average, yields the time averaged momentum equations, which in Cartesian form are:

$$\frac{\partial \rho}{\partial t} + \frac{\partial (\rho u_i)}{\partial x_i} = 0 \qquad (2.24)$$

and:

$$\rho \frac{Du_i}{Dt} = -\frac{\partial p}{\partial x_i} + \frac{\partial}{\partial x_i}\left[\mu\left(\frac{\partial u_i}{\partial x_j} + \frac{\partial u_j}{\partial x_i} - \frac{2}{3}\delta_{ij}\frac{\partial u_i}{\partial x_i}\right)\right] + \frac{\partial}{\partial x_i}(-\overline{\rho u_i' u_j'}) \qquad (2.25)$$

Equations (2.24) and (2.25) are called the Reynolds-averaged Navier-Stokes Equations. They have the same general form as the instantaneous versions, but the velocities and other solution variables now represent the time averaged values. However, the averaging procedure introduces additional unknown terms containing products of the fluctuating quantities, which act like additional stresses in the fluid

These additional terms are included to represent turbulence $(-\overline{\rho u_i' u_j'})$. They arise from the nonlinear convection term and are known as Reynolds stresses. These terms must be modelled by additional equations of known quantities, to "close" equation (2.25) in certain turbulence models. They describe the influence of the turbulent field on the mean flow and due to the chaotic nature of turbulence it is impossible to model these terms in a general way. Closure implies that there are a sufficient number of equations for all the unknowns, including the Reynolds-Stress tensor resulting from the averaging procedure. The equations used to close the system define the type of turbulence model.

2.6.3 Modelling Approaches

To obtain "closure" of the RANS equations, a variety of turbulence models have been developed by researchers, which vary in complexity and ability to solve the Reynolds stresses in a wide range of flow conditions.

A common method uses the approach suggested by Boussinesq[11], where it was assumed that the turbulent stresses are solved as the viscous stresses and, consequently, they are directly proportional to the velocity gradient. For the general Reynolds stress tensor, the Boussinesq assumption gives:

$$-\overline{\rho u_i' u_j'} = \mu_t \left(\frac{\partial u_i}{\partial x_j} + \frac{\partial u_j}{\partial x_i} \right) - \frac{2}{3} \left(\rho k + \mu_t \frac{\partial u_i}{\partial x_j} \right) \delta_{ij} \qquad (2.26)$$

where μ_t is the turbulent viscosity, and k the kinetic energy of turbulence is given by:

$$k = \frac{\overline{u_i' u_j'}}{2} \qquad (2.27)$$

The second term on the right hand side added on equation (2.26) ensures that the contribution from the normal stresses is included in the assumption.

Turbulence models can be classified in three main categories, according to how they solve the equations and whether or not they use the Boussinesq assumption. Models using the assumption can be referred to as Category I or turbulence viscosity models. Three such examples are the following:

a. Zero Equation model - Mixing Length model
b. One Equation model - Spalart-Almaras model
c. Two Equation model - k-ε model

The turbulent viscosity hypothesis is valid for many flow conditions; however there are exemptions and an alternative approach is available whereby closure of the Reynolds Equations without the assumption occurs. To achieve this, each of the terms in the Reynolds stress tensor is supplementary solved. This type of model is classed as Category II and an example presents the Reynolds Stress turbulence model. Models in this category are more computationally demanding compared to the Category I.

Category III models are defined as those that are not based entirely on the Reynolds Equations such as LES and the Detached Eddy Simulation (DES) models. In this case, a filtered set of conservation equations is modelled instead of the Reynolds Equations, although DES uses a "hybrid" formulation of RANS and LES equations. In CFX these two models are only available for transient simulations and therefore do not present an option for this study.

Another two-equation model available in CFX is the k-ω model and its derivatives, such as the Baseline (BSL) k-ω model and the Shear Stress Transport (SST) k-ω model. One of the advantages of the k-ω formulation is the near wall treatment for low-Reynolds number computations. The model does not involve the complex non-linear damping functions required for the k-ε model and it can be more robust. However, a high definition wall mesh resolution is required for this model. The boundary layer needs to be resolved with at least 10 nodes which, in the WRTB wall confined flow case, would result in excessive size of computational grid ($>1\text{x}10^6$ nodes approximately). The k-ω models are recommended for the accurate prediction of flow separation from a smooth surface. This is an important phenomenon particularly for airplane aerodynamics since the stall characteristics of a plane are controlled by the flow separation from the wing. Furthermore, the SST model is recommended for high accuracy boundary layer simulations; however a near wall a resolution of the boundary layer of more than 10 points is required[12]. As the Reynolds number of the WRTB study is not particularly low and boundary layer and flow separation phenomena are not explicitly solved, the k-ω based models were not applied.

Overall, CFX provides a variety of choice of turbulence models, however only the standard k-ε, Renormalization Group (RNG) k-ε and Reynolds Stress model (RSM) will be examined in detail, as they have been used during the course of this study.

2.6.4 The k-ε Model

The turbulent transport model predominantly used in this research is the k-ε turbulence model[12,13]. In fully turbulent flows, κ and ε are used to define the velocity scale θ and the length scale l as follows:

$$\theta = \kappa^{1/2} \tag{2.28}$$

$$l = \frac{\kappa^{3/2}}{\varepsilon} \tag{2.29}$$

The first transport equation models the turbulent kinetic energy k and the second equation models the rate of dissipation of energy ε from the turbulent flow. The turbulent kinetic energy and its rate of dissipation are obtained from the transport equations and are written, for an incompressible flow, as:

$$\frac{\partial \kappa}{\partial t} + u_i \frac{\partial \kappa}{\partial x_i} = \frac{\partial}{\partial x_i}\left(\frac{\mu t}{\rho \sigma_k} \frac{\partial \kappa}{\partial x_i} \right) + \frac{\mu_t}{\rho}\left(\frac{\partial u_i}{\partial x_j} + \frac{\partial u_j}{\partial x_i} \right) \frac{\partial u_i}{\partial x_j} - \varepsilon \qquad (2.30)$$

$$\frac{\partial \varepsilon}{\partial t} + u_i \frac{\partial \varepsilon}{\partial x_i} = \frac{\partial}{\partial x_i}\left(\frac{\mu t}{\rho \sigma_\varepsilon} \frac{\partial \varepsilon}{\partial x_i} \right) + C_1 \frac{\varepsilon}{\kappa} \frac{\mu_t}{\rho}\left(\frac{\partial u_i}{\partial x_j} + \frac{\partial u_j}{\partial x_i} \right) \frac{\partial u_i}{\partial x_j} - C_2 \frac{\varepsilon^2}{\kappa} \qquad (2.31)$$

where $\mu_t = \rho C_\mu \dfrac{\kappa^2}{\varepsilon}$ and C_μ is a constant (2.32)

The equations of the *k-ε* turbulence model contain five adjustable constants C_μ, C_1, C_2, σ_k and σ_ε. Their values have been determined from experiments using air and water[14] for fundamental turbulent shear flows, including homogeneous shear flows and decaying isotropic grid turbulence. Their values are given as:

$C_\mu = 0.09$, $C_1 = 1.44$, $C_2 = 1.92$, $\sigma_k = 1.0$ and $\sigma_\varepsilon = 1.3$.

The standard *k-ε* model is not highly recommended for use in the viscous sub-layer of a flow due to the small damping effect associated with solid boundaries. Modifications to the model, in order to improve performance at low Reynolds numbers, have been investigated by a number of researchers[14,15,16,17].

In general, the *k-ε* model is the most commonly used and tested turbulence model available in CFX. It has proved successful in determining a wide range of thin shear layer and recirculating flows as well as confined flows where the Reynolds shear stresses are the most important. However, the model is not reported to perform well in weak shear layers and

those of a rotating nature, e.g. strongly swirling flows. In addition it is not recommended for use in flows with large, rapid strains as in highly curved boundary layers and diverging passages, since it does not contain a description of the subtle effects of streamline curvature on turbulence. Secondary flows in long non-circular ducts, which are driven by anisotropic normal Reynolds stresses, can also not be predicted well. In all these cases, other turbulence models such as the RNG k-ε model and the RSM are expected to perform more accurately.

2.6.5 The RNG k-ε Model

The RNG model[18,19] belongs to the family of k-ε models and is derived using statistical techniques and analytical model constants. The RNG procedure systematically removes small scales of motion from the governing equations by expressing their effects in terms of larger scale motions and a modified viscosity. As small scale eddies are removed, the effective Reynolds number is decreased as the viscosity changes from its molecular value to an effective viscosity. This process is repeated iteratively, and the modified Navier-Stokes equations are computable on relatively course grids and at higher Reynolds numbers.

Based on this mathematical foundation to turbulence modelling, as opposed to semi-empirical approaches, the RNG provides a more general model and yields improved predictions of near wall flows, including separation. In the same way, flows with high streamline curvature, high strain rate, and low Reynolds number, as well as strong swirl, benefit from this model.

2.6.6 The Reynolds Stress Model

The RSM presents a more mathematically complex structure and it follows on from the work of Launder *et al*[20], whereby abandoning the isotropic eddy-viscosity hypothesis, the RSM closes the RANS equations by solving transport equations for the individual Reynolds stresses, in addition to an equation for the dissipation rate.

The Reynolds stress term is given by:

$$R_{ij} = -\frac{\tau_{ij}}{\rho} = \overline{u_i' u_j'} \tag{2.33}$$

The exact equation for the transport of R_{ij} takes the following form:

$$\frac{\partial \overline{u_i' u_j'}}{\partial t} + u_k \frac{\partial \overline{u_i' u_j'}}{\partial x_k} = -\left[\overline{u_i' u_k'} \frac{\partial u_j}{\partial x_k} + \overline{u_j' u_k'} \frac{\partial u_i}{\partial x_k} \right] + \overline{\frac{p}{\rho}\left(\frac{\partial u_i}{\partial x_j} + \frac{\partial u_j}{\partial u_i} \right)} + \frac{\mu}{\rho} \frac{\partial^2 \overline{u_i' u_j'}}{\partial x_k^2}$$

A B C D

$$-\frac{\partial}{\partial x_k}\left(\overline{u_i' u_j' u_k'} + \frac{\overline{u_j p}}{\rho}\delta_{ik} + \frac{\overline{u_i p}}{\rho}\delta_{jk} \right) - 2\frac{\mu}{\rho}\overline{\frac{\partial u_i}{\partial x_k}\frac{\partial u_j}{\partial x_k}} \tag{2.34}$$

E F

where $\frac{\partial \overline{u_i' u_j'}}{\partial t} = \frac{DR_{ij}}{Dt}$ and:

A is the convective transport term,

B is the stress production term,

C is the pressure strain term,

D is the viscous diffusion term,

E is the turbulent diffusion term and

F is the dissipation term.

Equation (2.34) describes six partial differential equations; one for the transport of each of the six independent Reynolds stresses: $\overline{u_1'^2}, \overline{u_2'^2}, \overline{u_3'^2}, \overline{u_1' u_2'}, \overline{u_1' u_3'}, \overline{u_2' u_3'}$. To obtain closure of equation (2.34) it is necessary to introduce some modelling assumption, as some of the terms are unknown.

The turbulent diffusive transport, the pressure strain and the dissipation rate are required to close the equation terms and CFX provides default values or data input tabs in the Pre-processing stage.

2.7 Combustion Modelling

There are five combustion models available in CFX, the Eddy Dissipation model (ED), the Finite Rate Chemistry model (FRC), the combined ED/FRC model, the Laminar Flamelet model (LF) and the Turbulent Flamespeed Closure model (TFC). Each is described in the following sections. Two of these models are well suited to the present study, and are described in more detail. The ED model was developed for use in a wide range of turbulent reacting flows covering premixed and diffusion flames, and due to its simplicity and robust performance has been widely applied in the prediction of industrial flames. The TFC model was designed specifically for partially pre-mixed turbulent flames such as that of the WRTB, but is a recent and relatively unproven development.

CFX has a chemical reaction library[12] from which specific reaction schemes can be selected. Alternatively new schemes can be created. Options include single-step and multi-step schemes (required for the FRC, FRC/ED and ED models), as well as flamelet libraries (required for the LF and TFC models). The available reaction schemes include a two-step reaction process for the combustion of CH_4 after the work of Westbrook and Dryer[21]. In the first step CH_4 reacts to CO and H_2, with oxidation of CO to CO_2 in the second step. Also available is a flamelet library for CH_4-air combustion.

The FRC model allows the computation of reaction rates described by the molecular interaction between the components in the fluid. This model is more suitable in flows where the reaction rate is dominated by chemical kinetics and kinetic data for the reaction rates is required. It is not recommended for highly turbulent flows (as found in the WRTB), and although it can work well with turbulence, it is intrinsically difficult to determine the reaction rate in such flows. The model also requires an initialisation for flame ignition, as it has temperature dependence of reaction rates, therefore an appropriate fluid domain initial

temperature has to be set. Furthermore, the FRC model has sensitivity to the initial time scale definition that can result in convergence instabilities[12].

An improvement over the FRC model, to counterbalance the limitations of turbulence and chemistry interaction, is the combined FRC/ED model. The effective reaction rate is computed to be the minimum of the FRC rate and the ED rate at all points. Clearly this adds to computational expense, but the model is recommended if reaction rates are limited by turbulent mixing in one area of the domain and limited by chemical kinetics somewhere else. It can be used for flames where chemical reaction rates are slow compared with the reactant mixing rates (highly turbulent flows). The model also requires an initialisation for flame ignition and, preferably, a temperature setting for flame extinction that disables the reaction wherever the temperature is less than the specified extinction temperature. The reaction rate is set to zero if the turbulent time scale is smaller than the chemical time scale value and therefore, when the model for flame extinction at high turbulence is activated, local extinction occurs. Furthermore, a value for the chemical time scale has to be provided and varied during the simulation, if necessary to a more suitable value, in order to accelerate the convergence of the solution. This model is more complex than the standard ED model.

In the ED/FRC model, (also in the ED model) transport equations for individual species are not solved. Instead, individual component concentrations for the species are derived from the predicted mixture fraction distribution. Reaction mechanisms that may be exceedingly complex are explicitly defined. However, the ED model is more robust than the combined ED/FRC model. Convergence instabilities can also be witnessed here[12], but can be reduced by utilizing the results file from a simulation, and then use them as initial values file running an ED model. Subsequently, the ED/FRC model can then be restarted with the new results file as initial input. This process adds complexity and far longer time scales to the solution.

2.7.1 Eddy Dissipation Model

The ED model is widely used for premixed and diffusion flames and is based on the concept that chemical reaction due to turbulence is fast relative to the transport processes in the flow.

When reactants mix at the molecular level, they instantaneously form products, so that no flame front is resolved as such. The model assumes that the reaction rate may be related directly to the time required to mix reactants at the molecular level. In turbulent flows, such as in the RTB, this mixing time is dominated by the eddy properties and, therefore, the rate is proportional to a mixing time defined by the turbulent kinetic energy, k, and rate of dissipation of energy, ε.

The ED model used in CFX is based on the work of Magnussen and Hjertager[22]. The following reaction is considered:

$$\nu_{fuel} + \nu_{oxidant} \rightarrow \nu_{product} \tag{2.35}$$

The model determines the reaction rate R_i as the minimum $R_i = \min(R_f, R_o, R_p)$ (i.e. limiting value) of three reaction rates:

$$R_f = A\rho\frac{\varepsilon}{k}(Y_f),\ R_o = A\rho\frac{\varepsilon}{k}\left(\frac{Y_o}{r_f}\right) \text{ and } R_p = AB\rho\frac{\varepsilon}{k}\left(\frac{Y_p}{1+r_f}\right) \tag{2.36}$$

The characteristic coefficients A and B are model constants and r_f is a stoichiometric coefficient defined as $r_f = \frac{M_o\nu_o}{M_f\nu_f}$.

Equations (2.36) highlight that the reaction rate is governed by the ratio of the large eddy mixing scale ε and k. Combustion proceeds whenever turbulence is present (i.e. $\varepsilon/k > 0$), and an ignition source is not required to initiate combustion. This is usually acceptable for non-premixed flames, in premixed flames however, the reactants will burn as soon as they enter the computational domain. Coefficients A and B can affect the reaction rate and the latter has an influence on the temperature dependency of the reaction. Lowering this constant will make the reaction rate more dependant on the product concentration. In CFX, the ED model does not present a selectable option for laminar flow combustion.

2.7.2 Laminar Flamelet Model and Probability Density Function

The LF model[23] can provide information on minor species and radicals such as CO and OH, and accounts for turbulent fluctuations in temperature and local extinction at high scalar dissipation rates, for the cost of solving only two transport equations. The combustion is assumed to occur in thin sheets with inner structure called Flamelets. The turbulent flame itself is treated as an ensemble of laminar Flamelets which are embedded into the flow field. An advantage of the LF model is that even though detailed information of molecular transport processes and elementary kinetic reactions are included in the model, the numerical resolution of small length turbulence and time scales is not necessary. This avoids solving nonlinear kinetics in fluctuating flow fields and improves the robustness of the method. Only two scalar equations have to be solved independent of the number of chemical species involved in the simulation. Information of laminar model flames are pre-calculated and stored in a library to reduce computational time.

The coupling of laminar chemistry with the fluctuating turbulent flow field is done by a statistical method, using a Probability Density Function (PDF). A PDF is any function $f(x)$ that describes the probability density in terms of the random input variable x when $f(x)$ is greater than or equal to zero for all values of x. The value of the integrated function over all values of x is 1. The probability of x being between a and b is given by:

$$P\{a < x \leq b\} = \int_a^b f(x)dx \qquad (2.37)$$

In the LF model the PDF used can be calculated at every point in the flow field by solving a PDF transport equation[12]. An advantage of this solution approach is that the non-linear chemical source term does not require modelling.

However, there are restrictions to this model. In certain flows it can only predict adiabatic conditions for the combusting mixture and it requires a chemical library to represent the reactions correctly. It is also limited to single mixture fractions and therefore will not in isolation predict accurately pre-mixed fuel/oxidiser combusting flows such as the flow mixture in the WRTB pilot burner.

2.7.3 Turbulent Flamespeed Closure Model

The TFC model has been developed in recent years; it can be applied to a wide range of flows and can be split into two independent parts. The first and most important part is a model for the progress of the global reaction, known as the TFC model. The second part is a model for the composition of the reacted and non-reacted fractions of the fluid, which uses the Laminar Flamelet with PDF approach (see Section 2.7.2). The mass fractions in the non-reacted fraction of the fluid are obtained by linear blending of fuel and oxidiser compositions.

The TFC model is the approach developed by Zimont *et al*[24]. In this model, designed for partially pre-mixed flames, a single variable C is used to describe the progress of the global reaction. The composition of the fluid is determined by blending the compositions of the non-reacted state (fresh gases) and the reacted state (burned gases), where C=0 corresponds to fresh materials and C=1 corresponds to fully reacted materials. In turbulent flow, a bimodal distribution of C is assumed.

At any given time and position in space the fluid is considered to be either fresh materials or fully reacted. The progress variable C is the probability for the instantaneous state of the fluid being reacted. This assumption is justified if the chemical reaction is fast compared to the integral turbulent time scales of the flow. The model is thus able to resolve a flame front, which is the border between the two possible states. It presents therefore a relative advantage in comparison to other combustion models such as the ED model.

The flame front moves with the turbulent flame speed S_T. In CFX the turbulent flame speed is derived by the following equation[25], which is validated for various fuels, including CH_4:

$$S_T = AGu'^{3/4} S_L^{1/2} \lambda_u^{-1/4} l_t^{1/4} \qquad (2.38)$$

where A is a model constant and G is a factor that accounts for reduction of the flame velocity due to large strain rate. This effect is modelled in terms of the probability for turbulence eddy dissipation ε, being larger than a critical value ε_{cr}. The factor G is proportional to the $\ln(\varepsilon_{cr}/\varepsilon)$ and for $\varepsilon>\varepsilon_{cr}$ flamelet extinction takes place.

Using a density weighted time averaging technique (Favre averaged), the reaction progress variable $\tilde{C}$ can be derived by a transport equation:

$$\frac{\partial\left(\overline{\rho}\tilde{C}\right)}{\partial t}+\frac{\partial\left(\overline{\rho}\tilde{u}_j\tilde{C}\right)}{\partial x_j}=\frac{\partial}{\partial x_j}\left(\frac{\mu_t}{\sigma_c}\frac{\partial\tilde{C}}{\partial x_j}\right)+\rho_u S_T\left|grad\,\tilde{C}\right| \qquad (2.39)$$

If the turbulent flame speed is known, this transport equation is closed and the value of the turbulent flame speed has been researched in many theoretical and experimental publications as well as derived using equation (2.38).

The definition of the reaction progress variable allows only the two states, burned and unburned. Because of this the mean state has to be:

$$\tilde{Y}_\alpha = C\tilde{Y}_{\alpha,fresh}+(1-C)\tilde{Y}_{\alpha,burned} \qquad (2.40)$$

The composition of the burned gas fraction $\tilde{Y}_{\alpha,burned}$ is computed using a laminar flamelet library with PDF.

2.7.4 NO model

In ANSYS CFX the NO model[12] is implemented by means of generic reactions with Arrhenius Temperature PDF reaction rates. Control for these reactions is the same as for Arrhenius rates, but with the upper and lower bounds specified for the temperature integration range. The NO model calculates mass fractions of NO formed in the combustion process. According to the Arrhenius law, the rate of a chemical reaction increases exponentially with the absolute temperature. Both thermal and prompt reaction schemes are included.

The NO formation model consists of different parts that include predefined reaction schemes for NO formation, integration of the reaction rates for NO formation over a

presumed PDF in order to account for turbulent fluctuations of temperature, and solving a transport equation for the temperature variance.

The thermal NO is formed from the combination of free radical O and N species, which are in abundance at high temperatures, using the three-step (extended) Zeldovich mechanism. When using the LF model, the O radical concentration can be taken without further assumptions from the solution since the model predicts it directly. However, when using the ED model O radical concentrations usually are not known directly but must be derived from other quantities. Here, the O radical concentration is estimated from the molecular oxygen dissociation.

In CFX, turbulence has a dominant impact on the NO formation rate and for the thermal NO mechanism there is a strong dependence of the rates on the temperature fluctuations due to their high activation energy. Temperature fluctuations, particularly positive fluctuations, can increase the predicted NO formed in flames and they are accounted for using the PDF statistical approach, as mentioned earlier. For the temperature variance equation used for the NO model, the equation is missing some physical aspects namely the production of temperature fluctuations due to heat release by chemical reaction. Heat release is fluctuating, too, because of turbulent fluctuations of the reactants. However, the temperature variance is only needed as input to the construction of a PDF.

Due to these characteristics of the CFX NO model, over-prediction of NO can occur, particularly in the case of the ED combustion model, where flame temperature predictions are closely related to the turbulence fluctuations. Nevertheless, these limitations can be counterbalanced with user adjustments in the model setup. The model parameter that can be adjusted is the temperature integration range. The predefined reaction schemes come with the range set to the interval, usually from 300 to 2300 degrees K. However it is recommended to adjust this to the maximum temperature range occurring[12], which for many applications is defined by the minimum inlet temperature and the adiabatic flame temperature.

2.8 Radiation Modelling

Radiation models are used to account for the radiative heat transfer that occurs within the model. Radiation is clearly an important aspect of RTB operation, because it is the primary mechanism of heat transfer to the surrounding furnace.

CFX provides four radiation models, which are all based on the radiative transfer equation (2.41) shown below, for an absorbing, emitting and scattering medium at position r in the direction *s*:

$$\frac{dI(r,\varsigma)}{ds}+(a+\sigma_s)I(r,\varsigma)=an^2\frac{\sigma T^4}{\pi}+\frac{\sigma_s}{4\pi}\int_0^{4\pi}I(r,\varsigma')\Phi(\varsigma\cdot\varsigma')d\Omega' \qquad (2.41)$$

where $(a+\sigma_s)\varsigma$ is the optical thickness (or opacity) of the medium.

Two of the models, the Discrete Transfer model (DT) and the Monte Carlo method (MC), are computationally intensive. The remaining two options, the P-1 model (also known as the Gibb's model) and the Rosseland (also known as Diffusion Approximation model), present an algebraic simplification on the solution of the radiative heat transfer equation. In the WRTB study, the thermal radiation model choice is significant as it influences substantially not only the quality, but also the computational time of the simulation.

The P-1 and Rosseland models are best suited to applications where the computational domain is optically "thick" (as for example in coal combustion modelling), due to their simplicity, although in this case all radiation models will produce similar results. Optical thickness is a measure of the ability of a given path length of gas to attenuate radiation of a given wavelength.

The P-1 model assumes that all surfaces are diffuse meaning that the reflection of incident radiation at the surface is isotropic with respect to the solid angle. There may be a loss of

accuracy, depending on the complexity of the geometry, if the domain optical thickness is small, as is the case with natural gas combustion.

The Rosseland approximation has a deficiency of prediction near walls and, although CFX applies special treatment to counterbalance this limitation, the model is inappropriate in the case of the WRTB where the resolution of the wall radiation heat transfer is critical.

Furthermore, where a "gray" spectral model is assumed (as is the case here), the DT and MC models are the preferred options due to its simplicity in the solution. The "gray" assumption makes the DT and MC approaches less computationally expensive. Only one radiative transfer equation must be solved as all total radiation quantities and their spectral counterparts are the same. The DT model in particular, is susceptible to significantly enhanced computational time scales if a different spectral model such as the "multiband" model is used[12].

Gray spectral models assume that all radiation quantities are uniform throughout the spectrum and this greatly simplifies the radiation calculation. This implies that the combustion air has the same radiative properties as the combustion products, although the latter contains a high percentage of CO_2 and H_2O, which are significant absorbers and emitters of thermal radiation. However, for combustion calculations where certain gases are absorbing in different regions of the spectrum and can be transparent for other regions, the errors in the total radiative flux are expected to be small.

Alternatively, a Multigray/Weighted Sum of Gray Gases[12] spectral model can be used in which the user must specify the weights/amplitudes and the absorption coefficients separately for each gas.

For the reasons given, only the DT and MC models are used in the present study. These are described further below.

2.8.1 The Discrete Transfer model

The DT model solves the radiative transfer equation throughout a domain by a method of ray tracing from surface elements on its boundaries. The model discretises the path along every traced ray in the sections formed by sectioning each ray in small uniform element boundaries and radiative energy is represented by a combination of the emitted intensity and the reflected component of the incident intensity[26]. The physical quantities in each element are assumed to be uniform. These rays have to be traced through the domain in the same way that the photons would be tracked in the MC model. Therefore, the model description for both MC and DT is similar. For the results to be accurate the elements must be chosen so that the radiation field is reasonably homogeneous inside them. This means, for example, that they must be small enough that the scattering optical depth is less than unity across each element.

The main assumption of the DT model is that the radiation leaving the surface element in a certain range of solid angles can be approximated by a single ray.

The primary advantages of the DT model are threefold. Firstly, it is a relatively simple model, no extra terms are introduced as non-linearities in the system due to scattering, diffuse reflection, or temperature dependency of radiation quantities is overcome by iteration of the solution, although, since the objective of thermal radiation modelling is to obtain the total volumetric absorption and emission, additional calculations are still needed. For the gray spectral model, the calculation is done only once for a unique radiation intensity field.

Secondly, the accuracy of the model can be increased by increasing the number of rays; however, there is a limitation on the number of rays used as the computational time increases exponentially.

Thirdly, the model can be applied to a wide range of optical domain thicknesses.

In addition, for gray spectrum gas models the DT model can be more efficient in computational time in comparison to the MC method and in situations where the same mesh is used in consecutive runs, the ray paths can be calculated once and then stored during iterations and subsequent model runs.

2.8.2 The Monte Carlo Model

In general, MC methods[27] are used in mathematics to solve various problems by generating suitable random numbers and observing that fraction of the numbers obeying some property or properties. The method is useful for obtaining numerical solutions to problems which are too complicated to solve analytically. The most common application of the MC method is MC integration. MC methods have proven efficient in solving coupled integral differential equations of radiation fields and energy transport, and these methods have also been used in computations which produce photorealistic images.

In CFX, the MC model assumes that the radiation intensity is proportional to the differential angular flux of photons and simulates the radiation field as a photon gas domain. These photons have to be traced through the domain in an intrinsic manner as the traced rays in the DT model. A photon is selected from a photon source and tracked through the system until its weight falls below some minimum. Each time the photon experiences a disturbance in the form of a surface intersection, scattering or absorption, the physical quantities are updated.

This process generates a complete history of that photon in the system. Many photon histories need to be generated to get good estimates of the physical quantities of interest in a system and this can result in extensive computational time. In theory, the Monte Carlo method is more accurate if sufficient histories are traced, but the DT model is computationally more efficient. In addition, the MC model is more susceptible to numerical errors that can lead to oscillatory solution residuals, due to mesh resolution, than the DT model.

2.9 Numerical Schemes

CFX uses a coupled, finite volume solver, which solves the hydrodynamic equations (for u, v, w, and p) as a single system. The finite volume is a method for representing and evaluating algebraic equations and, similar to the finite difference method, values are calculated at discrete places on a meshed geometry. "Finite volume" refers to the small volume surrounding each node point on a mesh. In the finite volume method, volume integrals in a partial differential equation that contain a divergence term are converted to surface integrals. These terms are then evaluated as fluxes at the surfaces of each finite volume. Because the flux entering a given volume is identical to that leaving the adjacent volume, the method is considered conservative. An advantage of the finite volume method is that it is easily formulated to allow for unstructured meshes. Furthermore, the finite volume method is preferable to other methods as a result of the fact that boundary conditions can be applied non-invasively. This is true because the values of the conserved variables are located within the volume element, and not at nodes or surfaces.

The coupled solver solution approach uses a fully implicit discretisation of the equations at any given time step. On the other hand, non-coupled (i.e. segregated solvers), as used by other CFD codes, employ a linear solution strategy where the momentum equations are first solved, using a guessed pressure, and an equation for a pressure correction is obtained. Because of the guess-and-correct nature of the linear system, a large number of iterations are typically required in addition to the need for the astute selecting of relaxation parameters for the variables. Coupled solvers are far more economical.

Discretization is the process of transferring continuous models and equations into discrete counterparts. This process is usually carried out as a first step toward making them suitable for numerical evaluation and implementation on mathematical computational software. In the finite volume grid method CFX integrates the computational equations in each finite volume, yielding discrete equations that conserve each quantity of the variables.

To complete the discretisation of the flow equations, different mathematical schemes are implemented in CFX. The three choices available during the model runs were the high resolution scheme, the central difference scheme and the upwind scheme.

The central difference scheme, although it is a well known solution method, it has an inability to identify the flow direction or the strength of convection relative to diffusion. The first order upwind scheme takes into account the flow direction when determining the value of a property at a cell face. The convection value of a property at a cell face is taken to be equal to the value of the upstream node. In the second order upwind scheme, higher order accuracy is achieved by extrapolating to the face of two upstream nodes instead of one.

These schemes offer robust performance for the CFX solver. However, they suffer from numerical diffusion effects that limit the accuracy of the solution. In this situation the effect varies according to the alignment of the mesh with the flow direction. It is therefore relatively straightforward to achieve highly accurate solutions to simple flow problems, such as flow in a duct where alignment of the mesh with the predominant flow is relatively simple, but not recommended in convoluted geometry analysis, as in the case of the WRTB.

The high resolution scheme[28] is an accurate method, as it reduces to first order near discontinuities and in the free stream where the solution has little variation. Furthermore, it has the desirable property of giving second order accurate gradient resolution while keeping solution variables physically bounded. This scheme was chosen for the model runs during this research study.

Another parameter that has an effect on the numerical solution is the time step. For steady state problems, the time step behaves like an acceleration parameter, to guide the approximate solutions in a physically based manner to a steady state solution. This reduces the number of iterations required for convergence to a steady state, or to calculate the solution for each time step in a time dependent analysis.

The solution procedure consists of two numerically intensive operations. For each time step the non linear equations are linearised and assembled into the solution matrix. The linear equations are solved using an algebraic multi grid method. The time step iteration is controlled by the global physical time step or local time step factor setting to advance the solution in time for a steady state simulation. In this case, there is only one linearization iteration per time step. For transient analyses, the time step and coefficient iterations are explicitly controlled.

At the end of every solver time step iteration, the residual sum for each of the converged variables is computed and stored, thus reducing the convergence history. For general flow problems in CFX, global quantities will stabilise within 20 to 30 time steps, but convergence will not be achieved until approximately 100 time steps have completed. For most applications, convergence should be achieved within 200 time steps due to the accelerated algorithms utilised by the CFX solver.

The CFX solver will terminate the run when the equation residuals calculated are below the residual target value. The default target residual value is 0.0001. A lower value of 0.00001 is classified as tight convergence, sometimes required for geometrically complex problems, and is the level used for the WRTB models.

2.9.1 The Finite Volume Grid

One of the first steps in computing a numerical solution is the construction of a grid, which is essentially a sub-division of the computational domain. The computational domain is created using standard CAD-type building block tools and by the use of Boolean operations (subtract, unite etc.). One advantage of the finite volume method over finite difference methods is that it does not require a structured mesh (although a structured mesh can also be used).

The geometrical mesh dictates where the equations are to be applied and is classified in structured/unstructured and single/multi-block and "hybrid" types. Unstructured meshes can

be generated automatically, using different types of cells (hybrid mesh) and structured meshes utilise single or multi-block cell arrangement.

For two dimensional applications, quadrilateral and triangular cells is the common, for three dimensional applications, hexahedral (prism), tetrahedral, pyramid and wedge shape cells. Single/multi-block or a hybrid combination of these cells can be used in both cases, with the hybrid combining prism wall elements with tetrahedral or wedge shape elements for the overall domain volume. The hybrid prismatic/tetrahedral strategy requires no solution interpolation or grid interfacing techniques as in the traditional block structured approach. The hexahedral portions of the grid reduce the memory requirements when compared with an all tetrahedral grid of the same resolution, and also reduces grid generation time substantially.

For a complex geometry such as the WRTB, an unstructured grid is far easier to create than a structured grid, and also far more versatile in terms of local grid refinement. This will lead to more accurate simulations, although for simpler problems such as an airfoil section, structured grids will give superior results.

The use of the unstructured hybrid mesh has specific advantages. The prismatic layers close to wall surfaces exhibit good orthogonal and clustering capabilities that are characteristic of a structured mesh nature. The structured nature allows for the implementation of multi grid convergence acceleration schemes, implicit methods, and also results in memory savings. The use of tetrahedral elements to complete the rest of the volume domain, allows single block generation for extremely complex geometries, as the tetrahedron is the simplest element in three dimensional form. Furthermore, the unstructured tetrahedral elements are well suited for cell adaptation, thus allowing the resolution of active features in the domain. The flexibility of the hybrid mesh generation approach automates an otherwise highly interactive procedure. The principal of a hybrid prism/tetrahedral unstructured mesh has been the preferred option during this study.

2.9.2 Modelling Wall Functions

The near wall modelling significantly impacts the fidelity of numerical solutions, as the walls present a main source of vorticity and turbulence. In the near wall region the solutions variables change with large gradients, and the momentum and other scalar transports occur more vigorously. The velocity changes rapidly from a value of zero at the wall (no-slip condition) to the free stream value a short distance away from the wall. This layer of high velocity gradient is known as the boundary layer.

Therefore, accurate representation of the flow in the near wall region determines successful predictions of confined flows, such as those seen in the WRTB. Previous work has shown that the near wall regions can be subdivided into three layers. In the inner most layer, the "viscous sub layer", the flow is almost laminar and the molecular viscosity plays a dominant role in momentum and heat or mass transfer. The outer most of the three layers is the fully turbulent layer, and in between, there is an interim region where the effects of molecular viscosity and turbulence are equally important.

Many meshes are not fine enough near a wall to accurately resolve the velocity profile in the boundary layer. Semi-empirical formulas named "wall functions" can be used in these cases to apply an assumed functional shape of the velocity profile. Other grids are fine enough that they do not require wall functions, and application of the latter has little effect. The majority of flows, fall somewhere in between these two extremes, where the boundary layer is partially resolved by nodes near the wall. Wall functions are then used to supplement accuracy where the nodes are not sufficiently clustered near the wall.

There are two approaches to modelling the near wall region. In one approach, the viscosity affected inner region (viscous sub layer and interim layer) is not resolved. Instead, wall functions are used to bridge the viscosity affected region between the wall and the fully turbulent region. The use of wall functions removes the need to modify the turbulence models to account for the presence of the wall. The wall function approach, however, is not very suitable in low Reynolds number flows, as the wall functions are not valid. In these flows the second approach must be used to solve the flow field correctly.

In the second approach, the turbulence models are modified to enable the viscosity affected region to be resolved with a hybrid mesh, all the way to the wall, including the viscous sub layer.

In CFX the first approach is used with most k-ε based turbulence models, although with an advancement on the standard wall functions, the scalable wall functions. Scalable wall functions overcome one of the major drawbacks of the standard wall function approach in that they can be applied on arbitrarily fine meshes. In the second approach, the code uses automatic near wall treatment that switches from wall functions to a low-Re near wall formulation.

As the flow velocities experienced in the WRTB simulations and experiments determine a moderate to high Reynolds number (typically Re>5000), the scalable wall function approach accounts for any mesh deficiencies. The scalable wall functions used in CFX are based on previous research[29].

One indicator of the closeness of the first node to the wall is the dimensionless wall distance y+ (y plus) and is used as a mesh quality measure for every CFD model. It is therefore dependent on the size of the mesh in the wall region.

At the lower limit, a value of y+ less than or equal to 11 indicates that the first node is within the laminar sub layer of the boundary flow. Values larger than this indicate that an assumed logarithmic shape of the velocity profile is being used to model the boundary layer portion between the wall and the first node.

The upper limit for y+ is a function of the models Reynolds number. For example, a large ship may have a Reynolds number of 10^9 and y+ can safely go to values much greater than 1000. For lower Reynolds numbers, as in the case of WRTB, the entire boundary layer might only extend to around y+ = 300.

This was more important when standard wall functions were used, as y+ values smaller than approximately 20 had to be avoided. If the value of y+ is too large, then wall functions will

impose wall type conditions further from the wall. The use of scalable wall functions in CFX has removed problems associated with the lower valid limit for y+ and, in the case of the WRTB, y+ values not exceeding 100 are considered acceptable.

2.9.3 Convergence and Stability

Poor convergence problems can be initiated by many factors. These can include low mesh quality, improper boundary condition selection and time step selection. Although relatively large time steps can be used, if the time step is too large the resulting convergence behaviour can be oscillatory. In this situation, a reduction of the time step size, by a factor of four, can enhance the convergence level; although, if no noticeable improvement, then the convergence problem can be caused by another factor. If the time step is too small, then convergence will be very slow. In addition, a small physical time step should be used for the cases of poor mesh quality, transonic flow, large regions of separated flow and outlet boundaries with simultaneous inflow and outflow.

Finally, in the case where there is a solid domain present in a multi domain simulation, as in the WRTB models, steady-state calculation can also produce convergence issues if the solid domain time scale is set the same as the global model time scale. Since there is no flow in a solid domain, the relevant time scales for the solution in the solid part of the domain can be much longer than the time scales in the fluid domain. Therefore, a much larger solid domain time scale has to be used in comparison to the fluid domain time scale.

2.10 References

1. Gupta A K, Lilley D G and Syred N, Swirl Flows, Abacus Press, 1984.
2. Tennekes H., Lumley J.L., A first source in turbulence. The MIT Press, 1972, Cambridge, Massachusetts, London.
3. Phylaktou H *et al*, IChE Symp Series 130, 525, 1992.
4. Kaufman F, "Chemical Kinetics and Combustion: Intricate Paths and Simple Steps", 19th Symposium on Combustion, Pittsburgh, PA, pp. 1-10, 1982.
5. Bowman C T, Hanson R K, Davidson D F, Gardiner W C Jr, Lissianski V, Smith G P, Golden D M, Frenklach M and Goldenberg M, *GRI-Mech* home page, http://www.me.berkeley.edu/gri-mech/.
6. S.R. Turns, An Introduction to Combustion, McGraw-Hill, New York, 1996.
7. Andrews G, Proceedings of course "Combustion in boilers and furnaces", March 2004 Energy and Resources Research Institute, University of Leeds, UK.
8. Baukal C.E., The John Zink Combustion Handbook, CRC Press, Boca Raton, FL, 2001.
9. Douglas J.F., Gasiorek J.M., Swaffield J.A., Fluid Mechanics, 4th Edition, 1979, Pitman International text, UK.
10. Lohner R., Applied CFD Techniques, (2001), An introduction based on finite element methods, John Willey & Sons Ltd, West Sussex, UK.
11. Hinze J O, Turbulence, Second edition, McGraw-Hill, Inc, 1975.
12. CFX 10 User Manual, ANSYS UK Software Solutions, Abingdon, Oxford, 2006.
13. Launder B.E. and Spalding D.B., Mathematical Models of Turbulence. Academic Press, London England, 1972.
14. Launder B E and Sharma B I, Application of the energy dissipation model of turbulence to the calculation of flow near a spinning disk, Lett. Heat Mass transfer, Vol. 1, pp 131-138, 1974.
15. Jones W P and Launder B E, 1972, The Prediction of laminarization with a two-equation model of turbulence, Intern Journal of Heat and Mass Transfer, Vol. 15, pp 301-314.
16. Lam C K G and Bremhorst K A, Modified form of k-ε model for predicting wall turbulence, Journal of Fluid Engineering, Vol. 103, pp. 456-460, 1981.

17. Patel V C, Rodi W and Scheuerer G, Turbulence models for near wall and low Reynolds number flows: A review, AIAA J, Vol.23, No 9, pp. 1308-1319, 1985.
18. Yakhot *et al*, "Renormalization Group Analysis of Turbulence", Introduction Basic Theory, J. of Science and Computing, Vol. 1, pp 1-51, 1986.
19. Choudhury D, Introduction to the Renormalization Group Method and Turbulence Modelling, Fluent Inc. Technical Memorandum TM-107, 1993.
20. Launder B E, Reece G J and Rodi W, Progress in the developments of a Reynolds-Stress Turbulence Closure. J Fluid Mech, 1975, Vol. 68, pp 537–66.
21. Westbrook C K & Dryer F L, "Simplified Reaction Mechanisms for the Oxidation of Hydrocarbon Fuels in Flames", Combustion Science and Technology Volume 27, pp 31-43, 1981
22. Magnussen B F and Hjertager B H, "On Mathematical Modelling of Turbulent Combustion with Special Emphasis on Soot Formation and Combustion" 16th Symp. (Int.) on Combustion, The Combustion Institute, pp 719, 1976
23. Peters, N. "Turbulent Combustion". Cambridge monographs on mechanics, Cambridge University Press, 2000.
24. Zimont V L *et al*, "An Efficient Computational Model for Premixed Turbulent Combustion at High Reynolds Numbers Based on a Turbulent Flame Speed Closure", J. Engineering for Gas Turbines and Power (Transactions of the ASME), Vol. 120, pp. 526- 532, 1998.
25. Zimont V L, "Gas Premixed Combustion at High Turbulence. Turbulent Flame Speed Closure Combustion Model", Proc of the Mediterranean Combustion Symposium, Inst di Ricerche sulla Combustione - CNR, Italy, pp 1155-1165, 1999
26. Lockwood, F. C. and Shah, N. G., Eighteenth Symposium (International) on Combustion, p. 1405, Combustion Institute, 1981.
27. Metropolis N and Ulam S, "The Monte Carlo Method", Journal of the American Statistical Association, Vol. 44, number 247, pp. 335–341, 1949.
28. Barth T J, and Jesperson D C, "The Design and Application of Upwind Schemes on Unstructured Meshes", AIAA, Paper 89-0366, 1989
29. Launder B E and Spalding B E, The numerical computation of turbulent flows, Comp Meth Appl Mech Eng, Vol. 3 pp 269-289, 1974.

3. PREVIOUS WORK

3.1 Introduction

Little attention has been given in the literature to detailed CFD analysis of the flow in RTBs, in comparison with the amount given to other types of industrial burner such as open-ended swirl[1], or non-swirl[2], burners and to fundamental studies of flames[3] .

Other work related to RTBs is concentrated more on heat transfer predictions and the effects of different types of fuels[4,5,6,7] than on the fluid dynamics of the combusting flow.

The summary of previous work presented in this chapter is restricted to studies concerning single-ended RTBs and concentrates around the issues of NOx emissions, burner reliability, flow profile and temperature distribution, which are the principal concerns of this work.

3.1.1 Mei and Meunier, 1997

The work of Mei and Meunier[8] involves experiments and CFD simulations of a single ended radiant tube (SER). The authors comment that most reported numerical studies on natural gas fired RTBs relate to open-ended designs[9,18]. The objective of this study was to model SER tube performance aspects such as thermal efficiency and thermal uniformity, and to comprehend the transfer phenomena in the SER tube with the help of the validated numerical model.

Figure 1 shows the SER arrangement used for the experiments and computations. The combustion model used in the computations is a probability density function (PDF) based approach with β and δ coefficients used typically in fuel/oxidant chemical reaction analysis, together with a Discrete Transfer radiation model. Both the standard k-ε turbulence model and a low-Re renormalised group (RNG) variant are used.

Figure 1: Schematic of SER

The paper presents cold flow validation examples of the turbulence models, concluding that the low-Re RNG model works well with a large range of Reynolds numbers. The low-Re RNG turbulence model is applicable for low Re flows, but the publication states that a slight deterioration in the performance appears with decreasing Reynolds numbers. Furthermore, in the example of coaxial pipe flow validation, all the turbulence models produced similar predictions, although the standard k-ε model predictions were not shown in some cases.

Figure 2 shows the predicted and measured values for temperature distribution along the inner and outer tubes for a low Re test. The study reports a sudden jump of temperature at the far end of the SER and the measurements indicate temperatures as high as 1370K for the inner tube and 1200K for the outer tube. This temperature jump is approximately 150K at the last section of the SER length and the authors state that the source for this jump can not be identified. The trend is reproduced by the RNG model which shows rather better agreement, but not by the standard k-ε model, although the RNG model over-predicts the measurements in the biggest part of the inner tube, and both models under-predict the measurements at the far end of the inner and outer tubes.

Figure 3 shows the predicted temperature field and it can only be assumed that the turbulence model used is the low-Re RNG model, as no reference has been made. The temperatures range from around 2300K at the flame front and reduce to approximately 1700K at the far end.

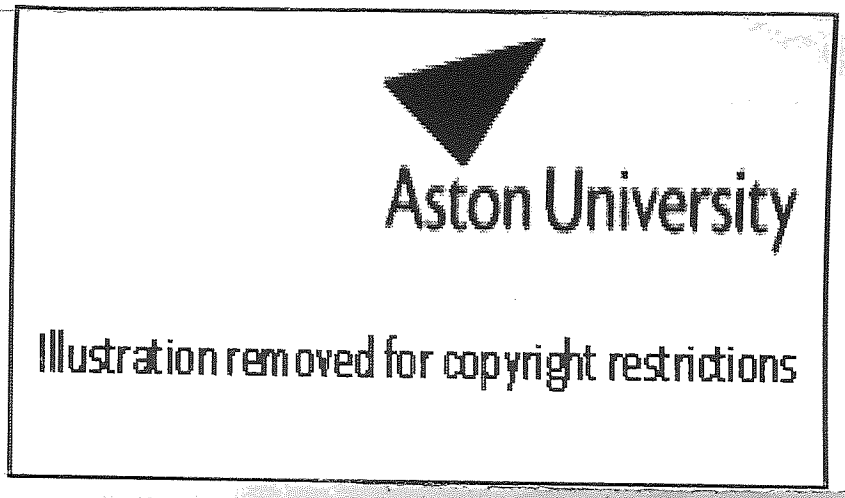

Figure 2: Comparison of predicted to measured wall temperatures

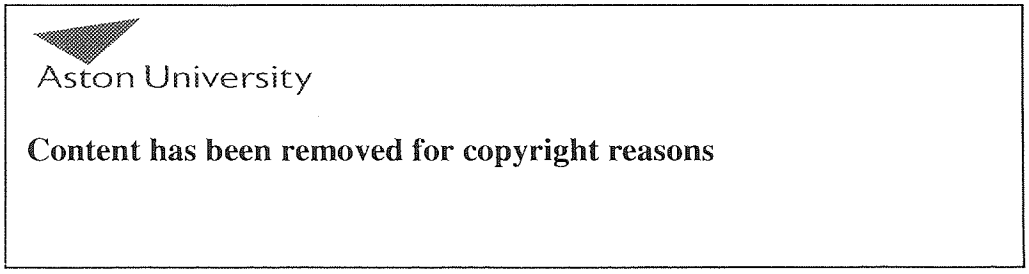

Figure 3: Predicted wall temperature field (contours degrees K) in test-1

The SER burner was mounted in a test furnace where the environment temperature throughout the experiment was controlled by adjustable rate of cooling air and to a thermal uniformity of approximately 10 %. As thermocouple measurements from the furnace walls are not published, one can only assume that the furnace environment presented a correct thermal load for the SER tube test.

In this case, a possible explanation of the temperature peaks at the far end of the burner walls can be flame impingement near the end of the outer tube, nevertheless the results presented in Figures 2 and 3 are not in direct correlation to justify this possibility. Figure 3 indicates a drop in flame temperature values towards the far end of the SER tube, although the authors state the CFD modelling needs to be more thorough.

Only a small amount of detail is given of the fuel nozzle design, the region of most importance to accurate modelling. Details such as the number, position and size of the fuel inlet ports determine the characteristics of the flame and the resulting flow. The authors state that although radiation is the dominant mode of heat transfer, predictions of the heat release pattern and the flame length are essential to estimate temperature uniformity and the peak temperature of the inner tube.

The design and operating conditions are somewhat different to the WRTB. The Reynolds number range is much lower (2500-5800 compared to >100000, as computed by the CFX solver), and the air flow does not have any swirl component prior to entering the combustion chamber. The fuel is premixed with a small amount of air (ratio unstated) before being injected into the main preheated air supply (again at unstated ratio). There is 21-23 % excess air overall (compared with 12-13% for the WRTB). There is no pilot flame, and no splitting of the air into primary and secondary flows.

The main computations are carried out on a 2D axi-symmetric mesh. There is a reference to a 3D model used near the injector nozzle area in order to obtain more detail of the local flow, although there are no results data presented in the paper. The geometrical mesh grid appears to be rather coarse (~2000 nodes). Convergence difficulties are remarked upon.

In this study there are no flue gas composition (NOx) predictions or experimental measurements presented.

3.1.2 Lankhorst and Velthuis, 1995

Lankhorst and Velthuis[10] from TNO Institute of Physics in Delft, Holland presented CFD combustion modelling results from a ceramic (SiC) single-ended RTB simulation. In this simulation they used the k-ε turbulence model, the Discrete Transfer radiation model and a single step combustion model[11] that assumes stoichiometric instantaneous reaction between fuel and oxidants into products.

The burner schematic can be seen below (Figure 4) and it indicates similarities with the WRTB design in the inner and outer tube and recuperation arrangement. It differs fundamentally however in the fuel nozzle design and in the absence of a flame tube for primary/secondary combustion, although there is a split of the combustion air into primary/secondary at a small annulus between the fuel nozzle itself and the inner tube. Furthermore, the WRTB incorporates fuel gas injected tangentially to the primary airflow, and also has a pilot burner; while the RTB tested here has a flat circular fuel nozzle with centrally located, forward firing fuel ports, no pilot burner, and has no air swirl.

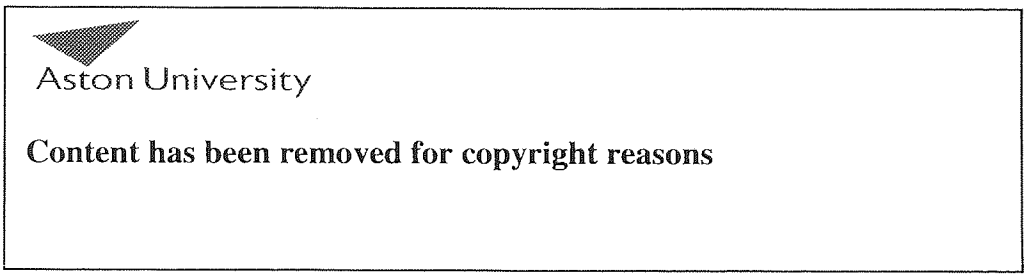

Figure 4: Schematic for RTB simulations

Figure 5 shows the near-nozzle region of the 2D numerical mesh used for the calculations which is of the order of 10000 control volumes in total. This relatively small number raises

issues of mesh sensitivity and adequate near-wall resolution, although the mesh is concentrated close to the nozzle where more resolution is required. 20000 iterations were necessary to obtain a residual in the total energy balance of less than 5%.

Figure 5: Numerical mesh for RTB simulations (detailed view close to nozzle)

Different boundary condition parameters were set on the fuel and air inlets and on the inner and outer walls. The boundary conditions varied were the burner thermal output (19-32 kW), the equivalence ratio (1.04-1.30), and the furnace load temperature (ambient-1200°C). The outer radiant tube temperature profiles were measured for these different boundary conditions. There are no NOx predictions or experimental measurements presented.

The authors conclude that in an RTB, internally convective heat transfer dominates over radiative heat transfer and tube temperature uniformity was found to be better at high furnace temperature. There is no reference to a Reynolds number; even though such flow conditions would never be laminar (for laminar pipe flow Re is typically less than 1000 and there is an indication of 50 m/s axial velocity on Figure 6).

Figure 6 shows the temperature and velocity fields of one simulation (boundary conditions unspecified). The presented data on velocity and temperature indicates a long flame with a peak velocity near the mid point of the burner tube. The flame front is flat and almost

cylindrical, and impinges on the end of the burner tube. The temperature peaks towards the end of the RTB at a maximum value of 2200°C.

Figure 6: Velocity and Temperature field for the reference simulation

The authors state that the flue gas temperature drops to approximately 570 °C due to the recuperative heat exchange in the annulus between the inner and burner air tube. No reference is made to the radiant (outer) tube boundary condition for the simulation and to the conductive heat transfer properties and temperature profile of the inner tube wall.

Simulation data are compared with experimental measurements[12] on the outer tube and it can only be assumed that the measurements were recorded on the same burner as in this study; the reference titles "ceramic recuperative RTB".

The data are presented in a comparison graph between the predicted and recorded measurements. The experimental measurements are limited to three thermocouple locations on the outer tube and are difficult to distinguish between the values. There is an amount of discrepancy between the experimental and predicted values, and the y axis temperature scale unnecessary exceeds the measured maximum values by 400 °C. A reduced scale would have allowed a more clear comparison of the presented data.

3.1.3 Feese and Lisin, 2003

Hauck manufacturing Co, Lebanon, Pa presents some CFD analysis of a recuperative ceramic type single-ended RTB[13]. The inner tube commences downstream of the nozzle (Figure 7), so that returning combustion products can be re-entrained into the flame (flue gas recirculation or FGR). This process results in reduced NOx emissions by reduction of the peak temperature, and also improved temperature uniformity of the outer radiant tube.

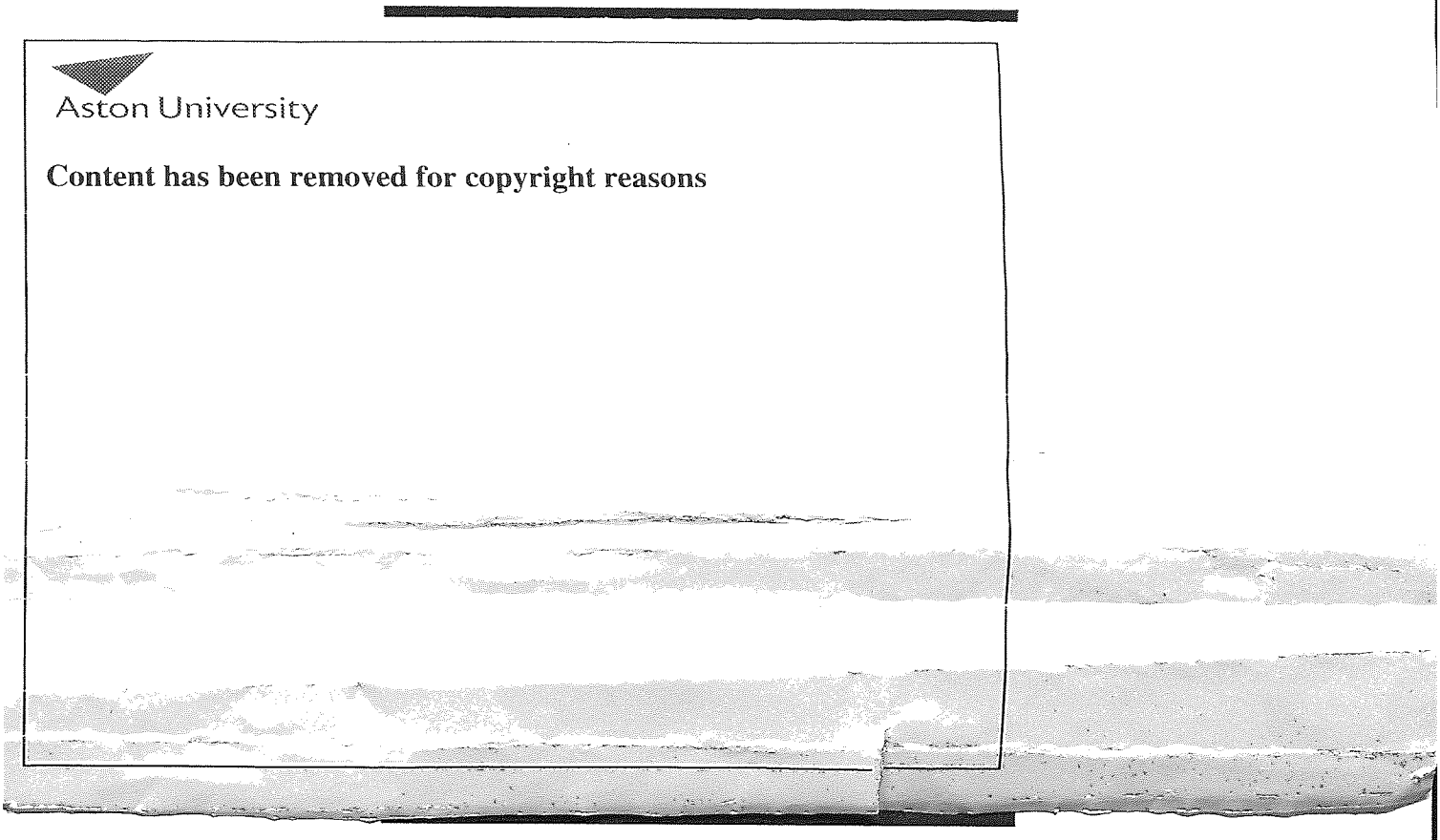

Figure 7: Velocity vectors and Temperature distribution along the radiant tube

The k-ε turbulence model and a probability density function (PDF) approach for combustion were used to model fluid dynamics, heat transfer and combustion processes inside the radiant tube. The resultant flow pattern and temperature distribution are shown in Figure 7.

There is a strong forced recirculation of cooled combustion products into the inner tube (FGR), which suppresses peak flame temperatures to 1980°C maximum (air preheat temperature is 325°C).

A 2D computational mesh is used. All components are modelled as thin walls, thus neglecting conductive heat transfer through the walls as well as flow effects caused by finite thicknesses. The information presented is typical of an industrial report, and does not reveal details that would allow an accurate scientific comparison with work performed at an academic level.

3.1.4 Jager, Mevissen, Munko and Kohne, 2005

The Department of Heat and Mass Transfer at RTWH Aachen, Germany, presents one of the most recent publications[14] in the area of CFD modelling and RTBs. The RTB has a firing rate of 39 kW, using fuel oil, which is nearly 50 % more than the WRTB, mainly due to the higher calorific value of the liquid fuel. NOx and CO emissions were measured at approximately 100 ppm and 25 ppm, respectively and at 3 % O_2 exhaust flue composition.

The RTWH Aachen RTB is intrinsically different to the WRTB as it incorporates forward firing fuel nozzle and a fuel vaporization tube, prior to the combustion chamber entry. Furthermore, is different in the primary/secondary combustion air passage arrangement, as it utilises FGR in order to reduce emissions and to promote internal recirculation in the fuel vaporization zone.

During the development of the RTB some isothermal flow numerical simulations were carried out for test validation purposes. Only a section of the RTB was modelled, around the primary/secondary air inlet, the vaporization tube (where FGR initiates) and the entry to the combustion chamber. The computational model considers a 30° slice which is then post processed and reproduced to enclose the whole 360° section of the RTB. This modelling technique does not predict accurately any significant tangential flow components, and is not recommended unless the flow is axisymetric, although the flow is not swirling.

The presented data are considerably difficult to interpret due to the poor pictorial quality and scale used. No experimental cold flow measurement methodology is described

here, although a reference has been made to one of the authors. The results show velocity contour predictions and one can only assume that the fuel nozzle flow has not been modelled. In addition, there is no description of model boundary conditions and therefore is difficult to comprehend the modelling and entrainment of the returning flow.

Test flow recirculation ratios have been calculated from mass flow value integration and show agreement with modelling results. There is no presentation of velocity component comparison data between experiment and model. Furthermore, there is no reference to supplementary combustion modelling work.

3.1.5 Gupta, Lilley and Syred, 1984

This publication[15] represents one of the most thorough literature review books on swirling flows, covering a large quantity of work published in relation to combusting flows in various configurations and swirl numbers. Although the review is over 20 years old, many of the studies reviewed remain directly relevant.

Figure 8 shows streamlines and velocity vectors from a combustor CFD computation that simulates coaxial jets entering a confined sudden enlargement, which is the same flow, principally, as in the WRTB.

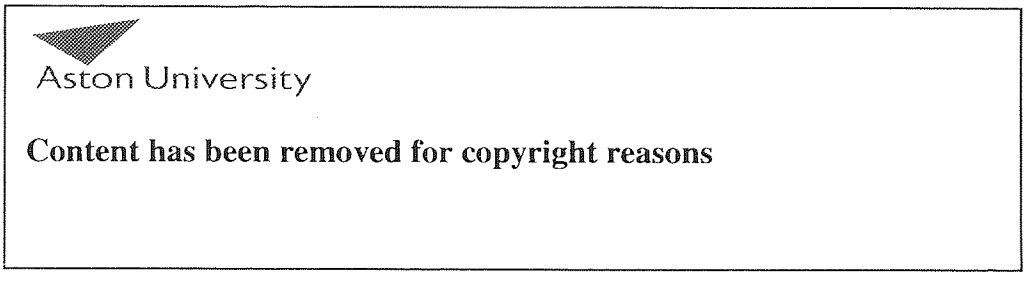

Figure 8: Calculated velocity streamlines for confined coaxial jets

The flow is non-reacting and isothermal. In this case the mass flux of the outer jet is much greater than that of the inner jet. The flow recirculation zones can be seen, similar to those witnessed in experimental flow visualisation studies. It is concluded that comparison with experimental values is instructive, although there is no presentation of experimental data.

Figure 9 represents a summary of the accuracy of predictions in combustor swirling recirculating non-reacting flow.

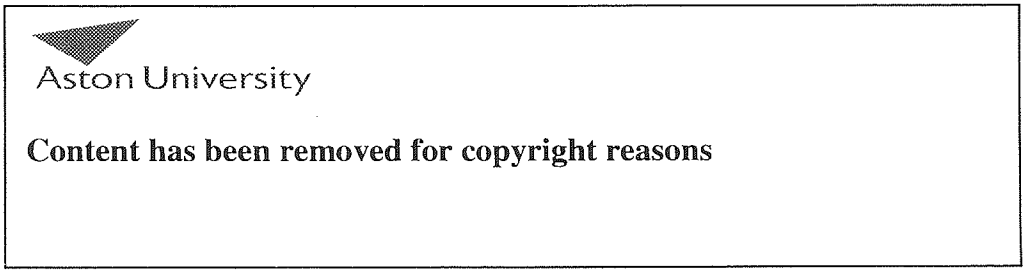

Figure 9: Summary of the accuracy of predictions in Combustor isothermal flows

The author states that due to the difficulties encountered with reacting flow predictions a substantial amount of work has been performed on combustor isothermal flows, particularly in the improvement of turbulence models. Furthermore, it is said that although qualitative agreement is possible between experiment and prediction of swirling recirculating flow in combustor geometries with chemical reaction taking place, quantitative agreement is generally poorer.

The temperature profiles shown on Figure 10 are predicted and measured temperature contours in an industrial combustor. The qualitative predictive capability is evident, although the model is two dimensional and the geometrical feature resolution is poor.

The pressure at the inlet of the combustion chamber reaches approximately 3.8 bar, as oppose to the WTRB which is measured in millibar. The figure presents a diffusion flame,

with a swirl number of 0.3. The swirl number is a non dimensional number that characterises the degree of swirl in a flow. It is related to the flow swirl angle, which in turn, is a function of the forward and rotational velocity components of the flow. In the case of the WRTB combusting flow the swirl number is approximately 0.65, indicating a higher swirl strength than the example shown.

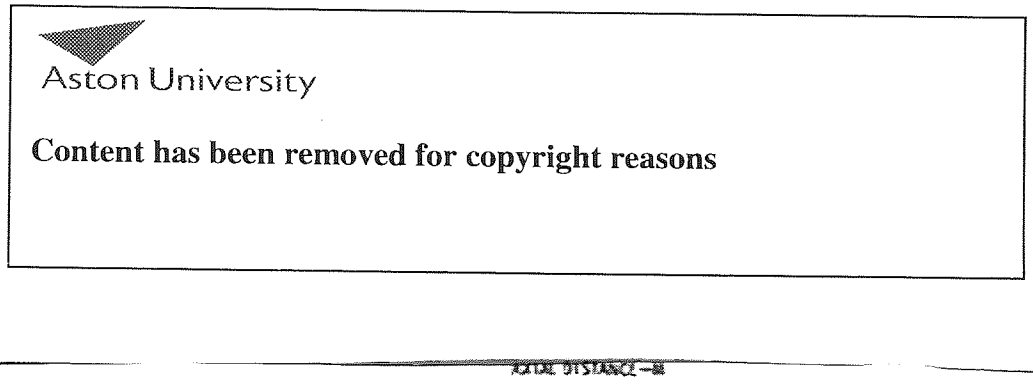

Figure 10: Predicted & experimental temperature contours in a Combustor

3.1.6 Blevins and Gore, 1995

Blevins and Gore[16] constructed an experimental radiant tube test facility, in order to study changes in flame structure, wall temperature and exhaust NOx emission index for a typical radiant tube over a range of thermal inputs (10, 15, 20 and 25 kW) and equivalence ratios. The height of each flame was measured with and without the quartz radiant tube for comparison between the confined and unconfined cases.

The RTB tested has a different fuel nozzle arrangement to the WRTB. It is centrally located with forward firing fuel jets, with the combustion air entering through swirl vanes surrounding the nozzle and giving a swirl number of 0.4. There is no secondary airflow and no pilot burner. The burner tube is made of quartz tube, so that radiant emissions can be measured. The diameter is similar to that of the WRTB.

It was observed that the 10 kW flame is long and orange while the 15, 20 and 25 kW flames are short and blue[17]. In addition, the confined walls of the RTB shortened the 20 and 25 kW flame length in comparison to the unconfined flame measurements. For the 10 and 15 kW cases, the RTB confined flame length increased substantially with the equivalence ratio, while the 20 and 25 kW flame length remained nearly unaffected.

The wall temperatures measured for the 20 kW flame were highest close to the burner, peaking at approximately 20 cm from the burner nozzle. The NOx results for the 20 kW at near stoichiometric conditions (Φ>0.9) indicate approximately 1.5 gr NOx per kg fuel, and for the 25 kW flame approximately 1.6 gr NOx per kg fuel. The authors state that the lowest NOx emissions in this study result from the 20 kW cases.

There are no cold flow field measurements or detailed fuel and combustion air flow rates given for the experiments.

3.1.7 Ramamurthy, Ramadhyani and Viskanta, 1994

A two-dimensional axisymmetric model was developed in this study for combusting, reacting and radiating flows[18] in radiant tubes. The model is based on previous work undertaken by the authors[19] where a study of low Reynolds number k-ε turbulence models was performed. In the latter modelling work the simulations were also two dimensional and they concluded that a modified low Reynolds number k-ε model[20] is recommended for simulating flows and convective heat transfer in RTBs, although most k-ε models tested would predict successfully isothermal flows.

In the published work the combustion process is represented by a one-step chemical reaction between fuel and oxidant and the use of a probability density function for the mixture fraction throughout the flow domain. In addition, the discrete ordinates approach is used for spectral radiative heat transfer calculations.

The authors state that due to the lack of detail flow and heat transfer measurements in RTBs comparisons were made against experimental measurements in a natural gas fired cylindrical gas-turbine combustor.

The comparison between experimental and computational results demonstrates some qualitative agreement for the flow temperature profile; nevertheless, the flow velocity profiles are substantially under-predicted by the model. The authors mention the inadequate characterisation of the inlet conditions in the model and errors in the experimental temperature measurements as the reasons for the weak quantitative agreement.

Furthermore, there are no NOx predictions or flue gas analysis presented and no attempt for heat transfer predictions through the combustion chamber walls has been made.

3.1.8 Marino J, 2002

This paper presents experimental studies of RTB performance carried out by Hauck Manufacturing Co, Lebanon, Pa.[21] The company conducted tests at its in-house research laboratory using thermocouples located at different positions along the radiant tube and inner tube of a 55 kW radiant tube burner. The exhaust temperature was 615°C with 3% O_2, 0% CO and 335 ppm NOx, although during operation in the production line furnace the emissions were 175 ppm higher.

At these operating conditions results indicate inner tube temperatures in excess of 1095°C. The temperature differential across the outer tube was about 30°C (995 to 1025°C). The measurements reveal a higher temperature region approximately 1/3 of the RTB length from the fuel nozzle position.

The fundamental difference of this RTB with the Wellman design is the thermal output and the longer tube length. Furthermore, details with regards to the burner fuel nozzle or the existence of primary/secondary combustion air zones are not published.

3.1.9 Scribano, Solero and Coghe, 2006

This paper[22] presents the results of an RTB experimental investigation, with thermal inputs varying between 12.8 and 18 kW. This investigation was conducted primarily to provide input data to CFD simulations and secondarily to improve the emissions of the RTB with the introduction of exhaust gas recirculation (EGR).

There are no significant details presented with regard to the overall burner dimensions, although the figures indicate an inner tube length of 1 m and inner diameter of 72 mm (smaller than the equivalent WRTB dimensions). Nevertheless, the main air flow has a swirl component prior to its delivery to the combusting chamber, and there is recuperation and the presence of a centrally mounted pilot tube burner, similar in principle to the WRTB.

The intrinsic difference to the WRTB is the forward firing fuel and air nozzle, in a co-axial arrangement between the two flows and the absence of primary/secondary air split. From the figures (as detail dimensions are not included) it can be seen that in this design the gas mixture discharges direct into the combustion chamber (inner tube), which has the same diameter as the air flow tube. The expected flow profiles would differ from the WRTB flow.

The peak temperatures recorded on the inner tube, which varied with the equivalence ratio, were between 1200 and 1400°C and the measured axial velocities indicated magnitudes up to 13 m/s approximately, relatively low for combusting flow. A central toroidal recirculation zone (CRTZ) was observed, just downstream of the fuel nozzle.

The EGR design employed here is similar to other designs[12] and entails a high momentum convergent burner nozzle and a sectioned inner tube, in order to achieve re-entrainment of the exhaust gases. It is reported that a NOx reduction of up to 50% was achieved while sustaining the flame stability and inner tube temperature uniformity.

There are no CFD results presented in this publication, although there is a reference to CFD modelling that has been used for the study of EGR in this type of RTB.

3.1.10 Summary

Table 1 below presents a summary of the reviewed publications to date.

Publication	Meshing and geometry detail	Flow and Flue gas results	Relevance to WRTB
Mei & Meunier	Mainly 2D mesh. Geometry detail representation average	Some velocity & temperature contours. No flue gas results.	Very relevant. Different CFD models used
Lankhorst & Velthuis	Mainly 2D mesh. Geometry detail representation average	Some velocity & temperature contours. No flue gas results.	Very relevant. Different CFD models used
Feese & Lisin	2D mesh. Geometry detail average	Some velocity but no NOx results.	Relevant but lacks detail
Jager, Mevissen, Munko & Kohne	3D mesh. Only fuel nozzle area represented	Isothermal flow, no combustion results.	Relevant but no hot flow study
Gupta, Lilley & Syred	2D mesh. Main focus on combustion chamber	Velocity & temperature results. No NOx results.	Relevant. Mainly Combustor results
Blevins & Gore	Experimental	Temperature & flue gas measurements.	Relevant, no CFD results
Ramamurthy, Ramadhyani & Viskanta	2D mesh	Velocity & temperature contours. No flue gas results.	Relevant but lacks detail and NOx results
Marino J	Experimental	Temperature & flue gas measurements.	Relevant, no CFD results
Scribano, Solero & Coghe	Experimental	Velocity/Temperature and flue gas measurements.	Relevant, no CFD results

Table 1: Summary of previous work publications

3.2 References

1. Stopford P, AEA Technology Engineering Software, Harwell, UK, Recent applications of CFD modelling in the power generation and combustion industries.
2. Orsino, Weber and Bollettini, Combustion Science and Technology, 170, pp. 1-34 (2001), Numerical simulation of combustion of natural gas with high-temperature air.
3. Gobby D, CFX Validation Report, CFX-VAL09/1002, Piloted Methane Jet Flame.
4. Fluent: User's Guide, 2006
5. Mochida A, Kudo K, Taniguchi H, Mizutani T, Hagi S, Nakamura Y, 1997 Joint Power Generation Conference Volume 1, Thermal Analysis in Radiant Tube Burner.
6. A Mochida, K Kudo, Y Mizitutani, M Hattori and Y Nakamura, Division of Mechanical Science, Hokkaido University, Japan, Transient Heat Transfer Analysis In Vacuum Furnaces Heated by Radiant Tube Burners.
7. Wolfgang V, Thomas E and Florian M, CFX Validation Report, CFX-VAL10/1002, Heat transfer predictions using advanced two-equation turbulence models.
8. Mei F. and Meunier H., HTD-Vol. 341, National Heat Transfer Conference, Volume 3, ASME 1997, Numerical and Experimental Investigation of a Single Ended Radiant Tube, Thermal Engineering Laboratory, Faculty Polytechnique de Mons, Belgium.
9. Harder R.F. Ramadhyani S. and Viskanta R., Evaluation and modelling of gas-fired radiant tubes, ASME proc 1988 national heat transfer conference Vol. 1, pP67-68.
10. Lankhorst A. and Velthuis F.M., Institute of Applied Physics, TNO-TPD TU-Delft, The Netherlands, Ceramic Recuperative Radiant Tube Burners: Simulations and Experiments, Transport Phenomena in Combustion Vol 2, (1995), pp1330-1341.
11. Kuo K.K., Principles of Combustion, John Wiley & Sons, New York, 1989.
12. Steringa J, Temperatuur – en emissiemetingen aan een keramische recuperatieve straalbuisbrander, Nederlandse Gasunie, The Netherlands, 1993.
13. Feese J, Lisin F, Hauck Manufacturing Co, Lebannon, USA, 2003, CFD Modelling Improves Burner Performance.
14. Kleine Jager F, Mcvissen L, Munko A, and Kohne H, "CFD modelling of a radiant tube burner for liquid and gaseous fuels", Progress in computational Fluid Dynamics. Vol. 5, No. 7, pp.406 413, 2005.

15. Gupta A K, Lilley D G and Syred N, Swirl Flows, Abacus Press, 1984.
16. L. G. Blevins L.G. and Gore J.P., Combustion Science and Technology, (1995), Vol.109, pp. 255-271A Study of Radiant Tube Flame Structure and NOx Emissions.
17. Halthore R.N. and Gouldin F.C., Laser Scattering Measurements for Gas Densities in a Swirling Flow Combustor. AIAA Journal, (1986). 24(7). 1129-1136.
18. Ramamurthy H., Ramadhyani S. and Viskanta R., A two dimensional axisymmetric model for combusting, reacting and radiating flows in radiant tubes, J. of Institute of Energy, Sept.1994, Volume 67, pp90-100.
19. Ramamurthy H., Ramadhyani S. and Viskanta R, A study of low-Reynolds Number k-ε turbulence models for radiant-tube applications, Journal of the Institute of Energy, December 1993, 66, pp 188-197.
20. Nagano Y and Hishida M, Improved form of the k-ε model for wall turbulent shear flows. J. Fluids Eng, 1987, 109, pp 156-160.
21. Marino J, Hauck Manufacturing Co, Lebanon, Pa, Industrial Heating (June 2002), SiC Radiant Tube Burner Technology handles High Operating Temperatures.
22. Scribano G, Solero G and Coghe A, Pollutant emissions reduction and performance optimization of an industrial radiant tube burner, Experimental Thermal and Fluid Science, Volume 30, pp 605-612, 2006

4. WORK PROGRAMME

4.1 The Need for Research

The two studies to date that have most relevance to the planned WRTB study are Lankhorst and Velthuis in 1995 and Mei and Meunier in 1997. Both studies used CFD methods, but each was limited to a two-dimensional axi-symmetric representation of the combustion zone only. Partly because of this, little attention was given to the fuel nozzle design and other internal design features. Also, the RTB design in each case was significantly different to the RTB. Neither design featured the splitting of the combustion air into primary and secondary zones, and neither used swirl. Both of the combustion models used in the two studies assumed single step chemistry and thus did not calculate CO, and neither calculated NO. Finally, agreement with experimental results was only partially achieved in both cases.

It is clear from the foregoing that improvements can be made in various areas primarily either due to poor overall quantitative agreement between experimental values and model predictions or simply due to the need for further development and modelling work. In the studies reviewed, CFD is used for the representation of RTB operating conditions although substantial work has been performed in gas combustors instead.

The RTB computational models have been constructed predominantly in two-dimensional sections or in relatively simple three-dimensional form. They can be improved in geometrical feature resolution, taking advantage of the present computational capabilities and the advancements made, over the years, on the performance of the mesh generation programs.

Furthermore, the present computational models have also evolved and utilised more advanced algorithms to enhance accuracy and robustness of predictions; a two-step combustion model instead of a single step for example, and to shorten substantially convergence timescales.

In addition, the reviewed RTB laboratory measurements present a good reference for the validation of the WRTB computational model and experimental measurements performed in this research, although comparisons can only be qualitative.

More generally, all the studies presented in the previous chapter either failed to resolve the internal flow in sufficient detail to examine the full effect of the burner design features on the combusting flow, or were focused more on the heat transfer characteristics without proper resolution of the combustion process. Commonly, the models used were two-dimensional. Furthermore, in all previous studies the burner being considered has significant design differences to the WRTB, a common difference being the lack of air swirl.

Overall, the previous work has neither highlighted the specific features of the WRTB as analysed in this study, nor revealed any direct similarities, justifying therefore the need for the presented research work. The following chapters, particularly Chapters 5, 6 and 7 demonstrate this.

4.2 Aims and Objectives

The study aims to calculate the flow field internal to the full RTB geometry from fuel and air inlet ports through to the flue gas outlet, including radiation and NOx production, using three-dimensional computational fluid dynamics. Full advantage will be taken of modern unstructured mesh and multigrid solver capabilities. Validation of the simulations will be provided by measured velocities, temperatures and NOx emissions from both isothermal and combusting experiments.

The main objective is:

- To comprehend the detailed fluid and thermodynamic behaviour of the burner in order to attempt improvements in burner lifetime, reduce emissions and enhance overall performance in a cost-effective manner.

Further objectives are:

- To investigate the problems in the burner combustion zone that are having a detrimental effect on burner lifetime and propose solutions. This will be achieved through detailed study of the temperature distribution in the local area.
- To attempt reduction in NO emissions by investigating a number of more radical design modifications, including flue gas recirculation and modifications in the fuel nozzle area.

The innovation within the study lays in the complete steady-state three-dimensional simulation of a complete RTB with full resolution of flow, radiation and combustion processes together with heat transfer processes in both solid and fluid domains, validated by experimental measurements. Spatial resolution will be substantially higher than in previous studies, permitting the faithful representation of important details such as the fuel nozzle region, the primary/secondary air passages, and the swirl-augmented recuperation zone.

4.3 Work Plan

In order to achieve these aims and objectives, the task is split into two parts, isothermal (cold flow) analysis and combusting (hot flow) analysis. In both parts, experimental tests using actual WRTB geometries will be carried out to provide unambiguous validation for the modelling work.

4.3.1 Isothermal Flow

Isothermal measurements are valuable as they do not require the full installation of the RTB, and allow the study of flow characteristics without the high costs of combustion experimentation. The isothermal flow field provides a good indication of the expected flow behaviour when combustion is initiated. Furthermore, it is intrinsically difficult to obtain detailed flow measurements in a combusting flow because of the high temperature environment. Validation of the isothermal flow presents the advantage of a less computationally demanding simulation, and turbulence coefficients and mesh resolution can be optimised at this stage with the outcomes then transferred to the combusting simulation.

Experimental cold flow velocity measurements will be taken at different planes inside the inner tube, as it necessary to comprehend the flow behaviour internal to the RTB in the region of most interest, the combustion chamber. The returning flow is not of interest at this stage, so the outer radiant tube will be omitted and the inner tube truncated to facilitate instrumentation access.

The isothermal model will not consider chemical reactions and heat transfer through the fluid and solid domains. The two main modelling objectives at this stage are mesh optimisation and turbulence model selection. The computational mesh will be optimised in the complex geometry of the air inlet passage and the fuel nozzles, and mesh sensitivity will also be examined. Then various turbulence models will be tested. Finally various features along the air inlet passage will be analysed in more detail.

4.3.2 Combustion Flow

The hot flow modelling takes certain validated features of the cold flow models and applies them to the combusting situation, with experimental data under combusting conditions providing final validation.

The experimental data will come from measurements taken in the Wellman test furnace. For practical reasons, the data will be limited to wall temperature measurements at various locations, together with flue gas analysis, at a single design condition. Model validation will be pursued by using different combustion and radiation models and fine-tuning other aspects until satisfactory agreement with the experimental data is reached. The isothermal flow computational mesh will be retained, but extended to cover the full gas path. The turbulence model will also be retained.

The validated model will then be used to analyse the WRTB internal flow, heat transfer processes and emissions characteristics in detail. The effects of certain RTB features will be considered, such as the fuel nozzle and the flame tube. Finally, the modelling will proceed to consider cost-effective design modifications to address the long-term in-service failure problems and relatively poor emissions performance of the WRTB, using all the observations and conclusions from the foregoing work

5. ISOTHERMAL FLOW

5.1. Introduction

An isothermal flow field provides a good indication of the expected flow behaviour when combustion is initiated. The isothermal model does not consider chemical reactions and heat transfer through the fluid and solid domains (constant temperature) and therefore is simpler to set up. The two main modelling objectives for the isothermal study are mesh optimisation and turbulence model selection. The WRTB computational mesh has to be optimised in the complex geometry of the air inlet passage (particularly around the recuperator coil) and the fuel nozzles, and a mesh sensitivity study can also be performed.

An important part of the cold (isothermal) flow study is the validation of the computational model by experimental measurements. Isothermal flow velocity measurements are taken at different planes inside the WRTB inner tube, as it is necessary to comprehend the flow behaviour internal to the RTB in the region of most interest, the combustion chamber. Furthermore, static pressure readings are also collected from tappings on the burner wall at certain locations, for further appreciation of the predicted flow velocities.

The cold flow measurements are an important part of any combustion flow study as they do not require the full installation of the RTB, and therefore are an efficient method of studying the velocity profile of a non-combusting flow, without the necessity of test equipment with prohibitive cost and complicated operation, such as a test furnace. Furthermore, there is a limited availability of test equipment that could withstand the extreme temperatures of combusting flow.

Split geometry computational models are also constructed to examine the feasibility of sectioning the overall WRTB geometry, in order to use the output of one model section as the input boundary for the consecutive model section. The aim is to use smaller mesh size models to achieve the same outcome with a complete RTB encompassing model, but with improved modelling time scales and without prohibiting memory limitations.

5.2. Experimental set-up

Experimental measurements of the cold air flow were made at the test facilities of Ingenieurbüro R-K Berger in Germany, an organisation with extensive experience in burner air flow testing, and particularly in the use of split-film anemometry using a triple-split hot-film probe. The author witnessed these tests and participated in the set-up of the burner in the experimental test frame and probe calibration runs, during which the difficulty of the calibration of this sensitive type of equipment became apparent. Velocity data have been obtained using a bi-directional triple-split hot-film probe placed in the recirculating region of the turbulent flow after the discharge face.

Figure 1 presents the set-up of the experimental apparatus. The probe was fully validated and calibrated for the test and previous work has shown that it provides measurements both of velocity and of flow angle to within an acceptable accuracy.[1]

This type of probe typically consists of three separate films deposited on a cylinder. The operating principle is based on the variation of the local heat transfer coefficient on a cylinder with the magnitude and direction of the oncoming flow velocity. Although these probes have a fairly low frequency response (150Hz) through the effects both of spatial averaging and of thermal inertia, they are invaluable in providing bi-directional velocity data. The probe is less accurate for measurements in low-intensity flows, however, it has been shown to provide measurements of three components of velocity to within an acceptable accuracy in flows such as these ($\pm$ 4% for velocities > ~5 m/s)[2].

The RTB was mounted horizontally on a rig which allowed the burner to be rotated around its longitudinal (Z) axis (Figure 2). The outer radiant tube was omitted and the inner tube greatly shortened to allow measurements, with the air exhausting into the laboratory. The key dimensions of the test RTB are shown in Figure 3.

The split-film probe was mounted such that it could traverse a diameter, so that by rotating the burner a full coverage of an axial plane could be obtained. Measurements were made at two such planes, Plane 1 at Z=0.778m (50mm downstream of the discharge face)

and Plane 2 at Z=0.828m (100mm downstream of the discharge face). These planes are clearly shown in Figure 13 in this section. In each case, 18 diameters were traversed at 10° intervals, with measurements taken at 7mm intervals on each traverse. Data were recorded and processed on a dedicated PC which also controlled the traverse. The burner was operated at a single condition corresponding to its rated design point (20 KW thermal input).

Air was supplied to the pilot and main air inlets and also to the fuel inlet (at the correct mass flow rate). Flow rates are given in Table 1 below.

Main air mass flow rate	0.00788 kg/s
Fuel air mass flow rate	0.000675 kg/s
Pilot air mass flow rate	0.000363 kg/s
Density of test air	1.178 kg/m^3

Table 1: Cold flow test - Experimental air flow rates

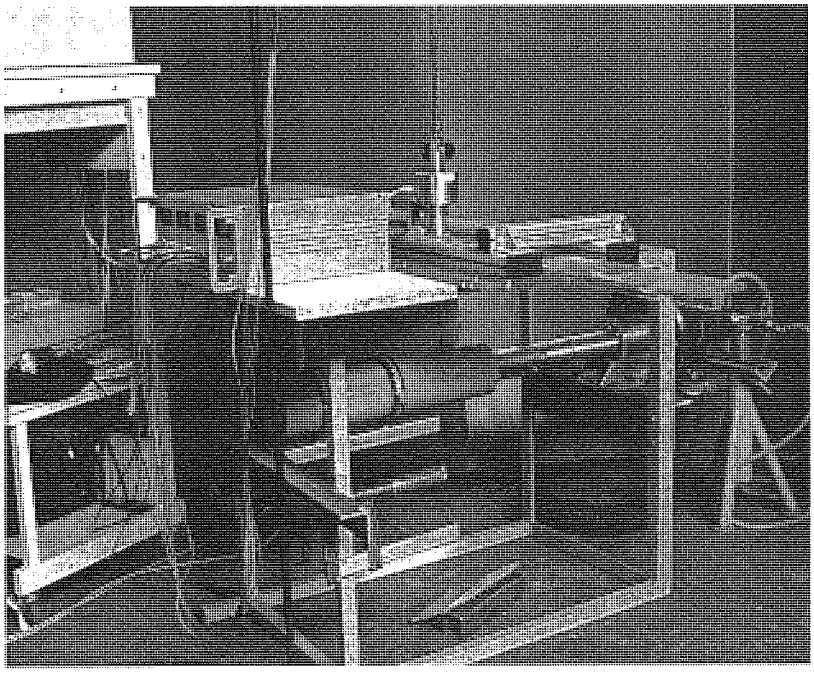

Figure 1: WRTB experimental apparatus and split film probe traverse

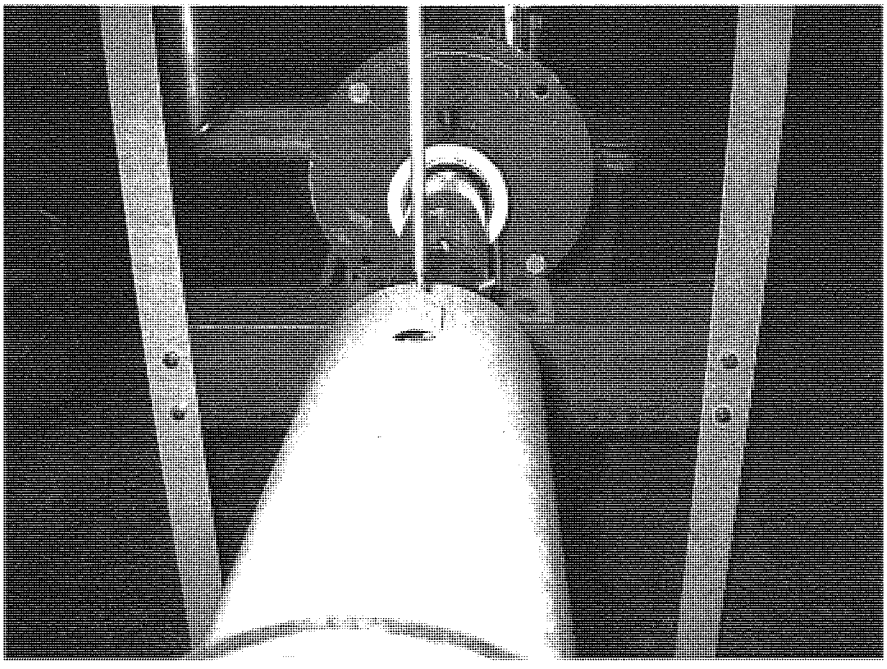

Figure 2: WRTB mounting plate and split film probe

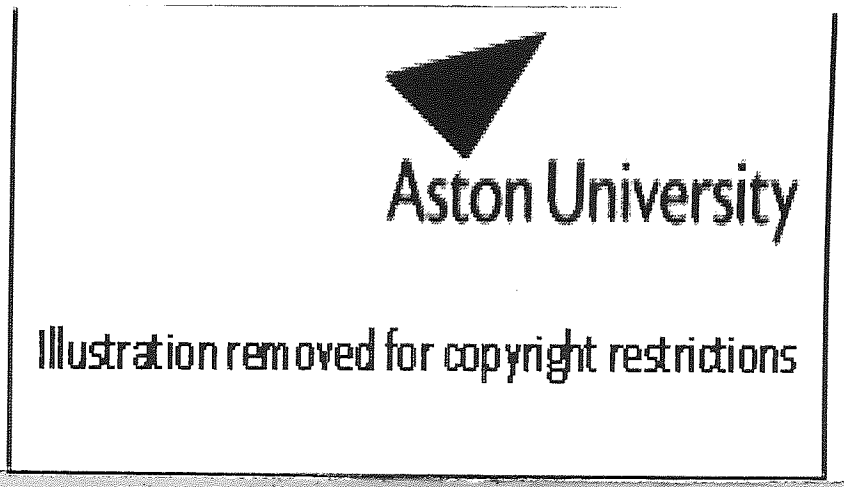

Figure 3: Cold flow WRTB - key design features and dimensions

(Pilot tube omitted-only front face shown)

5.3. Experimental results

The split-film probe was traversing along a constant axis and the RTB reference datum was rotating, hence producing the data in cylindrical coordinates. The data was then converted to Cartesian coordinates for direct comparison with the Cartesian system of the CFX models. The equations used for the conversion are detailed in the Appendix, part B.

A hand held pressure transducer was used to record the wall static pressures in axial locations at 0.458 m, 0.476 m and 0.497 m planes along the air tube wall, shown as Points 1, 2 and 3 in Figure 14. The transducer measured approximately 440 Pa, -43 Pa and -50 Pa respectively. The general reading accuracy of the transducer was ±2.5% at full scale.

The experimental results that can be seen in Figures 4-9, show axial, tangential and radial velocity (v_u, v_θ, and v_r) plotted against radial position for Planes 1 and 2. Each figure contains the maximum, minimum and average value from the 18 traverses, starting at -38.5 mm (probe entry side) and finishing at 45.5 mm. The inner tube walls are at ± 52.5 mm; however the first two measurements on the probe entry side are omitted, due to the local flow disturbance caused by the access hole in the inner tube wall.

Figures 7-9 reveal slight non-axisymmetric flow at the downstream plane, as indicated by the non-zero crossing of the radial and tangential velocities. Figure 9 shows high scatter due to the low magnitude of v_r at this plane.

The measurements indicate an amount of circumferential variation. This is probably due in part to the diminishing accuracy of the probe at the low velocity magnitudes in the region of the measurements (< 2 m/s). Some may also be due to the four-port fuel injection arrangement which may generate a lobe effect. However there is believed to be real circumferential maldistribution present, caused by radial and axial misalignments of the burner annuli on assembly. Maldistribution is defined as the maximum deviation of a property in a half-annulus from the non-maldistributed value, expressed as a percentage. Every attempt was made during assembly to eliminate these, but there was a limit to how successfully this could be accomplished given the specified component tolerances.

A central recirculation is clearly present, of approximately 50 mm in diameter at Plane 1 and 40 mm at Plane 2.

Figures 4 and 7 indicate that maximum (averaged) axial recirculation velocities are -1.25 m/s and -0.35 m/s respectively, compared with peak forward velocities of 1.6 m/s and 0.8 m/s. The corresponding predicted velocities are -1.1 m/s and -0.5 m/s, compared with peak forward velocities of 1.95 and 1.3 m/s respectively. These values are taken from the furthest radial location of the probe traverse, to counteract the effect of the burner wall access hole on the local flow and fall within the maximum and minimum test curves.

At the peak flux location, the swirl angles are ~30° at Plane 1, rising to ~45° at Plane 2 due to flow expansion. At Plane 1, the flow has a reasonably strong radially outward component, whereas as Plane 2 the flow is weakly inward.

In general, the confining walls generate the final shape of the flow velocity profile. Centrifugal forces and sudden expansion of the area, as the flow enters the combustion zone, cause radial outflow towards the walls. In addition, deceleration of the flow as the cross sectional area increases downstream of the discharge face sets up an adverse pressure gradient which augments the reverse flow. In the figures we can also see that reverse flow velocities are high, almost to the same magnitude as the forward flow in the same plane.

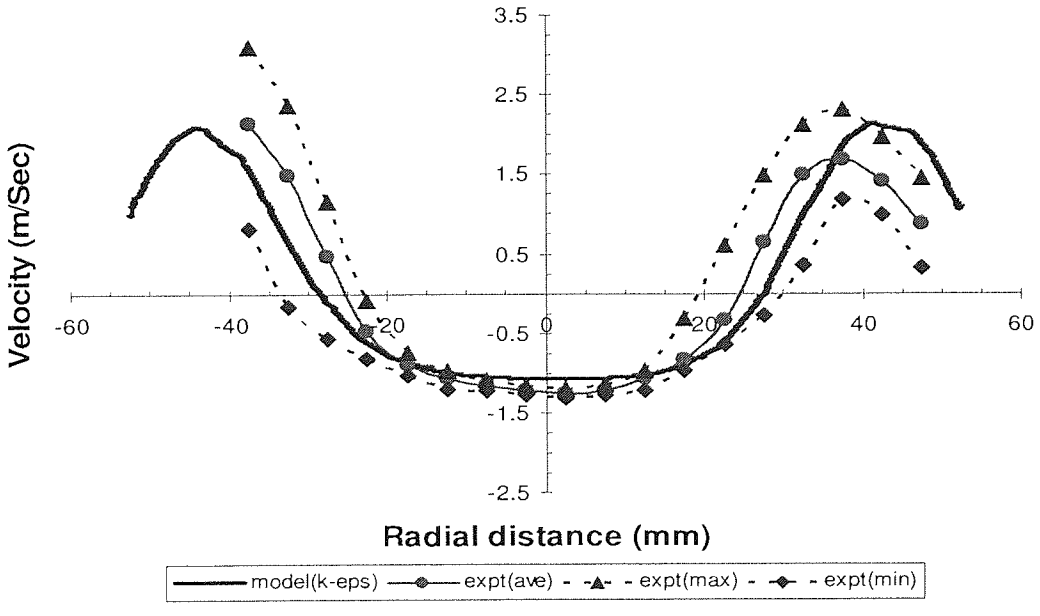

Figure 4: Plane 1 axial velocity v_u

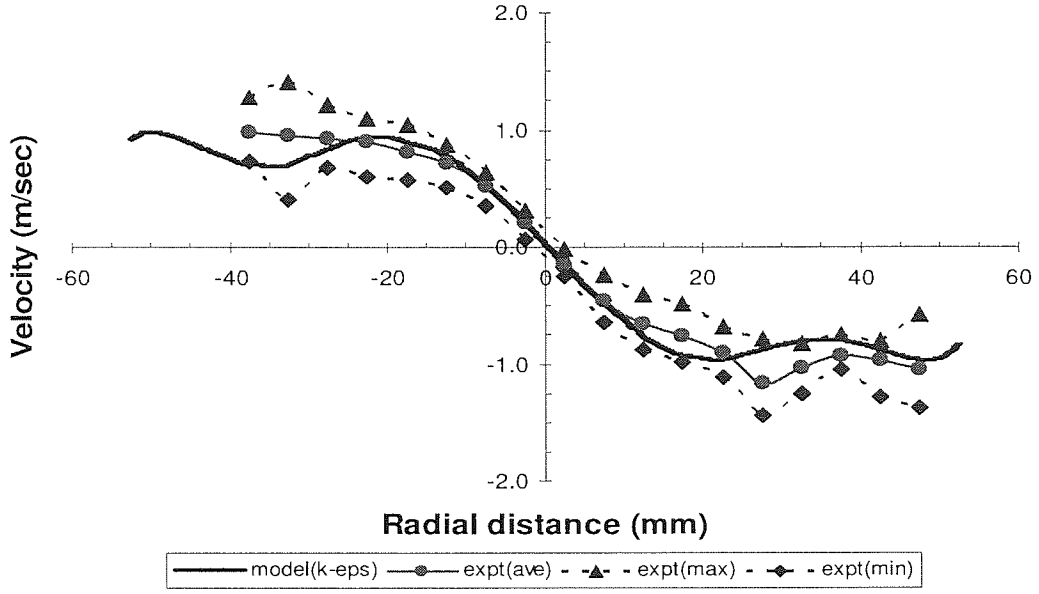

Figure 5: Plane 1 tangential velocity v_θ

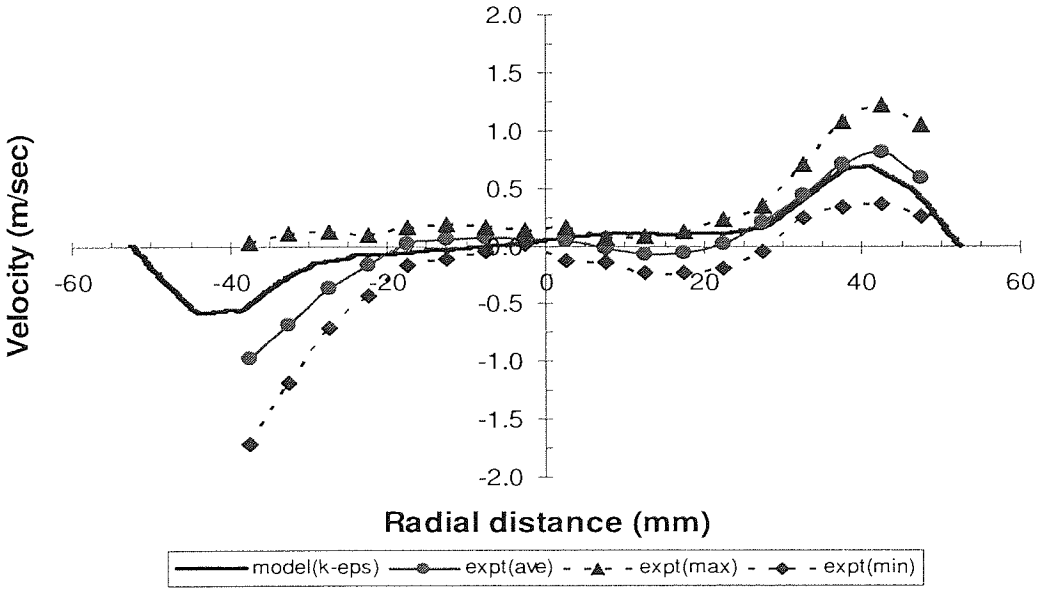

Figure 6: Plane 1 radial velocity v_r

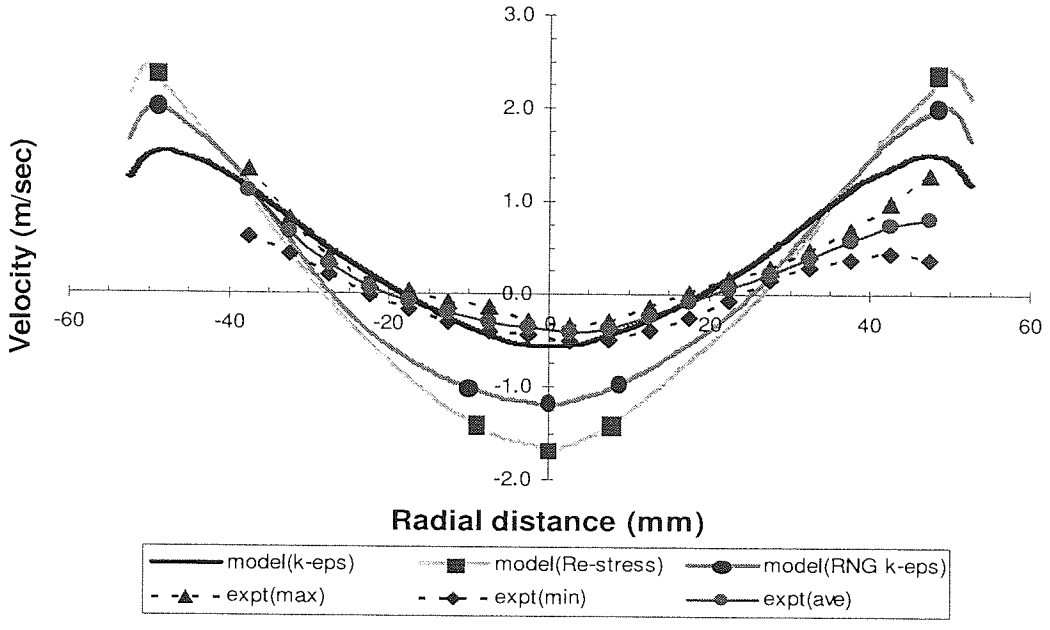

Figure 7: Plane 2 axial velocity v_a

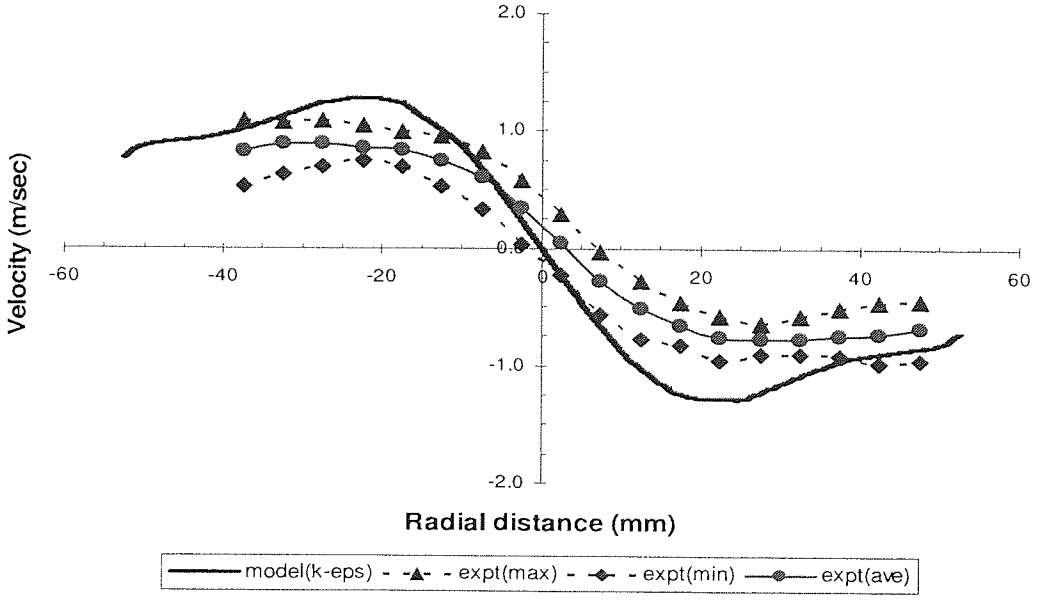

Figure 8: Plane 2 tangential velocity v_θ

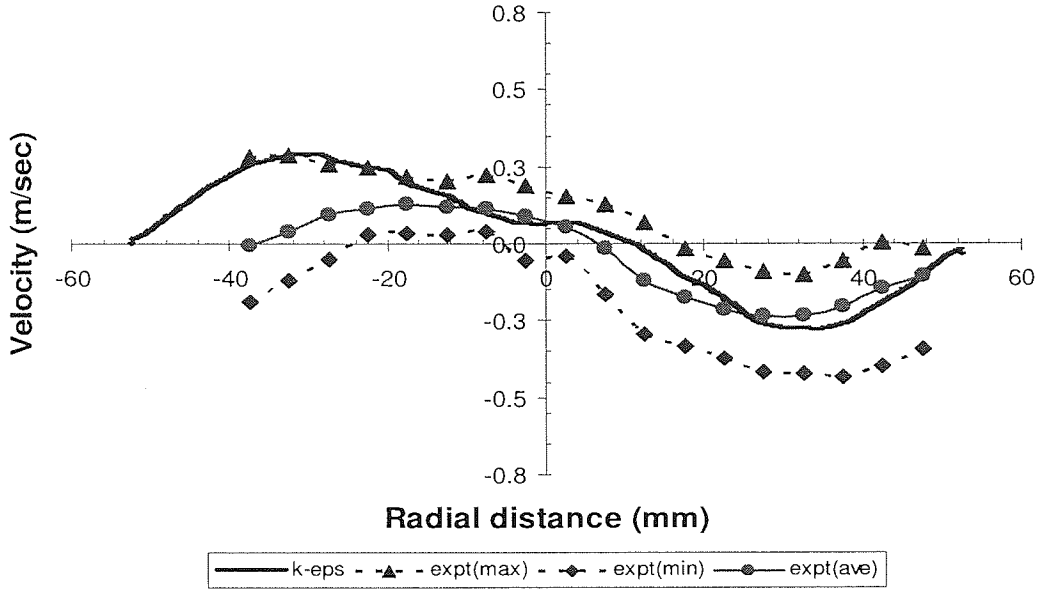

Figure 9: Plane 2 radial velocity v_r

5.4. Isothermal flow computational model

As the flows in the burner passages and the combustion chamber are both turbulent and swirling, the effect of different turbulence models is clearly important to resolve. Three models were examined; the standard k-ε model[3], the renormalisation-group (RNG) k-ε model[4] and the Launder–Reece–Rodi IP Reynolds Stress model[5].

All three models were described in Chapter 2. The k-ε model is a two-equation model solving transport equations for the turbulence kinetic energy k and the dissipation rate ε and is probably the most widely used turbulence model. The RNG k-ε model is another two-equation model, but is based on a modified system of Navier-Stokes equations which results in constants different from those in the standard k-ε model. The model gives a better treatment of near-wall turbulence effects and has been found to be superior in some swirling or separated flows[6]. In the Reynolds Stress model the Reynolds stresses which appear in the momentum equation are solved directly. The model is generally more accurate in strongly

swirling flows with high radial pressure gradients, but not as practical as one and two-equation models due to the extra computational cost and difficulties with convergence.

As part of the modelling strategy employed, a split geometry computational model was initially made, for a feasibility study with regards to sectioning the WRTB model, to avoid computational memory limitations due to excessive size mesh.

5.4.1. Split geometry mesh model

At commencement of the research work an initial model was made, as part of the WRTB modelling development, that extended up to the primary/secondary air split step plane (prior to the flame tube). This model was used to study the recirculating flow, as it passed through the step ring. A supplementary model was then made, starting from a plane (at 0.53 m axial location) were the flow was found to have less turbulence and recirculation present.

In this methodology, velocity and turbulence data is extracted out of the same plane in the first model and used as initial values for the inlet boundary condition for the supplementary model. This model is then used to examine the feasibility of modelling in sections rather than the whole of the WRTB geometry.

The "inlet" boundary set-up tab in CFX Pre has the option of importing velocity and turbulence data[7], and utilise them as initial values for the calculations. Cartesian velocity components and kinetic energy k (m^2/s^2) as well as energy dissipation ε (m^2/s^3) was exported in tabulated data form, from the plane located at 0.53 m of the first model. This data was then imported as initial values on the sectioned model as the air inlet was positioned at the same plane.

Supplementary modelling runs were made and post examination of the results data, by summing the air mass flow rate in the annulus downstream of the inlet plane, it was found that a discrepancy of approximately 2.28% in mass flow is present. Since the pilot and fuel nozzle have the same mass flow rate set as the complete model, this discrepancy was caused

by the inadequate representation of the WRTB main air flow, in the sectioned model. This difference would have an intrinsic effect on the combusting flow and it was decided that the modelling in sections is inadequate. The complete physical representation of the WRTB is therefore necessary and subsequent models adhered to this strategy.

5.4.2. Experimental test burner model

The full three-dimensional geometry of the test burner was reproduced in the model described here, with all significant physical features resolved. Computations were performed on meshes ranging from 220000 to 650000 nodes to test mesh dependency, but this was shown to be relatively minor. The computed axial velocity in the measurement planes changed on average by just 4% across this range. Figure 10 shows a comparison graph between three different mesh sizes tested (220000 to 650000 nodes) for the k-ε model. The graph presents the axial velocity distribution along the model's X-axis.

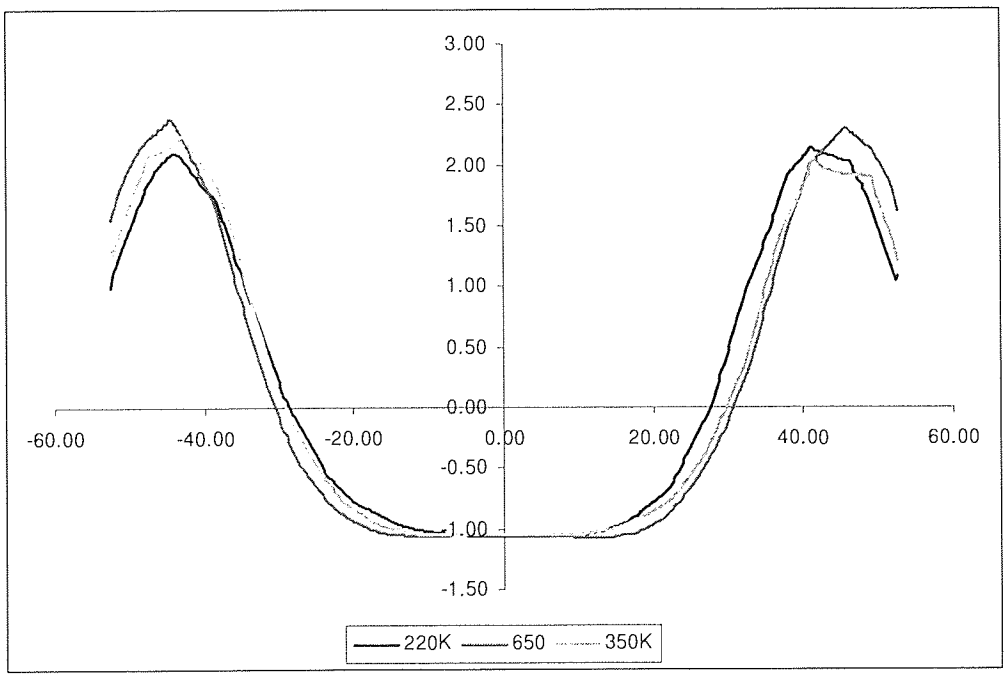

Figure 10: Plane 1 axial velocity v_u mesh size comparison graph

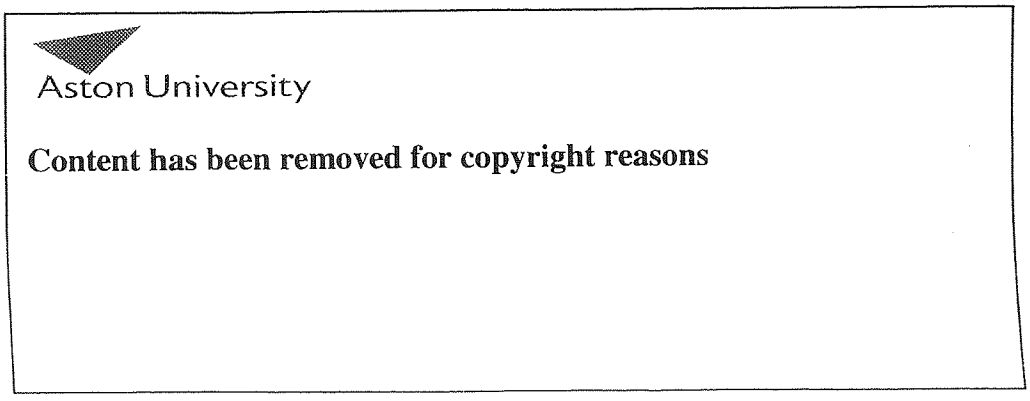

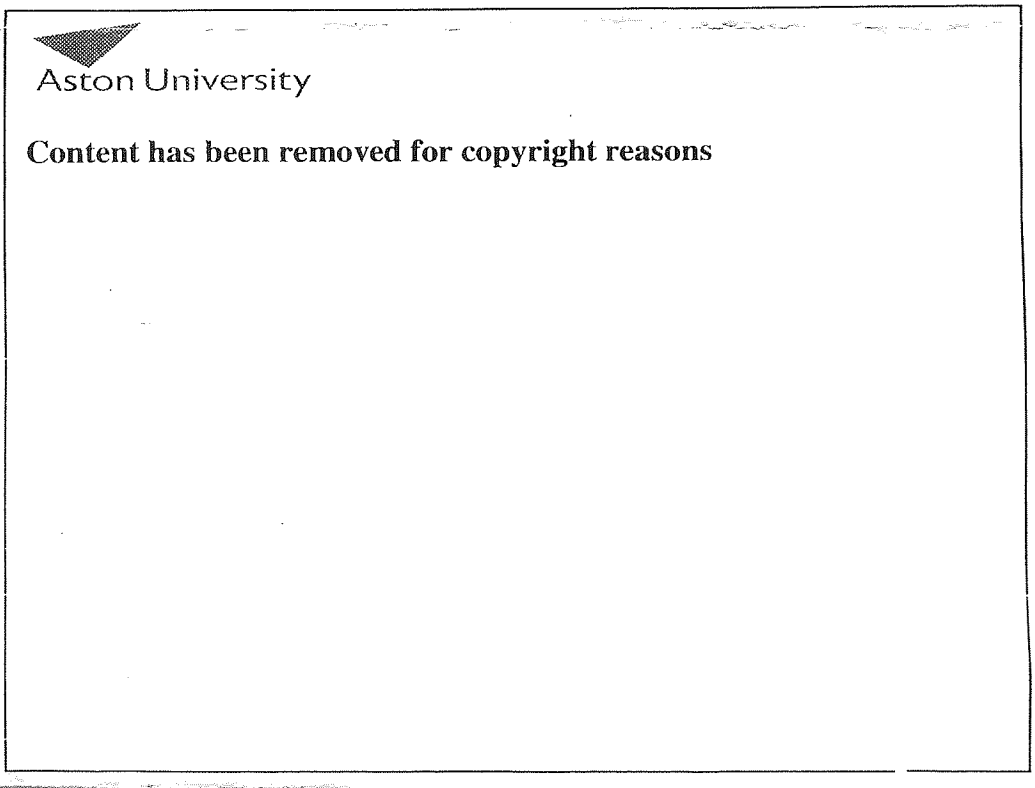

Figure 11: Mesh plane cut through annulus/swirler coil and step ring

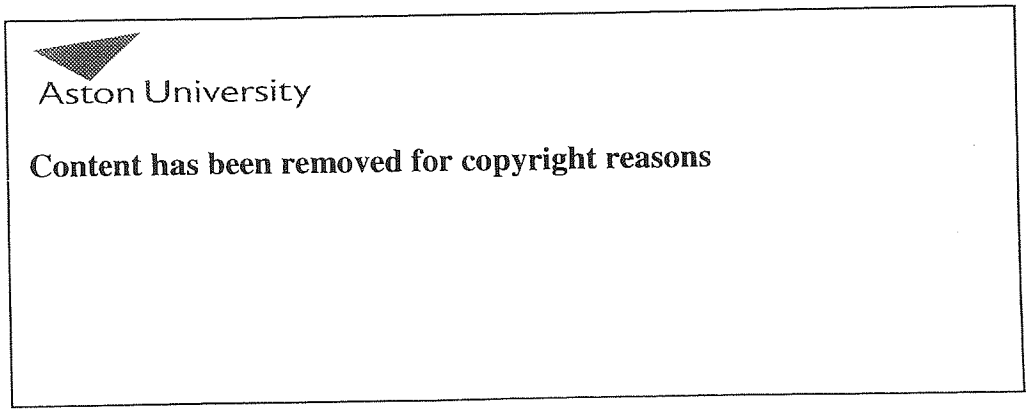

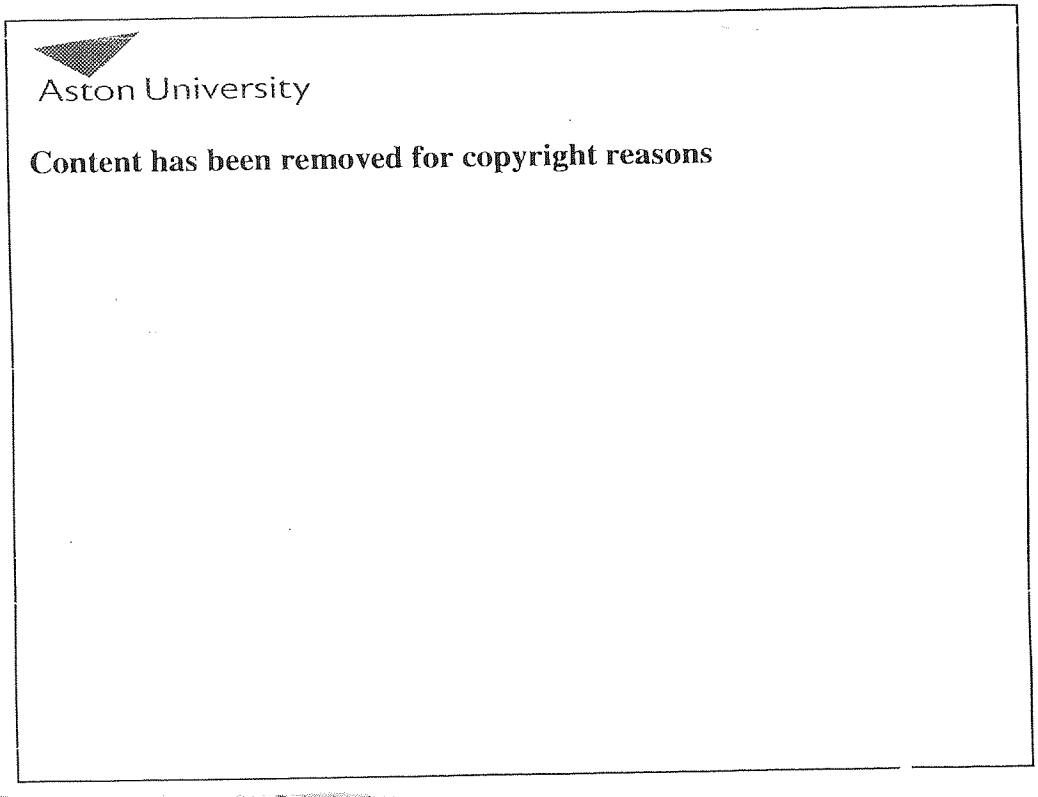

Figure 12: Mesh plane cut at fuel nozzle/combustion chamber

Some differences are indicated close to the wall boundaries, mainly due to the no-slip condition (zero velocity) boundary imposed on the wall and its interpretation by each mesh local wall function, which depends on the local mesh density. Nevertheless, the overall agreement is apparent.

The results presented are taken from a hybrid tetrahedral/prism element mesh of approximately 220000 nodes. Figures 11 and 12 present a section cut through the mesh, indicating the hybrid mesh structure and the overall mesh density change at details such as the coil and the fuel nozzle. The main advantage of the smaller mesh size validation, apart from the reduced time scales, is also the agreement with the computational memory limitation when it comes to the larger mesh requirements for the combusting flow.

Scalable wall functions were used (CFX default) for the models. The 220000 nodes hybrid element mesh produces y+ values <20 in the inner tube region and <100 in the air flow annulus (reasonable for turbulent flows), values that were in direct comparison to the other much higher mesh densities models. By comparison, the 650000 nodes mesh produced <70 in the air flow annulus and <15 for the inner tube region.

5.5. Modelling results and comparison with experiment

The computed results for the standard k-ε turbulence model are shown on Figures 4-9 as a bold line, corresponding to the X=0 traverse. Very little circumferential variation or non-axisymmetry was apparent in the simulations, hence other traverses are not shown. Figure 7 (v_u, Plane 2) also shows the equivalent results for the two other turbulence models.

It is clear from Figure 7 that the standard k-ε model gives the closest agreement, and this is supported by the results for the other components at Plane 2 and also from the Plane 1 results.

Both the Reynolds Stress and RNG k-ε models over-predict the recirculation strength at Plane 2, with the Reynolds Stress calculation exhibiting numerical problems related to the proximity of the outlet.

In an RTB, the solid wall boundaries cause large rates of turbulence generation, and the small length scale in these locations provides a ready sink for turbulence energy. One feature that makes an eddy viscosity model better in wall flows than in free flows is the fact that dissipation rates largely balance generation rates, which means that transport effects are relatively unimportant[8].

In these circumstances the turbulence energy equation reduces to a statement of the eddy-viscosity stress-strain relationship. Therefore, the ratio of production to dissipation of turbulence energy is a constant over most of the flow and this value is approximately unity. The k-epsilon model predicts better low swirling number confined flows but, still (even at confined flows) the Reynolds stress model is better at high swirl. The dissipation to generation rate is close to unity for low swirl case; however the same applies for the RNG k-epsilon model and the Reynolds stress model (at low swirl always).

Nevertheless, if the strain field is not "simple" - as in substantially swirling flows - there is no reason for the eddy viscosity stress strain relation to describe the resultant flow. Then a preferred choice is either a Reynolds stress model or a non-linear eddy viscosity model, in order to predict the flow behaviour more accurately.

The swirling flow characteristics internal to the WRTB combustion chamber can be assumed to be a close representation of a Rankine vortex. In this vortex there is a concentrated vorticity in its core region, a decay of the circumferential velocity as the distance from the core is increased and a constant axial velocity along the axis of the vortex. For most of the RTB flows the axial and tangential velocities are dominant and the third component is much smaller.

The lack of circumferential variation supports the theory that the maldistribution seen in the experiment is due to component misalignment, as in the computational geometry the annuli are axisymmetric and perfectly aligned. However the radial location of the peaks of v_u at Plane 1 are reasonably consistent for all experimental traverses, and show a slightly narrower jet than that in the computation. By Plane 2 a wall jet has formed in both

experiment and computation. Also, the experimental results for v_u at both planes appear to indicate a lower total mass flow than the computed results. The experimental mass flow is calculated to be approximately 30% less than the total computational mass flow of 0.0089136 kg/s (probe and pressure transducer accuracy level also implemented).

Given that the computational mass flows are correct and conserved axially, there must either be an error in the achieved experimental mass flows, or in the probe calibration. IRKB do not believe the probe calibration to be in error, and thus the experimental mass flow rate is suspect. A direct scaling down of the mass flow specified in the computations by a factor of about 1.5 would not only correct the mass flow error, but also improve agreement further in all of Figures 4-9

Figure 13 shows contours of v_u and velocity vectors in the region of the measurement planes for the standard k-ε model. The stagnation point on the centre line defines the axial extent of the central recirculation zone and is located approximately at two combustion chamber diameters downstream of the discharge face. A smaller external recirculation is also apparent. This aids interpretation of the experimental profiles, particularly the radially inward flow at Plane 2.

Figure 14 presents a relatively good agreement between the measured and predicted wall static pressure magnitude as the air flow passes through the step ring barrier, with an accuracy level of approximately 10-15% achieved in all three locations. This validation highlights further that the test air mass flow rate has an order of discrepancy, as the corresponding axial flow velocity in the annulus appears to be less than the calculated through the orifices used to control the apparatus flow supply.

Overall, the level of agreement between the experimental results and the computations using the k-ε turbulence model is believed sufficient to validate further analysis of the upstream flow and also to proceed to model the combusting flow in which swirl effects are further weakened due to the substantial increase in v_u as the density decreases.

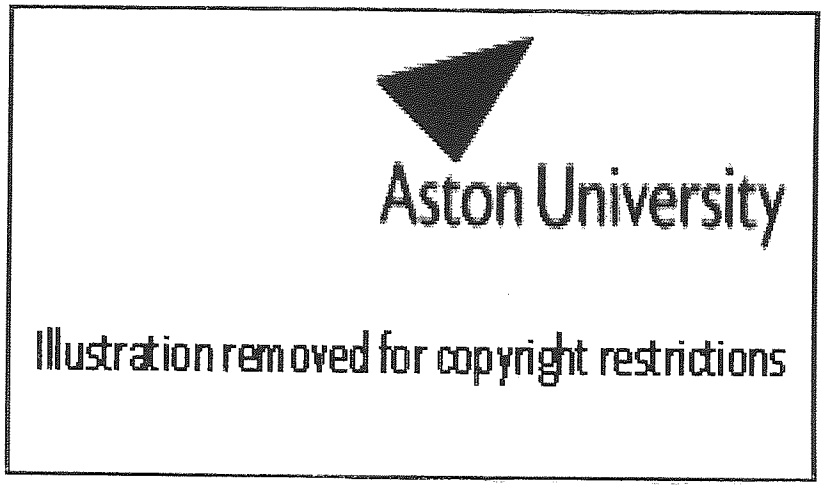

Figure 13: Contours of v_u and velocity vectors at combustion chamber inlet

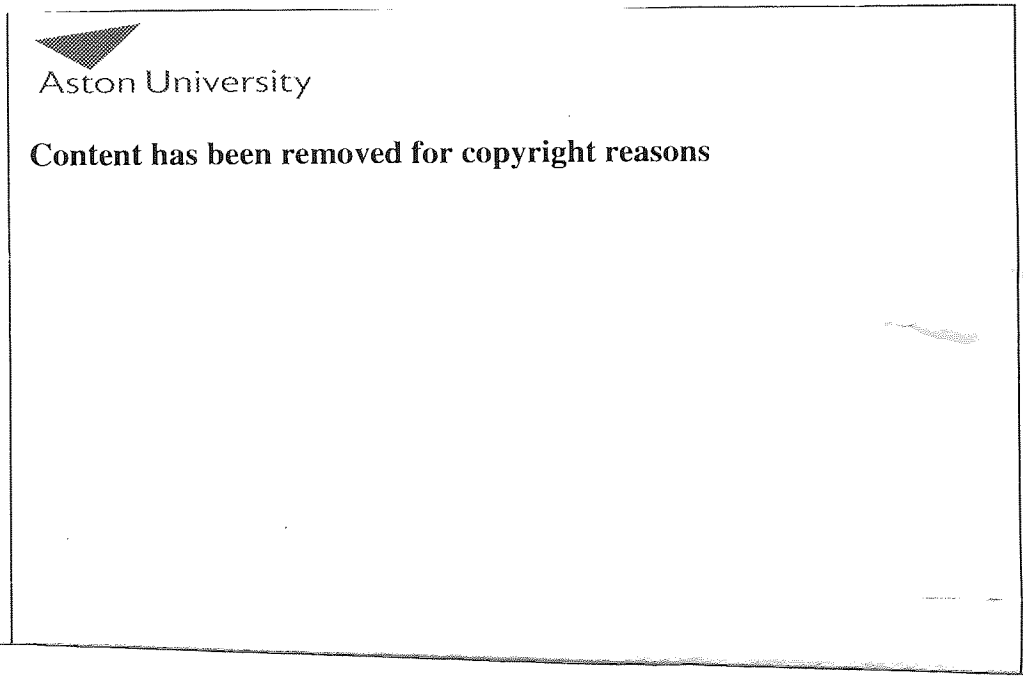

Figure 14: Contours of static pressure at the step ring

5.6. Discussion

A number of design features along the air inlet passage of the RTB have been included to modify the air flow so as either to enhance heat transfer, to improve circumferential uniformity, to change the degree of swirl, or to control combustion stoichiometry. The passage is narrow and not conducive to experimental velocity measurements; however a validated computational model allows insight to be gained.

The effectiveness of three such features are analysed here: the swirler, the step ring and the flame tube. In the real situation, the flow will not be isothermal but will increase in temperature along the annulus by about 500°C (mostly through the recuperator) and will thus accelerate considerably; however this should only have a second order effect on the flow patterns and behaviour reported below.

Figure 15 shows the variation of the mass flow averaged swirl angle, $\tan^{-1}(v_\theta/v_u)$, along the air inlet passage, together with mass flow maldistribution for simulations with and without a step ring. As explained earlier in this chapter, the latter is defined as the maximum deviation of mass flow in a half-annulus from the non-maldistributed value (using axial velocity contours at every plane), expressed as a percentage. The axial location of key features is shown.

Both of these parameters are critical to the subsequent combustion. Swirl angle at the combustion zone inlet must be relatively low in this type of burner to produce a long flame which does not attach immediately to the inner tube wall causing excessive local temperatures.

Circumferential maldistribution of air flow will lead to non-uniform stoichiometry and temperatures and must be minimised. The major features along the air passage influence these parameters either deliberately or otherwise, and these are now analysed.

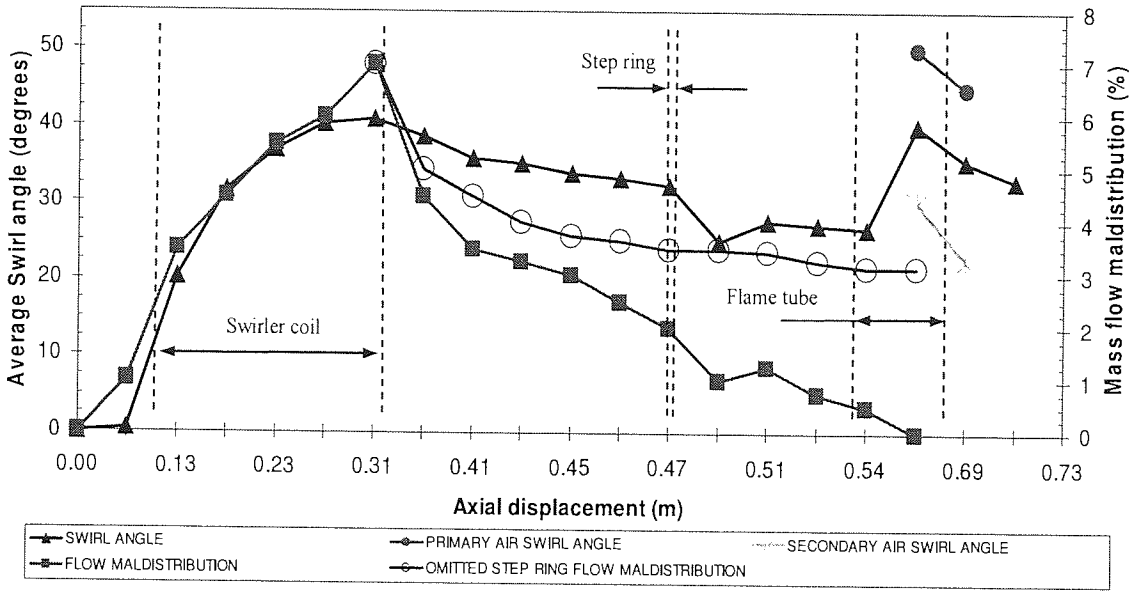

Figure 15: Mass flow averaged swirl angle and mass flow maldistribution versus axial location

The swirler is located in the recuperator section which begins 78 mm downstream of the air entry and extends for a further 235 mm. It is a single helical coil formed from bar of circular cross-section spot-welded to the inner wall. The coil has an axial pitch of 75 mm, giving a little over three full rotations at a mean helix angle of 63° (to the burner axis).

Due to considerations of assembly and thermal expansion, a 1mm nominal clearance exists between the coil and the outer (recuperator) wall. The purpose of the swirler is to increase sharply the total velocity of the air as it passes through the recuperator section, thus increasing the local film heat transfer coefficient.

The operating pressures of the airflows in this type of burner are, in general, low. The pressure at the main air flow inlet is approximately 31 mbar for the 20 KW heat output, thus the air flow is not pressure driven and the expected pressure drop caused by the coil

blockage effect is relatively small. The model indicates an average pressure loss value of 3.2 mbar between the swirler coil entry and exit plane.

Figure 16 shows flow streamlines through the swirler and Figure 17 presents flow streamlines in the swirler coil but with the coil gap omitted. The streamlines were originated at various locations circumferentially and radially at the air inlet.

All the streamlines pass at least twice through the clearance gap (Figure 16), thus retaining a strong axial component. The resulting mean swirl angle at the swirler exit is only 41° (Figure 15), despite the coil helix angle of 63° which the air would have been forced to follow without the gap, and despite the effective axial blockage provided by the coil of 78%.

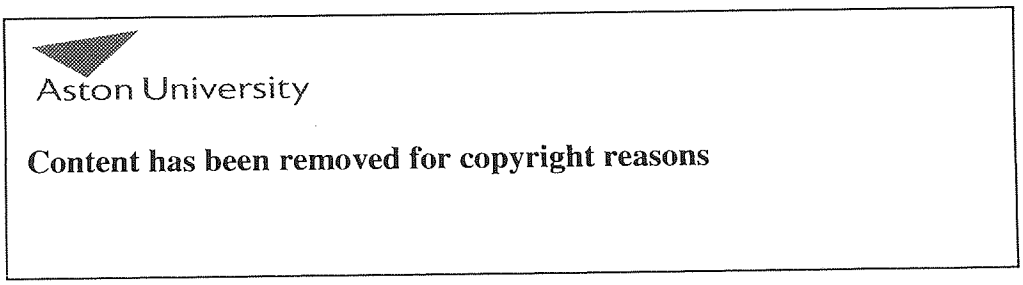

Figure 16: Flow streamlines through the swirler

A volume-averaged total velocity was calculated for the whole of the swirler passage and found to be 12.2 m/s. This compares with a value of 20.3 m/s if the flow were to follow the helix angle of 63°.

As film heat transfer coefficient varies as (mean velocity)$^{0.8}$ this implies that the coefficient will be about two-thirds of the value without the gap. As the film coefficient on the hot side of the recuperator wall can be shown to be comparable in magnitude, the presence of the gap is resulting in a reduction in overall heat transfer coefficient of about 20%.

Furthermore, reducing the coil pitch and increasing the coil length (to compensate) would also result in an increase of the swirl angle and consequently, the heat transfer coefficient.

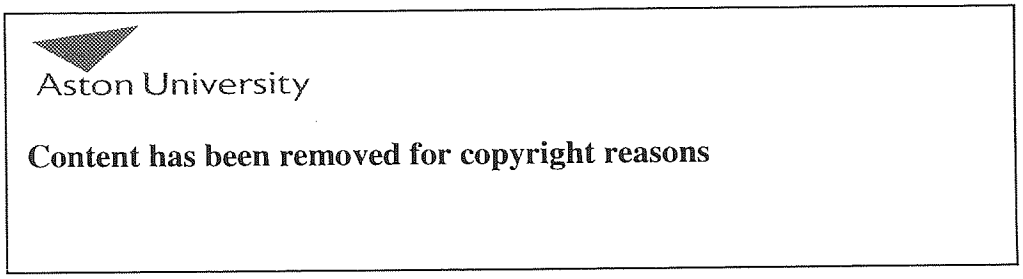

Figure 17: Flow streamlines through the swirler without the coil gap

The distribution of v_u at the swirler exit plane is shown in Figure 18. The flow maldistribution is apparent with the highest velocity at the coil pressure surface and from Figure 15 we can see that the flow maldistribution at this point is 7%.

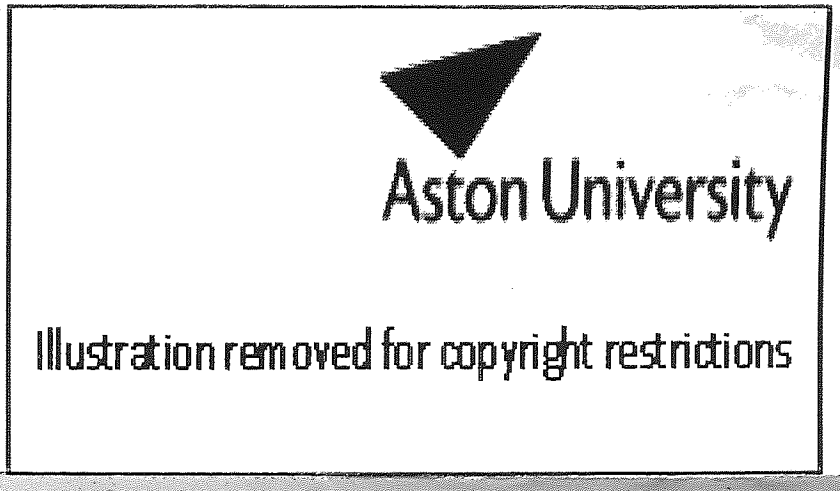

Figure 18: Contours of v_u at the swirler exit plane

The step ring presents a restriction to the flow in the form of a step on the inner wall of the annulus. The step extends 69% of the annulus height, and occupies 67% of the flow area. Its design intention is to remove some of the swirl and to correct some of the circumferential maldistribution created by the swirler coil.

Figure 19 shows contours of v_u and velocity vectors as the flow passes through the step ring, and the acceleration and recirculation behind the step are clear.

Figure 15 shows that between the swirler coil exit and the step ring, swirl angle falls in a linear fashion which is attributable to the removal of angular momentum by wall friction. This steady fall is resumed downstream of the step ring after the flow has recovered, at much the same rate.

The step ring has however caused a shift downwards in the profile of 3-4°, at a point where the swirl angle is around 30°. Thus the ring has not been particularly effective at removing swirl. The swirl that has been lost is attributable to the increase in turbulent kinetic energy caused by the ring, which must be at the expense of angular momentum.

At this point a supplementary model was created with the step ring omitted. When a simulation is carried out without the step ring, a similar profile is obtained (not shown) but without the downward shift.

Flow maldistribution with the step ring present also falls steadily along the annulus downstream of the swirler (Figure 15), and is almost completely eliminated at the flame tube inlet. A deviation of the profile is apparent just downstream of the step ring, but this is recovered.

However, results from the simulation without the step ring show a much less pronounced fall in maldistribution, and this is along the whole annulus, not only in the vicinity of the ring itself. Significant maldistribution remains at the flame tube inlet. Thus the step ring is exerting a corrective influence on maldistribution both upstream and downstream of its

location, the former being due most likely to pressure effects and the latter to turbulent mixing.

The step ring therefore functions poorly as a swirl remover, but rather better as a flow evener. Operational experience during development of the RTB confirms that removal of the step ring does have a major deleterious effect on combustion performance, consistent with the introduction of air maldistribution.

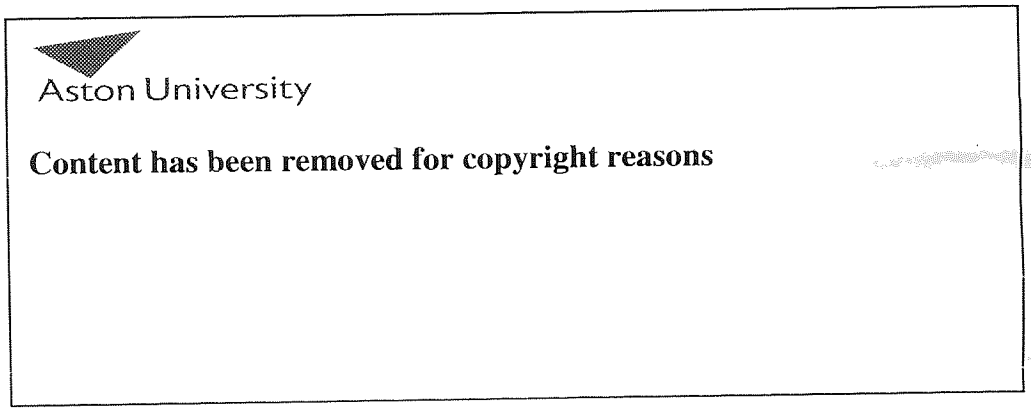

Figure 19: Contours of v_u and velocity vectors through the step ring

The flame tube splits the flow into primary and secondary components prior to the combustion zone (Figure 3). Upstream of the fuel ports, the flow areas of the primary and secondary passages are in the ratio 1.49:1, but the mass flows are in the ratio 0.89:1. At the fuel ports (where the primary passage area is at its minimum) the area ratio has fallen to

1.20:1, but the mass flow ratio (including the fuel air now) has only risen to 1.05:1. Hence the area ratio at the fuel ports does not give a good prediction of the mass flow (or more correctly volume flow) ratio at this point, and thus of the ratio of primary to secondary air.

Momentum has been lost in the primary due to the direction changes the flow has to make at flame tube entry, and the consequent flow separations and turbulence (Figure 20).

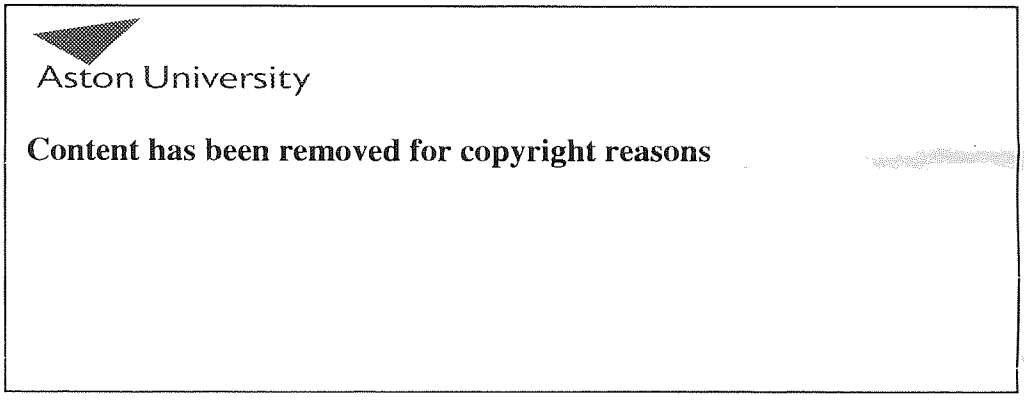

Figure 20: Contours of v_u and velocity vectors at the flame tube inlet

Considering the secondary (outer) passage, Figure 15 shows an initial small increase in swirl angle caused by the expansion just upstream of the flame tube (Figure 3), then a reduction along the flame tube to an exit value of about 22°.

In the primary passage, swirl angle first rises sharply to 50° due to the large expansion and loss of axial momentum. Introduction of both the fuel air and the pilot air then add

complexity to the flow, but by the exit of the flame tube the swirl angle has reduced to 45°. Once the flows recombine downstream of the discharge face, the mean swirl angle is 33°; however in the real situation combustion will have commenced and the associated axial acceleration will significantly reduce this. The swirl number S in our case is approximately around 0.5 -0.6.

Simulations will now be carried out of the fully combusting flow using a similar mesh and the k-ε turbulence model. The validated computational model itself is consecutively used in the combustion flow study. Certain geometry components have to be added, in order to describe the whole WRTB and further details are shown in Chapter 6.

The isothermal study has been the subject of a journal publication. The publication details are referenced in the Appendix part A. The CFX solver input definition file for the isothermal flow modelling is listed in Appendix C, and the experimental data from this test are listed in Appendix D. Finally, the swirl angle variable equations created in CFX Pre are presented in Appendix B.

5.7. References

1. A F Heenan *et al* Measured Science Technology, 1998, Volume 9, pp638-649.
2. Doiron M. D., Zingg D. W., Turbulent flow measurements with a triple-split hot-film probe, AIAA Journal, vol. 32, no. 9, pp1929-1931, 1994.
3. Launder B.E. and Spalding D.B., Mathematical Models of Turbulence. Academic Press, London England, 1972.
4. Choudhury D, Introduction to the Renormalization Group Method and Turbulence Modelling, Fluent Inc. Technical Memorandum TM-107, 1993.
5. Launder BE, Reece GJ, Rodi W. Progress in the developments of a Reynolds-stress turbulence closure. J. Fluid Mechanics; 68; 537-566; 1975.
6. N. G. Orfanoudakis *et al,* "Design, evaluation measurements and modelling of a small swirl stabilised laboratory burner", IFRF Combustion Journal, Article Number 200510, December 2005, ISSN 1562-479X.
7. CFX 10 User Manual, ANSYS UK Software Solutions, Abingdon, Oxford, 2006.
8. Launder BE, Spalding DB. Lectures in mathematical models of turbulence. London: Academic; 1972.

6. COMBUSTING FLOW - STANDARD BURNER

6.1 Introduction

In this section of the study, the WRTB combusting and heat transfer flow processes are analysed, and any areas for improvement, are highlighted.

In the previous chapter satisfactory agreement was obtained between experimental and computed velocity profiles in the combustion chamber region when using the k-ε turbulence model and reasonable mesh independence was obtained with 200,000 nodes. The cold flow validated mesh and turbulence model form the basis for combusting simulations described here.

The computational mesh is extended to cover component geometry that was not required for the isothermal flow study, and the combustion and heat transfer modelling options are selected. The isothermal flow predictions are utilised to comprehend the expected combusting flow of the RTB after the introduction of the chemical reaction libraries.

An important element of this section is the combusting flow model predictions validation by the RTB hot flow test measurements, taken in the Wellman test furnace. RTB wall temperatures and flue gas composition measurements are collected using equipment such as thermocouples and gas analyser, then analysed and, finally, validated against the combusting flow model. This methodology allows the examination of any discrepancies between experiment and modelling results, correction of any errors, and the "fine tuning" of the model, in order to enhance the accuracy of the predictions.

For unavoidable practical reasons, a longer variant of the RTB was used in the experimental hot flow test. Due to the length difference, the creation of two models was necessary, as the shorter, standard model is the main focus of this research. As the flow rates and heat output are the same for the two RTB models, the boundary conditions and

model settings for the validated long burner model can be reasonably expected to produce accurate results in the short burner model.

6.2 Experimental set-up

A section of the hot flow test WRTB with dimensions is shown in Figure 1. This figure also presents the thermocouple locations, used to record temperature data during the test. As mentioned previously, it is a longer version, by approximately 400 mm of the standard WRTB. This single-end recuperative type RTB has a nominal thermal input of 25 kW, with the combustion products circulating between the outer and the inner burner tubes and with a centrally-located pilot burner of nominal thermal input 1 kW.

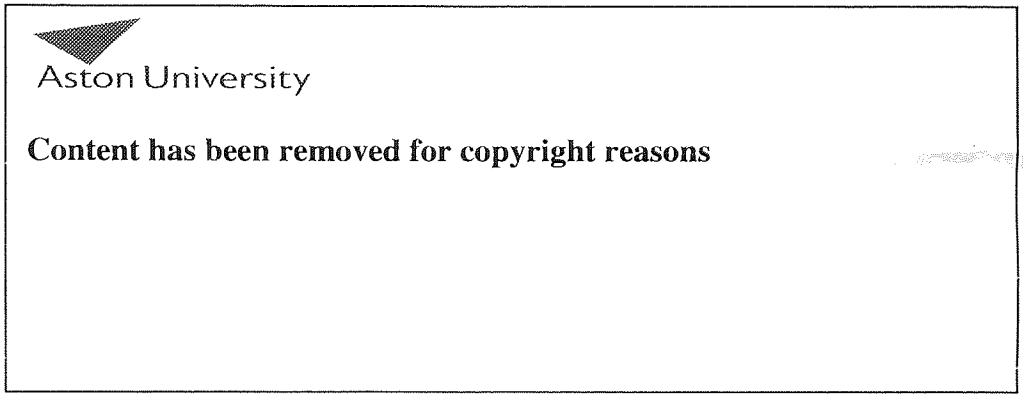

Figure 1: Hot flow WRTB - key design features, dimensions and thermocouple locations

Experimental measurements on the RTB under full combustion conditions were made by Wellman Furnaces in a single burner test furnace. The correct furnace temperature is achieved through supplementary firing from an open end type gas fired burner. The burner is mounted horizontally in the furnace through a mounting plate and combustion air and natural gas is fed to the RTB through the test furnace installation (see Figure 2). Air and fuel flow rates are controlled with the use of butterfly valves and variable area flow meters (Rotameters). The overall accuracy of the air/fuel flow feeding system is claimed to be ±2.5 % of full scale, due to the turbulence generated as the flow passes the butterfly valves.

In total 16 thermocouples were attached to the RTB air (see Figure 3), inner and outer radiant tubes with two extra thermocouples to measure the test ambient temperature and the RTB flue gas temperature at the exhaust outlet. The thermocouples were provided by TC Ltd[1] and were mineral insulated, type K, stainless steel sheath, qualified up to 1100°C and sensitivity of 41 μV/°C. A thin stainless shim was welded at the tip of the thermocouple that allowed the direct spot welding and contact on the metal surfaces of the RTB, minimizing the convection induced heat from the flue gas and ensuring the RTB wall temperatures were measured accurately.

The typical thermal accuracy of the combination was taken to be ± 2°C at the maximum operating temperature, taking account of the small loss through the shim/tube surface contact and for the overall thermocouple cable resistance increase due to extra length that was required for the test. Inconel metal clamp bands were also used to secure the thermocouple lengths on the metal tubes as they run along the RTB walls and through the furnace test ports (as shown in Figure 3).

To record the temperatures measured by the thermocouples two thermocouple data loggers were used, manufactured by Pico Technology Ltd[2], model TC-08, which utilises a USB interface connection to a portable computer with 8 channels thermocouple input. It can record temperatures up to 1820°C with automatic cold junction compensation and high interval resolution. The data logger accuracy range is ±0.5°C and consequently, the overall system accuracy level for the temperature range of 950 to 1100°C was determined to be

±2.5°C. For the temperature range between 500 and 950°C the accuracy increased to approximately ±1.5°C. The data loggers were connected to a portable computer by using the interface software provided. The two extra thermocouple readings for the ambient and flue gas temperatures were recorded using a hand held, digital data logger.

Exhaust flue gas composition measurements were recorded with the use of a Testo 350 portable gas analyser[3], which utilises pre-calibrated sensors with temperature control and can be used for temperatures up to 1800°C. The measurement accuracy by volume is 0.1 % for O_2, 0.01 % for CO_2 by volume, and 1 ppm by volume (ppmv) for CO and NO, and varies between 0.01 and 0.1 % by volume for other flue gas products. The analyser was also connected to a portable computer for data collection, and the data were then exported as spreadsheet tables.

The burner was operated at a single condition corresponding to its rated design point (25 kW thermal output). Air and natural gas fuel were supplied to the pilot and main burner air and fuel inlets accordingly. Flow rates are given in Table 1 below. Temperature and flue gas composition loggings were taken over a period of 2 hours, allowing for thermal saturation and for the RTB and furnace temperatures to reach steady state condition. The test furnace load temperature was set at approximately 940°C simulating the operating conditions of the RTB in a heat treating furnace.

Main burner air mass flow rate	0.00908244 kg/s
Main burner fuel mass flow rate	0.00045968 kg/s
Pilot burner air mass flow rate	0.00032642 kg/s
Pilot burner fuel mass flow rate	0.00001747 kg/s
Density of test ambient air	1.164 kg/m^3
Density of test fuel gas	0.704 kg/m^3

Table 1: Hot flow test - Experimental air and fuel gas flow rates

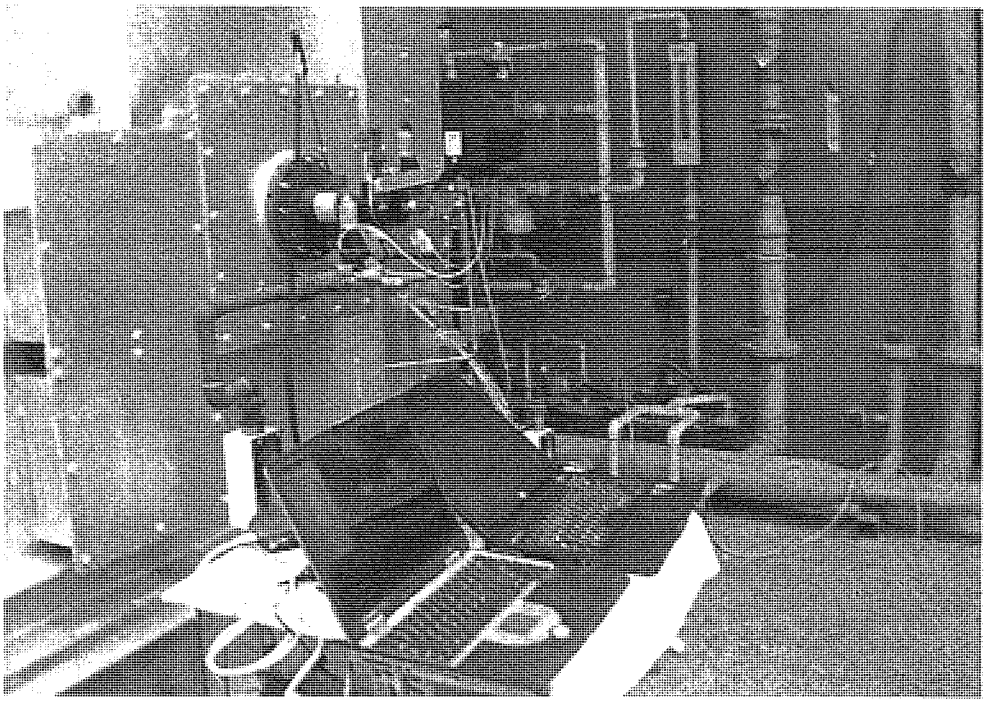

Figure 2: RTB experimental test furnace set-up

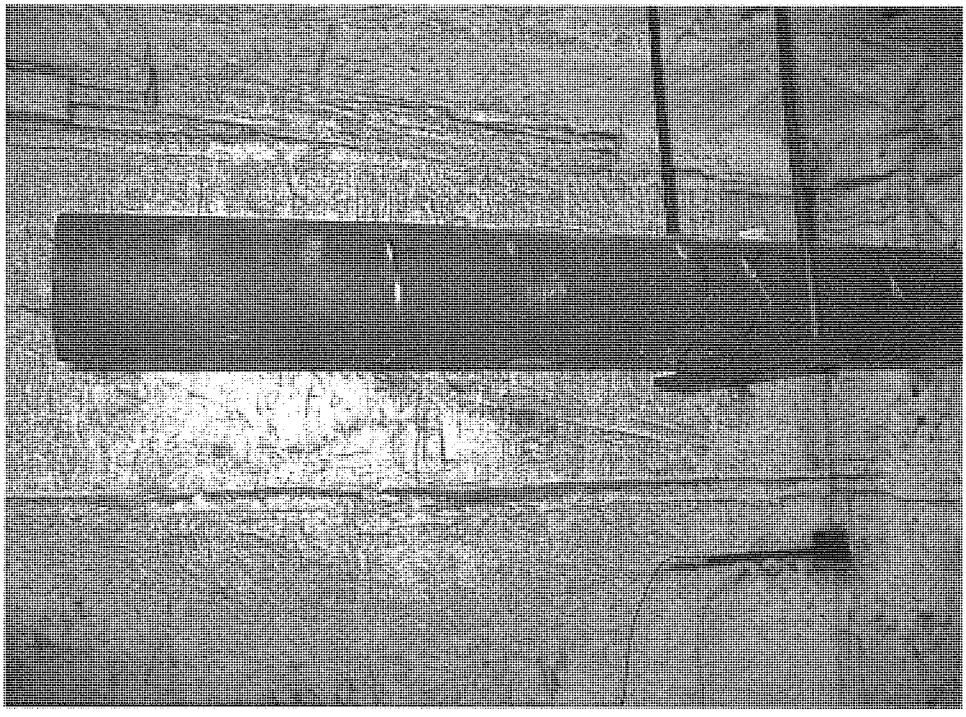

Figure 3: RTB in test furnace with thermocouples attached on radiant tube

6.3 Experimental results

The measured flue gas analysis is included in Table 2 (data are dry basis). The ambient temperature was 29.6°C. The nominal design operating point of 3% flue gas O_2 was closely achieved. The CO_2 gas volume accounted for approximately 10 % of the exhaust flue gas composition. The emitted CO at 12 ppmv is very low, but NO at 461 ppmv forms a basis for further study to improve environmental performance.

Exhaust Flue gas products	**Experimental**	**Computational (extended length burner)**		
		ED/DT[1] 1950 °C flame Temperature	**ED/DT[2] 2150 °C flame Temperature**	**TFC/DT[3] model**
O_2 (% by volume)	2.98	2.96	2.91	3.03
NOx (ppmv)	461	495	858	223
CO (ppmv)	12.31	0.12	0.12	1144
CO_2 (% by volume)	10.21	10.02	10.04	9.91
H_2O (% by volume)	-	16.69	16.72	16.59
Exhaust Temperature (°C)	696	874	876	876

Table 2: Experimental versus predicted exhaust flue gas measurements

[1] Eddy Dissipation combustion model in combination with Discrete Transfer radiation model using a temperature limiting subroutine
[2] Eddy Dissipation combustion model in combination with Discrete Transfer radiation model initial predicted solution
[3] Results from Turbulent Flame Closure combustion model (fresh gases inlet) in combination with Discrete Transfer radiation model

A final gas temperature of approximately 695°C was measured in the exhaust off-take. This defines an overall thermal efficiency of about 65%. This value compares well with other RTB manufacturer advertised data[4] (62 to 69 %), although improvements can be made.

Measured temperatures on the RTB air tube and inner tube upper surface may be seen in Figure 4. In the region of the recuperator exit the air tube wall temperature is approximately 610°C. Downstream of the step ring the wall temperature falls to 570°C and then increases again to 715°C at the start of the flame tube. The temperature drop is due to the increased wall film heat transfer coefficient in the air annulus resulting from the sharp increase (around 3 times the axial velocity component v_u for the cold flow) in velocity through the step ring restriction.

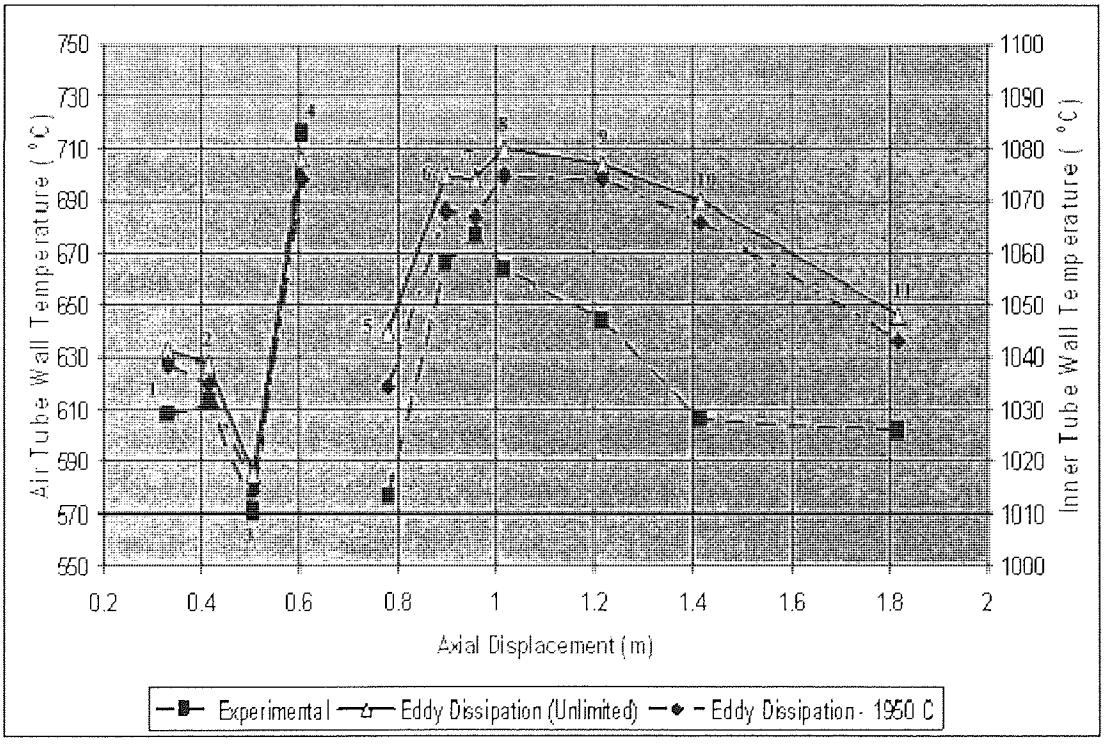

Figure 4: Experimental versus predicted wall temperatures
(Thermocouple locations indicated at positions 1 to 11)

The measured temperature profile on the air tube determines the temperature increase (~100°C) of the combustion air prior to its delivery to the combustion zone, additional to the air swirler coil annulus where most of the pre-heat energy recuperation has taken place already. The combustion air exits the recuperator coil at around 350°C and is therefore delivered to the fuel entry area at approximately 450°C.

The inner tube wall temperature along the upper surface shows a gentle profile, rising from 1014°C 50mm downstream of the discharge face to a peak of 1063°C at 230 mm, thereafter decreasing steadily towards a value of 1025°C at the end of the tube.

The four circumferentially-distributed thermocouples located at 230 mm downstream of the discharge face showed good circumferential uniformity at this station, with values of 1063°C (upper), 1063°C (right), 1072°C (lower) and 1068°C (left). These results tentatively suggest a reasonably axi-symmetric flame, with no serious flame attachment, however a small percentage of flame wall attachment is present. Values are well within material limits and would not, exclusively, result in premature burner failure.

6.4 Combusting flow computational models

The aim of the combusting flow simulations was first to achieve a satisfactory validation against experimental data, exploring the influence of combustion and radiation models in particular, and then to use the best simulation to analyse the detailed fluid flow, combustion and heat transfer characteristics of the design.

The full three-dimensional geometry of the RTB is reproduced with all significant physical features resolved. All the internal solid components except the air annulus inner wall are meshed to permit the resolution of solid conductive heat transfer, as a continuation of the cold flow model, with the air, inner and flame tubes and inner tube ceramic plug represented as solid walls. This allowed a hybrid prism/tetra meshing internal to the solid walls, which was coupled to the fluid domain hybrid unstructured mesh, internal to the RTB model, using the CFX Pre tools. The outer radiant tube and furnace wall were

modelled as thin surfaces. This modelling strategy allowed the study of the heat transfer through conduction in the solid wall domains, and therefore a more accurate heat transfer prediction within the RTB.

The solid wall domain materials, Inconel 601 for the inner and air tubes, Silicon Carbide for the flame tube and Ceramic fibre 1260 for the inner tube plug, were created in the CFX material library. The material physical and heat transfer properties, such as density, molecular weight, emmisivity, conductivity and specific heat capacity, were sourced from different references[5,6] and were inputted either as fixed values or as temperature dependant equations, where it was applicable, using the CFX command language editor.

The fluid domain was defined as a methane-air mixture. This allowed the use of the pre-defined reaction schemes and flamelet libraries. The inlet fuel and air mass flow rates were adjusted from their experimental values to compensate for the representation of typical UK natural gas[7] (which can include small amounts of gases such as ethane C_2H_6) as methane such that the correct thermal input and exhaust O_2 concentration were maintained. The appropriate air/fuel mass fractions were used to define air, fuel and premixed pilot inlet boundaries.

The outer radiant tube was modelled as a thin surface that was set as a fixed temperature boundary, at 975 °C, which was averaged from the experimental measured thermocouple measured values from the test furnace (the standard deviation between the different thermocouple locations on the outer tube was just 4.1°C). The surface sections modelling the furnace and internal burner wall (annulus inner wall) surfaces were set as adiabatic boundaries, as in steady state the net heat flux through these boundaries is assumed to be zero. This approach was considered accurate enough, as no significant thermal loss is expected through these surfaces, when they become saturated during the RTB operation. The initial temperature and flow conditions for the solid and fluid domains were set to simulate steady state combustion.

Two combustion models were tested, the Eddy Dissipation model (ED) and the Turbulent Flamespeed Closure model (TFC)[8], presented in more detail in Chapter 2. The ED model is widely used for premixed and diffusion flames and is based on the concept that chemical reaction is fast relative to the transport processes in the flow. The model assumes that the reaction rate may be related directly to the time required to mix reactants at the molecular level. In turbulent flows, such as in the RTB, this mixing time is dominated by the eddy properties and, therefore, the rate is proportional to a mixing time defined by the turbulent kinetic energy, k, and dissipation, ε.

In the ED model, the A and B coefficients were set to commonly used values 4 (default) and 0.5 respectively to reduce computational timescale. Default value for B is -1; however by increasing it to 0.5 makes the reaction dependent on the fuel and oxidant concentrations, thus accelerating the solution. For multi-step reaction schemes (as used here), $B = 0.5$ is not recommended because global extinction of the flame could occur, nevertheless this was not witnessed during the simulations.

A two-step methane-air reaction scheme after Westbrook and Dryer[9] was specified so that CO could be predicted, with an additional NO model[8] in which NO reaction rates are integrated over a temperature PDF, and temperature variance is transported (as described in Section 2.7).

In the TFC model, designed for partially pre-mixed flames, a single variable C is used to describe the progress of the global reaction. The composition of the fluid is determined by blending the compositions of the non-reacted state (fresh gases) and the reacted state (burned gases), where C=0 corresponds to fresh materials and C=1 corresponds to fully reacted materials. The model is thus able to resolve a flame front.

The composition of the burned gas fraction is computed from a laminar flamelet library. In this model the laminar flame speed must be set, and recommended values between 0.35 and 0.5 m/s were tested[8].

Two radiation models, the Discrete Transfer (DT) and Monte Carlo (MC) method[8] were tested, again described in detail in Chapter 2. The DT model solves the radiative transfer equation throughout a domain by a method of ray tracing from surface elements on its boundaries. The model discretises the path along every traced ray in the sections formed by sectioning each ray in small uniform element boundaries and radiative energy is represented by a combination of the emitted intensity and the reflected component of the incident intensity.

The MC model assumes that the radiation intensity is proportional to the differential angular flux of photons and simulates the radiation field as a photon gas domain. Individual photons have to be traced through the domain in an intrinsic manner, with a large number of histories required to give an accurate result. In theory, the MC method is more accurate if sufficient histories are traced, but the DT model is computationally much more efficient.

The Gray spectral and isotropic scattering options were selected for both models to aid convergence and reduce computational time.

6.4.1 Extended length burner model

As indicated earlier, the k-ε turbulence model was used throughout, applying the same default coefficients. All simulations were solved as steady state problems. The results presented here are taken from a hybrid tetrahedral/prism element mesh of approximately 300,000 nodes, with y+ values <20 in the combustion chamber region and <100 in the air flow annulus. This represents a sufficient mesh resolution, as explained in the theory chapter, using the scalable wall function (default) approach.

A finer mesh of 400,000 nodes was tested at one point, but mesh dependency effects were found to be small, the predicted wall temperatures in the thermocouple locations differentiated on average by just 2%. Larger mesh files were also created, although insufficient batch file memory allocation from the Microsoft Windows environment (2 GB memory limitation), prohibited their run in the CFX solver.

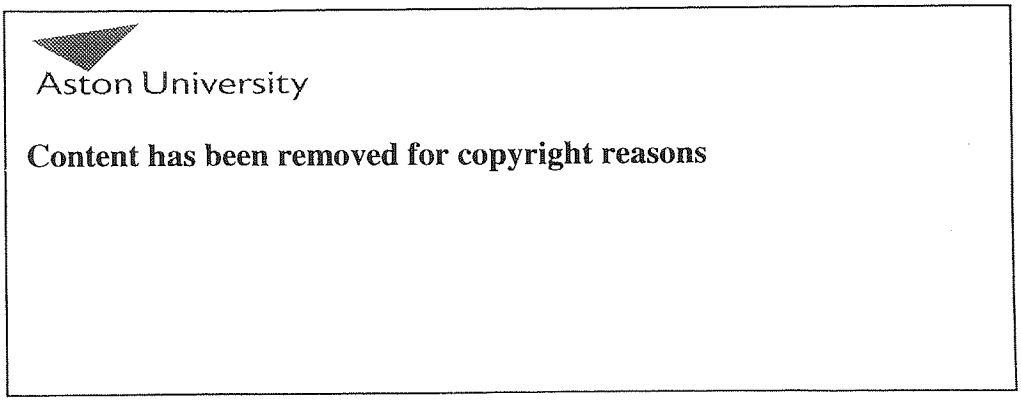

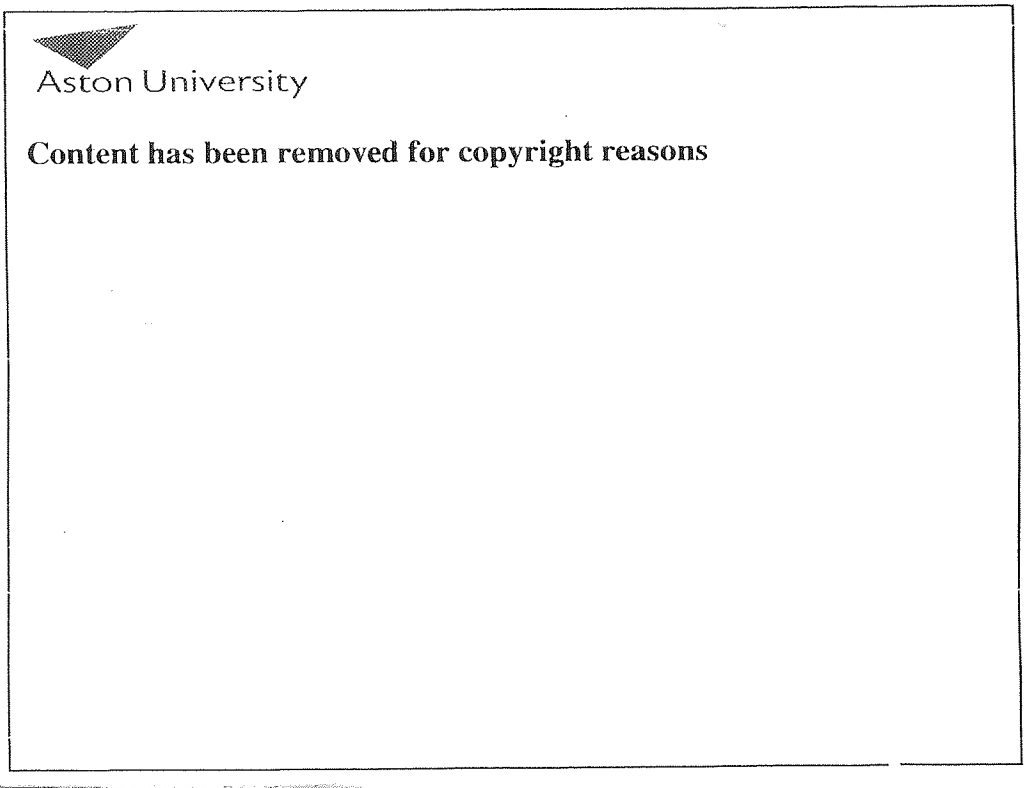

Figure 5: Fluid domain mesh plane cut through recuperator/step ring section

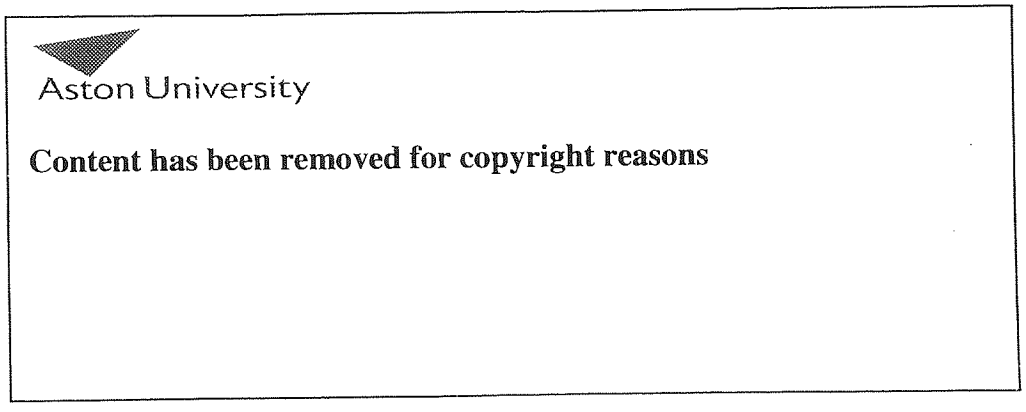

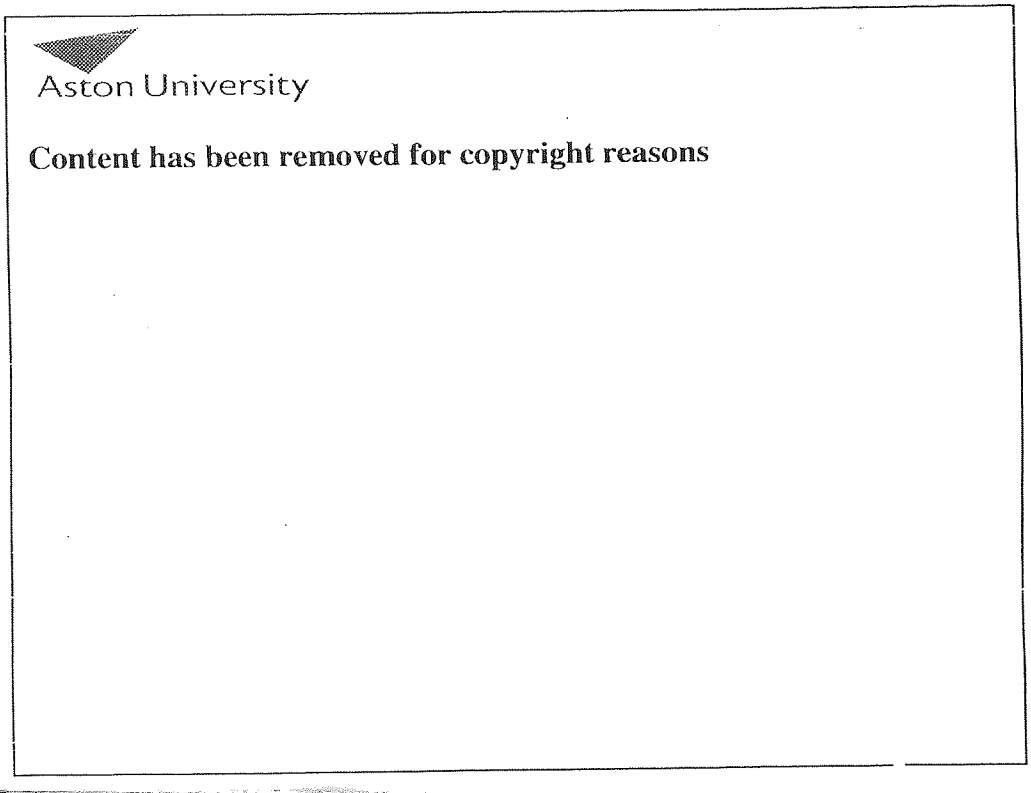

Figure 6: Fluid domain mesh plane cut fuel nozzle/combustion chamber

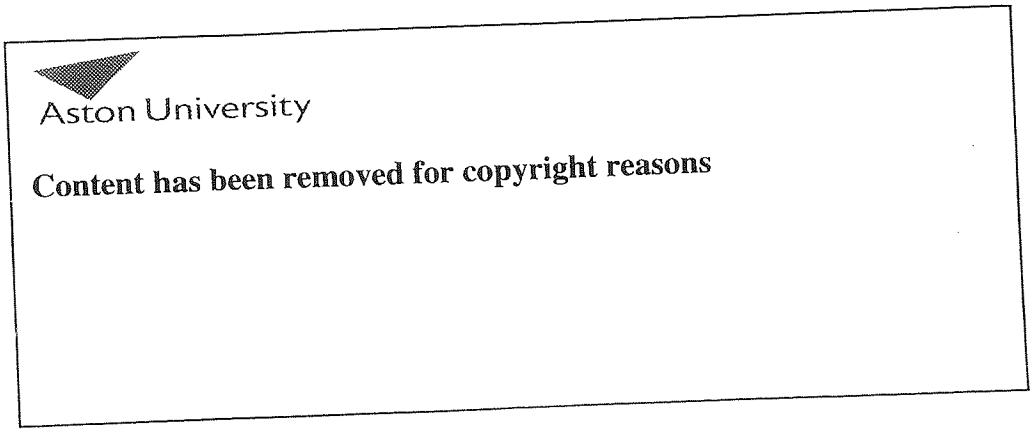

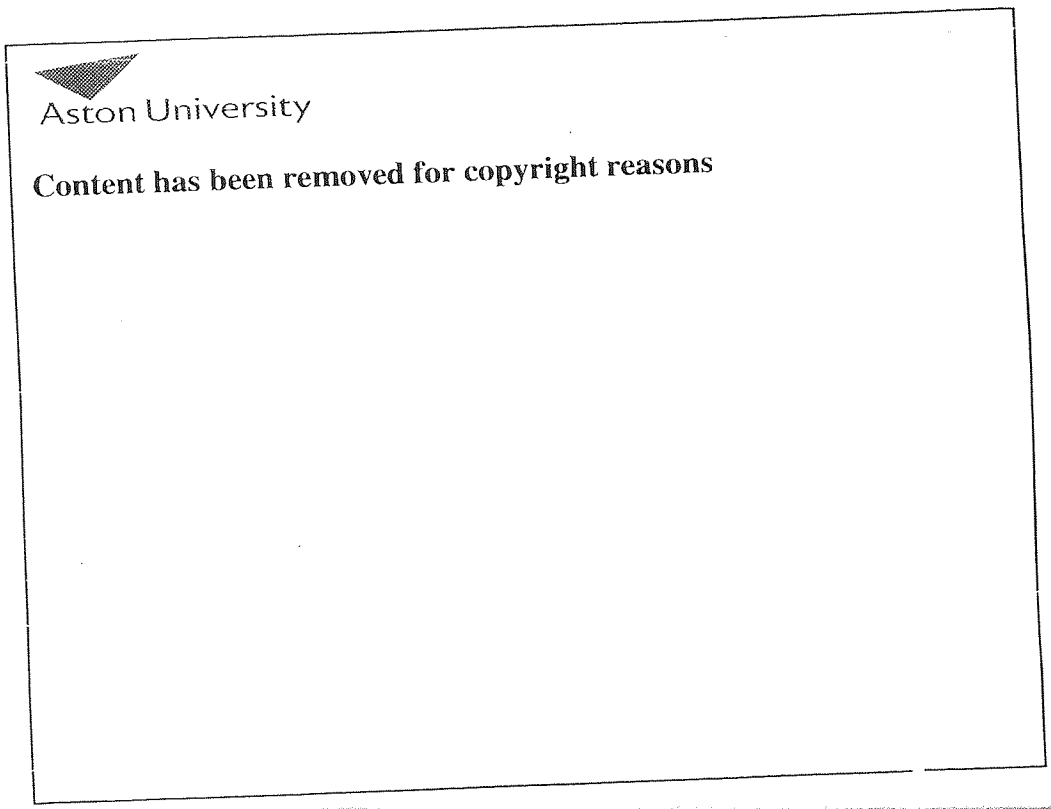

Figure 7: Solid wall domain mesh plane cut

Figures 5 and 6 present a section cut through the fluid domain mesh, showing the hybrid mesh structure and the overall mesh density change at details such as the coil and the fuel nozzle/flame tube area. They also show the surface mesh clarity on the burner inner wall and the increased mesh detail in the fuel nozzle and pilot tube area.

Figure 7 shows the meshing detail internal to solid domain walls for the air, flame, inner tubes and inner tube ceramic plug. The solid domains consist approximately from 37500 nodes for the air tube, 9000 nodes for the flame tube, 48000 nodes for the inner tube and 5000 nodes for the inner tube plug.

6.4.2 Standard length burner model

The RTB used in the hot flow test presented a longer version from the standard WRTB studied during this research. The only important difference between the two models is the elongated (by 400 mm) inner and radiant (outer) tubes as shown in Figure 8. All burner dimensions not shown are the same as presented in Figure 1. The computational grid in both cases is intrinsically the same, with the standard length WRTB model requiring fewer grid elements to complete the overall fluid domain.

Using the same methodology as previous models, a hybrid mesh of approximately 250000 nodes was created using the same surface and volume size nodes, and corresponding solid wall domain meshes coupled to the fluid domain. The solid domains consist approximately of 37500 nodes for the air tube, 9000 nodes for the flame tube, 34000 nodes for the inner tube and 5000 nodes for the inner tube plug.

Figure 8: Standard WRTB typical length schematic

6.5 Long RTB modelling results and comparison with experiment

Two variants of the ED model were tried, one with a peak temperature limitation, due to over-prediction (2150°C) of the flame temperature in the initial run. Different sources[10,11] predict a peak flame temperature of approximately 1950°C for the Wellman RTB test case conditions (preheat air temperature and equivalence ratio) which is approximately the adiabatic combustion temperature of methane-air mixture; hence this was specified as the limiting value.

Flue gas analysis results from simulations using the ED and TFC combustion models in combination with the DT radiation model are shown in Table 2. The concentrations and temperatures are mass flow averaged across the outlet boundary plane.

The computations using the MC radiation model suffered from convergence problems, particularly in combination with the ED combustion model. They indicated an oscillatory residual behaviour, possibly linked to a mesh characteristic, such as the local node spatial distribution in the combustion chamber (where most radiation occurs). However, experimenting with the model fluid domain time scales, to attempt to "break" the residual oscillatory solution, a degree of convergence was achieved, and it was observed that there was no significant difference between the DT and MC radiation model results. Thereafter, it was decided to use only the DT model for the subsequent computations.

The computational results from the ED model using the flame temperature limiting subroutine (first column) provide the best agreement with experimental values for NO, over-predicting by about 7%. Without the temperature limit the peak calculated temperature is 2150°C, and NO is over-predicted by a factor of two. This is unsurprising as thermal NO production is a direct function of peak temperature (exponentially increasing with temperature), and this is the dominant mechanism of NO formation here[10,11,12]. The flame temperature limiting subroutine however only affects the formation of NO, thus the two ED/DT result columns have nearly identical values.

The TFC model under-predicts NO by a factor of two, implying a significant under-prediction of peak temperature.

CO predictions with the ED models are reasonable in comparison with the experimental results in that both give very low values, although the small residual amount of CO seen in the experiment is not resolved by the simple two-step reaction model. The prediction of the dissociation of the reactants into products as part of the methane combustion is highly dependant on the oxidation of the CO, which turns predominantly into CO_2.

The O_2 and CO_2 predictions, on the other hand, have greater than 98 % accuracy in comparison to the experiment, and the mass flow averaged water content of the exhaust flue gas is approximately 16.7 %.

The TFC model however grossly over-predicts CO at 1144 ppmv. On investigating this discrepancy, it was found that the TFC model was not conserving mass correctly for O and H (both of which reduced by about 4 % through the domain). This behaviour could not be rectified, and casts serious doubt on the overall integrity of the TFC calculations. Alternative inlet boundary models (Fresh/Burned gases option) were tested however, the mass inaccuracies remained. The results were reported to ANSYS UK, which confirmed the findings and noted for future software release updates to correct the errors. No further results from the TFC model are presented.

Wall temperature predictions from the ED models are also presented in Figure 4 as point values at the same locations as the thermocouples. In the air tube region, predictions from both models closely match the experimental values (within 25°C) and correctly reproduce the temperature dip in the vicinity of the step ring. This gives confidence that the thermal behaviour of the burner in the recuperator region has been accurately simulated. The difference between the test and model values indicates also the effect, on the heat transfer predictions, of the adiabatic boundary condition set on the model furnace wall and burner inner wall surfaces. The temperature limit model is, overall, marginally more accurate.

Predicted temperatures on the inner tube show good agreement for the first third of the inner tube, with values over-predicted typically by 13°C for the temperature limit model and by 21°C for the standard model. Further downstream the agreement is slightly poorer, with values over-predicted typically by 27°C for the temperature limit model and by 31°C for the standard model. While the experimental values downstream of the peak temperature recorded in position 7 indicate an almost linearly decreasing temperature profile, the model shows a smaller gradient, with the last section of the inner tube (position 11) been closer to the test measurements. This is an indication that the model is predicting a slightly longer flame than in reality. The ED model interaction with the turbulence model however, has a tendency to over predict flame temperature and this is believed to be the reason to an extent, for the slightly longer flame prediction.

Exhaust flue temperature is calculated at 875°C, which is approximately 25 % higher than the experimental value. This value suggests that the RTB is working with an efficiency of approximately 55%, around 15% lower than the experimental results. Lowering the combustion flame temperature by 200°C (using the temperature limiting subroutine) does not have any effect on the flue gas temperature at the exhaust. This is expected, as the combustion temperature subroutine just limits the maximum flame temperature for the creation of NOx. A model with heat flux values set as boundary conditions on the furnace wall and burner inner wall surfaces was also tested (instead of adiabatic). This model predicted a flue gas temperature reduction of 25°C (from the over-predicted value) but it was not preferred due to not satisfactory convergence at the specified residual level.

Furthermore, the exhaust position on the WRTB is slightly further downstream and after a 90° bend, in comparison to the model. This would have an impact on the agreement, as the flue gas would lose some energy and reduce its temperature.

It is believed that the errors here may be due to coarse assumptions in the radiation model, such as a gray gas throughout with a single absorption coefficient, and also a constant emissivity along the inner and outer tube walls.

The radiation model is an additional energy transport mechanism. In combustion modelling however, switching radiation on, has an implication on the rate of energy diffusion out of the domain. During model runs the radiation model was first tried switched off. The predicted fluid domain temperatures were high and when the radiation model was selected, they converged into lower values. This has also been observed by other authors[13]. Therefore, if the radiation model is not solving that radiation heat transfer equation accurately enough, it can introduce an error (positive or negative) in the dissipation of energy out of the domain.

Furthermore, the number of rays, where radiation calculation takes place in the model, is also important. The DT method can present a ray effect. The use of adequate amount of rays is required to get a smooth solution as energy oscillations can appear in the temperature field[14], although increasing substantially the number of rays will have a detrimental effect in solution time. A model with double the default number of rays was tested (16 instead of 8 rays) and showed no effect on the predictions of wall temperatures, flow velocities, gas composition, as well as flow temperature contours; although it tripled the convergence timescale. Higher ray number model indicated excessive computational timescale, thus limiting the ray effect independence study to two runs.

In addition, as mentioned earlier, the default Gray model was used as it is convenient to average radiation properties over the whole spectrum; however gases only absorb and emit in discrete bands. A limitation of the Gray model in combustion calculations is that a single absorption coefficient is set, independent of the local gas composition. The error caused by this approximation is not large because combustion air is usually at lower temperatures than the products. There are studies however, which suggest that the use of the Weighted Sum of Gray gases spectral model in the DT method provides better representation of the non-gray radiative properties of CH_4 combustion media[15]. Nevertheless, in simulations where radiation plays a major role in the heat transfer of the system due to radiant wall boundaries (like in the WRTB model), the use of the Gray model can lead to an over-prediction of the energy absorbed by the fluid domain of the model and therefore, an over-prediction to the fluid domain temperature.

The overall combustion and radiation model errors however, are not large. Conclusively, the level of agreement between the experimental results and the computations using the temperature-limited ED combustion model in combination with the DT radiation model is believed sufficient to justify use of the model to explore the characteristics of the RTB in more detail.

6.6 Discussion - Heat transfer and fluid flow analysis

Figure 9 presents temperature contours on a plane through the RTB centre-line. The asymmetric temperature pattern in the combustion zone is related to the gently swirling flow.

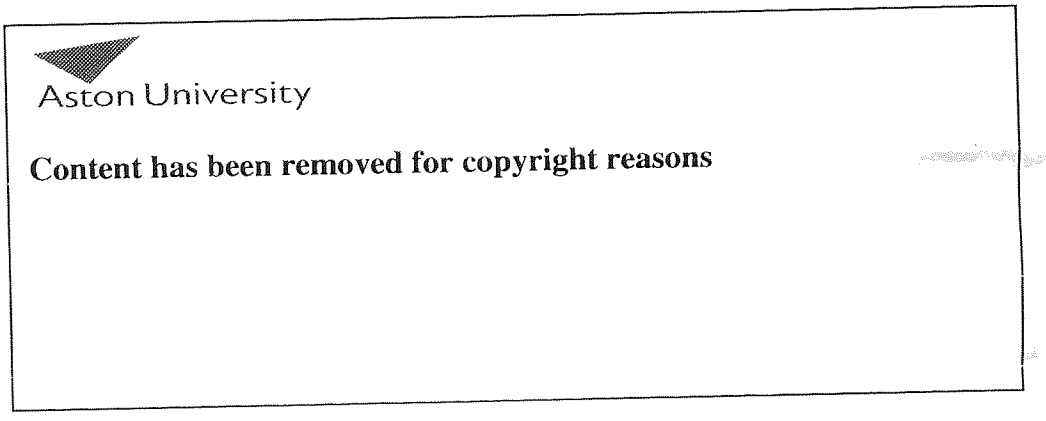

Figure 9: RTB Fluid domain temperature contours

The mean flow temperature falls by approximately 500°C along the length of the inner tube. The highest flame temperatures are between 150 and 500 mm from the discharge face. The heat release initiates in the recirculation zone downstream of the fuel ports and adjacent to the pilot nozzle, and it is reasonable to interpret this as a flame attachment point.

Detail view A in Figure 9 shows a very high temperature region impinging on the end of the flame tube, and flame attachment can be observed at this point in the real device, as shown in the photographs in Chapter 1. The flame tube is protected to some extent by the cooling effect of the secondary air outside it. Any reduction of this airflow, through non-axisymmetry on assembly or through deformation in service, would have a detrimental effect on flame tube longevity.

Detail view B of Figure 9 shows that the primary combustion airflow is delivered to the fuel nozzle at approximately 350°C, which is around 100°C less than the secondary airflow at the same axial plane. The secondary airflow temperature increases to approximately 600°C at the end of the flame tube.

Figure 10 presents temperature contours through the solid walls at the fuel nozzle area. The high temperature zones described earlier are clearly seen, with the tip of the pilot burner reaching more than 1000°C and the air and flame tubes reaching between 950 and 1000°C respectively.

Overall, the pilot burner wall is exposed to temperatures that are within its material limits (marginally); however it indicates a degree of flame attachment (also shown in Figure 9). Flow pattern change due to altering of flow passage areas (burner misalignment) or change in the stoichiometry (that would inevitably change the air/fuel flow cross flow dynamics), could result in long term failure. This is clearly shown in the photographs in Chapter 1, Section 1.1.3.

The inner wall ceramic plug prevents heat transfer between the two metal walls due to its low conductivity coefficient (the inner wall reaches more than 1100°C).

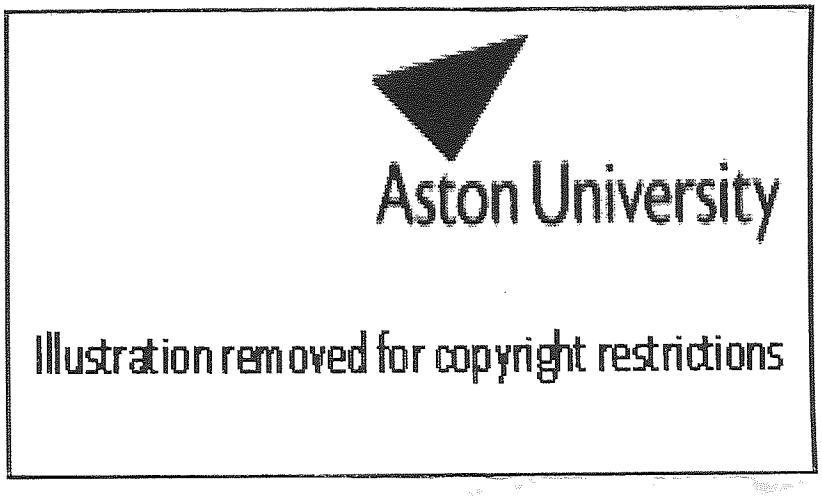

Figure 10: Contours of temperature at the burner inner and solid walls

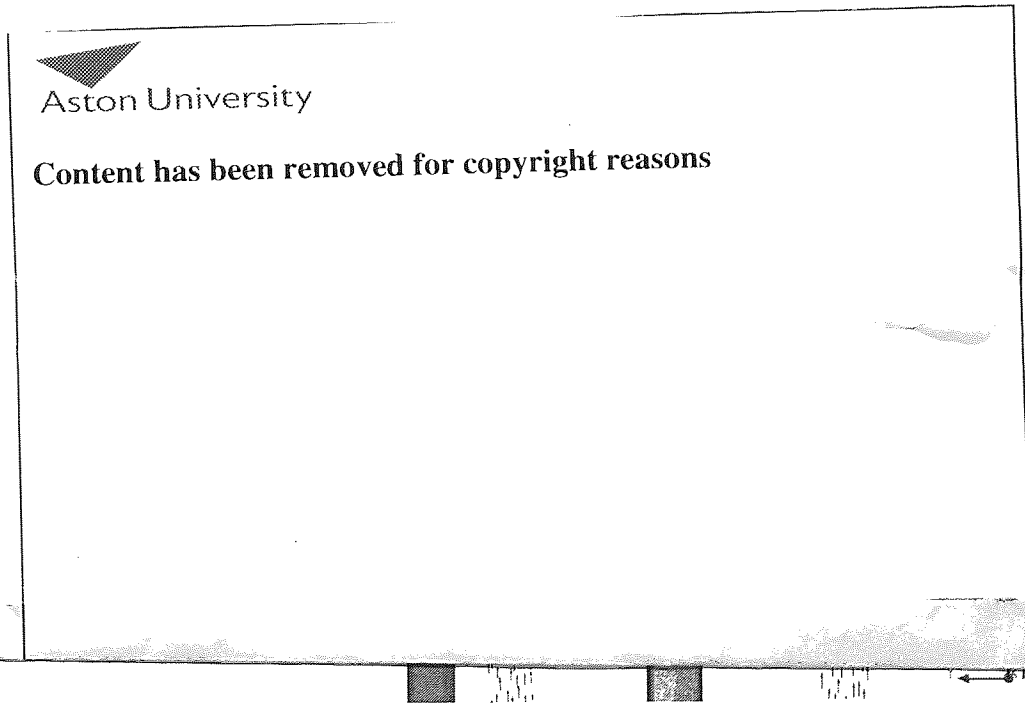

Figure 11: Contours of v_u through the step ring and at the flame tube entry

Figure 11 shows contours of v_u and velocity vectors as the flow passes through the step ring and the flame tube. The acceleration and recirculation behind the step ring are clear, as well as the recirculation prior to the flow entering the primary/secondary split at the flame tube. Both recirculation zones have not changed in size, in comparison to the cold flow (Chapter 5, paragraph 5.6). The velocities, as expected, have approximately doubled in magnitude throughout the flow passages.

The recuperator section, which extends axially from the exhaust gas outlet to the point at which the exhaust gas annulus narrows sharply, is designed to transfer as much heat as possible from the returning exhaust gas to the incoming main combustion air. This is aided by the sharp narrowing of the exhaust annulus, which causes acceleration and thus increased heat transfer coefficient, and by the swirler coil in the air annulus which also causes acceleration.

The exhaust gas enters this section at a mean temperature of 1043°C (mass-flow weighted average across the axial plane, as with all subsequent values) and leaves at 874°C; the air enters at 29°C and leaves at 215°C. 1.68kW of heat is transferred, with mean film coefficients (ignoring wall conduction) of 63 $W/m^2{}^oC$ for the exhaust gas and 52 $W/m^2{}^oC$ for the air. The mean overall coefficient is 28 $W/m^2{}^oC$.

In Chapter 5, it was estimated that eliminating leakage past the outer edge of the swirler coil could increase the mean film coefficient by about 50%. The modelling results now indicate that this would lead to an additional 300W of recuperation, or a fuel saving of about 1.2%.

The section of the burner from the recuperator to the inlet of the flame tube also achieves a degree of recuperation. However, compared to the recuperator the air velocity is steadily falling due to the reducing swirl component, and the exhaust gas velocity is much lower due to the large annulus height. The exhaust gas enters this section at a mean temperature of 1082°C and leaves at 1043°C; the air enters at 215°C and leaves at 306°C. 0.84kW of

heat is transferred, with mean film coefficients (ignoring wall conduction) of 30 $W/m^{2o}C$ for the exhaust gas and 34 $W/m^{2o}C$ for the air. The mean overall coefficient is 16 $W/m^{2o}C$.

As has been referred to earlier, there is a local increase in air film coefficient in the vicinity of the step ring which results in the drop in wall temperature seen in Figure 4.

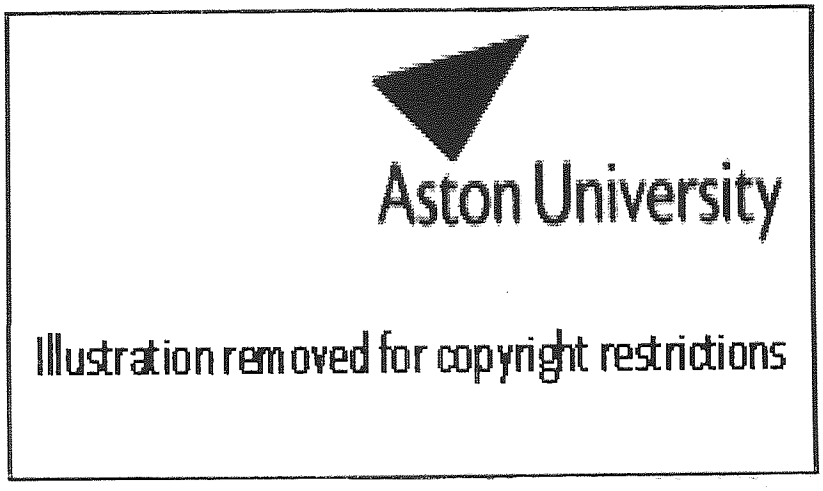

Figure 12: CH_4 and CO_2 mass fraction contours at the fuel nozzle and discharge face

Figure 12 shows the CH_4 fuel mass fraction immediately downstream of the fuel ports and the mass fraction of one of the reaction products (CO_2) further downstream, at the discharge face. The circumferential uniformity of the combustion CO_2 at the downstream plane (discharge face) shows that the mixing of fuel and air is adequate, despite there being only four ports. This is due to the high levels of turbulence induced by the cross flow.

Axial velocity contours and vectors in the region of the flame tube and the upstream part of the combustion zone are presented in Figure 13. In comparison to the isothermal study the

flow has gained substantial forward momentum, due to the energy release from the chemical reaction, and it achieves approximately 30 m/s at the discharge face.

A toroidal recirculation zone is present outside the main flame jet, formed by the sudden expansion, but this only extends about one inner tube diameter downstream. Beyond this, the jet expands to fill the tube.

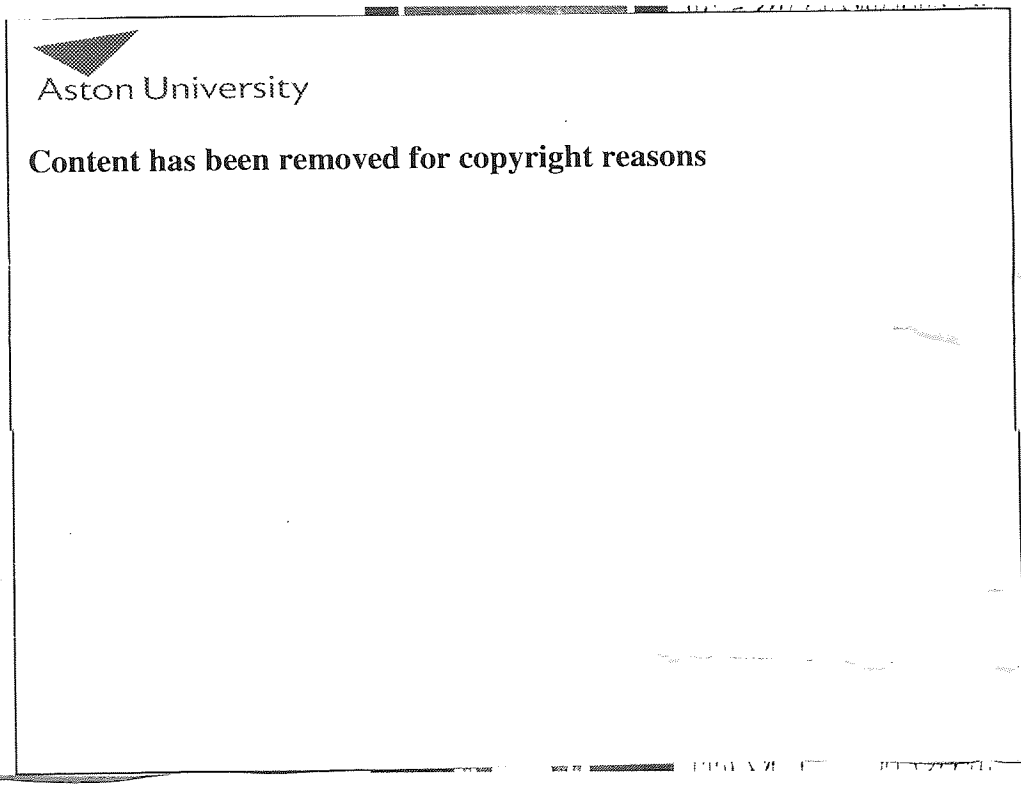

Figure 13: RTB central area contours of v_u and velocity vectors

A modest degree of swirl is still present - the mass flow averaged swirl angle at the discharge face is approximately 22°. This is however insufficient to form a central recirculation zone.

Figure 14 shows contours of axial velocity for the entire inner tube (crucifix and radiant tubes are omitted). It is clear that there is some asymmetry in the flow (as also indicated in

Figure 9) with jet attachment commencing earlier on one side of the tube. This is to be expected with confined gently swirling jets, and does not result in significant local hot spots on the inner tube wall.

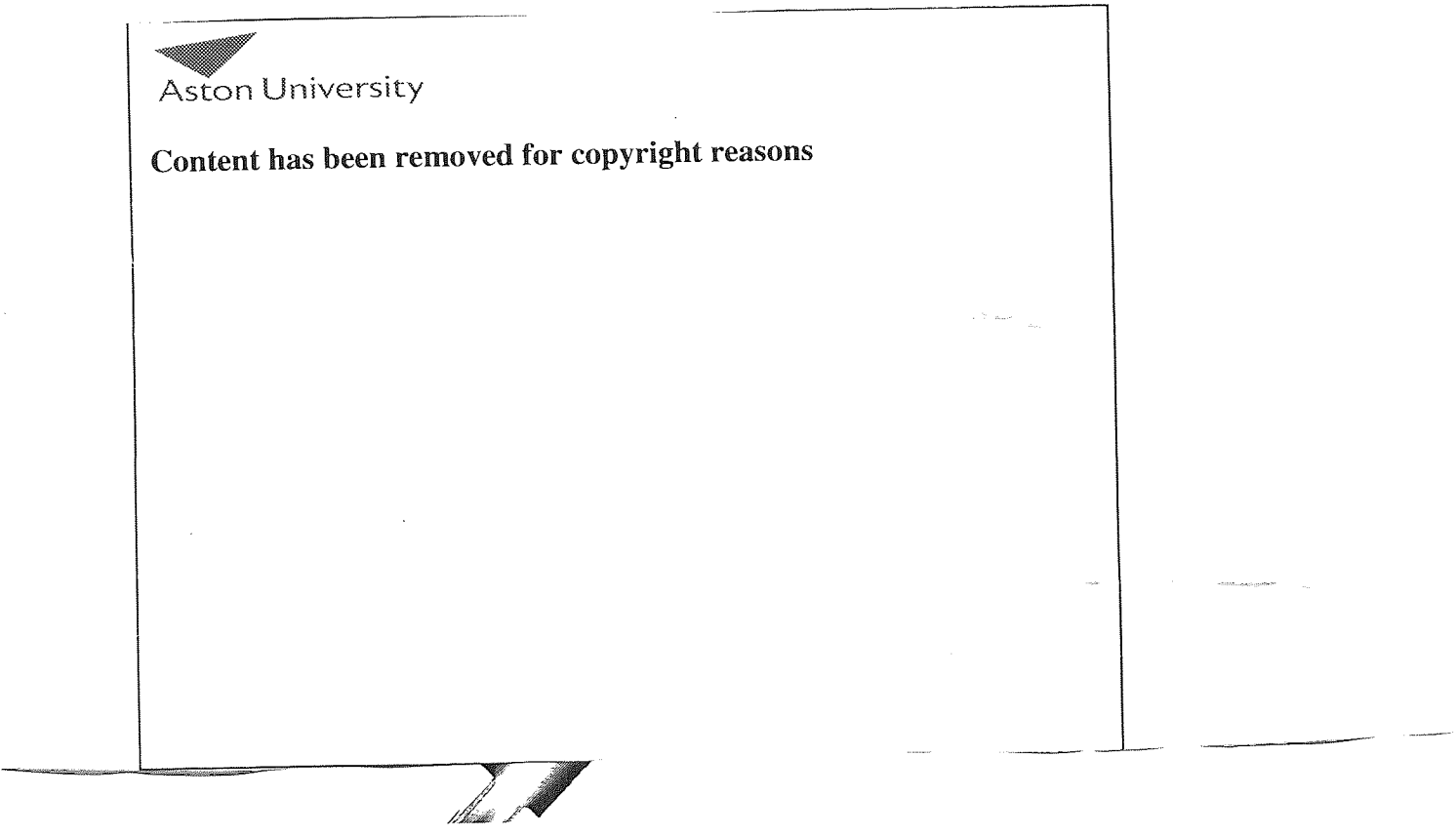

Figure 14: RTB inner tube combusting flow contours of v_u

Figure 15 presents the axial flow velocity at the crucifix, which is located at the end of the inner tube and separates it from the outer radiant tube. It also shows the flow swirl angle just upstream to the entrance of the crucifix. The crucifix is a feature (as shown in Chapter 1 burner drawings) that allows the correct placement of the inner tube within the burner.

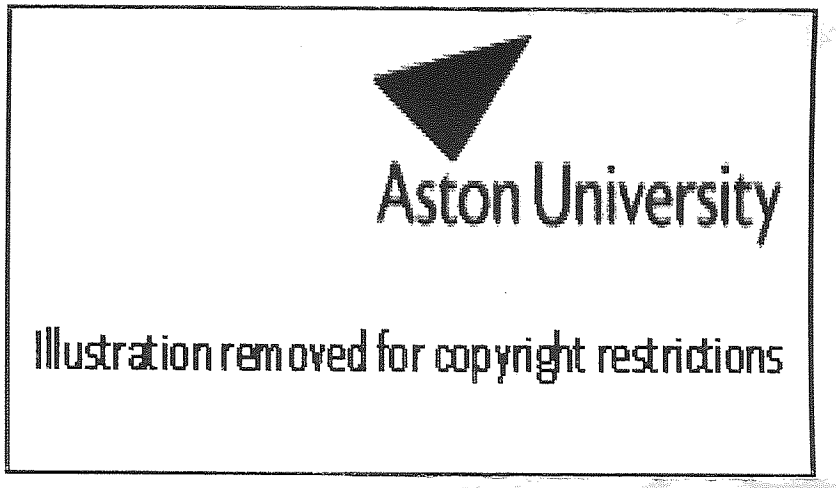

Figure 15: Contours of v_u and flow swirl angle at the crucifix

At this point the flow impacts the end wall, changes direction by 180°, and continues in the outer (between inner and radiant tubes) annulus. The reduced local magnitudes of the axial flow are expected due to the sudden deceleration, and the figure clearly shows the concentration of the reversed flow on the outer radii. Furthermore, the flow loses more than half of its swirl due to the sharp turn and the effect of the crucifix walls. The mass flow averaged swirl angle values shown, decrease from 12.5° to approximately 4.5°.

The section of the burner extending into the furnace delivers about 12 kW to the furnace. The mean heat flux along the radiant tube is 22.6 kW/m^2, and the uniformity of the measured temperatures indicate that local heat flux values will be very close to this mean. A uniform radiant tube temperature is imposed as a boundary condition, but it is nevertheless worthwhile to consider the heat flows that give rise to this uniformity.

Despite the mean gas temperature within the inner tube reaching a maximum of about 1850°C some 150mm downstream of the discharge face and falling to 1440°C at the inner tube exit, the inner tube wall remains within the range 1010-1065°C all along (Figure 4)

due to the thermally balancing effect of the returning gas flow in the surrounding annulus, which falls from 1390°C at inlet to 1120°C at exit.

That the inner tube is at a significantly lower temperature than the gases either side of it also indicates the major part played by radiation in the radial exchange. The radial flux to the radiant tube is composed of convective heat exchange from the returning gases, radiant emission from those gases, and unabsorbed net radiant emission from the inner tube wall. The former two fluxes decrease in magnitude along the path of the returning gases, and the latter flux increases, resulting in the approximately uniform combined flux.

6.7 Standard length burner model modelling results

As discussed earlier in this chapter, the model of the elongated version of the standard WRTB was necessary for the experimental validation. As the main subject of this study is the standard length WRTB, the methodology adopted was to model this with the same flow rates (and consequently net heat input), and boundary condition set-up as for the validated long burner model presented previously.

Figure 16 presents temperature contours on a plane through the standard length RTB. Again the swirl of the flame is visible as the temperature contours change laterally. The flow shows, as expected, intrinsic similarities with the predictions of the longer RTB model, with the flame length almost identical.

However, as the RTB length is shorter and net heat input the same, the efficiency of the burner is less, as the same amount of heat would need to be radiated if the efficiencies were to be the same. The standard length RTB presents a smaller radiant area by approximately 27 %. Therefore, the combusting flow exits the combustion chamber at higher temperature and this can be seen; the flow around the crucifix has lost approximately 400°C.

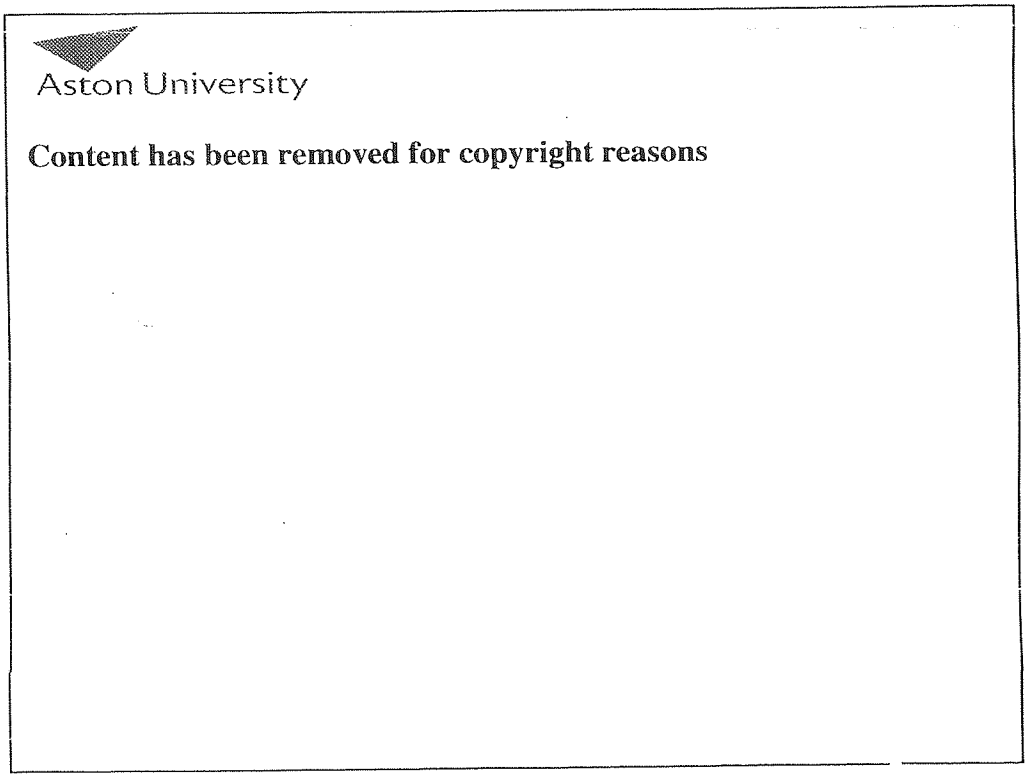

Figure 16: Standard length RTB fluid domain temperature contours

The radiant tube boundary surface is fixed at the same temperature as the long RTB, this introducing a small percentage error; as in real conditions a slightly higher temperature would be achieved. The flow therefore does not sustain its temperature difference along the return path and the predicted exhaust flue gas temperature is 934°C, some 60°C more than the longer RTB model exhaust temperature.

Consequently, the NO predictions are higher, at 571 ppmv, while the O_2 and CO mass flow averaged values are similar to the long RTB model at 2.92 % and 0.12 ppmv respectively.

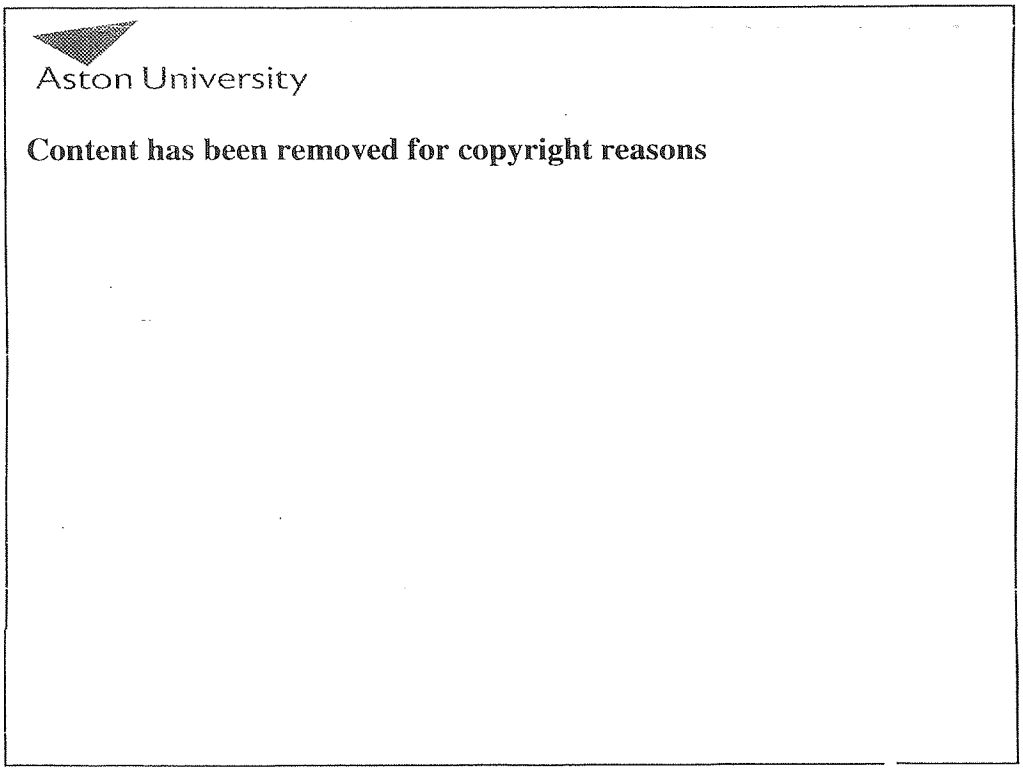

Figure 17: Standard length RTB contours of v_u and velocity vectors

Axial velocity contours and vectors in the region of the flame tube and the upstream part of the combustion zone are presented in Figure 17.

The similarities with the longer RTB flow are again apparent. In this case the toroidal recirculation zone outside the main flame jet appears slightly further downstream, which results in a slightly longer recirculation zone on this side. Again beyond this, the jet expands to fill the tube.

Conclusively, these results will be used for direct comparison with the RTB development models presented in the next chapter. As the main drive is the minimal alterations in the

standard length RTB geometry, the development focuses primarily on the fuel nozzle and the flame tube. The absolute values of the cross flow (fuel) velocity have an important role in the flow pattern and NOx emissions[16]; hence the redesign of the fuel ports is an attractive and relatively cost effective mitigation.

The results from the hot flow test have been used for an international journal publication. The publication details are referenced in the Appendix part A. The CFX solver input definition file for the combusting flow modelling is listed in Appendix C, and the experimental data from this test are listed in Appendix E. The reaction temperature limiting subroutine created in CFX is presented in Appendix B.

6.8 References

1. TC Ltd, Temperature Sensing, Measurement & Control, 2006, Uxbridge, UK.
2. Pico Technology Ltd, Data Acquisition Products, 2006, St Neots, Cambridgeshire, UK
3. Testo 350 Gas Analyser/454 Control Unit, Testo UK Ltd, 2006, Alton, Hampshire, UK
4. North American Mfg. Co., Low NOx Reverse Annulus Single Ended Radiant Tube Burner (RASERT™), Bulletin 4748, October 2006, OH 44105-5600, USA
5. J M Rhine, R J Tucker, Modelling of Gas-Fired Furnaces and Boilers, British Gas, 1991
6. W M Rohsenow & J P Hartnett, Handbook of Heat Transfer, Mc Graw Hill, USA, 1973
7. Andersen I. V., Dahl H. J. (2004). Composition of Natural Gas in Export Pipelines From Norway to United Kingdom, Gassco.
8. CFX 10 User Manual, ANSYS UK Software Solutions, Abingdon, Oxford, 2006.
9. Westbrook & Dryer, Simplified Reaction Mechanisms for the Oxidation of Hydrocarbon Fuels in Flames, Combustion Science and Technology Vol. 27, 1981.
10. Andrews G. (2004). Proceedings of course "Combustion in boilers and furnaces", Energy and Resources Research Institute, University of Leeds, UK.
11. Turns R. S., (2000). An Introduction to Combustion-concepts and applications, second edition, Mc Graw-Hill Series in mechanical Engineering, 2000.
12. Chomiak J, Combustion: A study in Theory, Fact and Application, Abacus Press, 1990
13. Keramida *et al.*, The discrete transfer radiation model in a natural gas-fired furnace, International J for Numerical Methods in Fluids, Vol 34, Iss 5, Pages 449 - 462, 2000.
14. Feldheim V and Lybaert P, Solution of radiative heat transfer problems with the discrete transfer method applied to triangular meshes, Journal of Computational and Applied Mathematics, Volume 168 , Issue 1-2, 2004.
15. Bressloff N, Moss J and Rubini P, CFD Prediction of Coupled Radiation Heat Transfer and soot production in Turbulent Flames, 26th Combustion Symposium, Naples, 1996.
16. Bandaru R and Turns S, "Turbulent jet flames in a Crossflow: Effects of some jet, crossflow, and pilot-flame parameters on Emissions, Combustion and Flame Journal, 121:137-151, 2000.

7. COMBUSTING FLOW - BURNER MODIFICATIONS

7.1 Introduction

The need to address further the in-service failure and relatively high NO emissions of the burner has emerged after evaluation of the combusting flow results. The main areas of concern are the reacting flow distribution around the fuel nozzle and flame tube area, as well as the slight misalignment of the combustion flame. Changes in this flow pattern have a direct effect on the flame and consequently on the NO production rate.

All the development models were created using, essentially, the same meshing and geometry techniques applied previously. This made the presentation in this chapter of individual mesh cut planes unnecessary, and secondly, the adhering to the CFD modelling (turbulence/combustion models etc) as successfully created previously.

The first model presented in this chapter addresses the WRTB failure due to the flame (and consequently pilot and air tubes) tube distortion. The model is created with the flame tube positioned eccentrically, and this highlights the flow behaviour in a non intended operation. The justification for this model is analysed in the relevant section that follows.

A supplementary model is presented, with the flame tube positioned further forward from its current location. This model looks at the heat transfer to the flame tube and to the adjacent air tube and the effect on the flame stoichiometry. The justification for this model was the use of a more heat resistant material in the flame tube.

In addition, five development models are created in order to attempt to improve the WRTB performance and to resolve these areas of concern. It has been said previously that the main drive behind these design modifications is the cost effectiveness of the solutions, as substantial re-design of the burner geometry is not economically feasible at this stage. Therefore, a logical step was to alter the fuel entry profile, by repositioning the fuel ports and varying their geometry, without the need for a new fuel nozzle installation. This

resulted in the increase in the number of ports and their alteration to a circular section, rather than rectangular.

Further attempts are made to reduce NO by modelling a smaller diameter flame tube and a flue gas recirculation model. The smaller overall diameter, but same wall thickness flame tube model, increases the combustion air flow passage in the primary air zone and investigates the result.

The flue gas recirculation model is an attempt to introduce this technique in the WRTB, by minimal alterations to the burner tubes and by redesigning the ceramic inner tube plug. Once more, the cost effectiveness of this modification plays an important role.

Finally the effect of a stronger swirling flow is studied with a model previously presented in the isothermal flow study. In this model the swirler coil gap is omitted, thus increasing the swirling velocity component of the flow as it exits the recuperator section.

7.2 Burner modification combusting models

7.2.1 Eccentric flame tube model

As has been discussed in previous chapters, the concentricity of the WRTB is subject to manufacturing and installation tolerances. These tolerances play an important role in the flow symmetry. All necessary steps are taken to ensure that the assembly remains as symmetrical as possible, prior to the installation in the furnace.

However, long term operation of the WRTB in a heat treating furnace augments local thermal stress, particularly in the hottest region near the discharge face, which in combination with gravitational effects produces a small lateral geometric misalignment due to a slight deformation (buckling) of the WRTB. This is witnessed by the manufacturer during furnace WRTB lifetime inspections and is primarily due to the high aspect ratio

(overall length/diameter) of this type of burner design. It has also been seen in the cold flow test burner, where the WRTB was previously sourced from an operating furnace.

This time dependant small misalignment results in the fuel nozzle being eccentric to the flame tube and the consequence is an asymmetric flow path for the fuel jets, as they exit the fuel ports. This was the main drive behind an eccentric flame tube WRTB model.

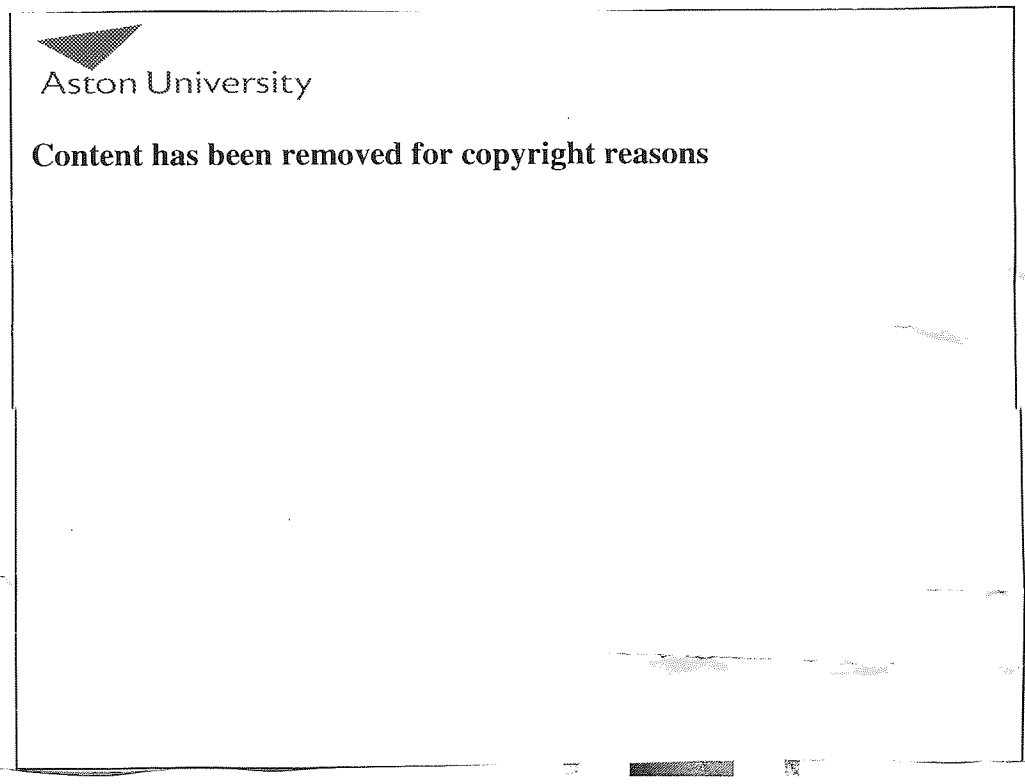

Figure 1: Eccentric flame tube model

Figure 1 indicates the basic dimensions and alterations made to the standard WRTB model, with the flame tube being eccentric to the centre line axis by just 1.25 mm. This value was a cumulative result after studying the tolerance level of every component and the misalignment observed on the cold flow test WRTB. It is envisaged that it represents the effect adequately; however it is believed that even larger burner eccentricities can result after long term operation.

7.2.2 Forward flame tube model

The location of the flame tube plays an important role in the configuration of the WRTB as has been analysed in Chapter 5. It defines the air flow ratio between the primary and secondary combustion zones and also prevents possible fame impingement on the burner air tube. As we have seen in Chapter 6, the end face of the burner air tube experiences higher temperatures due to its exposure in the combustion zone.

An attractive solution therefore, is to position the flame tube further forward in the assembly, thus preventing the flame heat transfer to the air tube. However, this could have an impact on the NO production, as the forward position increases reaction time due to the elongation of the primary air/fuel reacting zone. Nevertheless, the increase is not expected to be high.

The overall primary/secondary air ratio remains unchanged and no significant alterations to the flow pattern are expected. However, the forward positioning of the flame tube leaves the component exposed in the flame region, internal to the combustion chamber, and therefore introduces the risk of overheating of the flame tube downstream end surfaces. However, the introduction of a different material for the flame tube was decided for the production components, following the company's review of the research results to date. The new flame tube is produced out of a Silicon based composite alloy, Silicon Carbide (SiC), which has much higher conductivity (approximately three times) and melting point than the Inconel based alloy used previously. The new design was considered as a feasible solution that could be utilised in the production model and therefore justified this simulation.

The new material properties were specified in CFX, using the editing libraries and the new solid domain was created using the same mesh characteristics as previously. As can be seen in Figure 2, the flame tube is positioned forward by 20 mm, compared to its current installation, and therefore protrudes 10 mm from the discharge face.

The new position is considered practical, as it does not introduce any difficulty in the secure installation of the flame tube inside the air tube. Furthermore, an increased forward positioning would result in flow disturbance around the fuel nozzle ports step, as the upstream end face of the flame tube would be located inappropriately near.

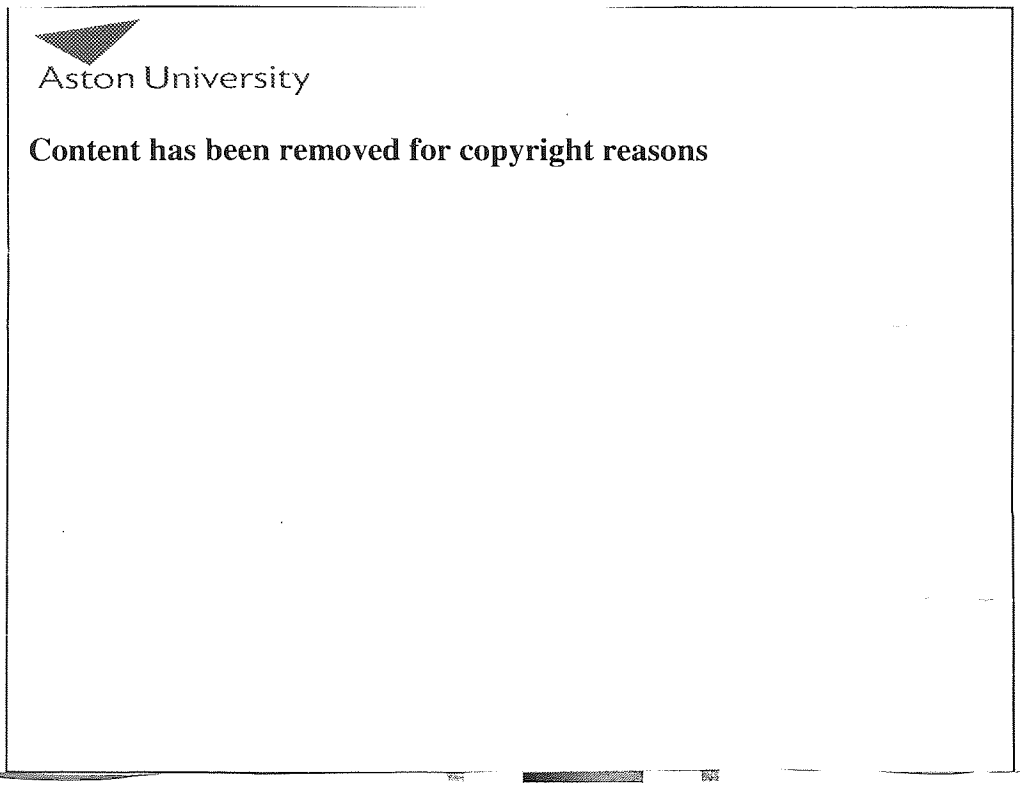

Figure 2: Forward flame tube model

7.2.3 12-hole 2 mm diameter fuel nozzle model

As has been discussed in the previous chapter, the currently used fuel nozzle has been shown to produce a good air/fuel mixture mainly due to the cross flow induced turbulence. Altering the fuel port design however, could represent a cost effective means of reducing the relatively high NO emissions levels seen earlier. It does not introduce the need for new

tooling or components to be made and can be easily incorporated into the current production burner.

After studying further possible designs, it was decided to introduce 12 equally spaced fuel ports, with a circular rather than rectangular cross section. Primarily, this is envisaged to represent a good comparison to the current design, as fuel is introduced more evenly to the primary combustion air, in an enhanced cross flow mixing pattern.

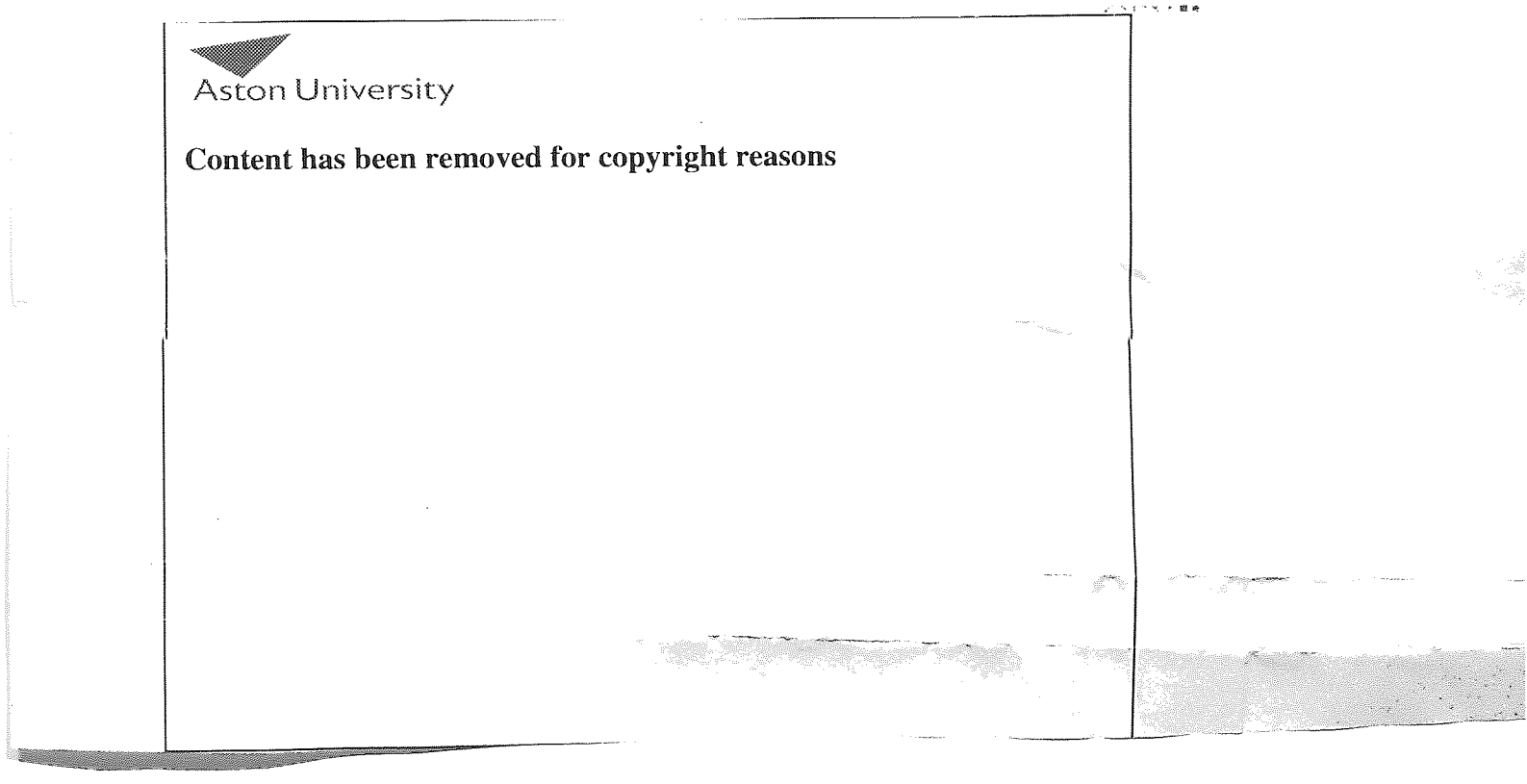

Figure 3: 12-hole 2 mm diameter fuel nozzle model

Figure 3 presents the new design; with the centreline of the fuel port position remain unchanged from the current location, for machining reasons. In addition, the overall area of the 12 ports (2 mm diameter) represents a significant reduction (approximately 3.7 times)

to the standard design, as it is desirable to study the effect of a much stronger fuel cross flow due to the expected increment in the fuel jet velocities.

Furthermore, the new design could introduce an enhanced fuel mass flow (fuel rich) in the primary zone and therefore provide an NO reduction, as it will marginally increase the secondary air fuel mass flow, due to the blockage effect of the stronger and more evenly circumferentialy distributed fuel cross flow.

7.2.4 Reduced diameter flame tube model

The area ratio between the primary/secondary flow passages defines the amount of air deliver in the primary combustion zone. As was analysed in Chapter 5, the current design of WRTB has a primary/secondary area ratio of 1.49:1 and increasing this would have a detrimental effect on the stoichiometry of the combustion flame. The primary combustion zone would become fuel rich and therefore may produce less NO.

However, it may also result in significant disturbance to the fuel cross flow as the proximity of the flame tube will introduce a wall pressure boundary. Nevertheless it was considered as an attractive design modification both for studying the combusting flow behaviour and as a relatively cost effective alteration to the current WRTB.

Figure 4 presents the reduced diameter flame tube model layout, with the inner diameter decreased by 4 mm (from 40.8 mm to 36.8 mm). The flame tube wall thickness remains unchanged and therefore represents an increase of the secondary air passage by approximately 35% as the new overall primary/secondary area ratio is approximately 0.64:1 at the flame tube upstream face.

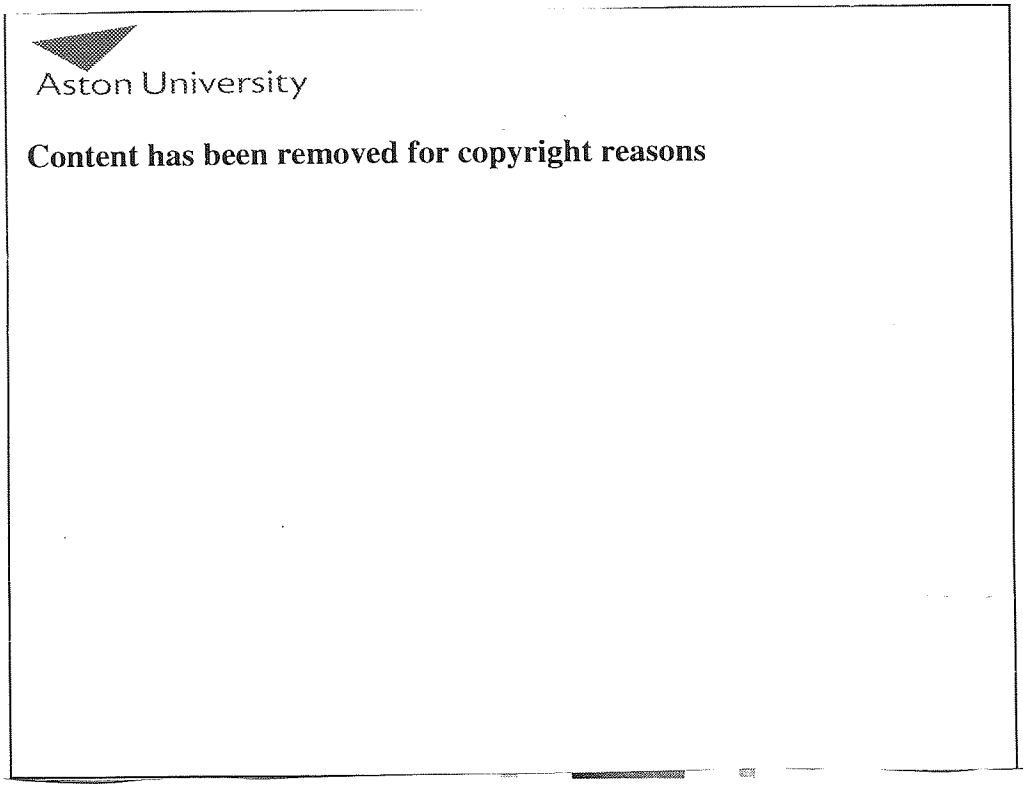

Figure 4: Reduced diameter flame tube model

7.2.5 Flue gas recirculation model

As has been analysed in the Theory chapter and has been acknowledged throughout burner combustion literature, flue gas recirculation (FGR) provides one the most effective ways for NO reduction in a combustion chamber. Near the end of the modelling development for this study, the principal of FGR was the subject of different modelling attempts.

The WRTB design however, makes the application convoluted, since the combustion jet velocity magnitudes experienced are not sufficient to achieve entrainment of the returning flue products back into the combustion chamber. This was firstly established after studying the pressure profile of the combusting flow in a model that had simply the inner tube plug omitted. This model indicated back flow from the combustion chamber and out to the returning flow path, which increased further the production of NO. Other attempts were made with partially removal of the inner tube plug material and positioning holes through

the ceramic inner tube plug as well, but with limited success. The concentrated modelling effort on the ceramic inner tube plug variants was justified by the simplicity and cost effectiveness of the application, as the aim was to avoid significant alterations to the standard burner component design. Nevertheless, this modelling stage was near the end of research programme modelling period, and useful conclusions were drawn from the supplementary development models that already existed. Therefore, it was decided to attempt a last modelling exercise, based on these conclusions, and endeavour a final NO reduction model.

A representative picture of this model is presented in Figure 5, and it shows clearly the steps taken to aid entrainment of the returning flue gas flow into the combustion chamber. As mentioned previously, this model accumulates some improvements in the design, already seen in previous models that will be analysed henceforth in this chapter. The first step taken was to include a 12 hole, 2 mm diameter fuel nozzle, as presented in section 7.2.3. It will be shown later in the chapter that this fuel nozzle produced a stronger axial component of the combustion flow and therefore represented an attractive alternative to the standard design in this application.

In addition, the flame tube design described in the section 7.2.2 is also used here, with forward positioning of the flame tube by 20 mm. As it will be shown in the figures to follow, this model enhanced the combusting flow symmetry at the discharge face and therefore, for the purpose of this modelling exercise, it was preferred to the standard WRTB flame tube position.

Furthermore, two final alterations to standard WRTB design were made that evolved from the conclusions drawn from previous FGR modelling attempts. The first is the shortening of the inner tube by 60 mm, which produced a gap of 10 mm between the upstream end of the inner tube and the discharge face, and aimed in the improvement of the recirculation flow. The second was the modification of the cross section of the ceramic inner tube plug, as clearly shown in Figure 5, but the standard design dimensional aspect ratio was retained. The model aimed at the entrainment of the returning flue gas into the combustion chamber.

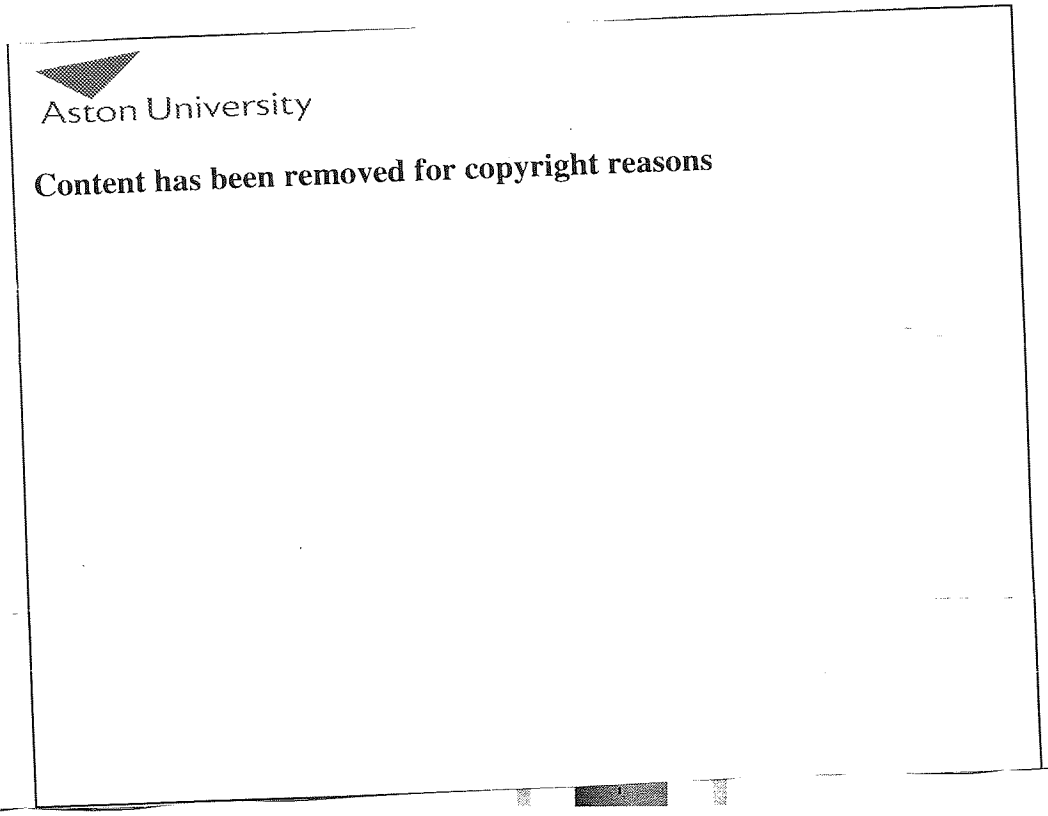

Figure 5: Flue gas recirculation model

7.2.6 Zero bypass swirler coil model

Finally, as the recuperation section overall heat transfer characteristics can be improved with the modification of the swirler coil ring and the omitting of the coil gap (as discussed in Chapters 5 and 6) a combustion prediction was made using the same model as before. However, this model does not incorporate the return path of the flow as there were meshing difficulties in modelling the coil ring as a separate solid domain, in contact between the burner inner wall and the air tube, and also outside the time scales envisaged for this study.

As there was no heat transfer modelled between the hot returning flow and the combustion air (as modelled previously) fixed temperature values were used as a wall boundary in the recuperator and the inner tube walls, to simulate the heat transfer on the swirling flow. These values are the average of the temperature profile predicted in the previous models

and they were set at 550°C and 1050°C respectively. It is clear that these boundary conditions do not represent in detail accuracy the heat transfer to the fluid and combusting flow; however it is believed that the errors introduced are relatively small. The main interest was to observe the effect of the higher swirling velocity component on the combusting flow as it reacts in the combustion chamber.

Furthermore, as the model was taken from the isothermal flow study, the inner tube has shorter length and increased diameter by 5 mm.

7.3 Discussion - Modelling results

As all the development models were set with the same fuel and air mass flow rates as in the standard WRTB model, essentially the same results were produced for the O_2 and CO mass flow averaged concentrations at the model exhaust and therefore only the NO results and exhaust flue gas temperatures are presented for each individual model. The subsequent results figures, focused on the combustion flame contours and flow velocity profiles for each model, as these would be the predictions that substantially differ in each case.

Figure 6 presents temperature contours of the combustion flame in the eccentric flame tube model. The deflection of the flame towards the upper the side of the WRTB is clear and it shows similar length to the standard burner flame.

Furthermore, there is a substantial change from the flow predicted in the standard WRTB, and it shows that if this eccentricity coincides with the flow turning angle at the discharge face, depending on the end positioning of the swirler coil ring, then the flame deflection will be enhanced further. In other words, the small asymmetry of the flame seen in the standard WRTB will be superimposed on the further deflection caused by the eccentric flame tube. This is due to the circumferential location of the swirler coil starting point during manufacturing, which is relatively arbitrary, as the constrained dimensions are only the axial location, coil pitch and coil length.

Figure 7 indicates the combusting flow impingement on the lower surface of the flame tube (which is closer by 1.25 mm to the fuel nozzle), the deflection of the flow towards the upper downstream end of the flame tube and the impingement on the upper surface of the inner tube, as the flame discharges in the combustion chamber. It also shows the higher temperature seen on the upper face of the flame and air tubes, approximately 50°C more than the lower end faces. The overall temperature profiles seen here, again, are in not in excess of the material limits used for the flame tube; however they are much closer and represent a clear indication that the long term effects are again time dependant. Any further eccentricity would most probably demonstrate a more imminent failure. It is believed that the distortion of the flame and air tubes shown in the photographs in Chapter 1 correspond to the flow patterns predicted in this model.

At this point it has to be said that in addition to the flame and air tubes distortion, a supplementary failure that has not been presented in this thesis (as it was considered the consequence of the air/flame tube failures), is an eventual damage on the inner tube. The flow deflection and impingement on the inner tube results in the wall material fatigue and eventually failure of the inner tube, which is followed by a failure of the radiant tube. The reason for the latter is the non-uniform distribution of temperature on the radiant tube, as the flame is no longer contained within the inner tube. The model shows a stronger impingement of the flame on the inner tube, with a longer recirculation zone on the opposite side, in comparison to the standard WRTB, and this represents another indication that the results closely predict the in service failure.

Finally, the model predicts 574 ppmv of NO concentration at the exhaust, which is not dissimilar to the standard WRTB model prediction of 571 ppmv, as referenced in the previous chapter. The model exhaust gas temperature prediction is identical to the standard WRTB (934°C). This highlights the fact that the observation of this eccentricity occurring in a real furnace WRTB, by measuring NO levels or exhaust temperature during maintenance inspections, is almost impossible until failure of the WRTB occurs.

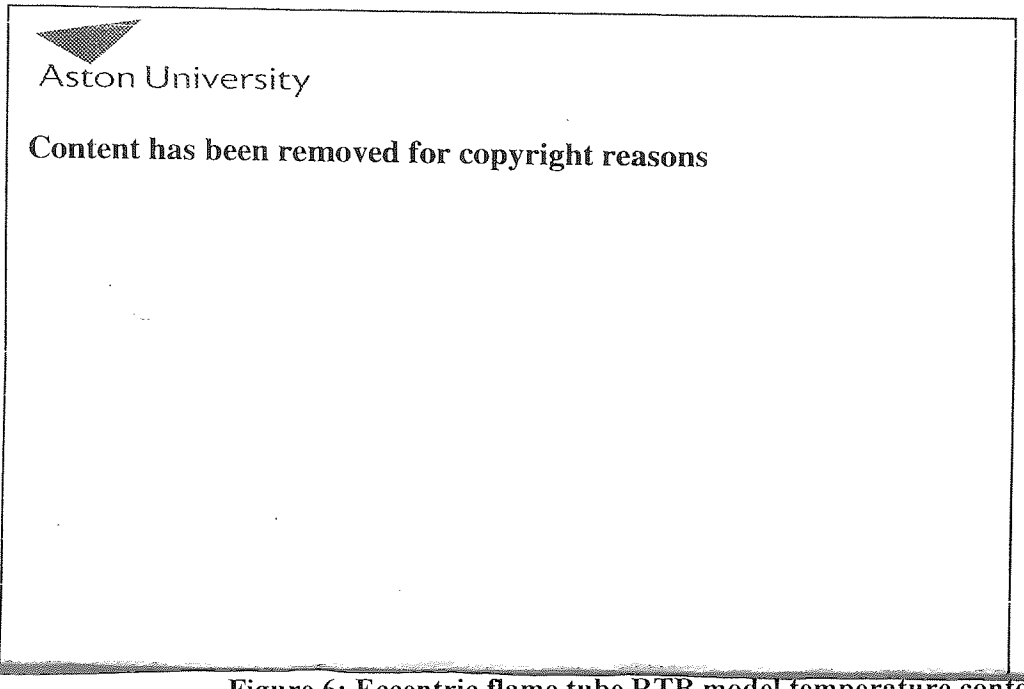

Figure 6: Eccentric flame tube RTB model temperature contours

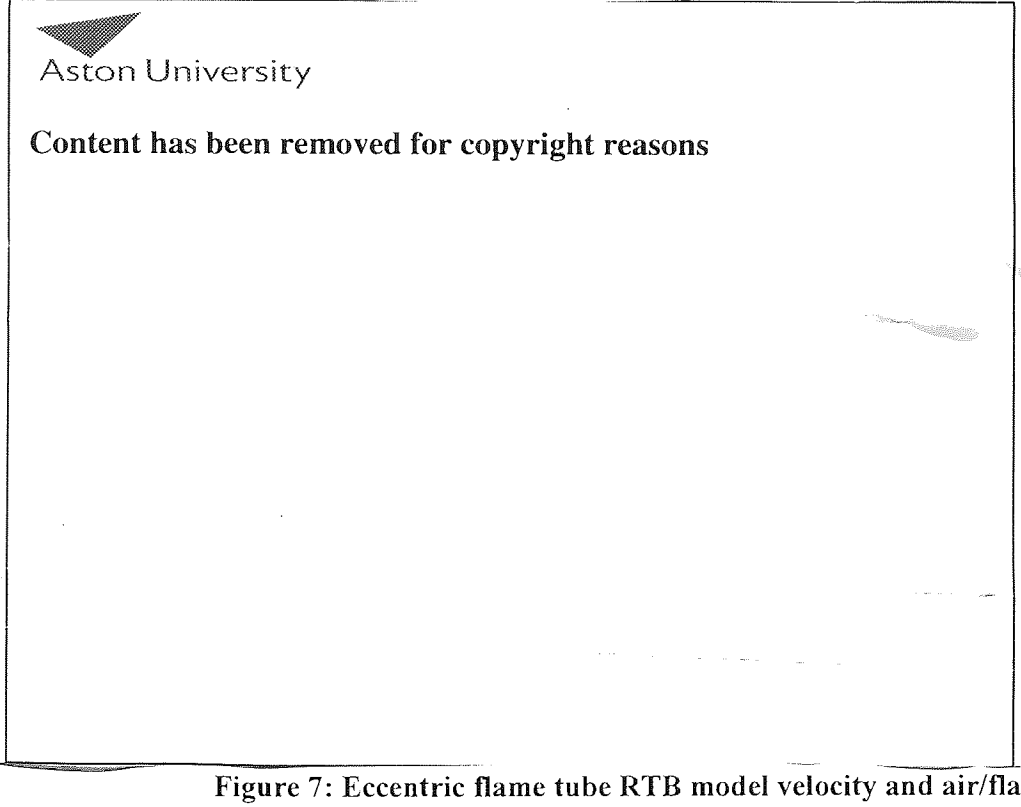

Figure 7: Eccentric flame tube RTB model velocity and air/flame tubes temperature contours

Figure 8 below, presents the temperature contours of the forward flame tube model. The flame appears wider and more symmetrical than the standard WRTB.

The solid wall temperature contours seen in Figure 9 indicate a higher flame tube temperature at the downstream end, by approximately 100°C, as expected. The SiC flame tube temperature is well within the material limits. The air tube end face shows a small decrease in surface temperature (even though is difficult to show in the current figure due to the scale used) by approximately 20°C, which is considered an improvement.

Figure 10 highlights the more symmetrical combustion flame with similar axial velocity magnitudes as the standard WRTB predictions and symmetrical recirculation zones near the discharge face. As a result of the wider flame however, the NO and exhaust gas temperature predictions, are increased by approximately 8.7% and 2.9% respectively (625 ppmv and 962°C). Nevertheless, the model is highlighting an improved flame shape, and wall temperature distribution, which is considered an enhancement to the current design.

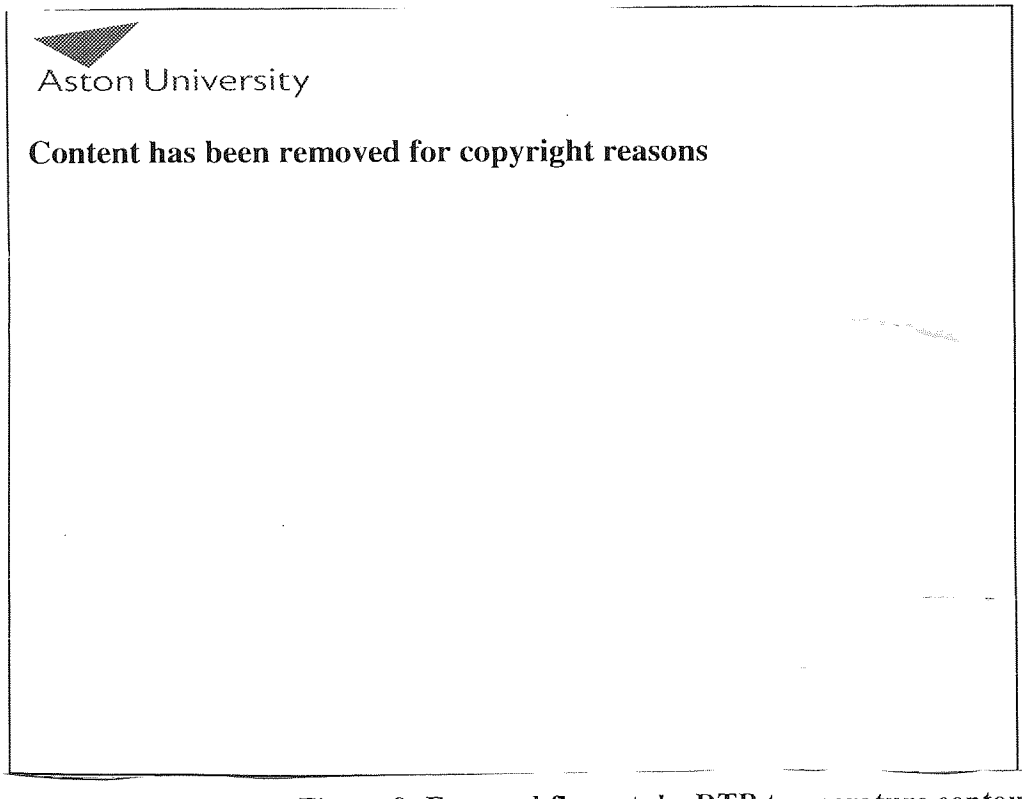

Figure 8: Forward flame tube RTB temperature contours

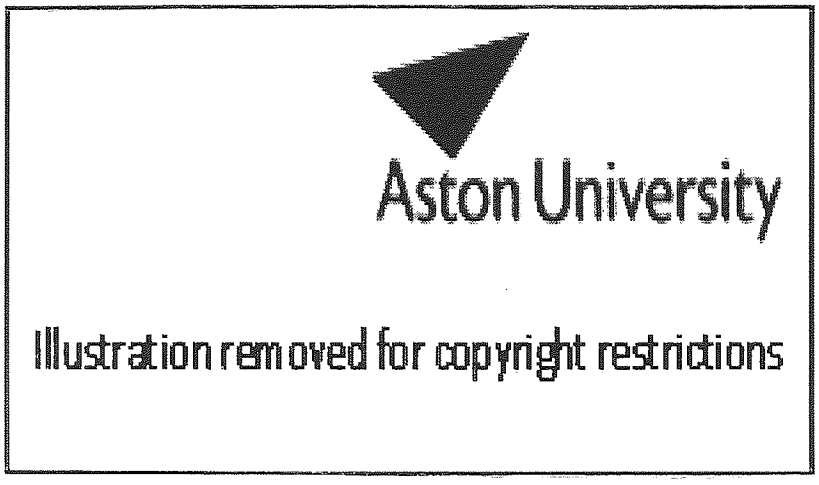

Figure 9: Forward flame tube RTB contours of temperature at the burner inner and solid walls

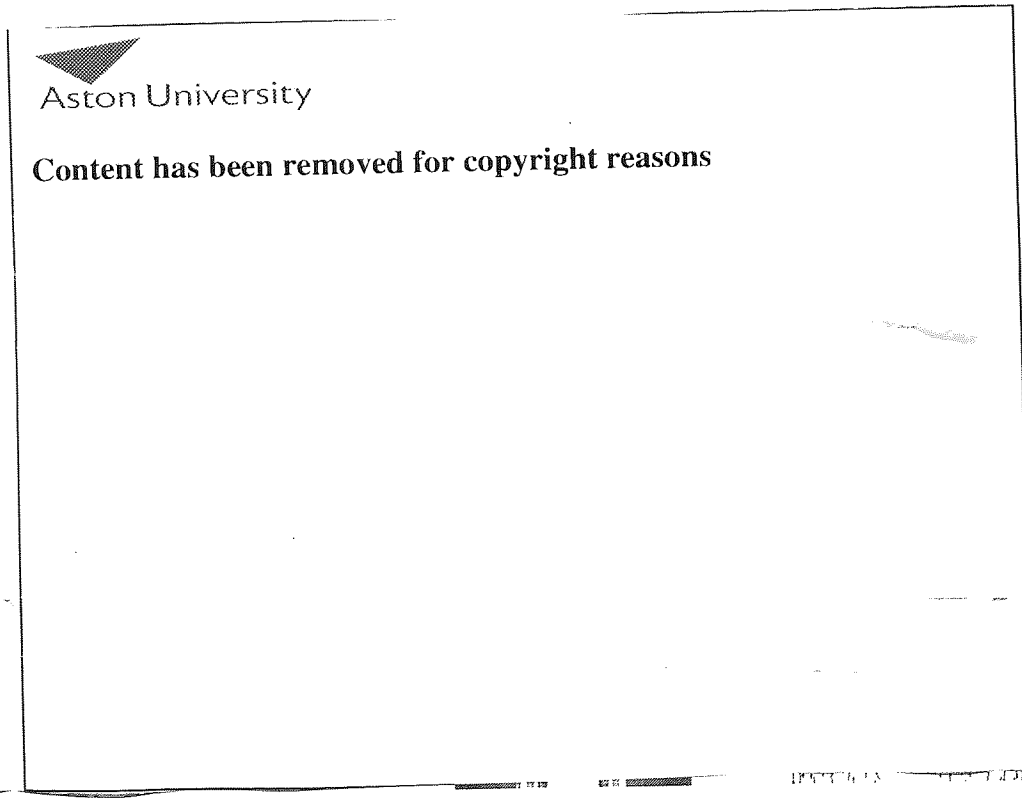

Figure 10: Forward flame tube RTB contours of v_u and velocity vectors

In Figure 11 we can see the predicted temperature contours for the 12-hole modified fuel nozzle. In this model the flame appears axisymetric, wider and approximately 10% longer than the standard WRTB model and represents, therefore, an improvement.

Figure 12 shows that, overall, the flame tube wall temperatures remain in approximately the same levels as in the standard WRTB, with a small increase in the distribution at the downstream end. However, the air tube shows an increase of approximately 50°C at the discharge end face. This indicates that the flame reaction zone is closer to the air tube end surface, mainly due to the more intense mixing in the primary zone and consequently, more intense heat release. The predicted temperatures however, remain within the material limits. The burner inner wall temperatures also indicate similar distribution with the standard WRTB, although the distribution on the pilot tube tip appears slightly higher.

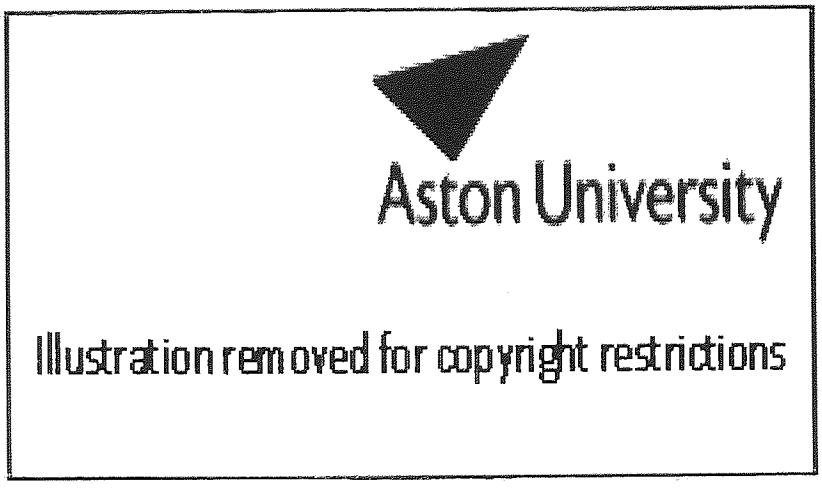

Figure 11: 12-hole 2 mm diameter fuel nozzle RTB temperature contours

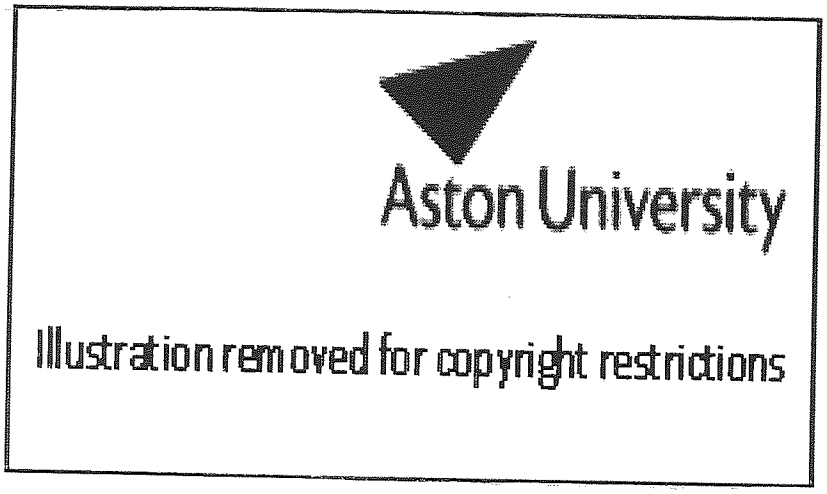

Figure 12: 12-hole 2 mm diameter fuel nozzle RTB contours of temperature at the burner inner and solid walls

Nevertheless, Figure 13 shows that overall predicted axial flow velocities are not dissimilar to the standard WRTB. The flow at the discharge face is nearly perfectly symmetrical, and the recirculation zones either side have almost identical length.

Figure 14 shows the CH_4 fuel mass fraction immediately downstream of the fuel ports and it clearly indicates the fuel flow uniformity and the nearly perfect circumferential mixing with the primary combustion air. The figure highlights the complete absence of a lobe effect in the flow, due to the high number of fuel ports, and also the limited presence of CH_4 in the near wall region, possibly due the high momentum impingement of the fuel jets on the flame tube.

The end result on the flue gas predictions, however, is not as envisaged. NO emissions are increased to 675 ppmv and the result of the longer and wider flame is the exhaust flue

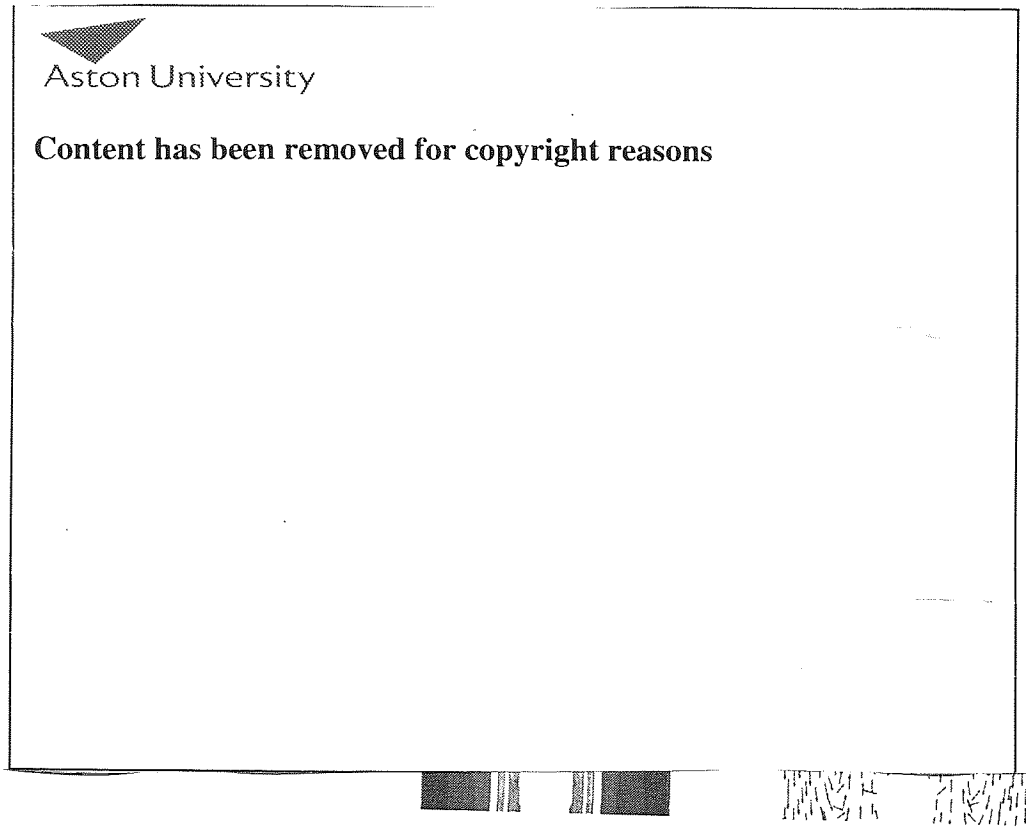

Figure 13: 12-hole 2 mm diameter fuel nozzle RTB contours of v_u and velocity vectors

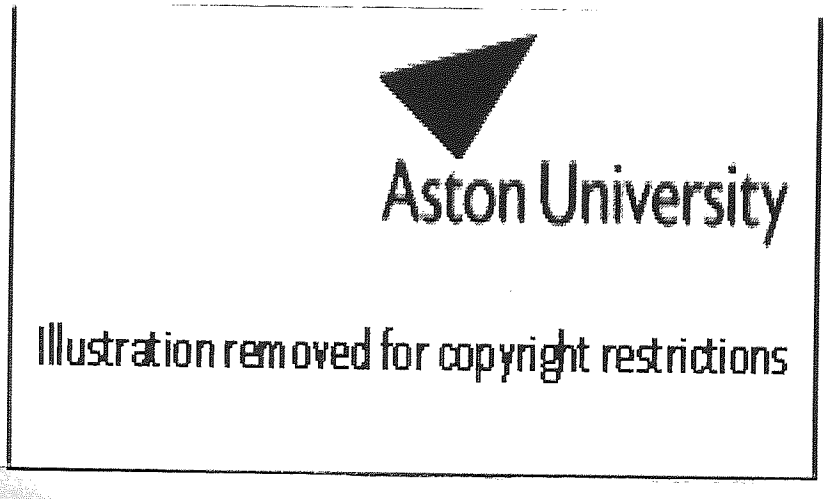

Figure 14: 12-hole 2 mm diameter fuel nozzle RTB CH_4 mass fraction contours at the fuel nozzle

gas temperature increment, by approximately 2.7% (960°C), which would have a small impact on the burner efficiency.

The overall improvements on the flow symmetry and flame length however, present this model as an attractive design modification to the standard WRTB but with a penalty in NOx emissions.

Figure 15 presents the reduced diameter flame tube model temperature predictions. Once more, the flame appears axisymetric, although much wider and longer than the standard length WRTB. It clearly shows that the flow reaction zone spans nearly two thirds of the combustion chamber length, and Figure 16 certifies this observation.

The axial velocities seen here at the discharge face are substantially lower than the standard WRTB. It can be said that the fuel flow is almost carried by the enhanced secondary air flow, downstream of the discharge face, and both flows react slowly as they progress. The main effect here is the close proximity of the flame tube walls that disturb significantly the fuel flow pattern. Clearly there is no adequate primary flow to aid mixing and reaction time is slow. This design would be better applied in a forward firing fuel nozzle where the proximity of the wall does not have the same effect.

These observations are further justified by the NO levels, predicted at the exhaust. The mass flow averaged value was approximately 697 ppmv, and this level represents the highest NO emissions predicted, in comparison to all other models. The flue gas temperature was predicted at 958°C; expected as the flame is much longer than standard length WRTB.

No further results are presented from this model as it has provided the worst NO emissions to date, nor has made any improvements to the burner efficiency. The more symmetrical flow seen here has been achieved by other models, without the penalty of the NO emissions increment.

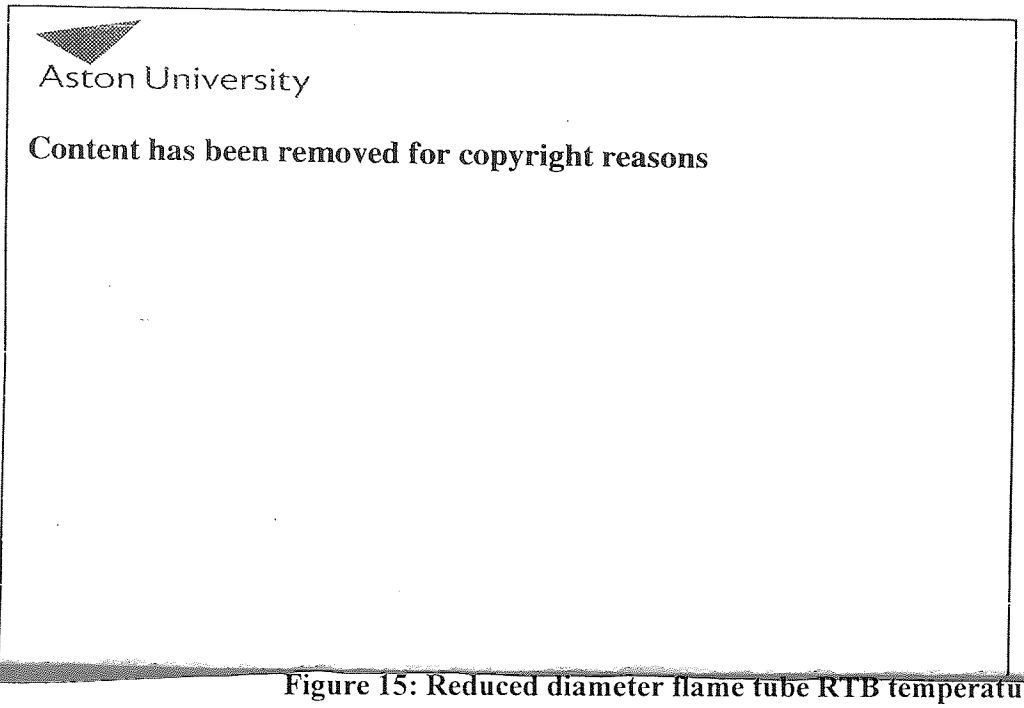

Figure 15: Reduced diameter flame tube RTB temperature contours

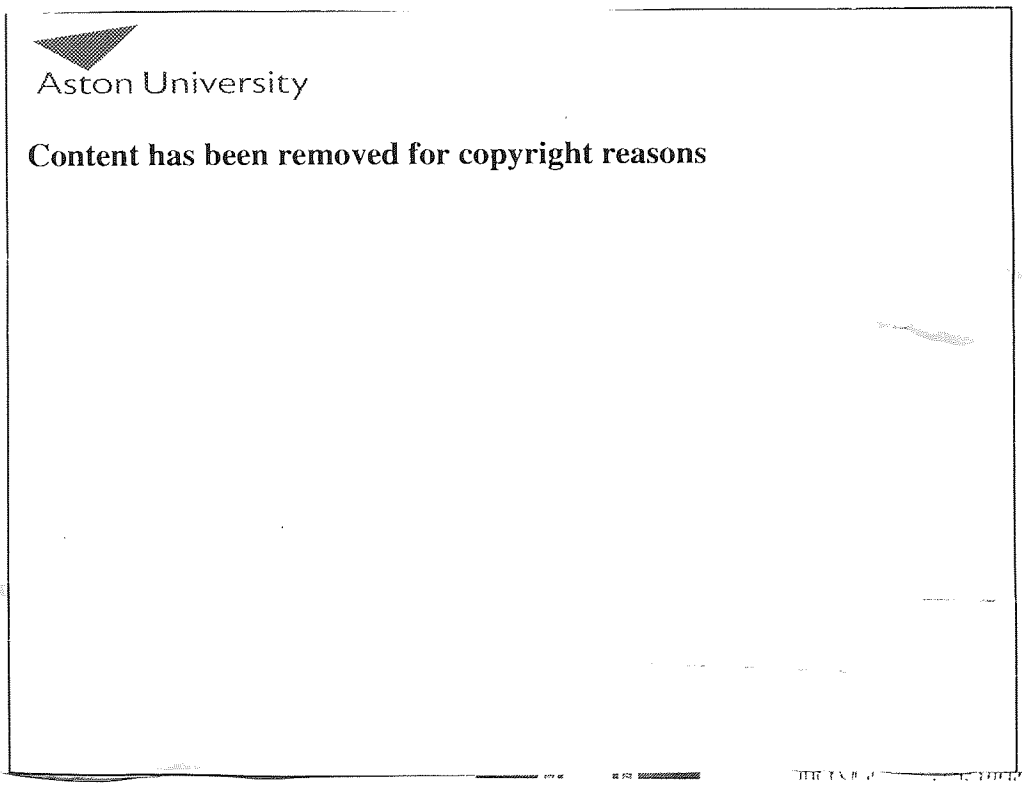

Figure 16: Reduced diameter flame tube RTB contours of v_u and velocity vectors

Figure 17 presents the FGR model temperature contours. The flame has the characteristics seen in the 12-hole fuel nozzle and the forward positioned flame tube models. The jet expands to fill the combustion chamber and the flame appears long, wide and symmetrical.

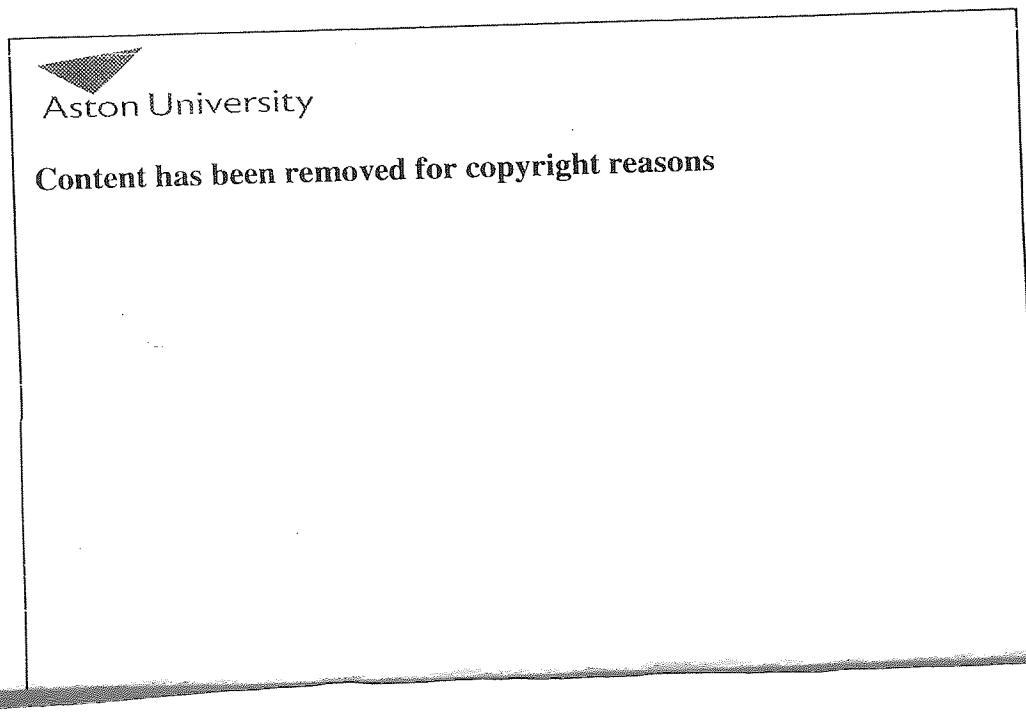

Figure 17: Flue gas recirculation RTB temperature contours

Figures 18 and 19 show the velocity profile of the combusting flow and highlight the unsuccessful attempt to re-entrain the flue gas returning flow, back into the combustion chamber. The flame near the discharge face is wider than the standard model, with the recirculation zones appearing long and narrow, and has a gentle swirl to one side.

The two recirculation zones seen here are located nearly at the opening between the inner wall and the modified ceramic plug, and although a small percentage of entrainment is achieved, the flow appears to be unable to sufficiently re-enter the combustion zone. The ventouri effect required is not fully achieved due to the lack of substantial flow momentum.

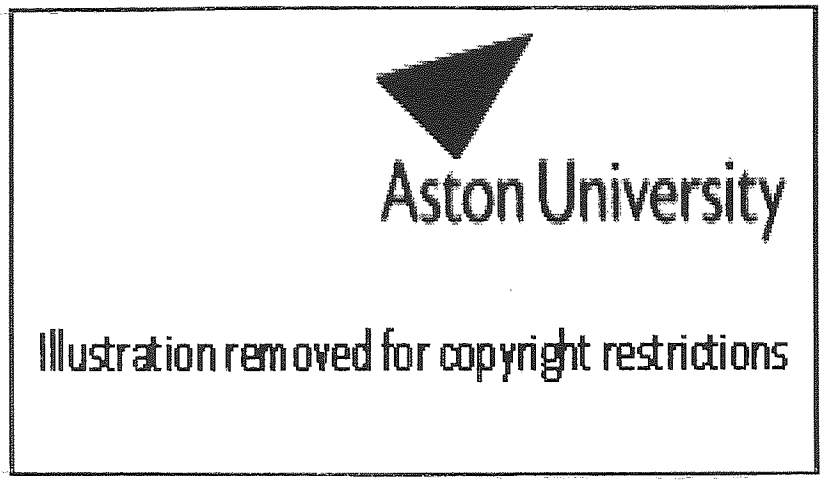

Figure 18: Flue gas recirculation RTB contours of v_u

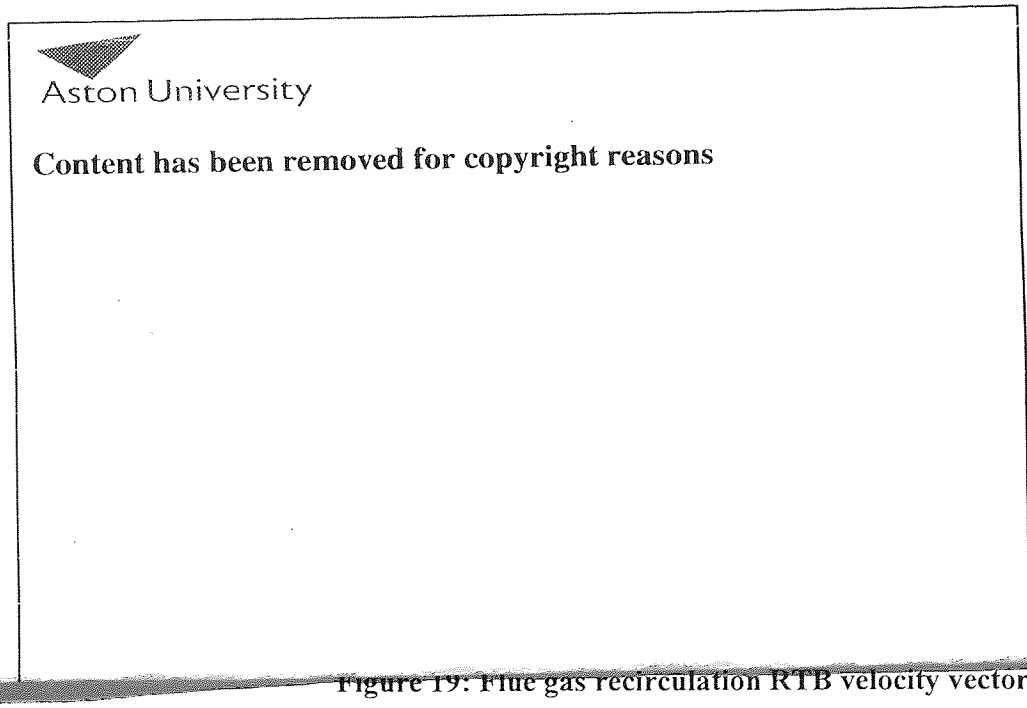

Figure 19: Flue gas recirculation RTB velocity vectors

The predicted NO of 596 ppmv certifies this, as it represents a much lower level than the 12-hole fuel nozzle prediction alone (675 ppmv) and an improvement on the forward flame tube prediction as well (626 ppmv).

However it still represents an increase of approximately 4% over the standard WRTB model (571 ppmv). The predicted flue gas temperature further certifies that there is some entrainment present, as it measures to 968°C, an increase of 34°C over the standard burner model (934°C). The forward positioned flame tube and 12-hole fuel nozzle models indicated similar increments in the flue gas temperatures, but higher NO emission levels.

The flue gas temperature increment of 34°C over the standard burner, for the FGR model, can be partially accounted by the radiative heat transfer from the flame to the returning flue gas flow in the gap between the inner tube and the ceramic plug.

Finally, figures 20 and 21 shows the zero bypass swirler coil model results. This model, as explained earlier, represents an attempt to comprehend the effect of the increased swirling flow out of the recuperator section.

An enhanced degree of swirl is apparent - the mass flow averaged swirl angle at the discharge face is approximately 28° an increase of 6° over the standard burner.

This is still however insufficient to form a central recirculation zone. The flow in this case deflects towards the inner tube, on the opposite side to the standard WRTB, highlighting the effect of the increased swirl.

The flame has lost some of each length, as expected, due to the enhanced circumferential velocity component and it appears wider at the discharge face. There is a stronger toroidal recirculation zone present on one side, compared to the standard burner model.

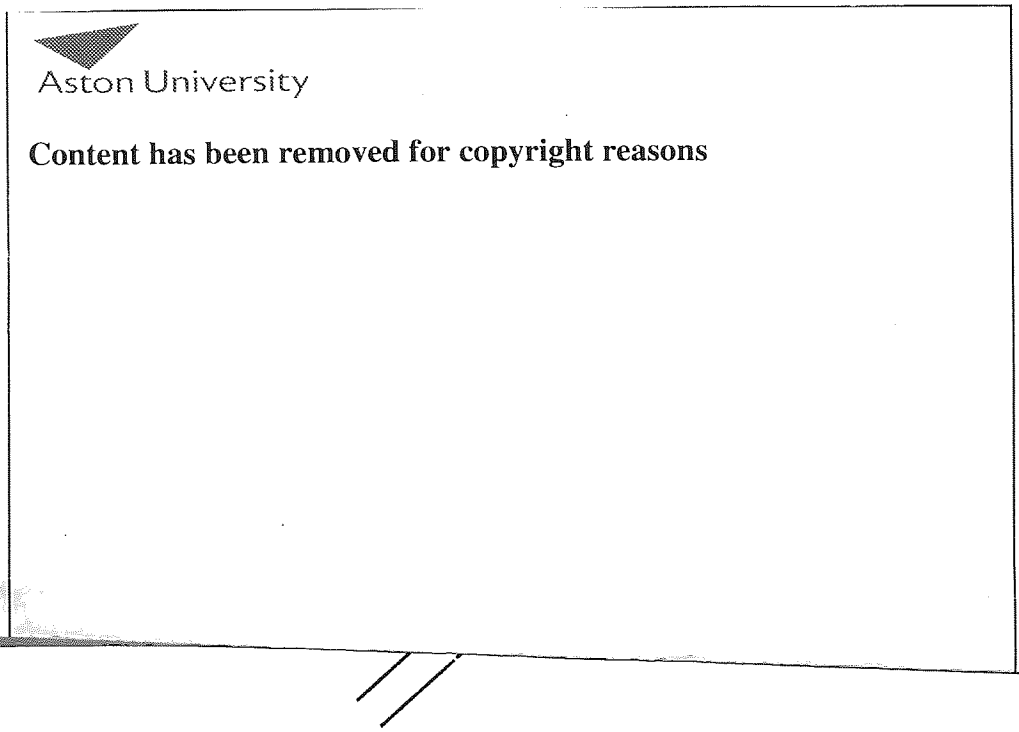

Figure 20: Zero bypass swirler coil RTB temperature contours

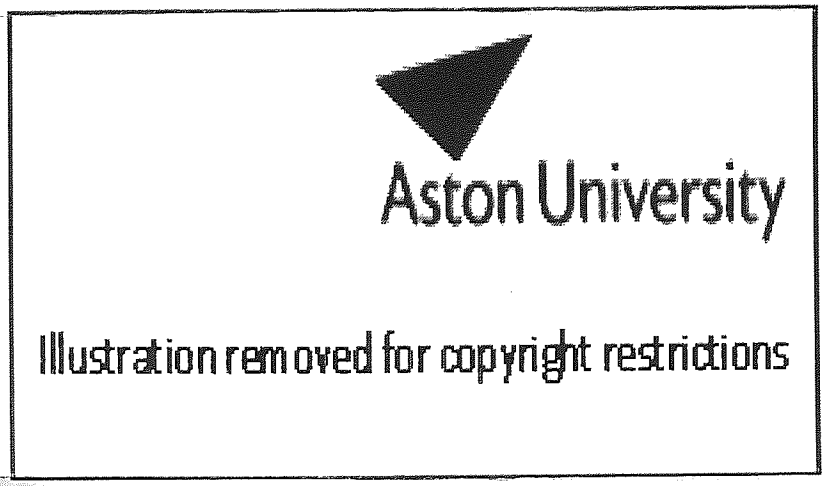

Figure 21: Zero bypass swirler coil WRTB contours of v_u and velocity vectors

The figure indicates that the flame attachment to the inner wall is stronger, which may affect the temperature uniformity on the surface. However, it is difficult to predict the end result with the current model, as there is no wall heat transfer modelled.

The modification would be to combine the zero bypass swirl coil design with another feature, such as the forward flame tube, that enhances the axial component of the combusting flow. Finally, as the model does not represent the correct length or exact features for the WRTB, flue gas emissions predictions are not reported.

8. CONCLUSIONS AND RECOMMENDATIONS

8.1 Conclusions

The study described here has conveyed benefits for both academic and industrial partners. The academic benefit (research student and academic establishment) is in the form of substantial skill enhancement of a main engineering expertise, such as CFD. The project has allowed the University to expand its research effort in the field of combustion modelling, and to publish scientific material. It has also provided the University with case study material for teaching purposes, which it can use to enhance the breadth of students learning experience. The industrial benefit is the fundamental knowledge obtained that enables the company to pursue design changes to further enhance lifetime, reliability and environmental performance.

The study has successfully generated a validated three dimensional representation of an RTB with full correlation between complex solid and fluid domains, high temperature heat transfer, radiation and combustion in a steady state chemically reactive fluid mixture. This has allowed detailed analysis of internal fluid flow/solid geometry interaction

8.1.1 Isothermal modelling

The study first focused on the combustion air flow and its delivery to the combustion zone. An isothermal computational model was developed to allow the examination of the flow characteristics as it enters the burner and progresses through the various sections prior to the discharge face in the combustion area. Important features identified include the air recuperator swirler coil, the step ring, the primary/secondary air splitting flame tube and the fuel nozzle.

Detailed experimental air flow velocity profiles were successfully obtained at two planes in the inner (combustion) tube of a truncated burner using a triple-split hot film probe.

The measured flow field revealed a strong central recirculation. A degree of circumferential maldistribution was evident which can be attributed to misalignments of the burner components on assembly. Also a mass flow discrepancy of approximately 30% of the total computational mass flow was evident which is believed to be a systematic error, possibly due to probe and pressure transducer miscalibration. Wall static pressure measurements and subsequent modelling results supported this.

Once the mass flow discrepancy was compensated for, satisfactory agreement was obtained between experimental and computed velocity profiles in the combustion chamber region when using the k-ε turbulence model.

Reasonable mesh independence was obtained with 220,000 nodes. Agreement was poorer with the RNG k-ε and Reynolds Stress models.

The presence of an air gap at the outer radius of the recuperator swirler has reduced the amount of swirl imparted to 41° compared with a swirler helix angle of 63°. This was estimated to result in a reduction in local film heat transfer coefficient of about one-third.

The step ring feature in the air flow passage downstream of the recuperator is relatively ineffective in removing swirl from the flow; a local drop is largely recovered downstream. However the ring is very effective in correcting circumferential flow maldistribution, to the extent that this is almost absent by the time the fuel inlet region is reached despite being significant at the swirler exit.

The partition between primary and secondary air flow which takes place at the flame tube is strongly influenced by the substantial step that the primary flow has to negotiate, to the extent that a simple calculation of flow passage area is not a good guide to ultimate flow split. Considering the secondary (outer) passage, an initial small increase in swirl angle caused by the expansion just upstream of the flame tube is seen, and then a reduction along the flame tube to an exit value of about 22°.

In the primary passage, swirl angle first rises sharply to 50° due to the large expansion and loss of axial momentum. Introduction of both the fuel air and the pilot air then add complexity to the flow, but by the exit of the flame tube the swirl angle has reduced to 45°. Once the flows recombine downstream of the discharge face, the mean swirl angle is 33°. The jet flow discharge velocity is approximately 11 m/s.

8.1.2 Combustion modelling

The study continued to address the combustion and heat transfer processes internal to the WRTB. A series of model geometries were developed based on the isothermal model but with additional features added to represent the complete burner. The previously validated k-ε turbulence model was used and reasonable mesh independence was obtained with 300,000 nodes.

Experimental combustion tests of the full burner were successfully carried out, with temperature data obtained at a range of locations within the burner and also gas analysis data at the burner exit.

Satisfactory experimental test result validation was ultimately obtained by computations using the ED combustion model and the DT radiation model. The TFC combustion model showed mass balance inaccuracies and the MC method radiation model indicated convergence problems with residual oscillatory solution.

The ED/DT combination showed good agreement with temperature measurements in the inner and outer walls of the burner, as well as with flue gas composition measured at the exhaust, although there was some over prediction of wall temperature in the downstream half of the inner tube. Agreement on NOx emissions was within 7%. These were initially over predicted, however, the use of a combustion flame temperature limiting subroutine allowed convergence to the experimental value of 451 ppmv.

A final gas temperature of approximately 695°C was measured in the exhaust off-take. This defines an overall thermal efficiency of about 65%. Exhaust flue temperature is calculated at 875°C, which is approximately 25 % higher than the experimental value. It is believed that the errors here may be due to coarse assumptions in the radiation model, such as a grey gas throughout with a single absorption coefficient, and also a constant emissivity along the inner and outer tube walls. Furthermore, the ED model combined with the k-ε turbulence model has a tendency to over predict flame temperature. However the successful reproduction of the experimental wall temperatures in the recuperator region suggests that errors in the returning gas temperature are unlikely to be large and it may be that the exhaust gas thermocouple was reading inaccurately or that the simplified model geometry at the burner exit introduced errors.

With the validated model, the effectiveness of certain WRTB features identified previously was analysed, and an analysis of the energy transfers throughout the burner was presented to identify the dominant mechanisms in each region.

At the recuperator section 1.68kW of heat is transferred, with mean film coefficients (ignoring wall conduction) of 63 $W/m^2{}^oC$ for the exhaust gas and 52 $W/m^2{}^oC$ for the air. The mean overall coefficient is 28 $W/m^2{}^oC$. The modelling results indicate that if the swirler coil gap was to be omitted this would lead to an additional 300W of recuperation, or a fuel saving of about 1.2%.

The section of the burner from the recuperator to the inlet of the flame tube also achieves a degree of recuperation. 0.84kW of heat is transferred, with mean film coefficients (ignoring wall conduction) of 30 $W/m^2{}^oC$ for the exhaust gas and 34 $W/m^2{}^oC$ for the air. The mean overall coefficient is 16 $W/m^2{}^oC$.

The section of the burner extending into the furnace delivers about 12 kW to the furnace. The mean heat flux along the radiant tube is 22.6 kW/m^2, and the uniformity of the measured temperatures indicate that local heat flux values will be very close to this mean.

Despite the mean gas temperature within the inner tube reaching a maximum of about 1850°C some 150mm downstream of the discharge face and falling to 1440°C at the inner tube exit, the inner tube wall remains within the range 1010-1065°C all along due to the thermally balancing effect of the returning gas flow in the surrounding annulus, which falls from 1390°C at inlet to 1120°C at exit.

That the inner tube is at a significantly lower temperature than the gases either side of it indicates the major part played by radiation in the radial exchange. The radial flux to the radiant tube is composed of convective heat exchange from the returning gases, radiant emission from those gases, and unabsorbed net radiant emission from the inner tube wall.

Mixing in the fuel injection zone is highly effective with just four fuel ports. The recuperator section is also effective, but performance could be improved with attention to the swirler design. The overall design is vulnerable to eccentricities of the various components due to manufacturing or assembly tolerances.

The flame is revealed to be long and narrow with a slight asymmetry. The mean flow temperature falls by approximately 500°C along the length of the inner tube. The highest flame temperatures are between 150 and 500 mm from the discharge face. The heat release initiates in the recirculation zone downstream of the fuel ports and adjacent to the pilot nozzle, and it is reasonable to interpret this as a flame attachment point. The tip of the pilot burner is reaching more than 1000°C and the air and flame tubes reaching between 950 and 1000°C respectively. The inner wall ceramic plug prevents heat transfer between the two metal walls due to its low thermal conductivity.

In comparison to the isothermal study the flow has gained substantial forward momentum, due to the energy release from the chemical reaction, and it achieves approximately 30 m/s at the discharge face. A toroidal recirculation zone is present outside the main flame jet, formed by the sudden expansion, but this only extends about one inner tube diameter downstream. Beyond this, the jet expands to fill the tube. A modest degree of swirl is still

present - the mass flow averaged swirl angle at the discharge face is approximately 22°. This is however insufficient to form a central recirculation zone.

8.1.3 Burner design mitigations

The eccentric flame tube model predicts impingement of the combusting flow on the lower surface of the flame tube, deflection of the flow towards the upper downstream end of the flame tube and impingement on the upper surface of the inner tube, as the flame discharges in the combustion chamber. The temperature seen on the upper face of the flame and air tubes is approximately 50°C more than the lower end faces. The overall temperature profiles seen are not in excess of the material limits used for the flame tube; however they are much closer than the ones seen in the standard WRTB model and may over time contribute to the distortion of the flame and air tubes seen in service. Any further eccentricity would result in a more imminent burner failure. NO concentration and gas temperature at the exhaust are unaffected.

In the forward flame tube model the flame appears wider and more symmetrical than the standard WRTB. A higher flame tube temperature is seen at the downstream end, by approximately 100°C. The flame tube temperature is well within the material limits. The air tube end face shows a small decrease in surface temperature by approximately 20°C, which is considered an improvement. Exhaust gas NO and temperature are increased by approximately 8.7% and 2.9% respectively (625 ppmv and 962°C).

In the 12-hole modified fuel nozzle the flame appears axisymetric, wider and approximately 10% longer than the standard WRTB model and represents, therefore, an improvement in this area. Overall, the flame tube wall temperatures remain approximately unchanged, with a small increase in the distribution at the downstream end. However, the air tube shows an increase of approximately 50°C at the discharge end face. This indicates that the flame reaction zone is closer to the air tube end surface. The predicted temperatures however, remain within the material limits. The burner inner wall temperatures also indicate similar distribution with the standard WRTB, although the distribution on the pilot tube tip appears

slightly larger. The CH_4 fuel mass fraction immediately downstream of the fuel ports indicates the fuel flow uniformity and the nearly perfect circumferential mixing with the primary combustion air. There is a complete absence of a lobe effect in the flow, due to the high number of fuel ports. However, NOx emissions are increased to 675 ppmv, from 451 ppmv, and the flue gas temperature increment is approximately 2.7% (960°C).

In the reduced diameter flame tube model the flame appears axisymetric, although much wider and longer than the standard length WRTB. The flow reaction zone spans nearly two thirds of the combustion chamber length. The axial velocities seen here at the discharge face are substantially lower than the standard WRTB. There is no adequate primary flow to aid mixing and reaction time is slow. This design would be better applied in a forward firing fuel nozzle. The mass flow averaged value of NO at the exhaust was approximately 697 ppmv, and this level presents the highest NO emissions predicted, in comparison to all other models. The flue gas temperature was predicted at 958°C.

In the FGR model the flame has the characteristics seen in the 12-hole fuel nozzle and the forward positioned flame tube models. The velocity profile of the combusting flow highlights the unsuccessful attempt to re-entrain the flue gas returning flow, back into the combustion chamber. Although a small percentage of entrainment is achieved, the flow appears to be unable to sufficiently re-enter the combustion zone. The venturi effect required is not fully achieved due to the lack of substantial flow momentum. The flame near the discharge face is wider than the standard WRTB model, with the recirculation zones appearing long and narrow, and has a gentle swirl to one side. The predicted NO of 596 ppmv represents a much lower level than the 12-hole fuel nozzle prediction alone and an improvement on the forward flame tube prediction. However it represents an increase of approximately 4% over the standard WRTB model. The predicted flue gas temperature of 968°C further certifies that there is some entrainment present, being an increase of 34°C over the standard burner model. The forward positioned flame tube and 12-hole fuel nozzle models indicated similar increments in the flue gas temperatures, but higher NO emission levels.

Finally, in the zero bypass swirler coil model an enhanced degree of swirl is apparent - the mass flow averaged swirl angle at the discharge face is approximately 28° an increase of 6° over the standard burner. This is still however insufficient to form a central recirculation zone. The flow in this case deflects towards the inner tube, on the opposite side to the standard WRTB, highlighting the effect of the increased swirl. The flame has lost some of each length and there is a stronger toroidal recirculation zone present on one side, compared to the standard burner model. The figure indicates that the flame attachment to the inner wall is stronger, which may affect the temperature uniformity on the surface. The mitigation would be to combine the zero bypass swirl coil design with another feature, such as the forward flame tube, that enhances the axial component of the combusting flow.

No modifications tested showed significant improvements in NO emission over the standard WRTB, and it may be concluded that the current WRTB design does not provide any room for substantial improvements in the reduction of NO emissions without major alterations in the geometry.

8.2 Recommendations for further work

Further CFD modelling should be carried out to develop an FGR variant of the WRTB. The inner burner tube should be redesigned to provide an easier entrainment path to the returning flow, with the tube walls converging towards the air tube, as seen in other FGR burner designs. The returning flow would follow the wall curvature and the recirculation zones, now contained within the inner tube, would create the necessary adverse pressure to achieve further entrainment. In addition, the ceramic plug could also provide more aid to the entrainment of the returning flow, with possibly a wedged section on the outer side, similar to the one used on the air tube (inner) side.

Further modelling is recommended to support a substantial redesign of the fuel nozzle and the introduction of fuel staging, as been applied in other burner designs referenced in the previous chapters. A supplementary gas fuel annulus would have to be incorporated in the burner design, with the outlet possibly located in a forward firing layout. This would

augment the fuel rich zone necessary for the production of low NO in the first stages of the combustion process, prior to mixing with the diluting secondary air flow. Additionally, the new fuel nozzle forward firing section would inherently enhance the axial component of the primary combusting flow, thus increasing the forward momentum of the jet, and consequently increasing the strength of the recirculation zones in the entrainment region. In an FGR design this would result in the increase of the venturi effect required to re-entrain the returning flue gas flow.

In addition, as some phenomena in the burner flow are time dependent, a more thorough modelling strategy is recommended in order to improve further agreement between model and experimental measurements.

These modelling recommendations are in areas such as the TFC combustion model and the correction of its errors. A more detail radiation modelling representation is recommended, as it would provide a more accurate prediction of the heat transfer in the fluid domain, as well as a transient analysis should be carried out to demonstrate the time independence of the solution, and to clarify any affiliation between the over-predicted flue gas temperatures of the combustion models.
A closer representation of the burner exit and burner combustion air inlet in the computational model is also recommended.

Finally, as the WRTB has a "turn down" control function during operation and once the desired furnace temperature has been reached, during re-start it is intrinsically difficult to accurately control the air and fuel flow rates (and therefore the WRTB equivalence ratio). The study has focused on one operating load condition, which predefines the air and fuel mass flow rates for the main burner. However it would be desirable for further modelling to study the effect of alterations to the equivalence ratio and its effect on the exhaust gas composition and thermal output of the WRTB.

APPENDIX

Appendix - A: Journal Publications

N. Tsioumanis, J.G. Brammer, and J. Hubert,
"Flow processes in a radiant tube burner: Isothermal flow",
Journal of Fuel, Volume 87, pp 103–111, ScienceDirect, Elsevier, 2008.
ISSN: 0016-2361

N. Tsioumanis, J.G. Brammer, and J. Hubert,
"Flow processes in a radiant tube burner: Combusting flow", article pending,
Journal of Fuel, ScienceDirect, Elsevier, 2008.

Appendix - B: User Variables and Subroutines

CFX Post Swirl angle variable

Due to the absence of the variable swirl angle from the CFX variable list a user defined swirl angle variable was created. A new user variable for tangential velocity v_t was created in CFX Post to use for the calculation of the air flow swirl angle. This is calculated as:

$$v_t = \frac{vx}{\sqrt{x^2+y^2}} - \frac{uy}{\sqrt{x^2+y^2}}$$

It is then possible to calculate the swirl angle at any point by:

$$\text{Swirl angle} = \text{atan}\left(\frac{v_t}{w}\right)$$

CFX Solver Temperature limiting subroutine

```
LIBRARY:
  VARIABLE: T
    Option = Definition
    Component Lower Bounds = 273
    Component Upper Bounds = 2223
  END
END
FLOW:
  SOLVER CONTROL:
    COMPRESSIBILITY CONTROL:
      Decreasing Temperature Relaxation = No
    END
  END
END
```

Converting between Cartesian and Cylindrical representations of points

The formulas below convert from Cartesian (x, y, z) coordinates to cylindrical polar r, ϕ and z coordinates and back again

$$x = r\cos\phi \qquad r = \sqrt{x^2+y^2}$$
$$y = r\sin\phi \qquad \phi = \tan^{-1} y/x$$
$$z = z \qquad z = z$$

Appendix - C: WRTB CFX Solver Input Files

The files listed here are the Solver input definition text files, as created by CFX Pre. These files list all the boundary conditions, fluid and solid domain set-up, libraries and subroutines selected and created for each run. Only the validated model definition files are presented.

Isothermal flow

```
This run of the CFX-5.7.1 Solver started at 17:3:52 on 29 Sep 2005 by
user Nick on NICKASTONUNI (intel_pentium_winnt5.1) using the command:

 "C:\Program Files\Ansys Inc\CFX\CFX-5.7.1\bin\perllib\cfx5solve.pl"
  -stdout-comms -batch -ccl -

Installed patches:

 * CFX-5.7.1 Service Pack 1 build 200501312320

Setting up CFX-5 Solver run ...


+--------------------------------------------------------------+
|                                                              |
|              CFX Command Language for Run                    |
|                                                              |
+--------------------------------------------------------------+

LIBRARY:
 MATERIAL: Air Ideal Gas
  Material Description = Air Ideal Gas (constant Cp)
  Material Group = Air Data, Calorically Perfect Ideal Gases
  Option = Pure Substance
  Thermodynamic State = Gas
  PROPERTIES:
   Option = General Material
   DYNAMIC VISCOSITY:
    Dynamic Viscosity = 1.831E-05 [kg m^-1 s^-1]
    Option = Value
   END
   REFRACTIVE INDEX:
    Option = Value
    Refractive Index = 1.0 [m m^-1]
   END
   SCATTERING COEFFICIENT:
    Option = Value
```

```
      Scattering Coefficient = 0.0 [m^-1]
     END
     ABSORPTION COEFFICIENT:
      Absorption Coefficient = 0.01 [m^-1]
      Option = Value
     END
     THERMAL CONDUCTIVITY:
      Option = Value
      Thermal Conductivity = 2.61E-2 [W m^-1 K^-1]
     END
     EQUATION OF STATE:
      Molar Mass = 28.96 [kg kmol^-1]
      Option = Ideal Gas
     END
     SPECIFIC HEAT CAPACITY:
      Option = Value
      Reference Pressure = 1 [atm]
      Reference Specific Enthalpy = 0. [J/kg]
      Reference Specific Entropy = 0. [J/kg/K]
      Reference Temperature = 25 [C]
      Specific Heat Capacity = 1.0044E+03 [J kg^-1 K^-1]
      Specific Heat Type = Constant Pressure
     END
    END
   END
  END
  EXECUTION CONTROL:
   PARALLEL HOST LIBRARY:
    HOST DEFINITION: nickastonuni
     Installation Root = C:\Program Files\Ansys Inc\CFX\CFX-5.7.1
     Host Architecture String = intel_pentium_winnt5.1
    END
   END
   PARTITIONER STEP CONTROL:
    Multidomain Option = Independent Partitioning
    Runtime Priority = Standard
    MEMORY CONTROL:
     Memory Allocation Factor = 1.0
    END
    PARTITIONING TYPE:
     MeTiS Type = k-way
     Option = MeTiS
     Partition Size Rule = Automatic
    END
   END
   RUN DEFINITION:
```

```
    Definition File = G:/nickswork/def files/Isothvalidmodel/isothvalidsimp\
lemodel220KmeshB23kepsOutlet.def
    Interpolate Initial Values = Off
    Run Mode = Full
  END
  SOLVER STEP CONTROL:
    Runtime Priority = Standard
    EXECUTABLE SELECTION:
      Double Precision = Off
    END
    MEMORY CONTROL:
      Memory Allocation Factor = 1.0
    END
    PARALLEL ENVIRONMENT:
      Number of Processes = 1
      Start Method = Serial
    END
  END
END
FLOW:
  SOLUTION UNITS:
    Angle Units = [rad]
    Length Units = [m]
    Mass Units = [kg]
    Solid Angle Units = [sr]
    Temperature Units = [K]
    Time Units = [s]
  END
  SIMULATION TYPE:
    Option = Steady State
  END
  DOMAIN: fluid domain
    Coord Frame = Coord 0
    Domain Type = Fluid
    Fluids List = Air Ideal Gas
    Location = Assembly
    DOMAIN MODELS:
      BUOYANCY MODEL:
        Option = Non Buoyant
      END
      DOMAIN MOTION:
        Option = Stationary
      END
      REFERENCE PRESSURE:
        Reference Pressure = 1 [atm]
      END
```

```
END
FLUID MODELS:
  COMBUSTION MODEL:
    Option = None
  END
  HEAT TRANSFER MODEL:
    Fluid Temperature = 300 [K]
    Option = Isothermal
  END
  THERMAL RADIATION MODEL:
    Option = None
  END
  TURBULENCE MODEL:
    Option = k epsilon
  END
  TURBULENT WALL FUNCTIONS:
    Option = Scalable
  END
END
INITIALISATION:
  Option = Automatic
  INITIAL CONDITIONS:
    Velocity Type = Cartesian
    CARTESIAN VELOCITY COMPONENTS:
      Option = Automatic
    END
    EPSILON:
      Option = Automatic
    END
    K:
      Option = Automatic
    END
    STATIC PRESSURE:
      Option = Automatic
    END
  END
END
BOUNDARY: air inlet
  Boundary Type = INLET
  Location = AIR INLET
  BOUNDARY CONDITIONS:
    FLOW DIRECTION:
      Option = Normal to Boundary Condition
    END
    FLOW REGIME:
      Option = Subsonic
```

```
    END
    MASS AND MOMENTUM:
     Mass Flow Rate = 0.007876 [kg s^-1]
     Option = Mass Flow Rate
    END
    TURBULENCE:
     Option = Medium Intensity and Eddy Viscosity Ratio
    END
   END
  END
  BOUNDARY: pilot
   Boundary Type = INLET
   Location = PILOT
   BOUNDARY CONDITIONS:
    FLOW DIRECTION:
     Option = Normal to Boundary Condition
    END
    FLOW REGIME:
     Option = Subsonic
    END
    MASS AND MOMENTUM:
     Mass Flow Rate = 0.0003626 [kg s^-1]
     Option = Mass Flow Rate
    END
    TURBULENCE:
     Option = Medium Intensity and Eddy Viscosity Ratio
    END
   END
  END
  BOUNDARY: fuel
   Boundary Type = INLET
   Location = FUEL
   BOUNDARY CONDITIONS:
    FLOW DIRECTION:
     Option = Normal to Boundary Condition
    END
    FLOW REGIME:
     Option = Subsonic
    END
    MASS AND MOMENTUM:
     Mass Flow Rate = 0.0006749 [kg s^-1]
     Option = Mass Flow Rate
    END
    TURBULENCE:
     Option = Medium Intensity and Eddy Viscosity Ratio
    END
```

```
    END
  END
  BOUNDARY: fluid domain Default
    Boundary Type = WALL
    Location = WALLS A,WALLS B,WALLS C,WALLS D
    BOUNDARY CONDITIONS:
      WALL INFLUENCE ON FLOW:
        Option = No Slip
      END
      WALL ROUGHNESS:
        Option = Smooth Wall
      END
    END
  END
  BOUNDARY: exhaust
    Boundary Type = OUTLET
    Location = OUTLET
    BOUNDARY CONDITIONS:
      FLOW REGIME:
        Option = Subsonic
      END
      MASS AND MOMENTUM:
        Option = Average Static Pressure
        Relative Pressure = 0 [Pa]
      END
      PRESSURE AVERAGING:
        Option = Average Over Whole Outlet
      END
    END
  END
END
OUTPUT CONTROL:
  BACKUP RESULTS: Backup Results 1
    File Compression Level = Default
    Iteration Interval = 20
    Option = Full
  END
  MONITOR OBJECTS:
    MONITOR BALANCES:
      Option = Full
    END
    MONITOR FORCES:
      Option = Full
    END
    MONITOR PARTICLES:
      Option = Full
```

```
    END
    MONITOR RESIDUALS:
     Option = Full
    END
    MONITOR TOTALS:
     Option = Full
    END
   END
   RESULTS:
    File Compression Level = Default
    Option = Full
   END
  END
  SOLVER CONTROL:
   ADVECTION SCHEME:
    Option = High Resolution
   END
   CONVERGENCE CONTROL:
    Length Scale Option = Conservative
    Maximum Number of Iterations = 2000
    Timescale Control = Auto Timescale
   END
   CONVERGENCE CRITERIA:
    Residual Target = 0.00001
    Residual Type = RMS
   END
   DYNAMIC MODEL CONTROL:
    Global Dynamic Model Control = On
   END
   EQUATION CLASS: continuity
    ADVECTION SCHEME:
     Option = High Resolution
    END
    CONVERGENCE CONTROL:
     Length Scale Option = Conservative
     Timescale Control = Auto Timescale
    END
   END
  END
 END
 COMMAND FILE:
  Version = 5.7
  Results Version = 5.7.1
 END
```

Combusting flow

```
This run of the CFX-10.0 Solver started at 20:37:0 on 7 Oct 2006 by
 user Nick on KTESIVIOS2 (intel_xeon64.sse2_winnt5.2) using the command:

 "C:\Program Files (x86)\Ansys Inc\CFX\CFX-10.0\bin\perllib\cfx5solve.pl"
  -stdout-comms -batch -ccl - -ccl temp_bound.ccl

Installed patches:

 * Documentation Update

Setting up CFX-5 Solver run ...


+--------------------------------------------------------------+
|                                                              |
|              CFX Command Language for Run                    |
|                                                              |
+--------------------------------------------------------------+

LIBRARY:
  VARIABLE: T
    Option = Definition
    MMS Name = TEMP
    Long Name = Temperature
    Tensor Type = SCALAR
    Quantity = Temperature
    Status = D
    User Level = 1
    Output to Postprocessor = Yes
    Output to Jobfile = No
    CEL Root = /FLOW/PHYSICS/MATERIALS/{Material}
    Component Bounds Flag = Yes
    Component Lower Bounds = 273
    Component Clip Factors = 0.5
    General Availability = ADAPTION, RESULTS, MONITOR, CEL, PTM_UR
    Physical Availability = THERMAL
    Variable Scope = PHASE, PARTICLE
    Variable Class = PROP
    Field Variable = True
    Component Upper Bounds = 2223
  END
  MATERIAL: CH4
    Material Description = Methane CH4
    Material Group = Gas Phase Combustion
```

```
Option = Pure Substance
Thermodynamic State = Gas
PROPERTIES:
  Option = General Material
  ABSORPTION COEFFICIENT:
    Absorption Coefficient = 1.0 [m^-1]
    Option = Value
  END
  DYNAMIC VISCOSITY:
    Dynamic Viscosity = 11.1E-06 [kg m^-1 s^-1]
    Option = Value
  END
  EQUATION OF STATE:
    Molar Mass = 16.04 [kg kmol^-1]
    Option = Ideal Gas
  END
  REFRACTIVE INDEX:
    Option = Value
    Refractive Index = 1.0 [m m^-1]
  END
  SCATTERING COEFFICIENT:
    Option = Value
    Scattering Coefficient = 0.0 [m^-1]
  END
  SPECIFIC HEAT CAPACITY:
    Option = NASA Format
    Reference Pressure = 1 [atm]
    Reference Temperature = 25 [C]
    LOWER INTERVAL COEFFICIENTS:
      NASA a1 = 0.07787415E+01 []
      NASA a2 = 0.01747668E+00 [K^-1]
      NASA a3 = -0.02783409E-03 [K^-2]
      NASA a4 = 0.03049708E-06 [K^-3]
      NASA a5 = -0.01223931E-09 [K^-4]
      NASA a6 = -0.09825229E+05 [K]
      NASA a7 = 0.01372219E+03 []
    END
    TEMPERATURE LIMITS:
      Lower Temperature = 300 [K]
      Midpoint Temperature = 1000 [K]
      Upper Temperature = 5000 [K]
    END
    UPPER INTERVAL COEFFICIENTS:
      NASA a1 = 0.01683479E+02 []
      NASA a2 = 0.01023724E+00 [K^-1]
      NASA a3 = -0.03875129E-04 [K^-2]
```

```
      NASA a4 = 0.06785585E-08 [K^-3]
      NASA a5 = -0.04503423E-12 [K^-4]
      NASA a6 = -0.01008079E+06 [K]
      NASA a7 = 0.09623395E+02 []
     END
    END
    THERMAL CONDUCTIVITY:
     Option = Value
     Thermal Conductivity = 343E-04 [W m^-1 K^-1]
    END
   END
END
MATERIAL: CO
 Material Description = Carbon Monoxide CO
 Material Group = Gas Phase Combustion
 Option = Pure Substance
 Thermodynamic State = Gas
 PROPERTIES:
  Option = General Material
  ABSORPTION COEFFICIENT:
   Absorption Coefficient = 1.0 [m^-1]
   Option = Value
  END
  DYNAMIC VISCOSITY:
   Dynamic Viscosity = 16.6E-06 [kg m^-1 s^-1]
   Option = Value
  END
  EQUATION OF STATE:
   Molar Mass = 28.01 [kg kmol^-1]
   Option = Ideal Gas
  END
  REFRACTIVE INDEX:
   Option = Value
   Refractive Index = 1.0 [m m^-1]
  END
  SCATTERING COEFFICIENT:
   Option = Value
   Scattering Coefficient = 0.0 [m^-1]
  END
  SPECIFIC HEAT CAPACITY:
   Option = NASA Format
   Reference Pressure = 1 [atm]
   Reference Temperature = 25 [C]
   LOWER INTERVAL COEFFICIENTS:
    NASA a1 = 0.03262452E+02 []
    NASA a2 = 0.01511941E-01 [K^-1]
```

```
      NASA a3 = -0.03881755E-04 [K^-2]
      NASA a4 = 0.05581944E-07 [K^-3]
      NASA a5 = -0.02474951E-10 [K^-4]
      NASA a6 = -0.01431054E+06 [K]
      NASA a7 = 0.04848897E+02 []
    END
    TEMPERATURE LIMITS:
      Lower Temperature = 300 [K]
      Midpoint Temperature = 1000 [K]
      Upper Temperature = 5000 [K]
    END
    UPPER INTERVAL COEFFICIENTS:
      NASA a1 = 0.03025078E+02 []
      NASA a2 = 0.01442689E-01 [K^-1]
      NASA a3 = -0.05630828E-05 [K^-2]
      NASA a4 = 0.01018581E-08 [K^-3]
      NASA a5 = -0.06910952E-13 [K^-4]
      NASA a6 = -0.01426835E+06 [K]
      NASA a7 = 0.06108218E+02 []
    END
  END
  THERMAL CONDUCTIVITY:
    Option = Value
    Thermal Conductivity = 251E-04 [W m^-1 K^-1]
  END
 END
END
MATERIAL: CO2
 Material Description = Carbon Dioxide CO2
 Material Group = Gas Phase Combustion
 Option = Pure Substance
 Thermodynamic State = Gas
 PROPERTIES:
  Option = General Material
  ABSORPTION COEFFICIENT:
    Absorption Coefficient = 1.0 [m^-1]
    Option = Value
  END
  DYNAMIC VISCOSITY:
    Dynamic Viscosity = 14.9E-06 [kg m^-1 s^-1]
    Option = Value
  END
  EQUATION OF STATE:
    Molar Mass = 44.01 [kg kmol^-1]
    Option = Ideal Gas
  END
```

```
    REFRACTIVE INDEX:
     Option = Value
     Refractive Index = 1.0 [m m^-1]
    END
    SCATTERING COEFFICIENT:
     Option = Value
     Scattering Coefficient = 0.0 [m^-1]
    END
    SPECIFIC HEAT CAPACITY:
     Option = NASA Format
     Reference Pressure = 1 [atm]
     Reference Temperature = 25 [C]
     LOWER INTERVAL COEFFICIENTS:
      NASA a1 = 0.02275725E+02 []
      NASA a2 = 0.09922072E-01 [K^-1]
      NASA a3 = -0.01040911E-03 [K^-2]
      NASA a4 = 0.06866687E-07 [K^-3]
      NASA a5 = -0.02117280E-10 [K^-4]
      NASA a6 = -0.04837314E+06 [K]
      NASA a7 = 0.01018849E+03 []
     END
     TEMPERATURE LIMITS:
      Lower Temperature = 300 [K]
      Midpoint Temperature = 1000 [K]
      Upper Temperature = 5000 [K]
     END
     UPPER INTERVAL COEFFICIENTS:
      NASA a1 = 0.04453623E+02 []
      NASA a2 = 0.03140169E-01 [K^-1]
      NASA a3 = -0.01278411E-04 [K^-2]
      NASA a4 = 0.02393997E-08 [K^-3]
      NASA a5 = -0.01669033E-12 [K^-4]
      NASA a6 = -0.04896696E+06 [K]
      NASA a7 = -0.09553959E+01 []
     END
    END
    THERMAL CONDUCTIVITY:
     Option = Value
     Thermal Conductivity = 145E-04 [W m^-1 K^-1]
    END
   END
  END
  MATERIAL: Fibre Plug 1260
   Material Description = Ceramic fibre 1260
   Material Group = CHT Solids
   Option = Pure Substance
```

```
  Thermodynamic State = Solid
  PROPERTIES:
   Option = General Material
   EQUATION OF STATE:
    Density = 250 [kg m^-3]
    Molar Mass = 77.6 [kg kmol^-1]
    Option = Value
   END
   REFRACTIVE INDEX:
    Option = Value
    Refractive Index = 1.7
   END
   SPECIFIC HEAT CAPACITY:
    Option = Value
    Reference Temperature = 25 [C]
    Specific Heat Capacity = (1001.64+0.1583*((T/1[K])-273))*1[J kg^-1 \
     K^-1]
    Specific Heat Depends On = Temperature
   END
   THERMAL CONDUCTIVITY:
    Option = Value
    Thermal Conductivity = (0.08+0.000143*((T/1[K])-273))*1[W m^-1 K^-1]
   END
  END
 END
 MATERIAL: H2O
  Material Description = Water Vapour
  Material Group = Gas Phase Combustion, Interphase Mass Transfer
  Option = Pure Substance
  Thermodynamic State = Gas
  PROPERTIES:
   Option = General Material
   ABSORPTION COEFFICIENT:
    Absorption Coefficient = 1.0 [m^-1]
    Option = Value
   END
   DYNAMIC VISCOSITY:
    Dynamic Viscosity = 9.4E-06 [kg m^-1 s^-1]
    Option = Value
   END
   EQUATION OF STATE:
    Molar Mass = 18.02 [kg kmol^-1]
    Option = Ideal Gas
   END
   REFRACTIVE INDEX:
    Option = Value
```

```
    Refractive Index = 1.0 [m m^-1]
   END
   SCATTERING COEFFICIENT:
    Option = Value
    Scattering Coefficient = 0.0 [m^-1]
   END
   SPECIFIC HEAT CAPACITY:
    Option = NASA Format
    Reference Pressure = 1 [atm]
    Reference Temperature = 25 [C]
    LOWER INTERVAL COEFFICIENTS:
     NASA a1 = 0.03386842E+02 []
     NASA a2 = 0.03474982E-01 [K^-1]
     NASA a3 = -0.06354696E-04 [K^-2]
     NASA a4 = 0.06968581E-07 [K^-3]
     NASA a5 = -0.02506588E-10 [K^-4]
     NASA a6 = -0.03020811E+06 [K]
     NASA a7 = 0.02590233E+02 []
    END
    TEMPERATURE LIMITS:
     Lower Temperature = 300 [K]
     Midpoint Temperature = 1000 [K]
     Upper Temperature = 5000 [K]
    END
    UPPER INTERVAL COEFFICIENTS:
     NASA a1 = 0.02672146E+02 []
     NASA a2 = 0.03056293E-01 [K^-1]
     NASA a3 = -0.08730260E-05 [K^-2]
     NASA a4 = 0.01200996E-08 [K^-3]
     NASA a5 = -0.06391618E-13 [K^-4]
     NASA a6 = -0.02989921E+06 [K]
     NASA a7 = 0.06862817E+02 []
    END
   END
   THERMAL CONDUCTIVITY:
    Option = Value
    Thermal Conductivity = 193E-04 [W m^-1 K^-1]
   END
  END
 END
 MATERIAL: Inconel 601
  Material Description = Inconel 601
  Material Group = CHT Solids
  Option = Pure Substance
  Thermodynamic State = Solid
  PROPERTIES:
```

```
    Option = General Material
    EQUATION OF STATE:
     Density = 8050 [kg m^-3]
     Density Depends On = Temperature
     Molar Mass = 56.3 [kg kmol^-1]
     Option = Value
    END
    REFRACTIVE INDEX:
     Option = Value
     Refractive Index = 2.5
    END
    SPECIFIC HEAT CAPACITY:
     Option = Value
     Reference Specific Enthalpy = 583160 [J kg^-1]
     Reference Temperature = 25 [C]
     Specific Heat Capacity = (442+0.269*((T/1[K])-273))*1[J kg^-1 K^-1]
     Specific Heat Depends On = Temperature
    END
    THERMAL CONDUCTIVITY:
     Option = Value
     Thermal Conductivity = (11+0.0168*((T/1[K])-273))*1[W m^-1 K^-1]
    END
  END
END
MATERIAL: N2
  Material Description = Nitrogen N2
  Material Group = Gas Phase Combustion
  Option = Pure Substance
  Thermodynamic State = Gas
  PROPERTIES:
    Option = General Material
    ABSORPTION COEFFICIENT:
     Absorption Coefficient = 1.0 [m^-1]
     Option = Value
    END
    DYNAMIC VISCOSITY:
     Dynamic Viscosity = 17.7E-06 [kg m^-1 s^-1]
     Option = Value
    END
    EQUATION OF STATE:
     Molar Mass = 28.01 [kg kmol^-1]
     Option = Ideal Gas
    END
    REFRACTIVE INDEX:
     Option = Value
     Refractive Index = 1.0 [m m^-1]
```

```
    END
    SCATTERING COEFFICIENT:
     Option = Value
     Scattering Coefficient = 0.0 [m^-1]
    END
    SPECIFIC HEAT CAPACITY:
     Option = NASA Format
     Reference Pressure = 1 [atm]
     Reference Temperature = 25 [C]
     LOWER INTERVAL COEFFICIENTS:
      NASA a1 = 0.03298677E+02 []
      NASA a2 = 0.01408240E-01 [K^-1]
      NASA a3 = -0.03963222E-04 [K^-2]
      NASA a4 = 0.05641515E-07 [K^-3]
      NASA a5 = -0.02444855E-10 [K^-4]
      NASA a6 = -0.01020900E+05 [K]
      NASA a7 = 0.03950372E+02 []
     END
     TEMPERATURE LIMITS:
      Lower Temperature = 300 [K]
      Midpoint Temperature = 1000 [K]
      Upper Temperature = 5000 [K]
     END
     UPPER INTERVAL COEFFICIENTS:
      NASA a1 = 0.02926640E+02 []
      NASA a2 = 0.01487977E-01 [K^-1]
      NASA a3 = -0.05684761E-05 [K^-2]
      NASA a4 = 0.01009704E-08 [K^-3]
      NASA a5 = -0.06753351E-13 [K^-4]
      NASA a6 = -0.09227977E+04 [K]
      NASA a7 = 0.05980528E+02 []
     END
    END
    THERMAL CONDUCTIVITY:
     Option = Value
     Thermal Conductivity = 259E-04 [W m^-1 K^-1]
    END
   END
  END
  MATERIAL: NO
   Material Description = Nitric Oxide NO
   Material Group = Gas Phase Combustion
   Option = Pure Substance
   Thermodynamic State = Gas
   PROPERTIES:
    Option = General Material
```

```
ABSORPTION COEFFICIENT:
  Absorption Coefficient = 1.0 [m^-1]
  Option = Value
END
DYNAMIC VISCOSITY:
  Dynamic Viscosity = 17.8E-06 [kg m^-1 s^-1]
  Option = Value
END
EQUATION OF STATE:
  Molar Mass = 30.01 [kg kmol^-1]
  Option = Ideal Gas
END
REFRACTIVE INDEX:
  Option = Value
  Refractive Index = 1.0 [m m^-1]
END
SCATTERING COEFFICIENT:
  Option = Value
  Scattering Coefficient = 0.0 [m^-1]
END
SPECIFIC HEAT CAPACITY:
  Option = NASA Format
  Reference Pressure = 1 [atm]
  Reference Temperature = 25 [C]
  LOWER INTERVAL COEFFICIENTS:
    NASA a1 = 0.03376542E+02 []
    NASA a2 = 0.01253063E-01 [K^-1]
    NASA a3 = -0.03302751E-04 [K^-2]
    NASA a4 = 0.05217810E-07 [K^-3]
    NASA a5 = -0.02446263E-10 [K^-4]
    NASA a6 = 0.09817961E+05 [K]
    NASA a7 = 0.05829590E+02 []
  END
  TEMPERATURE LIMITS:
    Lower Temperature = 300 [K]
    Midpoint Temperature = 1000 [K]
    Upper Temperature = 5000 [K]
  END
  UPPER INTERVAL COEFFICIENTS:
    NASA a1 = 0.03245435E+02 []
    NASA a2 = 0.01269138E-01 [K^-1]
    NASA a3 = -0.05015890E-05 [K^-2]
    NASA a4 = 0.09169283E-09 [K^-3]
    NASA a5 = -0.06275419E-13 [K^-4]
    NASA a6 = 0.09800840E+05 [K]
    NASA a7 = 0.06417294E+02 []
```

```
    END
   END
   THERMAL CONDUCTIVITY:
    Option = Value
    Thermal Conductivity = 238E-04 [W m^-1 K^-1]
   END
  END
 END
 MATERIAL: O2
  Material Description = Oxygen O2
  Material Group = Gas Phase Combustion
  Option = Pure Substance
  Thermodynamic State = Gas
  PROPERTIES:
   Option = General Material
   ABSORPTION COEFFICIENT:
    Absorption Coefficient = 1.0 [m^-1]
    Option = Value
   END
   DYNAMIC VISCOSITY:
    Dynamic Viscosity = 19.2E-06 [kg m^-1 s^-1]
    Option = Value
   END
   EQUATION OF STATE:
    Molar Mass = 31.99 [kg kmol^-1]
    Option = Ideal Gas
   END
   REFRACTIVE INDEX:
    Option = Value
    Refractive Index = 1.0 [m m^-1]
   END
   SCATTERING COEFFICIENT:
    Option = Value
    Scattering Coefficient = 0.0 [m^-1]
   END
   SPECIFIC HEAT CAPACITY:
    Option = NASA Format
    Reference Pressure = 1 [atm]
    Reference Temperature = 25 [C]
    LOWER INTERVAL COEFFICIENTS:
     NASA a1 = 0.03212936E+02 []
     NASA a2 = 0.01127486E-01 [K^-1]
     NASA a3 = -0.05756150E-05 [K^-2]
     NASA a4 = 0.01313877E-07 [K^-3]
     NASA a5 = -0.08768554E-11 [K^-4]
     NASA a6 = -0.01005249E+05 [K]
```

```
      NASA a7 = 0.06034738E+02 []
    END
    TEMPERATURE LIMITS:
      Lower Temperature = 300 [K]
      Midpoint Temperature = 1000 [K]
      Upper Temperature = 5000 [K]
    END
    UPPER INTERVAL COEFFICIENTS:
      NASA a1 = 0.03697578E+02 []
      NASA a2 = 0.06135197E-02 [K^-1]
      NASA a3 = -0.01258842E-05 [K^-2]
      NASA a4 = 0.01775281E-09 [K^-3]
      NASA a5 = -0.01136435E-13 [K^-4]
      NASA a6 = -0.01233930E+05 [K]
      NASA a7 = 0.03189166E+02 []
    END
  END
  THERMAL CONDUCTIVITY:
    Option = Value
    Thermal Conductivity = 266E-04 [W m^-1 K^-1]
  END
 END
END
MATERIAL: Silicon carbide
 Material Description = Silicon carbide
 Material Group = CHT Solids
 Option = Pure Substance
 Thermodynamic State = Solid
 PROPERTIES:
  Option = General Material
  EQUATION OF STATE:
    Density = 3100 [kg m^-3]
    Molar Mass = 40.101 [kg kmol^-1]
    Option = Value
  END
  REFRACTIVE INDEX:
    Option = Value
    Refractive Index = 2.6
  END
  SPECIFIC HEAT CAPACITY:
    Option = Value
    Reference Temperature = 25 [C]
    Specific Heat Capacity = (275.554+0.9309*((T/1[K])-273))*1[J kg^-1 \
      K^-1]
    Specific Heat Depends On = Temperature
  END
```

```
    THERMAL CONDUCTIVITY:
     Option = Value
     Thermal Conductivity = (198.97-0.114*((T/1[K])-273))*1[W m^-1 K^-1]
    END
   END
  END
  MATERIAL: methane air mixture
   Material Description = Methane Air mixture
   Material Group = Gas Phase Combustion
   Option = Reacting Mixture
   Reactions List = Methane Air WD2 NO PDF
   Thermodynamic State = Gas
   MIXTURE PROPERTIES:
    Option = Ideal Mixture
    ABSORPTION COEFFICIENT:
     Absorption Coefficient = 0.01 [m^-1] + 1.0 [m^-1]*(CO2.molf + \
      H2O.molf)
     Option = Value
    END
    REFRACTIVE INDEX:
     Option = Value
     Refractive Index = 1.0
    END
    SCATTERING COEFFICIENT:
     Option = Value
     Scattering Coefficient = 0. [m^-1]
    END
   END
  END
  REACTION: Methane Air WD2 NO PDF
   Additional Materials List = CH4, O2, CO, CO2, H2O, NO, N2
   Option = Multi Step
   Reaction Description = Methane Air Two Step and NO Formation with \
    Temperature PDF
   Reactions List = Methane Oxygen WD2, NO Formation Methane PDF
  END
  REACTION: Methane Oxygen WD2
   Option = Multi Step
   Reactions List = WD2 Methane Oxidation, WD2 CO Oxidation
  END
  REACTION: NO Formation Methane PDF
   Option = Multi Step
   Reaction Description = NO Formation with Temperature PDF for Methane
   Reactions List = Thermal NO PDF, Prompt NO Methane PDF
  END
  REACTION: Prompt NO Methane PDF
```

```
  Option = Single Step
  Reaction Description = Prompt NO Formation by Methane with Temperature PDF
  COMBUSTION MODEL:
   Option = Finite Rate Chemistry
  END
  FORWARD REACTION RATE:
   Lower Temperature = 300 [K]
   Option = Arrhenius with Temperature PDF
   Pre Exponential Factor = 6.4E+6 [s^-1] * (mw/density)^1.5
   Temperature Exponent = 0
   Upper Temperature = 2300 [K]
   REACTION ACTIVATION:
    Activation Temperature = 36510 [K]
    Option = Activation Temperature
   END
  END
  PRODUCTS:
   Materials List = NO
   Option = Child Materials
   CHILD MATERIAL: NO
    Option = Stoichiometric
    Stoichiometric Coefficient = 1.0
   END
  END
  REACTANTS:
   Materials List = O2, N2, CH4
   Option = Child Materials
   CHILD MATERIAL: O2
    Option = Stoichiometric
    Reaction Order = 0.5
    Stoichiometric Coefficient = 0.5
   END
   CHILD MATERIAL: N2
    Option = Stoichiometric
    Reaction Order = 1.0
    Stoichiometric Coefficient = 0.5
   END
   CHILD MATERIAL: CH4
    Option = Stoichiometric
    Reaction Order = 1.0
    Stoichiometric Coefficient = 0.0
   END
  END
 END
 REACTION: Thermal NO PDF
  Option = Single Step
```

```
  Reaction Description = Thermal NO Formation with Temperature PDF
  COMBUSTION MODEL:
   Option = Finite Rate Chemistry
  END
  FORWARD REACTION RATE:
   Lower Temperature = 300 [K]
   Option = Arrhenius with Temperature PDF
   Pre Exponential Factor = 1.8E+11 [kmol^-1 m^3 s^-1] * 12.567E+3 \
    [kmol^0.5 m^-1.5 K^0.5]
   Temperature Exponent = -0.5
   Upper Temperature = 2300 [K]
   REACTION ACTIVATION:
    Activation Temperature = 38370 [K] + 31096 [K]
    Option = Activation Temperature
   END
  END
  PRODUCTS:
   Materials List = NO
   Option = Child Materials
   CHILD MATERIAL: NO
    Option = Stoichiometric
    Stoichiometric Coefficient = 2.0
   END
  END
  REACTANTS:
   Materials List = N2, O2
   Option = Child Materials
   CHILD MATERIAL: N2
    Option = Stoichiometric
    Reaction Order = 1.0
    Stoichiometric Coefficient = 1.0
   END
   CHILD MATERIAL: O2
    Option = Stoichiometric
    Reaction Order = 0.5
    Stoichiometric Coefficient = 1.0
   END
  END
 END
 REACTION: WD2 CO Oxidation
  Option = Single Step
  FORWARD REACTION RATE:
   Option = Arrhenius
   Pre Exponential Factor = (10.^14.6) [mol^-0.75 cm^2.25 s^-1]
   Temperature Exponent = 0.0
   REACTION ACTIVATION:
```

```
      Activation Energy = 40. [kcal mol^-1]
      Option = Activation Energy
    END
  END
  PRODUCTS:
    Materials List = CO2
    Option = Child Materials
    CHILD MATERIAL: CO2
      Option = Stoichiometric
      Stoichiometric Coefficient = 1.0
    END
  END
  REACTANTS:
    Materials List = CO, O2, H2O
    Option = Child Materials
    CHILD MATERIAL: CO
      Option = Stoichiometric
      Reaction Order = 1.0
      Stoichiometric Coefficient = 1.0
    END
    CHILD MATERIAL: O2
      Option = Stoichiometric
      Reaction Order = 0.25
      Stoichiometric Coefficient = 0.5
    END
    CHILD MATERIAL: H2O
      Option = Stoichiometric
      Reaction Order = 0.5
      Stoichiometric Coefficient = 0.0
    END
  END
END
REACTION: WD2 Methane Oxidation
  Option = Single Step
  FORWARD REACTION RATE:
    Option = Arrhenius
    Pre Exponential Factor = 1.5E7 [s^-1]
    Temperature Exponent = 0.
    REACTION ACTIVATION:
      Activation Energy = 30. [kcal mol^-1]
      Option = Activation Energy
    END
  END
  PRODUCTS:
    Materials List = CO, H2O
    Option = Child Materials
```

```
    CHILD MATERIAL: CO
     Option = Stoichiometric
     Stoichiometric Coefficient = 1.0
    END
    CHILD MATERIAL: H2O
     Option = Stoichiometric
     Stoichiometric Coefficient = 2.0
    END
   END
   REACTANTS:
    Materials List = CH4, O2
    Option = Child Materials
    CHILD MATERIAL: CH4
     Option = Stoichiometric
     Reaction Order = -0.3
     Stoichiometric Coefficient = 1.0
    END
    CHILD MATERIAL: O2
     Option = Stoichiometric
     Reaction Order = 1.3
     Stoichiometric Coefficient = 1.5
    END
   END
  END
END
EXECUTION CONTROL:
 PARALLEL HOST LIBRARY:
  HOST DEFINITION: ktesivios2
   Installation Root = C:\Program Files (x86)\Ansys Inc\CFX\CFX-%v
   Host Architecture String = intel_xeon64.sse2_winnt5.2
  END
 END
 PARTITIONER STEP CONTROL:
  Multidomain Option = Independent Partitioning
  Runtime Priority = Standard
  MEMORY CONTROL:
   Memory Allocation Factor = 1.0
  END
  PARTITIONING TYPE:
   MeTiS Type = k-way
   Option = MeTiS
   Partition Size Rule = Automatic
  END
 END
 RUN DEFINITION:
  Definition File = \
```

```
E:/MODELS/CFXDef/Final400mmLongerEDmodel/FuSoMoEDMAirCH4DTMkeps300K
mesh\
      0.00908244Airmfr400mmlongerRT.def
    Interpolate Initial Values = Off
    Run Mode = Full
  END
  SOLVER STEP CONTROL:
    Runtime Priority = Standard
    EXECUTABLE SELECTION:
      Double Precision = Off
    END
    MEMORY CONTROL:
      Memory Allocation Factor = 1.2
    END
    PARALLEL ENVIRONMENT:
      Number of Processes = 1
      Start Method = Serial
    END
  END
END
FLOW:
  DOMAIN: fluid domain
    Coord Frame = Coord 0
    Domain Type = Fluid
    Fluids List = methane air mixture
    Location = Assembly
    BOUNDARY: exhaust
      Boundary Type = OUTLET
      Location = EXHAUST
      BOUNDARY CONDITIONS:
        FLOW REGIME:
          Option = Subsonic
        END
        MASS AND MOMENTUM:
          Option = Average Static Pressure
          Relative Pressure = 0 [Pa]
        END
        PRESSURE AVERAGING:
          Option = Average Over Whole Outlet
        END
        THERMAL RADIATION:
          Option = Local Temperature
        END
      END
    END
```

```
BOUNDARY: air inlet
 Boundary Type = INLET
 Location = AIR INLET
 BOUNDARY CONDITIONS:
  COMPONENT: CH4
   Mass Fraction = 0.0
   Option = Mass Fraction
  END
  COMPONENT: CO2
   Mass Fraction = 0.0
   Option = Mass Fraction
  END
  COMPONENT: H2O
   Mass Fraction = 0.0
   Option = Mass Fraction
  END
  COMPONENT: NO
   Mass Fraction = 0.0
   Option = Mass Fraction
  END
  COMPONENT: O2
   Mass Fraction = 0.232
   Option = Mass Fraction
  END
  COMPONENT: CO
   Mass Fraction = 0.0
   Option = Mass Fraction
  END
  FLOW DIRECTION:
   Option = Normal to Boundary Condition
  END
  FLOW REGIME:
   Option = Subsonic
  END
  HEAT TRANSFER:
   Option = Static Temperature
   Static Temperature = 300 [K]
  END
  MASS AND MOMENTUM:
   Mass Flow Rate = 0.00908244 [kg s^-1]
   Option = Mass Flow Rate
  END
  THERMAL RADIATION:
   Option = Local Temperature
  END
  TURBULENCE:
```

```
    Option = Medium Intensity and Eddy Viscosity Ratio
   END
  END
END
BOUNDARY: fuel
 Boundary Type = INLET
 Location = FUEL
 BOUNDARY CONDITIONS:
  COMPONENT: CH4
   Mass Fraction = 1
   Option = Mass Fraction
  END
  COMPONENT: CO2
   Mass Fraction = 0.0
   Option = Mass Fraction
  END
  COMPONENT: H2O
   Mass Fraction = 0.0
   Option = Mass Fraction
  END
  COMPONENT: NO
   Mass Fraction = 0.0
   Option = Mass Fraction
  END
  COMPONENT: O2
   Mass Fraction = 0.0
   Option = Mass Fraction
  END
  COMPONENT: CO
   Mass Fraction = 0.0
   Option = Mass Fraction
  END
  FLOW DIRECTION:
   Option = Normal to Boundary Condition
  END
  FLOW REGIME:
   Option = Subsonic
  END
  HEAT TRANSFER:
   Option = Static Temperature
   Static Temperature = 305 [K]
  END
  MASS AND MOMENTUM:
   Mass Flow Rate = 0.00045968 [kg s^-1]
   Option = Mass Flow Rate
  END
```

```
    THERMAL RADIATION:
     Option = Local Temperature
    END
    TURBULENCE:
     Option = Medium Intensity and Eddy Viscosity Ratio
    END
   END
  END
  BOUNDARY: pilot
   Boundary Type = INLET
   Location = PILOT
   BOUNDARY CONDITIONS:
    COMPONENT: CH4
     Mass Fraction = 0.05081
     Option = Mass Fraction
    END
    COMPONENT: CO2
     Mass Fraction = 0.0
     Option = Mass Fraction
    END
    COMPONENT: H2O
     Mass Fraction = 0.0
     Option = Mass Fraction
    END
    COMPONENT: NO
     Mass Fraction = 0.0
     Option = Mass Fraction
    END
    COMPONENT: O2
     Mass Fraction = 0.220214
     Option = Mass Fraction
    END
    COMPONENT: CO
     Mass Fraction = 0.0
     Option = Mass Fraction
    END
    FLOW DIRECTION:
     Option = Normal to Boundary Condition
    END
    FLOW REGIME:
     Option = Subsonic
    END
    HEAT TRANSFER:
     Option = Static Temperature
     Static Temperature = 315 [K]
    END
```

```
    MASS AND MOMENTUM:
     Mass Flow Rate = 0.00034389 [kg s^-1]
     Option = Mass Flow Rate
    END
    THERMAL RADIATION:
     Option = Local Temperature
    END
    TURBULENCE:
     Option = Medium Intensity and Eddy Viscosity Ratio
    END
  END
 END
 BOUNDARY: radiant tube
  Boundary Type = WALL
  Location = RADIANT TUBE
  BOUNDARY CONDITIONS:
   HEAT TRANSFER:
    Fixed Temperature = 1240 [K]
    Option = Fixed Temperature
   END
   THERMAL RADIATION:
    Diffuse Fraction = 0.85
    Emissivity = 0.7594
    Option = Opaque
   END
   WALL INFLUENCE ON FLOW:
    Option = No Slip
   END
   WALL ROUGHNESS:
    Option = Smooth Wall
   END
  END
 END
 BOUNDARY: fluid flame tube Side 1
  Boundary Type = INTERFACE
  Location = FLAME TUBE
  BOUNDARY CONDITIONS:
   HEAT TRANSFER:
    Option = Conservative Interface Flux
   END
   THERMAL RADIATION:
    Diffuse Fraction = 0.85
    Emissivity = 0.8938
    Option = Opaque
   END
   WALL INFLUENCE ON FLOW:
```

```
    Option = No Slip
   END
  END
 END
 BOUNDARY: fluid inner tube Side 1
  Boundary Type = INTERFACE
  Location = INNER TUBE
  BOUNDARY CONDITIONS:
   HEAT TRANSFER:
    Option = Conservative Interface Flux
   END
   THERMAL RADIATION:
    Diffuse Fraction = 0.85
    Emissivity = 0.774344
    Option = Opaque
   END
   WALL INFLUENCE ON FLOW:
    Option = No Slip
   END
  END
 END
 BOUNDARY: fluid air tube Side 1
  Boundary Type = INTERFACE
  Location = AIR TUBE
  BOUNDARY CONDITIONS:
   HEAT TRANSFER:
    Option = Conservative Interface Flux
   END
   THERMAL RADIATION:
    Diffuse Fraction = 0.85
    Emissivity = 0.692744
    Option = Opaque
   END
   WALL INFLUENCE ON FLOW:
    Option = No Slip
   END
  END
 END
 BOUNDARY: fluid inner tube plug Side 1
  Boundary Type = INTERFACE
  Location = PLUG
  BOUNDARY CONDITIONS:
   HEAT TRANSFER:
    Option = Conservative Interface Flux
   END
   THERMAL RADIATION:
```

```
    Diffuse Fraction = 0.15
    Emissivity = 0.817
    Option = Opaque
   END
   WALL INFLUENCE ON FLOW:
    Option = No Slip
   END
  END
 END
 BOUNDARY: fluid domain inner wall
  Boundary Type = WALL
  Location = INNER WALL
  BOUNDARY CONDITIONS:
   HEAT TRANSFER:
    Option = Adiabatic
   END
   THERMAL RADIATION:
    Diffuse Fraction = 0.85
    Emissivity = 0.651944
    Option = Opaque
   END
   WALL INFLUENCE ON FLOW:
    Option = No Slip
   END
   WALL ROUGHNESS:
    Option = Smooth Wall
   END
  END
 END
 BOUNDARY: radiant tube adiavatic
  Boundary Type = WALL
  Location = RADIANT TUBE ADIAVATIC
  BOUNDARY CONDITIONS:
   HEAT TRANSFER:
    Option = Adiabatic
   END
   THERMAL RADIATION:
    Diffuse Fraction = 0.15
    Emissivity = 0.791
    Option = Opaque
   END
   WALL INFLUENCE ON FLOW:
    Option = No Slip
   END
   WALL ROUGHNESS:
    Option = Smooth Wall
```

```
  END
 END
END
DOMAIN MODELS:
 BUOYANCY MODEL:
  Option = Non Buoyant
 END
 DOMAIN MOTION:
  Option = Stationary
 END
 REFERENCE PRESSURE:
  Reference Pressure = 1 [atm]
 END
END
FLUID MODELS:
 COMBUSTION MODEL:
  Eddy Dissipation Model Coefficient A = 4.0
  Eddy Dissipation Model Coefficient B = 0.5
  Option = Eddy Dissipation
 END
 COMPONENT: CH4
  Option = Automatic
 END
 COMPONENT: CO2
  Option = Automatic
 END
 COMPONENT: H2O
  Option = Automatic
 END
 COMPONENT: N2
  Option = Constraint
 END
 COMPONENT: NO
  Option = Transport Equation
 END
 COMPONENT: O2
  Option = Automatic
 END
 COMPONENT: CO
  Option = Automatic
 END
 HEAT TRANSFER MODEL:
  Option = Thermal Energy
 END
 THERMAL RADIATION MODEL:
  Option = Discrete Transfer
```

```
    SCATTERING MODEL:
     Option = Isotropic
    END
    SPECTRAL MODEL:
     Option = Gray
    END
   END
   TURBULENCE MODEL:
    Option = k epsilon
    EPSILON COEFFICIENTS:
     TURBULENT FLUX CLOSURE:
      Option = Eddy Diffusivity
     END
    END
    K COEFFICIENTS:
     TURBULENT FLUX CLOSURE:
      Option = Eddy Diffusivity
     END
    END
   END
   TURBULENT WALL FUNCTIONS:
    Option = Scalable
   END
  END
  INITIALISATION:
   Option = Automatic
   INITIAL CONDITIONS:
    Velocity Type = Cartesian
    CARTESIAN VELOCITY COMPONENTS:
     Option = Automatic
    END
    COMPONENT: CH4
     Option = Automatic
    END
    COMPONENT: CO2
     Option = Automatic
    END
    COMPONENT: H2O
     Option = Automatic
    END
    COMPONENT: NO
     Option = Automatic
    END
    COMPONENT: O2
     Mass Fraction = 0.232
     Option = Automatic with Value
```

```
    END
    COMPONENT: CO
     Option = Automatic
    END
    EPSILON:
     Option = Automatic
    END
    K:
     Option = Automatic
    END
    RADIATION INTENSITY:
     Option = Automatic
    END
    STATIC PRESSURE:
     Option = Automatic
    END
    TEMPERATURE:
     Option = Automatic with Value
     Temperature = 1000 [K]
    END
   END
  END
 END
 DOMAIN: flame tube
  Domain Type = Solid
  Location = Assembly 2
  Solids List = Silicon carbide
  BOUNDARY: fluid flame tube Side 2
   Boundary Type = INTERFACE
   Location = FLAMETUBE
   BOUNDARY CONDITIONS:
    HEAT TRANSFER:
     Option = Conservative Interface Flux
    END
    WALL ROUGHNESS:
     Option = Smooth Wall
    END
   END
  END
  DOMAIN MODELS:
   DOMAIN MOTION:
    Option = Stationary
   END
  END
  INITIALISATION:
   Option = Automatic
```

```
  INITIAL CONDITIONS:
   TEMPERATURE:
    Option = Automatic with Value
    Temperature = 1273 [K]
   END
  END
 END
 SOLID MODELS:
  HEAT TRANSFER MODEL:
   Option = Thermal Energy
  END
  THERMAL RADIATION MODEL:
   Option = None
  END
 END
END
DOMAIN: inner tube
 Domain Type = Solid
 Location = Assembly 3
 Solids List = Inconel 601
 BOUNDARY: fluid inner tube Side 2
  Boundary Type = INTERFACE
  Location = INNER TUBE 2
  BOUNDARY CONDITIONS:
   HEAT TRANSFER:
    Option = Conservative Interface Flux
   END
   WALL ROUGHNESS:
    Option = Smooth Wall
   END
  END
 END
 BOUNDARY: inner tube inner tube plug Side 1
  Boundary Type = INTERFACE
  Location = INNER TUBE PLUG SURFACE
  BOUNDARY CONDITIONS:
   HEAT TRANSFER:
    Option = Conservative Interface Flux
   END
   WALL ROUGHNESS:
    Option = Smooth Wall
   END
  END
 END
 DOMAIN MODELS:
  DOMAIN MOTION:
```

```
    Option = Stationary
   END
  END
  INITIALISATION:
   Option = Automatic
   INITIAL CONDITIONS:
    TEMPERATURE:
     Option = Automatic with Value
     Temperature = 1300 [K]
    END
   END
  END
  SOLID MODELS:
   HEAT TRANSFER MODEL:
    Option = Thermal Energy
   END
   THERMAL RADIATION MODEL:
    Option = None
   END
  END
END
DOMAIN: inner tube plug
 Domain Type = Solid
 Location = Assembly 4
 Solids List = Fibre Plug 1260
 BOUNDARY: air tube inner tube plug Side 2
  Boundary Type = INTERFACE
  Location = AIR TUBE SURFACE
  BOUNDARY CONDITIONS:
   HEAT TRANSFER:
    Option = Conservative Interface Flux
   END
   WALL ROUGHNESS:
    Option = Smooth Wall
   END
  END
 END
 BOUNDARY: fluid inner tube plug Side 2
  Boundary Type = INTERFACE
  Location = INNER TUBE PLUG
  BOUNDARY CONDITIONS:
   HEAT TRANSFER:
    Option = Conservative Interface Flux
   END
   WALL ROUGHNESS:
    Option = Smooth Wall
```

```
    END
   END
  END
  BOUNDARY: inner tube inner tube plug Side 2
   Boundary Type = INTERFACE
   Location = INNER TUBE SURFACE
   BOUNDARY CONDITIONS:
    HEAT TRANSFER:
     Option = Conservative Interface Flux
    END
    WALL ROUGHNESS:
     Option = Smooth Wall
    END
   END
  END
  DOMAIN MODELS:
   DOMAIN MOTION:
    Option = Stationary
   END
  END
  INITIALISATION:
   Option = Automatic
   INITIAL CONDITIONS:
    TEMPERATURE:
     Option = Automatic with Value
     Temperature = 1000 [K]
    END
   END
  END
  SOLID MODELS:
   HEAT TRANSFER MODEL:
    Option = Thermal Energy
   END
   THERMAL RADIATION MODEL:
    Option = None
   END
  END
 END
 DOMAIN: air tube
  Domain Type = Solid
  Location = Assembly 5
  Solids List = Inconel 601
  BOUNDARY: air tube Default
   Boundary Type = WALL
   Location = AIR TUBE OUTER
   BOUNDARY CONDITIONS:
```

```
    HEAT TRANSFER:
     Option = Adiabatic
    END
   END
  END
  BOUNDARY: fluid air tube Side 2
   Boundary Type = INTERFACE
   Location = AIR TUBE 2
   BOUNDARY CONDITIONS:
    HEAT TRANSFER:
     Option = Conservative Interface Flux
    END
    WALL ROUGHNESS:
     Option = Smooth Wall
    END
   END
  END
  BOUNDARY: air tube inner tube plug Side 1
   Boundary Type = INTERFACE
   Location = AIR TUBE INNER
   BOUNDARY CONDITIONS:
    HEAT TRANSFER:
     Option = Conservative Interface Flux
    END
    WALL ROUGHNESS:
     Option = Smooth Wall
    END
   END
  END
  DOMAIN MODELS:
   DOMAIN MOTION:
    Option = Stationary
   END
  END
  INITIALISATION:
   Option = Automatic
   INITIAL CONDITIONS:
    TEMPERATURE:
     Option = Automatic with Value
     Temperature = 850 [K]
    END
   END
  END
  SOLID MODELS:
   HEAT TRANSFER MODEL:
    Option = Thermal Energy
```

```
    END
    THERMAL RADIATION MODEL:
     Option = None
    END
   END
  END
  DOMAIN INTERFACE: fluid flame tube
   Boundary List1 = fluid flame tube Side 1
   Boundary List2 = fluid flame tube Side 2
   Connection Type = Automatic
   Interface Type = Fluid Solid
  END
  DOMAIN INTERFACE: fluid inner tube
   Boundary List1 = fluid inner tube Side 1
   Boundary List2 = fluid inner tube Side 2
   Connection Type = Automatic
   Interface Type = Fluid Solid
  END
  DOMAIN INTERFACE: fluid air tube
   Boundary List1 = fluid air tube Side 1
   Boundary List2 = fluid air tube Side 2
   Connection Type = Automatic
   Interface Type = Fluid Solid
  END
  DOMAIN INTERFACE: air tube inner tube plug
   Boundary List1 = air tube inner tube plug Side 1
   Boundary List2 = air tube inner tube plug Side 2
   Connection Type = Automatic
   Interface Type = Solid Solid
  END
  DOMAIN INTERFACE: fluid inner tube plug
   Boundary List1 = fluid inner tube plug Side 1
   Boundary List2 = fluid inner tube plug Side 2
   Connection Type = Automatic
   Interface Type = Fluid Solid
  END
  DOMAIN INTERFACE: inner tube inner tube plug
   Boundary List1 = inner tube inner tube plug Side 1
   Boundary List2 = inner tube inner tube plug Side 2
   Connection Type = Automatic
   Interface Type = Solid Solid
  END
  OUTPUT CONTROL:
   BACKUP RESULTS: Backup Results 1
    File Compression Level = Default
    Iteration Interval = 20
```

```
    Option = Standard
  END
  RESULTS:
    File Compression Level = Default
    Option = Standard
  END
END
SIMULATION TYPE:
  Option = Steady State
END
SOLUTION UNITS:
  Angle Units = [rad]
  Length Units = [m]
  Mass Units = [kg]
  Solid Angle Units = [sr]
  Temperature Units = [K]
  Time Units = [s]
END
SOLVER CONTROL:
  ADVECTION SCHEME:
    Option = High Resolution
  END
  COMPRESSIBILITY CONTROL:
    Decreasing Temperature Relaxation = No
  END
  CONVERGENCE CONTROL:
    Length Scale Option = Conservative
    Maximum Number of Iterations = 5000
    Solid Timescale = 100000 [s]
    Solid Timescale Control = Physical Timescale
    Timescale Control = Auto Timescale
  END
  CONVERGENCE CRITERIA:
    Residual Target = 0.00001
    Residual Type = RMS
  END
  DYNAMIC MODEL CONTROL:
    Global Dynamic Model Control = On
  END
  EQUATION CLASS: continuity
    ADVECTION SCHEME:
      Option = High Resolution
    END
    CONVERGENCE CONTROL:
      Length Scale Option = Conservative
      Timescale Control = Auto Timescale
```

```
    END
   END
  END
END
COMMAND FILE:
  Version = 10.0
  Results Version = 10.0
END
```

Appendix - D: Experimental results - Cold Flow

Note: X axis represents longitudinal position. X = 50 mm is Plane 1, X = 100 mm is Plane 2

****
VERSUCHSANSTALT FUER VERFAHRENSTECHNIK, L.& C. STEINMUELLER GMBH
GESCHWINDIGKEITSMESSUNG MIT TRIPLE-SPLIT-FILMSONDE AM:26.04.2005
****

GASTEMPERATUR IM MODELL : 20.0 grad C

VERSUCHSNUMMER: B21

KOMMENTAR ZUR VERSUCHSNUMMER:
Brennermessung Einstellung 1 Splitfilmmessung mit Sonde Nr14

X	Z	Y	ALPHA	THETA	W	W(X)	W(Y)	W(Z)
mm	mm	mm	grad	grad	m/s	m/s	m/s	m/s
50	0	15	303.4	101.4	1.89	1.54	-0.37	1.02
50	0	20	316.9	93.1	1.52	1.04	-0.08	1.11
50	0	25	6.5	82.3	0.95	-0.11	0.13	0.93
50	0	30	41.6	84.5	1.07	-0.71	0.1	0.8
50	0	35	57.6	81.9	1.22	-1.02	0.17	0.65
50	0	40	66.7	84.2	1.31	-1.2	0.13	0.51
50	0	45	73.5	82.7	1.27	-1.2	0.16	0.36
50	0	50	87	85.3	1.24	-1.24	0.1	0.07
50	0	55	96.8	82.5	1.3	-1.28	0.17	-0.15
50	0	60	109.4	87.2	1.32	-1.25	0.07	-0.44
50	0	65	117.7	87.7	1.26	-1.11	0.05	-0.58
50	0	70	125.8	83.8	1.18	-0.95	0.13	-0.69
50	0	75	140.6	83.2	1.01	-0.63	0.12	-0.77
50	0	80	160.6	73.2	0.86	-0.27	0.25	-0.78
50	0	85	198	77.9	1.16	0.35	0.24	-1.07
50	0	90	233.7	77.3	1.56	1.22	0.34	-0.9
50	0	95	232.2	76.6	1.55	1.19	0.36	-0.92
50	0	100	239	78.6	1.56	1.31	0.31	-0.79
50	10	15	301.6	100.3	1.93	1.62	-0.34	0.99
50	10	20	311.8	100.7	1.73	1.27	-0.32	1.13
50	10	25	338.6	94	1.31	0.48	-0.09	1.22
50	10	30	30.3	89.8	1.03	-0.52	0	0.89
50	10	35	59.6	83	1.13	-0.97	0.14	0.57
50	10	40	65.3	84	1.29	-1.16	0.13	0.53
50	10	45	70.9	83.6	1.3	-1.22	0.15	0.42
50	10	50	82.5	87.1	1.23	-1.22	0.06	0.16
50	10	55	96.7	87.1	1.21	-1.2	0.06	-0.14
50	10	60	111.5	87.1	1.28	-1.19	0.06	-0.47
50	10	65	122.8	86.1	1.31	-1.1	0.09	-0.71
50	10	70	131.4	86	1.15	-0.86	0.08	-0.76
50	10	75	149.4	77.6	1.05	-0.52	0.23	-0.88
50	10	80	181.7	74.7	0.96	0.03	0.25	-0.92

50	10	85	229.8	79.1	1.3	0.98	0.25	-0.83
50	10	90	241.2	75.3	1.75	1.48	0.44	-0.82
50	10	95	239.4	71.3	1.68	1.37	0.54	-0.81
50	10	100	241.7	73	1.27	1.07	0.37	-0.58
50	20	15	298.1	107.3	2.22	1.87	-0.66	1
50	20	20	310.9	105.9	2.08	1.51	-0.57	1.31
50	20	25	341.2	103.5	1.2	0.38	-0.28	1.1
50	20	30	7	97	1.01	-0.12	-0.12	1
50	20	35	53.9	89.3	1.21	-0.98	0.02	0.71
50	20	40	61.8	87.8	1.32	-1.16	0.05	0.62
50	20	45	70.6	87.2	1.29	-1.22	0.06	0.43
50	20	50	82.8	87.4	1.24	-1.23	0.06	0.16
50	20	55	101.1	82.9	1.27	-1.24	0.16	-0.24
50	20	60	114.5	86.5	1.27	-1.16	0.08	-0.53
50	20	65	124.1	86.9	1.28	-1.06	0.07	-0.72
50	20	70	129.4	84.1	1.2	-0.92	0.12	-0.75
50	20	75	149.5	79.7	1.01	-0.5	0.18	-0.85
50	20	80	200.6	76	1.41	0.48	0.34	-1.28
50	20	85	240.1	76.4	1.9	1.6	0.45	-0.92
50	20	90	246.6	70.1	1.99	1.71	0.68	-0.74
50	20	95	240.5	62.4	2.06	1.59	0.95	-0.9
50	20	100	222.9	55.2	1.32	0.74	0.75	-0.79
50	30	15	297.4	108.9	2.51	2.11	-0.81	1.09
50	30	20	303.2	110.7	1.82	1.43	-0.64	0.93
50	30	25	345.8	110.2	1.07	0.25	-0.37	0.97
50	30	30	39.8	101.4	1.11	-0.7	-0.22	0.83
50	30	35	53.6	93.1	1.26	-1.01	-0.07	0.75
50	30	40	63.2	88.2	1.3	-1.16	0.04	0.59
50	30	45	68.6	88.5	1.31	-1.22	0.03	0.48
50	30	50	84.3	85.8	1.27	-1.26	0.09	0.13
50	30	55	100.1	87.3	1.26	-1.23	0.06	-0.22
50	30	60	112.3	86.8	1.27	-1.17	0.07	-0.48
50	30	65	121.3	90.5	1.27	-1.08	-0.01	-0.66
50	30	70	135.8	85.6	1.25	-0.87	0.1	-0.89
50	30	75	151.8	81.7	1.05	-0.49	0.15	-0.92
50	30	80	213.6	77.2	1.44	0.78	0.32	-1.17
50	30	85	242.3	74.8	2.32	1.98	0.61	-1.04
50	30	90	247.1	68.2	2.4	2.06	0.89	-0.87
50	30	95	244.7	60	2.2	1.72	1.1	-0.81
50	30	100	223.8	52.5	1.69	0.93	1.02	-0.97
50	40	15	294.3	112.3	2.72	2.3	-1.04	1.04
50	40	20	297.5	109.9	2.23	1.86	-0.76	0.97
50	40	25	323.9	109.8	1.37	0.76	-0.46	1.04
50	40	30	33.8	105.6	1.09	-0.58	-0.29	0.87
50	40	35	51.9	94.8	1.21	-0.95	-0.1	0.74
50	40	40	57.6	93.3	1.29	-1.09	-0.07	0.69
50	40	45	66.6	89.9	1.28	-1.17	0	0.51
50	40	50	81.9	86.1	1.27	-1.26	0.09	0.18
50	40	55	100.4	88.9	1.24	-1.22	0.02	-0.22
50	40	60	112.6	88.8	1.28	-1.18	0.03	-0.49
50	40	65	126.1	91.1	1.24	-1	-0.02	-0.73
50	40	70	137.9	87.9	1.2	-0.81	0.04	-0.89

50	40	75	159.2	79.2	1.06	-0.37	0.2	-0.97
50	40	80	213.7	76.9	1.55	0.84	0.35	-1.25
50	40	85	244.7	73.7	2.44	2.12	0.69	-1
50	40	90	248.3	66.6	2.65	2.26	1.05	-0.9
50	40	95	245.3	59	2.37	1.84	1.22	-0.85
50	40	100	212.7	49.3	1.61	0.66	1.05	-1.02
50	50	15	292.9	113.1	2.94	2.49	-1.15	1.05
50	50	20	298.5	109.6	2.4	1.99	-0.81	1.08
50	50	25	315.4	114.6	1.49	0.95	-0.62	0.96
50	50	30	21.5	111.3	1.11	-0.38	-0.4	0.96
50	50	35	43.1	96.2	1.25	-0.85	-0.13	0.91
50	50	40	56.9	94.6	1.35	-1.12	-0.11	0.73
50	50	45	65.3	90.8	1.29	-1.17	-0.02	0.54
50	50	50	80	87.2	1.26	-1.24	0.06	0.22
50	50	55	99.4	88.4	1.26	-1.24	0.03	-0.21
50	50	60	116.5	89	1.35	-1.21	0.02	-0.6
50	50	65	126.5	89.4	1.31	-1.05	0.01	-0.78
50	50	70	135.5	89.2	1.18	-0.83	0.02	-0.84
50	50	75	161.7	79.1	1.13	-0.35	0.21	-1.05
50	50	80	223.5	79.4	1.67	1.13	0.31	-1.19
50	50	85	245.9	72.6	2.37	2.07	0.71	-0.92
50	50	90	249.4	66	2.64	2.26	1.07	-0.85
50	50	95	244.2	60.6	2.36	1.85	1.16	-0.89
50	50	100	210.9	54.1	1.71	0.71	1	-1.19
50	60	15	290.1	113.4	3.1	2.67	-1.23	0.98
50	60	20	293.4	112.1	2.51	2.14	-0.95	0.92
50	60	25	318.7	116.3	1.42	0.84	-0.63	0.96
50	60	30	20.3	110	1.17	-0.38	-0.4	1.03
50	60	35	41.1	96.4	1.28	-0.83	-0.14	0.96
50	60	40	55.2	90.1	1.38	-1.13	0	0.79
50	60	45	64.7	89.3	1.33	-1.2	0.02	0.57
50	60	50	77.8	86.8	1.27	-1.24	0.07	0.27
50	60	55	99.2	90.1	1.21	-1.19	0	-0.19
50	60	60	113.3	90.7	1.29	-1.18	-0.02	-0.51
50	60	65	126.4	91	1.29	-1.04	-0.02	-0.77
50	60	70	137.4	92.8	1.26	-0.85	-0.06	-0.93
50	60	75	171.4	85.8	1.12	-0.17	0.08	-1.11
50	60	80	223.8	78.9	1.72	1.17	0.33	-1.22
50	60	85	242.4	73.3	2.38	2.02	0.68	-1.06
50	60	90	247	67	2.74	2.32	1.07	-0.98
50	60	95	246.3	60.8	2.46	1.96	1.2	-0.86
50	60	100	222.8	58.6	1.87	1.08	0.97	-1.17
50	70	15	290.3	114.3	3.28	2.8	-1.35	1.04
50	70	20	292.8	113.8	2.76	2.33	-1.11	0.98
50	70	25	310.2	116.3	1.57	1.07	-0.7	0.91
50	70	30	13.6	111.4	1.19	-0.26	-0.43	1.08
50	70	35	43.3	97.5	1.28	-0.87	-0.17	0.93
50	70	40	53	94	1.33	-1.06	-0.09	0.8
50	70	45	62.6	92	1.34	-1.18	-0.05	0.61
50	70	50	79.5	85.8	1.22	-1.19	0.09	0.22
50	70	55	99.7	88.7	1.21	-1.19	0.03	-0.2
50	70	60	115.3	93.2	1.25	-1.13	-0.07	-0.54

50	70	65	128.5	92.9	1.31	-1.02	-0.07	-0.81
50	70	70	137.3	93.2	1.22	-0.83	-0.07	-0.9
50	70	75	166.4	86.5	1.14	-0.27	0.07	-1.11
50	70	80	207.2	79.2	1.43	0.64	0.27	-1.25
50	70	85	238.9	72.7	2.38	1.95	0.71	-1.17
50	70	90	247.1	66.5	2.53	2.14	1.01	-0.9
50	70	95	244.3	61.4	2.4	1.9	1.15	-0.91
50	70	100	226.4	62.6	1.88	1.21	0.86	-1.15
50	80	15	288.4	115.6	3.42	2.92	-1.48	0.97
50	80	20	291.4	114.7	2.75	2.32	-1.15	0.91
50	80	25	310.2	114.6	1.68	1.17	-0.7	0.99
50	80	30	12.3	109.8	1.19	-0.24	-0.4	1.09
50	80	35	41.4	96.1	1.28	-0.84	-0.14	0.96
50	80	40	49.4	90.7	1.35	-1.02	-0.02	0.88
50	80	45	62.4	89.5	1.35	-1.19	0.01	0.62
50	80	50	76.9	88.6	1.24	-1.21	0.03	0.28
50	80	55	99.4	88.6	1.21	-1.2	0.03	-0.2
50	80	60	113.6	90.9	1.28	-1.17	-0.02	-0.51
50	80	65	131.9	93.6	1.31	-0.97	-0.08	-0.87
50	80	70	136.6	97.4	1.22	-0.83	-0.16	-0.88
50	80	75	158	90	1.11	-0.42	0	-1.03
50	80	80	207.5	80.4	1.53	0.69	0.25	-1.33
50	80	85	233.1	73.1	2.18	1.67	0.63	-1.25
50	80	90	243.7	68.3	2.43	2.02	0.9	-1
50	80	95	244.9	61.1	2.15	1.71	1.04	-0.8
50	80	100	204.2	62.3	1.69	0.62	0.79	-1.37
50	90	15	287.8	117	3.57	3.03	-1.62	0.97
50	90	20	293.4	114.4	2.85	2.38	-1.18	1.03
50	90	25	311.4	115	1.64	1.11	-0.69	0.98
50	90	30	8.1	107.7	1.16	-0.16	-0.35	1.1
50	90	35	34.9	93	1.28	-0.73	-0.07	1.05
50	90	40	50.1	87	1.35	-1.04	0.07	0.87
50	90	45	67.2	89.5	1.3	-1.19	0.01	0.5
50	90	50	81	88.1	1.28	-1.26	0.04	0.2
50	90	55	96.8	89.9	1.26	-1.25	0	-0.15
50	90	60	113.2	90.4	1.24	-1.14	-0.01	-0.49
50	90	65	123.1	96.5	1.3	-1.09	-0.15	-0.71
50	90	70	134.7	96.1	1.2	-0.85	-0.13	-0.84
50	90	75	154.8	94.3	1.07	-0.46	-0.08	-0.97
50	90	80	211.8	81.7	1.54	0.8	0.22	-1.29
50	90	85	230.6	74.5	1.82	1.35	0.49	-1.11
50	90	90	241.7	70	2.14	1.77	0.73	-0.95
50	90	95	237.7	66.7	2.16	1.68	0.86	-1.06
50	90	100	236.5	70.5	1.84	1.45	0.61	-0.96
50	100	15	287	117.5	3.66	3.1	-1.69	0.95
50	100	20	294	115.5	2.76	2.27	-1.19	1.01
50	100	25	308.9	115.9	1.53	1.07	-0.67	0.86
50	100	30	3.9	103.1	1.13	-0.08	-0.26	1.1
50	100	35	39.6	89.6	1.28	-0.81	0.01	0.98
50	100	40	49.9	89.5	1.32	-1.01	0.01	0.85
50	100	45	60	86	1.28	-1.11	0.09	0.64
50	100	50	78.2	88.4	1.21	-1.18	0.03	0.25

50	100	55	96.5	88.3	1.3	-1.29	0.04	-0.15
50	100	60	113.1	93.8	1.34	-1.23	-0.09	-0.53
50	100	65	126.6	98.9	1.24	-0.98	-0.19	-0.73
50	100	70	135.7	99	1.24	-0.85	-0.19	-0.87
50	100	75	157	94.9	1.03	-0.4	-0.09	-0.94
50	100	80	197.2	88.8	1.14	0.34	0.02	-1.09
50	100	85	229.2	77.5	1.66	1.23	0.36	-1.06
50	100	90	237.6	71.9	1.93	1.55	0.6	-0.98
50	100	95	225.7	68	1.76	1.17	0.66	-1.14
50	100	100	236.2	73.9	1.46	1.16	0.41	-0.78
50	110	15	286.9	118	3.64	3.07	-1.71	0.93
50	110	20	293.7	116.2	2.69	2.21	-1.19	0.97
50	110	25	318.2	115.8	1.46	0.88	-0.64	0.98
50	110	30	15.9	103.4	1.05	-0.28	-0.24	0.98
50	110	35	39	88.2	1.23	-0.77	0.04	0.96
50	110	40	50	85.1	1.31	-1	0.11	0.84
50	110	45	60.6	85.1	1.25	-1.09	0.11	0.61
50	110	50	77.7	87.8	1.23	-1.2	0.05	0.26
50	110	55	95.5	87.2	1.3	-1.29	0.06	-0.12
50	110	60	119	96.1	1.32	-1.14	-0.14	-0.64
50	110	65	125.6	96.5	1.31	-1.06	-0.15	-0.76
50	110	70	134.5	101.1	1.16	-0.81	-0.22	-0.8
50	110	75	149.8	99.3	1.03	-0.51	-0.17	-0.88
50	110	80	192.4	86	1.1	0.24	0.08	-1.07
50	110	85	222.1	80.9	1.56	1.03	0.25	-1.14
50	110	90	233.7	73.1	1.73	1.33	0.5	-0.98
50	110	95	230	70.2	1.66	1.2	0.56	-1.01
50	110	100	226.6	71.7	1.25	0.87	0.39	-0.82
50	120	15	288.2	117.4	3.36	2.83	-1.54	0.93
50	120	20	294	118.4	2.2	1.77	-1.05	0.79
50	120	25	322.2	113	1.27	0.71	-0.5	0.92
50	120	30	25.9	95.6	1.08	-0.47	-0.1	0.97
50	120	35	47.1	83.6	1.24	-0.9	0.14	0.84
50	120	40	51.6	82.6	1.32	-1.03	0.17	0.81
50	120	45	62.2	83.9	1.3	-1.15	0.14	0.6
50	120	50	80.4	88.6	1.23	-1.21	0.03	0.21
50	120	55	95.8	91.9	1.29	-1.28	-0.04	-0.13
50	120	60	107.9	92.2	1.29	-1.22	-0.05	-0.39
50	120	65	121.8	97.2	1.27	-1.07	-0.16	-0.66
50	120	70	162.2	102.9	1.05	-0.31	-0.23	-0.98
50	120	75	162.4	101.6	0.95	-0.28	-0.19	-0.89
50	120	80	191.5	85.4	1.35	0.27	0.11	-1.32
50	120	85	229	80.5	1.62	1.21	0.27	-1.05
50	120	90	234.7	74.8	1.66	1.31	0.43	-0.92
50	120	95	230.1	69.1	1.66	1.19	0.59	-0.99
50	120	100	223.8	79	1.37	0.93	0.26	-0.97
50	130	15	288.8	117.5	3.06	2.57	-1.41	0.88
50	130	20	301.7	116.7	1.83	1.39	-0.82	0.86
50	130	25	332.6	111.3	1	0.43	-0.37	0.83
50	130	30	28.1	92.3	1	-0.47	-0.04	0.88
50	130	35	44.6	85.8	1.18	-0.83	0.09	0.84
50	130	40	53.6	84.3	1.22	-0.98	0.12	0.72

50	130	45	62.1	84.4	1.32	-1.16	0.13	0.61
50	130	50	79	89	1.23	-1.2	0.02	0.23
50	130	55	95.3	88.9	1.28	-1.27	0.03	-0.12
50	130	60	107	92.1	1.27	-1.21	-0.05	-0.37
50	130	65	122.5	96	1.21	-1.02	-0.13	-0.65
50	130	70	127.5	101.1	1.12	-0.87	-0.22	-0.67
50	130	75	208.9	98.5	1.28	0.61	-0.19	-1.11
50	130	80	207.5	89.7	1.21	0.56	0.01	-1.08
50	130	85	234.6	80.4	1.65	1.32	0.28	-0.94
50	130	90	235.5	74.7	1.68	1.34	0.44	-0.92
50	130	95	225.5	70.1	1.59	1.06	0.54	-1.05
50	130	100	219.5	77.2	1.47	0.91	0.33	-1.11
50	140	15	291.8	117.2	2.23	1.84	-1.02	0.74
50	140	20	306.1	117.2	1.35	0.97	-0.62	0.71
50	140	25	346.5	105.9	0.9	0.2	-0.25	0.84
50	140	30	40.2	91.2	0.99	-0.64	-0.02	0.76
50	140	35	49.1	83.2	1.16	-0.87	0.14	0.75
50	140	40	54.7	81.2	1.27	-1.02	0.19	0.72
50	140	45	64.8	85.6	1.27	-1.15	0.1	0.54
50	140	50	81.3	85.3	1.22	-1.2	0.1	0.18
50	140	55	91.3	87.1	1.26	-1.26	0.06	-0.03
50	140	60	109.1	95	1.35	-1.27	-0.12	-0.44
50	140	65	112.6	95.9	1.23	-1.13	-0.13	-0.47
50	140	70	122.4	100.6	0.97	-0.81	-0.18	-0.51
50	140	75	145.8	92.8	0.85	-0.48	-0.04	-0.7
50	140	80	223.5	91.8	1.46	1.01	-0.05	-1.06
50	140	85	232.7	78.5	1.72	1.34	0.34	-1.02
50	140	90	234.5	69.6	1.83	1.39	0.64	-0.99
50	140	95	228.4	66	1.57	1.07	0.64	-0.95
50	140	100	211	73.6	1.44	0.71	0.41	-1.18
50	150	15	305.5	110.5	1.88	1.43	-0.66	1.02
50	150	20	327.2	108.2	1.77	0.91	-0.55	1.41
50	150	25	8.3	98.8	0.89	-0.13	-0.14	0.87
50	150	30	46.1	86.8	1.04	-0.75	0.06	0.72
50	150	35	52.2	84.3	1.19	-0.93	0.12	0.72
50	150	40	54	83.4	1.21	-0.97	0.14	0.71
50	150	45	66.3	86	1.23	-1.12	0.09	0.49
50	150	50	75.8	88.9	1.28	-1.24	0.02	0.31
50	150	55	90.3	95.3	1.31	-1.3	-0.12	-0.01
50	150	60	107.1	90.7	1.33	-1.28	-0.02	-0.39
50	150	65	112	101.8	1.12	-1.02	-0.23	-0.41
50	150	70	120.6	94.5	1.14	-0.98	-0.09	-0.58
50	150	75	160	94.9	0.86	-0.29	-0.07	-0.81
50	150	80	191	76.5	1.3	0.24	0.3	-1.24
50	150	85	235.7	75.8	1.85	1.48	0.45	-1.01
50	150	90	233.7	65.3	1.63	1.19	0.68	-0.87
50	150	95	226	64.2	1.67	1.08	0.72	-1.04
50	150	100	193.4	76.3	1.39	0.31	0.33	-1.31
50	160	15	312.2	94.9	1.16	0.86	-0.1	0.78
50	160	20	339.8	91.5	0.84	0.29	-0.02	0.79
50	160	25	39.1	90	0.88	-0.56	0	0.69
50	160	30	47.4	88.7	1.1	-0.81	0.02	0.75

50	160	35	53.5	86.5	1.16	-0.93	0.07	0.69
50	160	40	54.5	85.7	1.22	-0.99	0.09	0.7
50	160	45	67.1	82.9	1.28	-1.17	0.16	0.49
50	160	50	81.4	86.4	1.24	-1.22	0.08	0.19
50	160	55	94.4	85.4	1.23	-1.23	0.1	-0.09
50	160	60	104.8	91.2	1.32	-1.28	-0.03	-0.34
50	160	65	111.3	92.3	1.3	-1.21	-0.05	-0.47
50	160	70	124.8	95.4	1.02	-0.84	-0.1	-0.58
50	160	75	162.7	95.8	0.85	-0.25	-0.09	-0.81
50	160	80	209.9	85.8	1.42	0.7	0.1	-1.23
50	160	85	239.8	78.1	1.78	1.51	0.37	-0.88
50	160	90	236.1	72.3	1.97	1.55	0.6	-1.05
50	160	95	230.5	66.9	1.74	1.23	0.68	-1.02
50	160	100	213.7	75.7	1.49	0.8	0.37	-1.2
50	170	15	319.1	88.5	1.23	0.81	0.03	0.93
50	170	20	11.5	86.6	0.81	-0.16	0.05	0.79
50	170	25	36.9	85.5	0.89	-0.53	0.07	0.71
50	170	30	50.9	87.5	0.96	-0.74	0.04	0.6
50	170	35	56	82.3	1.16	-0.95	0.16	0.64
50	170	40	58.1	86	1.24	-1.05	0.09	0.66
50	170	45	65.6	88.7	1.2	-1.1	0.03	0.5
50	170	50	80.3	86	1.22	-1.2	0.08	0.21
50	170	55	92.7	86.6	1.26	-1.26	0.07	-0.06
50	170	60	100.4	92.1	1.29	-1.26	-0.05	-0.23
50	170	65	110	92.8	1.17	-1.1	-0.06	-0.4
50	170	70	121.2	90.1	0.94	-0.8	0	-0.49
50	170	75	152.8	89.7	0.76	-0.35	0	-0.68
50	170	80	239.2	83.6	1.75	1.5	0.2	-0.89
50	170	85	237.5	79.5	1.8	1.49	0.33	-0.95
50	170	90	236.4	69.7	1.88	1.47	0.65	-0.98
50	170	95	221.9	65.6	1.88	1.15	0.78	-1.28
50	170	100	209.3	73.3	1.53	0.72	0.44	-1.28
50	180	15	326.6	101.5	1.56	0.84	-0.31	1.28
50	180	20	308.5	80.1	0.65	0.5	0.11	0.4
50	180	25	9.3	86.7	0.85	-0.14	0.05	0.84
50	180	30	48.3	89.5	0.98	-0.73	0.01	0.65
50	180	35	53.4	87.9	1.12	-0.9	0.04	0.67
50	180	40	56.5	84.7	1.22	-1.01	0.11	0.67
50	180	45	65.9	86.1	1.18	-1.08	0.08	0.48
50	180	50	77.1	83.5	1.2	-1.16	0.13	0.26
50	180	55	94.6	89.5	1.32	-1.32	0.01	-0.11
50	180	60	107.2	89.5	1.31	-1.25	0.01	-0.39
50	180	65	114.1	91.6	1.15	-1.05	-0.03	-0.47
50	180	70	122.4	91	0.91	-0.77	-0.02	-0.49
50	180	75	158.6	77.3	0.82	-0.29	0.18	-0.74
50	180	80	218.2	81.5	1.84	1.13	0.27	-1.43
50	180	85	236.1	77.3	1.98	1.6	0.43	-1.08
50	180	90	237.9	67.1	1.87	1.46	0.73	-0.91
50	180	95	223.5	61.9	1.62	0.98	0.76	-1.03
50	180	100	193.9	73	1.4	0.32	0.41	-1.3
100	0	15	318.8	85.6	1.54	1.01	0.12	1.15
100	0	20	324.4	85.5	1.28	0.74	0.1	1.04

100	0	25	335.1	85.9	1.05	0.44	0.08	0.95
100	0	30	346.7	86.9	0.88	0.2	0.05	0.86
100	0	35	5.3	88.7	0.7	-0.06	0.02	0.7
100	0	15	317.8	85.9	1.55	1.04	0.11	1.14
100	0	20	323.3	85.4	1.27	0.76	0.1	1.02
100	0	25	335.6	86.1	1.04	0.43	0.07	0.94
100	0	30	349.9	85.8	0.79	0.14	0.06	0.77
100	0	35	8	84.1	0.68	-0.09	0.07	0.67
100	0	40	26.6	83.9	0.63	-0.28	0.07	0.56
100	0	45	45.7	81.6	0.45	-0.32	0.07	0.31
100	0	50	74.5	85.4	0.4	-0.39	0.03	0.11
100	0	55	112.2	83.9	0.47	-0.44	0.05	-0.18
100	0	60	139.9	94.3	0.59	-0.38	-0.04	-0.45
100	0	65	163.2	97.2	0.8	-0.23	-0.1	-0.76
100	0	70	173.4	99.5	0.88	-0.1	-0.14	-0.86
100	0	75	182.2	105.2	0.81	0.03	-0.21	-0.78
100	0	80	191	106.2	0.82	0.15	-0.23	-0.77
100	0	85	200.6	108.1	0.77	0.26	-0.24	-0.69
100	0	90	216	111.5	0.79	0.43	-0.29	-0.59
100	0	95	225.4	107.3	0.91	0.62	-0.27	-0.61
100	0	100	234.2	98.6	1.13	0.9	-0.17	-0.65
100	10	15	313.4	86.5	1.56	1.13	0.1	1.07
100	10	20	322.1	84.5	1.32	0.81	0.13	1.04
100	10	25	334.4	87.8	1.05	0.45	0.04	0.95
100	10	30	349.3	88.2	0.87	0.16	0.03	0.85
100	10	35	7.7	89.2	0.75	-0.1	0.01	0.74
100	10	40	26	88.4	0.62	-0.27	0.02	0.56
100	10	45	40.1	86.8	0.51	-0.33	0.03	0.39
100	10	50	73.9	81.6	0.41	-0.39	0.06	0.11
100	10	55	106.7	88.9	0.46	-0.44	0.01	-0.13
100	10	60	148.5	100.1	0.62	-0.32	-0.11	-0.52
100	10	65	163.7	99.5	0.82	-0.23	-0.14	-0.77
100	10	70	175.7	103.3	0.88	-0.06	-0.2	-0.86
100	10	75	184.5	102.9	0.87	0.07	-0.2	-0.85
100	10	80	194.9	104	0.86	0.22	-0.21	-0.81
100	10	85	206	102	0.79	0.34	-0.16	-0.69
100	10	90	215.2	102.3	0.88	0.5	-0.19	-0.71
100	10	95	229.3	100.5	1.01	0.76	-0.18	-0.65
100	10	100	236.3	96.3	1.27	1.05	-0.14	-0.7
100	20	15	312.2	86.6	1.59	1.18	0.09	1.07
100	20	20	321.8	87.4	1.31	0.81	0.06	1.03
100	20	25	336	88.8	1.07	0.43	0.02	0.97
100	20	30	349.4	89.8	0.85	0.16	0	0.84
100	20	35	8.7	92.9	0.76	-0.12	-0.04	0.75
100	20	40	24.8	89.1	0.64	-0.27	0.01	0.58
100	20	45	39.8	88.6	0.54	-0.35	0.01	0.41
100	20	50	67.8	91.9	0.4	-0.37	-0.01	0.15
100	20	55	102	95.3	0.4	-0.39	-0.04	-0.08
100	20	60	141.6	102.6	0.61	-0.37	-0.13	-0.47
100	20	65	162.9	104.5	0.82	-0.23	-0.2	-0.76
100	20	70	172.8	104.7	0.91	-0.11	-0.23	-0.88
100	20	75	185.5	105.6	0.95	0.09	-0.26	-0.91

100	20	80	196.2	103.4	0.94	0.26	-0.22	-0.88
100	20	85	207.2	100.9	0.96	0.43	-0.18	-0.84
100	20	90	221.2	100.2	1.02	0.66	-0.18	-0.76
100	20	95	231.6	96.8	1.14	0.89	-0.13	-0.71
100	20	100	238.8	94.1	1.4	1.2	-0.1	-0.73
100	30	15	309.4	86.8	1.64	1.26	0.09	1.04
100	30	20	319.5	86	1.37	0.89	0.1	1.04
100	30	25	333.3	87.5	1.03	0.46	0.04	0.92
100	30	30	353	94.2	0.83	0.1	-0.06	0.83
100	30	35	8.8	93.4	0.76	-0.12	-0.04	0.75
100	30	40	23.8	93.6	0.69	-0.28	-0.04	0.63
100	30	45	42.7	94.6	0.52	-0.35	-0.04	0.38
100	30	50	67.7	93.5	0.45	-0.42	-0.03	0.17
100	30	55	101.5	98.8	0.42	-0.41	-0.07	-0.08
100	30	60	146.8	109.4	0.57	-0.3	-0.19	-0.45
100	30	65	163.4	110.4	0.75	-0.2	-0.26	-0.67
100	30	70	176.4	108.1	0.91	-0.05	-0.28	-0.86
100	30	75	186.9	106.3	1	0.12	-0.28	-0.96
100	30	80	197.4	104.4	1.05	0.3	-0.26	-0.97
100	30	85	208	101.9	1.08	0.5	-0.22	-0.93
100	30	90	218.5	99.2	1.15	0.71	-0.18	-0.89
100	30	95	231.6	97.5	1.28	0.99	-0.17	-0.79
100	30	100	240.7	94.3	1.53	1.33	-0.12	-0.75
100	40	15	306.9	87.7	1.66	1.33	0.07	1
100	40	20	320.6	87	1.32	0.84	0.07	1.02
100	40	25	337.9	89.8	1	0.37	0	0.92
100	40	30	348.8	92.6	0.88	0.17	-0.04	0.86
100	40	35	9.6	95.3	0.77	-0.13	-0.07	0.76
100	40	40	22.6	96.7	0.7	-0.27	-0.08	0.65
100	40	45	37.8	92.6	0.53	-0.32	-0.02	0.42
100	40	50	69.7	96.4	0.43	-0.4	-0.05	0.15
100	40	55	103.4	108.2	0.42	-0.39	-0.13	-0.09
100	40	60	137.4	105.4	0.64	-0.41	-0.17	-0.45
100	40	65	166.7	110.7	0.78	-0.17	-0.28	-0.71
100	40	70	177	110	0.97	-0.05	-0.33	-0.91
100	40	75	185.2	108	1.03	0.09	-0.32	-0.97
100	40	80	196.4	106.8	1.11	0.3	-0.32	-1.02
100	40	85	207.7	106.3	1.15	0.51	-0.32	-0.97
100	40	90	220	101.4	1.22	0.77	-0.24	-0.92
100	40	95	233.6	98.6	1.38	1.09	-0.21	-0.81
100	40	100	241.7	95.1	1.61	1.41	-0.14	-0.76
100	50	15	304.9	86.9	1.69	1.39	0.09	0.97
100	50	20	317.5	89.2	1.27	0.86	0.02	0.94
100	50	25	337	91.3	0.97	0.38	-0.02	0.9
100	50	30	353.3	94.1	0.84	0.1	-0.06	0.83
100	50	35	9	96.4	0.79	-0.12	-0.09	0.78
100	50	40	22.7	97	0.73	-0.28	-0.09	0.67
100	50	45	36.1	99.1	0.65	-0.38	-0.1	0.52
100	50	50	56.5	103.7	0.45	-0.37	-0.11	0.24
100	50	55	98.7	106.4	0.41	-0.39	-0.12	-0.06
100	50	60	146.3	110.2	0.51	-0.26	-0.18	-0.4
100	50	65	163	113.7	0.8	-0.21	-0.32	-0.7

100	50	70	176.2	112	0.96	-0.06	-0.36	-0.88
100	50	75	188.5	112.1	1.01	0.14	-0.38	-0.93
100	50	80	193.2	110.2	1.11	0.24	-0.38	-1.02
100	50	85	208.5	109.9	1.22	0.55	-0.42	-1.01
100	50	90	221.3	107.1	1.29	0.81	-0.38	-0.92
100	50	95	233.3	102	1.42	1.11	-0.29	-0.83
100	50	100	239.7	97	1.66	1.43	-0.2	-0.83
100	60	15	302.7	88.1	1.7	1.43	0.06	0.92
100	60	20	316.6	89.5	1.25	0.86	0.01	0.91
100	60	25	334.1	93.2	0.93	0.41	-0.05	0.84
100	60	30	355.9	94	0.8	0.06	-0.06	0.8
100	60	35	9.6	97.7	0.81	-0.13	-0.11	0.79
100	60	40	19.3	100.5	0.72	-0.23	-0.13	0.67
100	60	45	35.7	96.1	0.6	-0.35	-0.06	0.49
100	60	50	51.9	102.7	0.5	-0.38	-0.11	0.3
100	60	55	86.2	105.4	0.39	-0.38	-0.1	0.02
100	60	60	135.8	115.6	0.53	-0.33	-0.23	-0.34
100	60	65	161.6	118.5	0.75	-0.21	-0.36	-0.63
100	60	70	178.5	115.6	0.93	-0.02	-0.4	-0.84
100	60	75	185.7	115.3	1.07	0.1	-0.46	-0.96
100	60	80	195.4	116.8	1.11	0.26	-0.5	-0.96
100	60	85	203.9	115.8	1.2	0.44	-0.52	-0.99
100	60	90	219.1	112.2	1.3	0.76	-0.49	-0.93
100	60	95	231.1	106.9	1.49	1.11	-0.43	-0.9
100	60	100	242.3	99.9	1.63	1.42	-0.28	-0.75
100	60	15	305.8	92.9	1.47	1.19	-0.07	0.86
100	60	20	320.7	92.7	1.05	0.66	-0.05	0.81
100	60	25	340.5	88.6	0.89	0.3	0.02	0.84
100	60	30	1.5	84.5	0.81	-0.02	0.08	0.8
100	60	35	12.1	84.8	0.73	-0.15	0.07	0.71
100	60	40	21	84.9	0.69	-0.25	0.06	0.64
100	60	45	39.2	81.9	0.66	-0.41	0.09	0.5
100	60	50	67.9	86.5	0.39	-0.36	0.02	0.15
100	60	55	99.5	85.8	0.42	-0.41	0.03	-0.07
100	60	60	139.8	95.6	0.64	-0.41	-0.06	-0.48
100	60	65	167.9	107.2	0.73	-0.15	-0.22	-0.68
100	60	70	180.9	105.3	0.85	0.01	-0.22	-0.82
100	60	75	188.3	108.5	1	0.14	-0.32	-0.94
100	60	80	195.3	112	1	0.24	-0.37	-0.89
100	60	85	207.2	112.7	1.05	0.44	-0.4	-0.86
100	60	90	221.1	110.4	1.1	0.68	-0.38	-0.78
100	60	95	231.4	105.8	1.2	0.9	-0.33	-0.72
100	60	100	242	103.7	1.14	0.98	-0.27	-0.52
100	70	15	304.4	96.4	1.45	1.19	-0.16	0.81
100	70	20	321.5	94.3	1.13	0.7	-0.08	0.88
100	70	25	341.1	88.6	0.89	0.29	0.02	0.84
100	70	30	357.1	85	0.8	0.04	0.07	0.8
100	70	35	9.1	84	0.81	-0.13	0.08	0.79
100	70	40	23.1	85.9	0.73	-0.29	0.05	0.67
100	70	45	35.7	85.8	0.6	-0.35	0.04	0.48
100	70	50	53	86.9	0.47	-0.38	0.03	0.28
100	70	55	98.6	90.3	0.41	-0.4	0	-0.06

100	70	60	144.8	105.1	0.51	-0.28	-0.13	-0.4
100	70	65	166.5	111.5	0.65	-0.14	-0.24	-0.59
100	70	70	179.7	111.2	0.8	0	-0.29	-0.75
100	70	75	189.1	110.4	0.93	0.14	-0.33	-0.86
100	70	80	194.6	114.2	0.87	0.2	-0.36	-0.77
100	70	85	206.3	113.2	0.99	0.4	-0.39	-0.82
100	70	90	217.1	113.8	1.07	0.59	-0.43	-0.78
100	70	95	229.9	113.3	1.01	0.71	-0.4	-0.6
100	70	100	234.5	109.5	1.03	0.79	-0.34	-0.56
100	80	15	300.7	97.3	1.44	1.23	-0.18	0.73
100	80	20	319.3	94.6	1.05	0.69	-0.08	0.8
100	80	25	340.3	90.6	0.91	0.31	-0.01	0.85
100	80	30	358.9	87.7	0.8	0.02	0.03	0.8
100	80	35	11.5	87.5	0.81	-0.16	0.04	0.8
100	80	40	19.8	84.4	0.84	-0.28	0.08	0.79
100	80	45	27.4	86.6	0.68	-0.31	0.04	0.6
100	80	50	42.7	97	0.43	-0.29	-0.05	0.31
100	80	55	91	96.2	0.39	-0.38	-0.04	-0.01
100	80	60	139.1	110.9	0.46	-0.28	-0.16	-0.32
100	80	65	167.2	113.4	0.65	-0.13	-0.26	-0.58
100	80	70	178.3	112.5	0.81	-0.02	-0.31	-0.75
100	80	75	189.2	113.5	0.93	0.14	-0.37	-0.84
100	80	80	197.7	115.7	0.96	0.26	-0.42	-0.83
100	80	85	204.3	116.1	0.96	0.36	-0.42	-0.79
100	80	90	216.9	117.4	0.9	0.48	-0.41	-0.64
100	80	95	225.1	115.7	0.82	0.53	-0.36	-0.52
100	80	100	226.1	107.8	0.7	0.48	-0.21	-0.46
100	90	15	301.5	97.2	1.46	1.23	-0.18	0.76
100	90	20	318.1	96.5	1.06	0.7	-0.12	0.78
100	90	25	341.7	93.1	0.87	0.27	-0.05	0.82
100	90	30	357.6	87.7	0.82	0.03	0.03	0.82
100	90	35	7.8	87.4	0.91	-0.12	0.04	0.9
100	90	40	16.7	87.7	0.79	-0.23	0.03	0.75
100	90	45	24.4	84.9	0.74	-0.31	0.07	0.68
100	90	50	40.2	85.6	0.5	-0.32	0.04	0.38
100	90	55	81	90.2	0.39	-0.39	0	0.06
100	90	60	125.9	104.1	0.5	-0.39	-0.12	-0.28
100	90	65	163.9	116.3	0.61	-0.15	-0.27	-0.53
100	90	70	181.7	113.1	0.76	0.02	-0.3	-0.7
100	90	75	192.7	111.4	0.85	0.17	-0.31	-0.77
100	90	80	199.7	112.9	0.93	0.29	-0.36	-0.81
100	90	85	206.9	115.9	0.91	0.37	-0.4	-0.73
100	90	90	215.5	111	0.9	0.49	-0.32	-0.68
100	90	95	218.7	103.8	0.74	0.45	-0.18	-0.56
100	90	100	217.1	99.4	0.61	0.37	-0.1	-0.48
100	100	15	298.4	97.6	1.42	1.24	-0.19	0.67
100	100	20	320.6	94.9	1.11	0.7	-0.09	0.85
100	100	25	337.5	87.9	0.97	0.37	0.04	0.9
100	100	30	355.3	87	0.87	0.07	0.05	0.87
100	100	35	5.1	84.8	0.95	-0.08	0.09	0.94
100	100	40	11.9	85.1	0.82	-0.17	0.07	0.8
100	100	45	23.4	86.2	0.77	-0.3	0.05	0.7

100	100	50	35	85.4	0.59	-0.33	0.05	0.48
100	100	55	70	93.5	0.42	-0.39	-0.03	0.14
100	100	60	120.1	110	0.4	-0.33	-0.14	-0.19
100	100	65	154.7	125.5	0.51	-0.18	-0.29	-0.37
100	100	70	174.9	116.3	0.67	-0.05	-0.29	-0.59
100	100	75	192.4	114	0.81	0.16	-0.33	-0.72
100	100	80	197.9	113.3	0.87	0.25	-0.34	-0.76
100	100	85	206.8	110.7	0.89	0.38	-0.31	-0.74
100	100	90	213.9	106.7	0.86	0.46	-0.25	-0.68
100	100	95	216.2	98.5	0.81	0.48	-0.12	-0.65
100	100	100	215.8	95.1	0.71	0.41	-0.06	-0.57
100	110	15	299.7	95.5	1.44	1.24	-0.14	0.71
100	110	20	321.4	93	1.16	0.72	-0.06	0.9
100	110	25	339.5	87.8	0.94	0.33	0.04	0.88
100	110	30	356.1	84.8	0.97	0.07	0.09	0.96
100	110	35	3.7	84	0.99	-0.06	0.1	0.98
100	110	40	9.5	83.9	0.88	-0.15	0.09	0.87
100	110	45	20.3	83.5	0.83	-0.29	0.09	0.78
100	110	50	37.8	82.1	0.58	-0.35	0.08	0.45
100	110	55	73.9	87.4	0.45	-0.43	0.02	0.12
100	110	60	116.7	108.1	0.43	-0.36	-0.13	-0.18
100	110	65	148.2	114.4	0.52	-0.25	-0.21	-0.4
100	110	70	173.6	122.6	0.62	-0.06	-0.33	-0.52
100	110	75	187.8	115.6	0.75	0.09	-0.32	-0.67
100	110	80	194.5	103.2	0.83	0.2	-0.19	-0.78
100	110	85	207.8	104.5	0.9	0.41	-0.22	-0.77
100	110	90	213.8	102.1	0.88	0.48	-0.19	-0.72
100	110	95	217	98	0.95	0.56	-0.13	-0.75
100	110	100	216.2	95.2	0.84	0.49	-0.08	-0.67
100	120	15	301.4	90.8	1.53	1.31	-0.02	0.8
100	120	20	323.5	89.3	1.22	0.73	0.01	0.98
100	120	25	340.4	84.4	1.14	0.38	0.11	1.07
100	120	30	354.8	84.4	1.05	0.09	0.1	1.04
100	120	35	5.1	82.2	1	-0.09	0.14	0.99
100	120	40	9.6	82.2	0.97	-0.16	0.13	0.95
100	120	45	21.3	84.1	0.79	-0.29	0.08	0.74
100	120	50	33	82.5	0.64	-0.34	0.08	0.53
100	120	55	61.8	87.3	0.41	-0.36	0.02	0.2
100	120	60	110.2	97.6	0.41	-0.38	-0.05	-0.14
100	120	65	146.4	110.6	0.48	-0.25	-0.17	-0.37
100	120	70	167.8	118.6	0.54	-0.1	-0.26	-0.46
100	120	75	188	109.9	0.76	0.1	-0.26	-0.71
100	120	80	197.1	109.6	0.83	0.23	-0.28	-0.74
100	120	85	204.5	104.5	0.9	0.36	-0.23	-0.79
100	120	90	212.5	98	1.02	0.54	-0.14	-0.85
100	120	95	217.4	96.6	1.06	0.64	-0.12	-0.84
100	120	100	217.3	92.3	1.02	0.62	-0.04	-0.81
100	130	15	302.8	87	1.6	1.34	0.08	0.87
100	130	20	322.9	85.5	1.35	0.81	0.11	1.07
100	130	25	339.8	82.5	1.14	0.39	0.15	1.06
100	130	30	353.2	80.6	0.97	0.11	0.16	0.95
100	130	35	3.5	79.3	1	-0.06	0.18	0.98

100	130	40	9.3	80.7	0.95	-0.15	0.15	0.92
100	130	45	16.7	79.1	0.87	-0.25	0.16	0.82
100	130	50	33.6	77.8	0.71	-0.38	0.15	0.58
100	130	55	58.5	81.5	0.48	-0.4	0.07	0.25
100	130	60	98.7	86.3	0.41	-0.41	0.03	-0.06
100	130	65	140.4	106.6	0.43	-0.26	-0.12	-0.32
100	130	70	170.7	108	0.53	-0.08	-0.16	-0.5
100	130	75	181.3	105.9	0.6	0.01	-0.17	-0.58
100	130	80	195.8	106.5	0.78	0.2	-0.22	-0.72
100	130	85	205.6	104.8	0.87	0.36	-0.22	-0.75
100	130	90	214.1	100.2	1.05	0.58	-0.19	-0.86
100	130	95	219.2	94.8	1.11	0.7	-0.09	-0.86
100	130	100	220	93.9	1.14	0.73	-0.08	-0.87
100	140	15	308.3	81.9	1.58	1.23	0.22	0.97
100	140	20	325.7	79.7	1.32	0.73	0.24	1.07
100	140	25	342.7	77.6	1.15	0.34	0.25	1.08
100	140	30	355.7	78.5	1.01	0.07	0.2	0.99
100	140	35	2.7	78.9	0.95	-0.04	0.18	0.93
100	140	40	7.6	79.3	0.92	-0.12	0.17	0.9
100	140	45	18.9	79.1	0.88	-0.28	0.17	0.82
100	140	50	29.4	77	0.67	-0.32	0.15	0.57
100	140	55	51.1	83.2	0.46	-0.35	0.05	0.29
100	140	60	99.1	85	0.44	-0.43	0.04	-0.07
100	140	65	134.4	97.3	0.47	-0.33	-0.06	-0.32
100	140	70	158.9	103	0.54	-0.19	-0.12	-0.49
100	140	75	175.6	106.3	0.65	-0.05	-0.18	-0.62
100	140	80	196.6	102.2	0.86	0.24	-0.18	-0.8
100	140	85	205.7	101.5	0.96	0.41	-0.19	-0.85
100	140	90	214.4	97.2	1.06	0.59	-0.13	-0.87
100	140	95	219.6	93	1.27	0.81	-0.07	-0.98
100	140	100	222	91.5	1.17	0.78	-0.03	-0.87
100	150	15	311.1	78.6	1.43	1.06	0.28	0.92
100	150	20	329.7	76.2	1.2	0.59	0.29	1.01
100	150	25	340.7	75	0.99	0.32	0.26	0.91
100	150	30	354.9	75.2	0.93	0.08	0.24	0.9
100	150	35	0.3	77.4	0.93	0	0.2	0.9
100	150	40	7.7	77.3	0.92	-0.12	0.2	0.89
100	150	45	15.5	74.4	0.83	-0.21	0.22	0.77
100	150	50	27.1	75.5	0.64	-0.28	0.16	0.56
100	150	55	59.2	76	0.48	-0.4	0.12	0.24
100	150	60	93.1	81.8	0.48	-0.47	0.07	-0.03
100	150	65	139.3	89.3	0.46	-0.3	0.01	-0.35
100	150	70	161.3	102.3	0.52	-0.16	-0.11	-0.48
100	150	75	177.6	103.5	0.65	-0.03	-0.15	-0.63
100	150	80	193.4	100	0.73	0.17	-0.13	-0.7
100	150	85	204.9	97	1	0.42	-0.12	-0.9
100	150	90	215.9	94.4	1.12	0.65	-0.09	-0.9
100	150	95	220.6	92.8	1.26	0.82	-0.06	-0.96
100	150	100	222.6	92.2	1.21	0.82	-0.05	-0.89
100	160	15	314.2	77.1	1.05	0.73	0.23	0.71
100	160	20	329.4	74.5	0.96	0.47	0.26	0.8
100	160	25	343.7	74.5	0.88	0.24	0.24	0.82

100	160	30	350.6	74	0.89	0.14	0.25	0.85
100	160	35	0.1	76	0.9	0	0.22	0.87
100	160	40	5.9	76.9	0.91	-0.09	0.21	0.88
100	160	45	17.2	77.4	0.86	-0.25	0.19	0.8
100	160	50	28.8	74.8	0.66	-0.31	0.17	0.56
100	160	55	60	74.1	0.52	-0.43	0.14	0.25
100	160	60	96.7	76.9	0.49	-0.48	0.11	-0.06
100	160	65	129.9	87.2	0.44	-0.34	0.02	-0.28
100	160	70	156.2	98.1	0.56	-0.22	-0.08	-0.51
100	160	75	179.1	96.9	0.67	-0.01	-0.08	-0.66
100	160	80	193.6	101.8	0.73	0.17	-0.15	-0.69
100	160	85	205.9	99.1	0.97	0.42	-0.15	-0.87
100	160	90	215.7	96.1	1.12	0.65	-0.12	-0.91
100	160	95	223.1	95.1	1.31	0.89	-0.12	-0.95
100	160	100	225.6	93.2	1.29	0.92	-0.07	-0.9
100	170	15	314.3	79.5	0.86	0.6	0.16	0.59
100	170	20	327.8	77.9	0.81	0.42	0.17	0.67
100	170	25	344.6	75.3	0.81	0.21	0.21	0.75
100	170	30	352.6	78	0.81	0.1	0.17	0.79
100	170	35	358.4	77.4	0.96	0.03	0.21	0.94
100	170	40	5.9	77.9	0.85	-0.08	0.18	0.82
100	170	45	13.8	77.1	0.74	-0.17	0.17	0.7
100	170	50	31.2	72.2	0.61	-0.3	0.19	0.5
100	170	55	57.9	74.7	0.51	-0.42	0.13	0.26
100	170	60	98.1	76.4	0.5	-0.48	0.12	-0.07
100	170	65	134.9	87.1	0.52	-0.37	0.03	-0.37
100	170	70	160.9	97.5	0.5	-0.16	-0.07	-0.47
100	170	75	178.8	94.7	0.66	-0.01	-0.05	-0.66
100	170	80	193.1	97	0.74	0.17	-0.09	-0.72
100	170	85	206.3	97	0.98	0.43	-0.12	-0.88
100	170	90	217.7	96.2	1.08	0.66	-0.12	-0.85
100	170	95	224.6	89.7	1.32	0.93	0.01	-0.94
100	170	100	228	92.3	1.4	1.04	-0.06	-0.93
100	180	15	305.7	86.3	0.91	0.73	0.06	0.53
100	180	20	325	80.5	0.78	0.44	0.13	0.63
100	180	25	335.2	80.5	0.78	0.32	0.13	0.7
100	180	30	350	78.4	0.83	0.14	0.17	0.8
100	180	35	357.8	77.8	0.86	0.03	0.18	0.84
100	180	40	6.4	80.4	0.79	-0.09	0.13	0.77
100	180	45	11.4	76.3	0.75	-0.14	0.18	0.71
100	180	50	29.8	72.9	0.65	-0.31	0.19	0.54
100	180	55	53.9	69.7	0.44	-0.33	0.15	0.24
100	180	60	100.9	75.9	0.52	-0.5	0.13	-0.1
100	180	65	132.7	82.7	0.54	-0.39	0.07	-0.36
100	180	70	154.5	91.6	0.6	-0.26	-0.02	-0.54
100	180	75	173.6	95.2	0.62	-0.07	-0.06	-0.62
100	180	80	196.8	98.9	0.78	0.22	-0.12	-0.73
100	180	85	209.6	98.2	0.89	0.44	-0.13	-0.77
100	180	90	219.3	94.5	1.11	0.7	-0.09	-0.85
100	180	95	226.1	94.3	1.36	0.98	-0.1	-0.94
100	180	100	229	92.8	1.44	1.09	-0.07	-0.95

Appendix E: Experimental results - Hot Flow

The first 100 recordings from the sampled data are presented here. The total number of samples logged exceeded 2500. Each column is presenting temperatures in degrees K and the sampling rate is every second.

Inner tube 1	Inner tube 2	Inner tube 3	Inner tube 4	Inner tube 5	Inner tube 6
1011.87	1055.95	1055.83	1047.34	1029.74	1029.45
1011.86	1055.95	1055.82	1047.32	1029.72	1029.35
1011.85	1055.93	1055.8	1047.3	1029.69	1029.31
1011.84	1055.94	1055.81	1047.31	1029.7	1029.32
1011.8	1055.9	1055.77	1047.29	1029.64	1029.24
1011.78	1055.89	1055.77	1047.3	1029.65	1029.28
1011.77	1055.9	1055.76	1047.3	1029.65	1029.29
1011.77	1055.89	1055.75	1047.29	1029.64	1029.27
1011.78	1055.9	1055.75	1047.3	1029.64	1029.26
1011.76	1055.89	1055.75	1047.3	1029.66	1029.32
1011.76	1055.87	1055.73	1047.28	1029.65	1029.28
1011.75	1055.84	1055.71	1047.26	1029.64	1029.25
1011.75	1055.83	1055.71	1047.27	1029.62	1029.35
1011.77	1055.84	1055.71	1047.27	1029.63	1029.34
1011.75	1055.83	1055.71	1047.27	1029.62	1029.35
1011.77	1055.81	1055.69	1047.25	1029.61	1029.28
1011.79	1055.83	1055.69	1047.26	1029.59	1029.3
1011.8	1055.84	1055.71	1047.27	1029.63	1029.33
1011.81	1055.85	1055.71	1047.26	1029.62	1029.26
1011.83	1055.86	1055.71	1047.27	1029.62	1029.28
1011.87	1055.91	1055.74	1047.29	1029.65	1029.27
1011.89	1055.92	1055.78	1047.29	1029.66	1029.26
1011.9	1055.93	1055.79	1047.32	1029.68	1029.28
1011.92	1055.94	1055.81	1047.32	1029.67	1029.25
1011.93	1055.96	1055.82	1047.34	1029.71	1029.35
1011.96	1055.95	1055.82	1047.32	1029.68	1029.27
1011.98	1056	1055.84	1047.34	1029.72	1029.36
1011.99	1056.02	1055.89	1047.35	1029.73	1029.38
1012	1056.04	1055.92	1047.37	1029.74	1029.39
1012.01	1056.05	1055.93	1047.38	1029.75	1029.35
1012.03	1056.06	1055.95	1047.38	1029.76	1029.33
1012.04	1056.07	1055.95	1047.39	1029.75	1029.34
1012.06	1056.08	1056.02	1047.39	1029.79	1029.4
1012.07	1056.08	1056.03	1047.43	1029.79	1029.4
1012.07	1056.07	1056.02	1047.43	1029.79	1029.44
1012.07	1056.08	1056.02	1047.44	1029.78	1029.42
1012.06	1056.09	1056.01	1047.45	1029.78	1029.39
1012.06	1056.06	1056	1047.43	1029.76	1029.35
1012.05	1056.07	1055.98	1047.43	1029.76	1029.32
1012.06	1056.06	1055.96	1047.41	1029.74	1029.41
1012.05	1056.06	1055.95	1047.39	1029.72	1029.35
1012.06	1056.06	1055.95	1047.4	1029.73	1029.34
1012.03	1056.06	1055.94	1047.38	1029.71	1029.29

1012.03	1056.05	1055.92	1047.37	1029.69	1029.27
1012.04	1056.06	1055.94	1047.37	1029.7	1029.34
1012.04	1056.04	1055.93	1047.36	1029.68	1029.3
1012.03	1056.04	1055.95	1047.37	1029.69	1029.36
1012.04	1056.04	1055.93	1047.36	1029.68	1029.3
1012.03	1056.04	1055.96	1047.37	1029.67	1029.32
1012.05	1056.03	1055.96	1047.37	1029.67	1029.31
1012.06	1056.06	1055.98	1047.39	1029.68	1029.3
1012.07	1056.07	1055.97	1047.38	1029.68	1029.32
1012.07	1056.08	1055.98	1047.39	1029.69	1029.33
1012.11	1056.11	1055.98	1047.4	1029.69	1029.31
1012.12	1056.17	1055.99	1047.4	1029.7	1029.35
1012.14	1056.19	1056.02	1047.41	1029.71	1029.33
1012.17	1056.23	1056.05	1047.42	1029.74	1029.4
1012.2	1056.26	1056.07	1047.43	1029.74	1029.47
1012.18	1056.24	1056.06	1047.43	1029.75	1029.43
1012.25	1056.28	1056.09	1047.44	1029.75	1029.44
1012.27	1056.32	1056.13	1047.46	1029.76	1029.46
1012.29	1056.33	1056.15	1047.48	1029.79	1029.47
1012.31	1056.34	1056.16	1047.49	1029.79	1029.43
1012.31	1056.34	1056.18	1047.51	1029.8	1029.46
1012.33	1056.34	1056.17	1047.5	1029.8	1029.43
1012.36	1056.35	1056.19	1047.53	1029.81	1029.46
1012.36	1056.35	1056.19	1047.54	1029.82	1029.45
1012.37	1056.33	1056.18	1047.55	1029.83	1029.49
1012.37	1056.31	1056.18	1047.55	1029.84	1029.46
1012.37	1056.32	1056.19	1047.55	1029.84	1029.46
1012.36	1056.29	1056.19	1047.55	1029.84	1029.46
1012.36	1056.27	1056.17	1047.56	1029.85	1029.47
1012.34	1056.26	1056.15	1047.55	1029.85	1029.49
1012.33	1056.26	1056.14	1047.54	1029.82	1029.37
1012.32	1056.26	1056.13	1047.55	1029.82	1029.33
1012.33	1056.26	1056.14	1047.54	1029.82	1029.37
1012.3	1056.25	1056.12	1047.53	1029.79	1029.31
1012.29	1056.23	1056.11	1047.54	1029.8	1029.36
1012.28	1056.22	1056.1	1047.54	1029.78	1029.38
1012.28	1056.21	1056.1	1047.53	1029.78	1029.39
1012.28	1056.2	1056.1	1047.53	1029.77	1029.35
1012.25	1056.19	1056.09	1047.51	1029.75	1029.24
1012.24	1056.19	1056.07	1047.51	1029.73	1029.21
1012.25	1056.19	1056.06	1047.5	1029.74	1029.23
1012.25	1056.19	1056.06	1047.49	1029.72	1029.25
1012.25	1056.2	1056.07	1047.52	1029.74	1029.29
1012.25	1056.19	1056.06	1047.5	1029.72	1029.26
1012.26	1056.23	1056.07	1047.52	1029.73	1029.3
1012.28	1056.25	1056.1	1047.54	1029.74	1029.26
1012.31	1056.28	1056.13	1047.56	1029.75	1029.24
1012.31	1056.3	1056.14	1047.56	1029.76	1029.29
1012.31	1056.3	1056.14	1047.56	1029.77	1029.32
1012.35	1056.32	1056.14	1047.57	1029.77	1029.31

1012.36	1056.34	1056.16	1047.61	1029.81	1029.36
1012.38	1056.34	1056.16	1047.61	1029.83	1029.32
1012.39	1056.34	1056.17	1047.62	1029.84	1029.28
1012.4	1056.35	1056.18	1047.63	1029.84	1029.33
1012.43	1056.36	1056.18	1047.63	1029.84	1029.32
1012.45	1056.38	1056.19	1047.63	1029.86	1029.34

Outer tube 7	Outer tube 8	Outer tube 9	Outer tube 10	Outer tube 11	Outer tube 12
969.78	968.9	976.07	978.85	971.24	970.27
969.68	968.82	975.95	978.71	970.94	970.05
969.52	968.71	975.86	978.58	970.78	970.25
969.4	968.58	975.8	978.51	970.92	970.67
969.42	968.53	975.81	978.53	971.23	971.24
969.48	968.56	975.84	978.61	971.51	971.84
969.53	968.67	975.92	978.73	971.92	972.6
969.72	968.84	976.06	978.92	972.43	973.28
969.9	968.99	976.17	979.07	972.78	973.83
970.1	969.17	976.34	979.31	973.7	974.84
970.3	969.41	976.57	979.61	974.06	975.26
970.55	969.7	976.84	979.92	974.81	976.68
970.87	970.03	977.15	980.3	975.84	978.44
971.09	970.25	977.34	980.54	976.91	979.66
971.46	970.63	977.63	980.94	977.61	981.02
971.76	970.97	977.91	981.38	978.59	982.42
972.02	971.28	978.18	981.78	979.43	983.17
972.24	971.62	978.45	982.16	980.18	984.17
972.37	971.87	978.65	982.4	980.68	984.66
972.5	972.11	978.83	982.6	980.86	984.37
972.57	972.22	978.94	982.7	981.23	984.49
972.54	972.29	978.98	982.77	981.39	984.31
972.54	972.33	978.99	982.73	981	983.78
972.54	972.29	978.96	982.62	979.96	983.25
972.47	972.21	978.87	982.51	978.87	982.26
972.36	972.09	978.72	982.35	978.26	981.52
972.22	971.97	978.59	982.14	977.57	980.72
972.15	971.86	978.51	982.01	977.18	980.14
971.96	971.61	978.34	981.76	976.44	978.99
971.74	971.36	978.13	981.46	975.71	977.61
971.5	970.98	977.88	981.15	974.89	976.55
971.22	970.65	977.59	980.75	973.91	975.49
970.89	970.2	977.24	980.28	973.05	974.11
970.53	969.84	976.92	979.87	972.41	972.87
970.32	969.66	976.72	979.64	972.13	972.41
970.23	969.49	976.5	979.37	972.06	971.76
970.11	969.35	976.35	979.19	971.77	971.66
970	969.29	976.27	979.07	971.79	971.47
969.94	969.25	976.29	979.02	972.1	971.39
969.93	969.21	976.31	979.03	972.39	971.89
969.93	969.17	976.27	979.08	972.93	972.61
969.97	969.2	976.32	979.16	973.3	972.87
970	969.24	976.42	979.3	973.58	973.95

970.17	969.34	976.58	979.45	974.23	974.63
970.41	969.45	976.74	979.65	975.18	975.31
970.7	969.71	976.94	979.94	976.32	976.27
970.97	969.95	977.17	980.22	977.09	978.02
971.23	970.26	977.41	980.56	978.01	979.44
971.47	970.51	977.6	980.85	978.37	980.31
971.8	970.96	977.94	981.29	979.04	981.19
972.13	971.37	978.33	981.75	979.98	982.04
972.4	971.66	978.6	982.12	980.23	983.14
972.61	971.88	978.78	982.41	980.41	983.56
972.75	972.11	978.96	982.62	980.61	984.15
972.9	972.27	979.13	982.74	980.67	984.29
972.93	972.37	979.17	982.76	980.18	984.71
972.9	972.44	979.18	982.74	979.75	984.32
972.85	972.46	979.14	982.7	979.45	983.54
972.77	972.36	979.03	982.57	978.8	982.96
972.68	972.29	978.92	982.41	978.38	982.02
972.52	972.15	978.8	982.32	978.12	981.38
972.3	971.94	978.67	982.2	977.43	980.29
972.15	971.76	978.55	982.08	976.96	979.54
971.92	971.48	978.33	981.83	976.21	978.24
971.71	971.19	978.09	981.52	975.36	977.11
971.38	970.83	977.78	981.13	974.44	975.79
971.06	970.44	977.47	980.71	973.5	974.41
970.8	970.04	977.15	980.27	972.64	973.04
970.57	969.72	976.83	979.85	972.02	971.85
970.39	969.51	976.65	979.61	971.7	971.35
970.13	969.25	976.4	979.29	971.25	970.91
969.99	969.08	976.23	979.05	971.16	970.43
969.88	968.98	976.15	978.92	971.34	970.41
969.79	968.9	976.1	978.83	971.44	970.9
969.74	968.83	976.04	978.78	971.58	971.31
969.74	968.79	976.02	978.78	972.04	971.5
969.75	968.76	976.01	978.83	972.41	972.24
969.82	968.81	976.04	978.9	972.91	973.06
970	968.89	976.14	979.04	973.57	973.6
970.2	969.08	976.34	979.31	974.42	974.67
970.37	969.3	976.53	979.61	975.28	976.19
970.53	969.5	976.67	979.85	976.03	976.64
970.64	969.61	976.76	979.98	976.34	978.9
970.91	970	977.08	980.39	977.51	980.63
971.18	970.31	977.46	980.84	978.44	981.86
971.4	970.65	977.77	981.27	979.15	982.42
971.67	971	977.97	981.52	978.86	982.53
971.81	971.33	978.21	981.75	979.22	983.11
971.93	971.47	978.34	981.9	979.66	983.7
972.1	971.7	978.53	982.12	979.78	983.61
972.22	971.84	978.65	982.26	979.44	982.88
972.32	971.97	978.76	982.36	979.18	981.93
972.32	972	978.83	982.4	978.84	981.2
972.29	971.98	978.88	982.39	978.49	980.49

972.2	971.9	978.8	982.27	978.02	980.07
972.04	971.83	978.67	982.15	977.73	979.63
971.86	971.59	978.43	981.87	976.7	978.3
971.7	971.33	978.2	981.55	975.93	977.1
971.52	971.1	977.96	981.27	975.23	975.94

Position 1A	Position1B	Position1C	Position1D	Burner tube 1	Burner tube 2	Burner tube 3
1064.01	1063.51	1071.64	1061.85	697.61	675.79	920.39
1064.01	1063.51	1071.64	1061.85	697.61	675.79	919.86
1064.01	1063.51	1071.64	1061.85	697.61	675.79	918.9
1064.08	1063.44	1071.59	1061.73	699.17	674.69	836.59
1064.08	1063.44	1071.59	1061.73	699.17	674.69	918.53
1064.08	1063.44	1071.59	1061.73	699.17	674.69	918.31
1064.08	1063.44	1071.59	1061.73	699.17	674.69	918.2
1064.08	1063.44	1071.59	1061.73	699.17	674.69	918.35
1064.08	1063.44	1071.59	1061.73	699.17	674.69	918.3
1063.8	1063.2	1071.47	1061.71	698.52	675.3	794.79
1063.8	1063.2	1071.47	1061.71	698.52	675.3	919.13
1063.8	1063.2	1071.47	1061.71	698.52	675.3	919.66
1063.8	1063.2	1071.47	1061.71	698.52	675.3	920.27
1063.8	1063.2	1071.47	1061.71	698.52	675.3	922
1063.75	1063.06	1071.38	1061.66	697.72	675	796.89
1063.75	1063.06	1071.38	1061.66	697.72	675	923.06
1063.75	1063.06	1071.38	1061.66	697.72	675	924.24
1063.75	1063.06	1071.38	1061.66	697.72	675	925.08
1063.75	1063.06	1071.38	1061.66	697.72	675	925.87
1063.75	1063.06	1071.28	1061.78	698.03	676.2	842.04
1063.75	1063.06	1071.28	1061.78	698.03	676.2	927.95
1063.75	1063.06	1071.28	1061.78	698.03	676.2	928.31
1063.75	1063.06	1071.28	1061.78	698.03	676.2	928.57
1063.75	1063.06	1071.28	1061.78	698.03	676.2	928.71
1063.82	1063.27	1071.42	1061.99	698.67	675.06	799.82
1063.82	1063.27	1071.42	1061.99	698.67	675.06	928.62
1063.82	1063.27	1071.42	1061.99	698.67	675.06	928.21
1063.82	1063.27	1071.42	1061.99	698.67	675.06	927.77
1063.82	1063.27	1071.42	1061.99	698.67	675.06	927.21
1064.03	1063.49	1071.73	1062.06	699.13	675.64	799.49
1064.03	1063.49	1071.73	1062.06	699.13	675.64	925.55
1064.03	1063.49	1071.73	1062.06	699.13	675.64	925.55
1064.03	1063.49	1071.73	1062.06	699.13	675.64	924.71
1064.03	1063.49	1071.73	1062.06	699.13	675.64	924.28
1064.29	1063.42	1071.64	1061.87	699.06	674.18	797.38
1064.29	1063.42	1071.64	1061.87	699.06	674.18	922.49
1064.29	1063.42	1071.64	1061.87	699.06	674.18	921.75
1064.29	1063.42	1071.64	1061.87	699.06	674.18	921.36
1064.29	1063.42	1071.64	1061.87	699.06	674.18	920.99
1064.29	1063.42	1071.64	1061.87	699.06	674.18	920.51
1064.2	1063.25	1071.5	1061.92	698.46	676.05	795.78
1064.2	1063.25	1071.5	1061.92	698.46	676.05	920.07
1064.2	1063.25	1071.5	1061.92	698.46	676.05	920.01

1064.2	1063.25	1071.5	1061.92	698.46	676.05	920.12
1064.2	1063.25	1071.5	1061.92	698.46	676.05	920.53
1064.06	1063.32	1071.5	1062.11	698.44	675.64	795.95
1064.06	1063.32	1071.5	1062.11	698.44	675.64	922.06
1064.06	1063.32	1071.5	1062.11	698.44	675.64	921.59
1064.06	1063.32	1071.5	1062.11	698.44	675.64	922.73
1064.06	1063.32	1071.5	1062.11	698.44	675.64	923.58
1064.34	1063.37	1071.5	1061.78	700.52	674.82	798.35
1064.34	1063.37	1071.5	1061.78	700.52	674.82	925.06
1064.34	1063.37	1071.5	1061.78	700.52	674.82	926.71
1064.34	1063.37	1071.5	1061.78	700.52	674.82	927.27
1064.34	1063.37	1071.5	1061.78	700.52	674.82	927.54
1064.2	1063.37	1071.5	1061.92	698.2	675.25	800.13
1064.2	1063.37	1071.5	1061.92	698.2	675.25	928.04
1064.2	1063.37	1071.5	1061.92	698.2	675.25	928.06
1064.2	1063.37	1071.5	1061.92	698.2	675.25	928.09
1064.2	1063.37	1071.5	1061.92	698.2	675.25	928.01
1064.22	1063.46	1071.73	1062.13	696.51	676.2	842.91
1064.22	1063.46	1071.73	1062.13	696.51	676.2	927.69
1064.22	1063.46	1071.73	1062.13	696.51	676.2	927.49
1064.22	1063.46	1071.73	1062.13	696.51	676.2	926.77
1064.22	1063.46	1071.73	1062.13	696.51	676.2	926.71
1064.51	1063.77	1071.83	1062.18	698.18	677.47	799.06
1064.51	1063.77	1071.83	1062.18	698.18	677.47	925.4
1064.51	1063.77	1071.83	1062.18	698.18	677.47	924.95
1064.51	1063.77	1071.83	1062.18	698.18	677.47	923.6
1064.51	1063.77	1071.83	1062.18	698.18	677.47	923.33
1064.51	1063.77	1071.83	1062.18	698.18	677.47	922.11
1064.48	1063.65	1071.69	1062.11	698.5	676.4	796.81
1064.48	1063.65	1071.69	1062.11	698.5	676.4	920.72
1064.48	1063.65	1071.69	1062.11	698.5	676.4	919.98
1064.48	1063.65	1071.69	1062.11	698.5	676.4	919.07
1064.48	1063.65	1071.69	1062.11	698.5	676.4	919.27
1064.25	1063.58	1071.69	1062.23	699.06	675.73	836.38
1064.25	1063.58	1071.69	1062.23	699.06	675.73	918.57
1064.25	1063.58	1071.69	1062.23	699.06	675.73	918.56
1064.25	1063.58	1071.69	1062.23	699.06	675.73	918.7
1064.25	1063.58	1071.69	1062.23	699.06	675.73	919.32
1064.39	1063.63	1071.8	1062.09	699.78	676.01	795.99
1064.39	1063.63	1071.8	1062.09	699.78	676.01	920.28
1064.39	1063.63	1071.8	1062.09	699.78	676.01	920.8
1064.39	1063.63	1071.8	1062.09	699.78	676.01	921.82
1064.39	1063.63	1071.8	1062.09	699.78	676.01	924.33
1064.32	1063.42	1071.59	1062.09	698.39	675.6	798
1064.32	1063.42	1071.59	1062.09	698.39	675.6	924.86
1064.32	1063.42	1071.59	1062.09	698.39	675.6	925.51
1064.32	1063.42	1071.59	1062.09	698.39	675.6	926.03
1064.32	1063.42	1071.59	1062.09	698.39	675.6	926.32
1064.37	1063.53	1071.83	1062.13	697.22	676.42	799.53
1064.37	1063.53	1071.83	1062.13	697.22	676.42	926.72
1064.37	1063.53	1071.83	1062.13	697.22	676.42	926.9

1064.37	1063.53	1071.83	1062.13	697.22	676.42	926.82
1064.37	1063.53	1071.83	1062.13	697.22	676.42	926.69
1064.48	1063.53	1071.71	1062.01	699.26	676.72	841.98
1064.48	1063.53	1071.71	1062.01	699.26	676.72	925.94
1064.48	1063.53	1071.71	1062.01	699.26	676.72	925.19

Exhaust flue gas measurements

% O2	ppmv CO	ppmv NO	ppmv NO2	ppmv NOx	mg/m3 NOx
2.85	0	397	9.3	406.3	827
2.85	0	397	9.3	406.3	827
2.85	0	397	9.3	406.3	827
2.84	0	397	9.5	406.5	827
2.84	0	397	9.5	406.5	827
2.85	0	397	9.5	406.5	827
2.85	0	397	9.5	406.5	827
2.85	0	397	9.5	406.5	827
2.86	0	398	9.5	407.5	829
2.86	0	398	9.5	407.5	829
2.84	0	398	9.5	407.5	829
2.84	0	399	9.5	408.5	830
2.84	0	399	9.5	408.5	830
2.83	0	398	9.5	407.5	828
2.83	0	398	9.5	407.5	828
2.84	0	398	9.5	407.5	828
2.84	0	398	9.7	407.7	829
2.84	0	398	9.7	407.7	829
2.84	0	399	9.5	408.5	829
2.84	0	399	9.5	408.5	829
2.84	0	399	9.3	408.3	830
2.84	0	399	9.3	408.3	830
2.84	0	399	9.3	408.3	830
2.84	0	399	9.3	408.3	830
2.84	0	399	9.3	408.3	830
2.84	0	399	9.1	408.1	828
2.84	0	399	9.1	408.1	828
2.85	0	399	9.1	408.1	829
2.85	0	398	9.3	407.3	829
2.85	0	398	9.3	407.3	829
2.87	0	399	9.5	408.5	831
2.87	0	399	9.5	408.5	831
2.84	0	399	9.5	408.5	829
2.84	0	400	9.5	409.5	831
2.84	0	400	9.5	409.5	831
2.82	0	401	9.5	410.5	832
2.82	0	401	9.5	410.5	832
2.83	0	401	9.5	410.5	832
2.83	0	401	9.5	410.5	832
2.86	0	401	9.5	410.5	834
2.86	0	400	9.5	409.5	832

2.86	0	400	9.5	409.5	832
2.87	0	400	9.5	409.5	833
2.87	0	400	9.7	409.7	833
2.84	0	400	9.7	409.7	832
2.84	0	400	9.5	409.5	831
2.84	0	400	9.5	409.5	831
2.83	0	399	9.5	408.5	830
2.83	0	399	9.5	408.5	830
2.86	0	399	9.5	408.5	831
2.86	0	399	9.5	408.5	830
2.86	0	399	9.5	408.5	830
2.88	0	399	9.5	408.5	831
2.88	0	399	9.5	408.5	831
2.86	0	399	9.5	408.5	830
2.86	0	398	9.7	407.7	830
2.86	0	398	9.7	407.7	830
2.84	0	399	9.9	408.9	831
2.84	0	399	9.9	408.9	831
2.86	0	399	9.9	408.9	832
2.86	0	400	9.7	409.7	834
2.86	0	400	9.7	409.7	834
2.88	0	399	9.5	408.5	832
2.88	0	399	9.5	408.5	832
2.9	0	400	9.5	409.5	834
2.9	0	400	9.5	409.5	834
2.9	0	400	9.5	409.5	834
2.9	0	400	9.5	409.5	835
2.9	0	400	9.5	409.5	835
2.88	0	400	9.7	409.7	833
2.88	0	400	9.7	409.7	833
2.87	0	400	9.7	409.7	833
2.87	0	399	9.7	408.7	832
2.87	0	399	9.7	408.7	832
2.87	0	399	9.9	408.9	832
2.87	0	399	9.9	408.9	832
2.86	0	399	9.9	408.9	832
2.86	0	399	9.5	408.5	831
2.86	0	399	9.5	408.5	831
2.88	0	400	9.5	409.5	834
2.88	0	400	9.5	409.5	834
2.91	0	400	9.5	409.5	835
2.91	0	401	9.7	410.7	838
2.91	0	401	9.7	410.7	838
2.91	0	401	9.9	410.9	838
2.91	0	401	9.9	410.9	838
2.89	0	402	9.9	411.9	839
2.89	0	402	9.9	411.9	839
2.86	0	402	9.9	411.9	838
2.86	0	403	9.9	412.9	841
2.86	0	403	9.9	412.9	841
2.86	0	403	10.1	413.1	840

2.86	0	403	10.1	413.1	840
2.87	0	403	10.1	413.1	840
2.87	0	400	10.1	410.1	836
2.87	0	400	10.1	410.1	836
2.92	0	399	9.9	408.9	834
2.92	0	399	9.9	408.9	834
2.95	0	399	9.9	408.9	836

ppm SO2	℃ FT	℃ AT	%CO2	l/min
0	694	27.6	10.28	0.87
0	694	27.6	10.28	0.87
0	694	27.6	10.28	0.87
0	694.3	27.6	10.29	0.87
0	694.3	27.6	10.29	0.87
0	694.6	27.6	10.28	0.86
0	694.6	27.6	10.28	0.86
0	694.6	27.6	10.28	0.86
0	694.6	27.6	10.28	0.86
0	693.8	27.7	10.28	0.86
0	693.8	27.7	10.29	0.86
0	693.5	27.7	10.29	0.86
0	693.5	27.7	10.29	0.86
0	693.5	27.7	10.3	0.86
0	694.5	27.7	10.3	0.86
0	694.5	27.7	10.29	0.86
0	694.8	27.7	10.29	0.86
0	694.8	27.7	10.29	0.86
0	694.4	27.7	10.29	0.86
0	694.4	27.7	10.29	0.86
0	694.4	27.7	10.29	0.87
0	693.1	27.6	10.29	0.87
0	693.1	27.6	10.29	0.87
0	692.4	27.6	10.29	0.87
0	692.4	27.6	10.29	0.87
0	692.4	27.6	10.29	0.87
0	692.8	27.6	10.29	0.87
0	692.8	27.6	10.28	0.87
0	693	27.6	10.28	0.87
0	693	27.6	10.28	0.87
0	693	27.6	10.27	0.87
0	693.4	27.6	10.27	0.87
0	693.4	27.6	10.29	0.87
0	693	27.7	10.29	0.87
0	693	27.7	10.29	0.87
0	693	27.7	10.3	0.87
0	693	27.6	10.3	0.87
0	693	27.6	10.3	0.87
0	693.3	27.6	10.3	0.87
0	693.3	27.6	10.28	0.87
0	693.3	27.6	10.28	0.87
0	693.1	27.6	10.28	0.87

0	693.1	27.6	10.27	0.87
0	693.1	27.6	10.27	0.87
0	693.1	27.6	10.29	0.86
0	693	27.6	10.29	0.86
0	693	27.6	10.29	0.86
0	693	27.6	10.29	0.86
0	692.7	27.6	10.29	0.86
0	692.7	27.6	10.28	0.86
0	693.2	27.6	10.28	0.86
0	693.2	27.6	10.28	0.86
0	693.2	27.6	10.27	0.86
0	693.5	27.7	10.27	0.86
0	693.5	27.7	10.28	0.86
0	693.2	27.7	10.28	0.86
0	693.2	27.7	10.28	0.86
0	693.2	27.7	10.29	0.86
0	693.5	27.6	10.29	0.86
0	693.5	27.6	10.28	0.86
0	694.1	27.5	10.28	0.86
0	694.1	27.5	10.28	0.86
0	694.1	27.5	10.27	0.86
0	693.8	27.6	10.27	0.86
0	693.8	27.6	10.26	0.86
0	693.3	27.6	10.26	0.86
0	693.3	27.6	10.26	0.86
0	693	27.6	10.26	0.86
0	693	27.6	10.26	0.86
0	693	27.6	10.27	0.86
0	693.6	27.5	10.27	0.86
0	693.6	27.5	10.27	0.87
0	693.9	27.5	10.27	0.87
0	693.9	27.5	10.27	0.87
0	693.9	27.5	10.27	0.87
0	693.7	27.6	10.27	0.87
0	693.7	27.6	10.28	0.86
0	693	27.6	10.28	0.86
0	693	27.6	10.28	0.86
0	693	27.6	10.27	0.86
0	693.1	27.5	10.27	0.86
0	693.1	27.5	10.25	0.86
0	693.2	27.5	10.25	0.86
0	693.2	27.5	10.25	0.86
0	693.2	27.5	10.25	0.86
0	693.2	27.5	10.25	0.86
0	693.2	27.5	10.26	0.86
0	693.9	27.5	10.26	0.86
0	693.9	27.5	10.28	0.86
0	693.8	27.5	10.28	0.86
0	693.8	27.5	10.28	0.86
0	693.8	27.5	10.28	0.87